Modelling and Optimisation of Electrochemical and Bioelectrochemical Systems for Environmental Sustainability

Ziming Yang

St Cross College

Department of Engineering Science

A thesis submitted for the degree of

Doctor of Philosophy

Abstract

The growing depletion of fossil fuels and its associated environmental concerns have drawn significant attention. Recent research is oriented towards finding alternative renewable energies or the technologies used for the valorisation of carbon dioxide (CO_2). In this context, bioelectrochemical systems (BESs) and electrochemical CO_2 reduction reaction (ECO2RR) systems have emerged and rapidly developed. Yet, their applications face a number of challenges, mostly related to their poor performance and unclear fundamental mechanisms.

Microbial fuel cells (MFCs), as an archetype and the most studied example of BESs, are the one and only technology to directly convert chemical energy to electricity through the microbially catalysed anodic oxidation processes. Nevertheless, the practical application of MFCs is much hindered due to the lower level of the power output. The design of a stable multi-species biofilm offers a perspective for improving the performance of MFCs. A one-dimensional (1D) dynamic numerical model for a 'fermenter-electrochemically active bacteria (EAB)' type of biofilm is established and adopted to explore the relationships between input variables and the MFC's performance (i.e. biofilm composition and current density) with different mechanisms of anodic extracellular electron transfer (AEETs) in various operating modes. The contrasting results between different operating modes are shown to be mainly induced by the different length of the available time and the different manner of the substrate supply. For instance, MR1 proportion decreases with biofilm thickness in the batch mode, while an opposite trend manifests in the continuous mode with both AEET mechanisms. On the other hand, the contrasting results between different AEETs are attributed to the different intrinsic characteristics of the different electron acceptor. It has been shown that a lesser degree of spatial variation in the fractions of the two species, greater overall growth of MR1 in the biofilm, and higher attainable current density in the case of DET. Some counter-intuitive occasions imply the complex interplays among a series of processes within the multi-species biofilm. The optimal operating conditions towards better performance have also been suggested in this work, such as 15 kΩ for the external resistance in batch with MET; 1×10^{-8} and 1×10^{-7} $\mathrm{L/s}$ for the flowrate in the continuous MFCs with MET and DET, respectively; and 100 μm for the biofilm thickness with moderate conductivity (i.e. 2.5×10^{-6} $\mathrm{S/m}$) in the continuous MFC with DET.

Microbial electrosynthesis cells (MESs), as another typical type of BESs, have significant potential for transforming CO_2 to valuable products through the microbially catalysed cathodic reduction processes without intensive energy input. While the MESs technology is promising, it is still in infancy and its performance (i.e. product yield and production rate) is not satisfactory. As MESs marry microbiological catalysis to electrochemistry through the mechanism of cathodic extracellular electron transfer (CEETs), a deeper insight into CEETs is vital to effectively improve the system's performance. In accordance with the experimental observations and hypothesis, two types of CEETs are interactively integrated in this work into a 1D dynamic mathematical model. Additionally, this numerical study incorporates the detailed biofilm metabolism, microbial kinetics processes and pH effects. By using this experimentally and quantitatively validated model, the governing CEET mechanism in the simulated system is identified as the 'direct-conduction' type; and the impact of several parameters (including applied cathode potentential, initial pH value, specific surface area of the biofilm matrix, biofilm thickness and the specific gas-liquid interfacial area) is analysed. The simulation results have suggested that, for the system modelled in this work, the applied cathode potential of -1.2 V (vs Ag/AgCl) is the optimal value to gain a higher value of acetate production rate and acetate yield simultaneously. The numerical results show that local pH plays an important role in product yield and production rate. A larger value for both the specific surface area of the biofilm matrix and the biofilm thickness is preferable to obtain a higher acetate production rate. Regarding the specific gas-liquid interfacial area, the acetate production rate can be improved when the area increases to $\sim 1\ \mathrm{m}^{-1}$. It would become less effective to improve the acetate production rate by further increasing the specific gas-liquid interfacial area (i.e. $> 1\ \mathrm{m}^{-1}$).

Similar to the MESs technology, ECO2RR is capable of achieving sustainable CO_2 valorisation by consuming water and electricity only. Depending on the catalyst type (generally metal catalysts), CO_2 can be reduced to different valuable chemicals. However, the lower product yield, which is rooted in the intrinsic problems of CO_2 (such as larger mass transfer resistance and lower solubility), prevent ECO2RR from being put into actual use. The integration of a gas diffusion electrode (GDE) into an ECO2RR system could effectively minimise those aforementioned limitations by separating gas and liquid phase. To obtain better performance (i.e. amplified current density and higher product yield), a GDE-based ECO2RR system is modelled and tested to find the optimal design (such as the optimal catalyst loading and porosity) and operating conditions (such as the optimal applied cathode potential). The numerical results show that product yield is improved as the applied cathode potential becomes

more negative. Regarding the specific electrical energy consumption, an optimal value of the applied cathode potential of $-0.5\ \mathrm{V}$ (vs Reversible Hydrogen Electrode, RHE) exists. The simulation results have suggested that a low loading with a sparse arrangement of catalyst particles in the catalyst layer is optimal to gain the maximum product yield, while higher energy efficiencies may prefer a more compact (i.e. thin and dense) catalyst layer. The simulation results also show that GDE is scalable as it retains stable performance when its geometrical surface area varies. This result offers a theoretical basis in the further commercialisation of this strategy.

Overall, the findings from these model-based analyses are instrumental for offering a holistic understanding of respective systems and for furthering these systems towards successful industrial applications.

Acknowledgements

Foremost, I would like to express my special thanks to my supervisor, Prof. Aidong Yang, who provided me with advice and the possibility to complete this thesis. Also, I would like to give my sincere thanks to Prof. Eileen Yu, for her kind support and valuable feedback on my research.

Thanks to Dr. Lei Xing, Dr. Peng Song and Dr. Chao Chen, for their encouragement, help and particularly their insightful comments about COMSOL. I would like to acknowledge my friends and co-workers: Dr. Da Li, Dr. Hang Xiang, Dr. Paniz Izadi, Dr. Chao Chen, Dr. Hong Zeng and Mr. Till Weidner. My thanks also go to Prof. Jin Xuan and Prof. Shaoan Chen for showing interest in my research.

I am very grateful to the China Scholarship Council for funding my research and studentship.

Last but not the least, I am very much thankful to my family, for their unwavering love and support.

Publications

Journal paper

Z. Yang, D. Li, L. Xing, H. Xiang, J. Xuan, S. Cheng, E. H. Yu*, A. Yang*, Modeling and Upscaling Analysis of Gas Diffusion Electrode-Based Electrochemical Carbon Dioxide Reduction Systems, ACS Sustainable Chem. Eng., 2021, 9, 1, 351-361.

https://doi.org/10.1021/acssuschemeng.0c07387

Z. Yang, A. Yang*, Modelling the Impact of Operating Mode and Electron Transfer Mechanism in Microbial Fuel Cells with Two-Species Anodic Biofilm, Biochem. Eng. J., 2020, 158, 107560.

https://doi.org/10.1016/j.bej.2020.107560

Conference paper

Z. Yang, A. Yang*, Modelling and Analysis of Microbial Fuel Cells with a Two-Species Anode Biofilm, in: Proc. 30th Eur. Symp. Comput. Aided Process Eng., 2020, 48, 1591-1596.

https://doi.org/10.1016/B978-0-12-823377-1.50266-4

Nomenclature

Symbols

a_V	Specific surface area for the biofilm matrix, m^{-1}
a_{gl}	Specific gas-liquid interfacial area, m^{-1}
a_{sl}	Specific solid-liquid interfacial area, m^{-1}
A	Area, m^2
b	Process coefficient, dimensionless
C	Concentration (for the soluble components), M
D	Molecular diffusivity (diffusion coefficient), $m^2\ s^{-1}$
d	Diameter, m
E^0	Standard mediator redox potential, V
f_e^o	Fraction of the EAB's substrate used for energy generation, dimensionless
F	Faraday constant, $C\ mol^{-1}$
FE	Faraday efficiency, %
f	Factor, dimensionless/ Coefficient, dimensionless
g	Gravitational acceleration, $m\ s^{-2}$
H	Henry's constant, Pa M^{-1}/Height, m
i_L	Limiting current density, $A\ m^{-2}$
i_o	Exchange current density, $A\ m^{-2}$
I	Overall current, A
i	Current density, $A\ m^{-2}$
J	Molar flux, $mol\ m^{-2}\ s^{-1}$
K_{GL}	Overall mass transfer coefficient, $m\ s^{-1}$
k_l^{eff}	Effective conductivities for electrolyte, $S\ m^{-1}$
k_s^{eff}	Effective solid conductivity, $S\ m^{-1}$
K	Equilibrium constant, depending on the specific reaction
k	Reaction constant, depending on the specific reaction
L	Thickness, m
M	Half-saturation (Monod) constant, M/Molar weight, $kg\ mol^{-1}$
m	Mass loading, $kg\ m^{-2}$

n	The number of electrons transferred, dimensionless
P	Pressure, Pa
PY	Product (i.e. formate) yield, kg s^{-1}
Q	Source term, its unit relying on the specific reactions
q	Volumetric flowrate, m^3 s^{-1}
R_{ext}	External resistance, Ω
R_g	Ideal gas constant, J K^{-1} mol^{-1}
R_{int}	Internal resistance, Ω
R_{mem}	Specific resistance of membrane, Ω
R	(Volumetric) reaction rate, mol m^{-3} s^{-1}
r	(Surface) reaction rate, mol m^{-2} s^{-1}/Radius, m
S	Stoichiometry, dimensionless/ Saturation coefficient, dimensionless
$S(\tau)$	Sigmoid function, dimensionless
$SEEC$	Specific electrical energy consumption, kWh kg $(\text{formate})^{-1}$
T	Operating temperature, K
t	Time, s
u	Velocity, m s^{-1}
u_L	$\frac{dL_F}{dt}$, m s^{-1}
V_C	Applied cathode potential, V
V_{app}	Applied/required potential, V
V	Volume, m^3
v	Advective velocity, m s^{-1}
W	Molar weight, kg mol^{-1}/ Width, m
X	Concentration (for the biomass), kg m^{-3}
x	Molar fraction, dimensionless
Y	Yield coefficient, depending on the specific reaction
z	Valence of ionic species,dimensionless
α	Charge transfer coefficient, dimensionless
β	Transfer coefficient, dimensionless
γ	Degree of reduction, mol mol^{-1}
ζ	Converted coordination, dimensionless
η	Overpotential, V/$(\varphi_{M_c} - \varphi_s)$, V

κ	Permeability, m^2
μ	Specific growth rate, s^{-1}/Dynamic viscosity, Pa s
ξ	Scale-up factor, dimensionless
ρ	Density, kg m^{-3}
φ	Potential, V
ω	Mass fraction, dimensionless
ϵ	Porosity, dimensionless
δ_d	Diffusion layer thickness, m
δ_{ele}	Thickness of the electrolyte thin film, m
θ_b	Volume fraction of the total biomass in the biofilm, dimensionless
$\vartheta(\mathrm{pH})$	Function of pH, dimensionless
ΔH	Change of heat, kJ mol^{-1}
ΔS	Change of entropy, J mol^{-1} K^{-1}
$\Delta_{sol}H$	Enthalpy of dissolution, J mol^{-1}

Subscripts

A	Active acetogens
a	Anode
act	Activation overpotential
B	Biotic reactions
BL	Bulk liquid phase
b	Total biomass
C	Cathode
CL	Catalyst layer
c	Cathode
cat	Catalyst
con	Concentration overpotential
dea	Cell death process
E	Electrode/Electrochemical reactions
EAB	Electrochemically active bacteria
$ELEC$	Electrolyte channel
EXT	Extension

eq	Equilibrium state
F	Biofilm
FB	Fermentative bacteria
f	Flow
$GASC$	Gas chamber
GDL	Gas diffusion layer
g	Mixture gas/gas
gro	Autotrophic growth
H	Homogeneous reactions
I	Inactive acetogens
IS	Intermediate substrate (EAB's substrate)
i	Biomass/Gaseous species
in	Inlet flow
j	Soluble components/Aqueous species
k	Gaseous species, $k \neq i$
LBL	Liquid boundary layer
l	Mixture liquid
M_a	Anodic potential corresponding to the half maximum specific growth rate
M_c	Cathodic potential corresponding to the half maximum specific growth rate
Mo	Oxidised form of the mediator (FMN)
Mr	Reduced form of the mediator ($FMNH_2$)
m	Medium
mem	Membrane
opt	Optimum
ox	Oxidation reaction
P	Gas-liquid mass transfer (phase transfer) reaction
PS	Primary substrate (FB's substrate)
p	Porous
q	(General) soluble components
red	Reduction reaction
s	Local (solid) electric potential
W	Pure water

Superscripts

$*$	Modified
C	Conduction-based extracellular electron transfer mechanism
HER	Hydrogen evolution reaction
M	Mediator-based extracellular electron transfer mechanism
max	Maximum
min	Minimum
o	Intrinsic characteristics
ref	Reference condition
eff	Effective
0	Initial state

Abbreviations

AD	Anaerobic digestion
AEET	Anodic extracellular electron transfer mechanism
AEM	Anion exchange membrane
BES	Bioelectrochemical system
BPM	Bipolar exchange membrane
CCS	Carbon capture and storage
CCU	Carbon capture and utilisation
CCUS	Carbon capture, utilisation and storage
CDET	Cathodic direct conduction-based extracellular electron transfer
CEET	Cathodic extracellular electron transfer mechanism
CEM	Cation exchange membrane
CL	Catalyst layer
CMET	Cathodic mediator-based extracellular electron transfer
CNT	Carbon nanotube
DET	(Anodic) direct conduction-based extracellular electron transfer
dual-CEET	Dual-cathodic electron transfer mechanism
E. coli	*Escherichia coli*
EA	Electron acceptor
EAB	Electrochemically active bacteria
ECO2RR	Electrochemical CO_2 reduction reaction

ED	Electron donor
EET	Extracellular electron transfer
ELEC	Electrolyte channel
FB	Fermentative bacteria
FE	Faraday efficiency
GASC	Gas chamber
GDE	Gas diffusion electrode
GDL	Gas diffusion layer
GHG	Greenhouse gas
HER	Hydrogen evolution reaction
HNQ	2-hydroxy-1,4-naphtboquinone
LBL	Liquid boundary layer
LCA	Life cycle analysis
MDC	Microbial desalination cell
MEA	Membrane electrode assembly
MEC	Microbial electrolysis cell
MES	Microbial electrosynthesis cell
MET	(Anodic) mediator-based extracellular electron transfer
MFC	Microbial fuel cell
MRC	Microbial remediation cell
MSC	Microbial solar cell
OER	Oxygen evolution reaction
PCE	Tetrachloroethene
PY	Product yield
RDS	Rate-determining step
S. oneidensis	*Shewanella oneidensis*
SEEC	Specific electrical energy consumption
TCE	Trichloroethene
TEA	Techno-economic analysis

Contents

List of Figures

List of Tables

Chapter 1 Introduction

1.1 Background

Rapid civilisation and industrialisation have not only offered humanity a convenient life but also brought a series of unprecedented challenges[1]. Owing to the advantages of abundance, low-cost and high heating value[2], fossil fuels are still the current main pillars for the global energies[3] and economies[4]. On the other hand, it is getting difficult to fulfil the energy demand with fossil fuels alone[2]. It has been predicted that global energy consumption would be doubled within the next thirty years, and even tripled by the year of 2100[2]. In addition to the increasing demand for energy, the depletion of fossil fuels makes it imperative to explore other fuels/chemicals that can fill the potential energy gaps[2] or completely replace fossil fuels[4]. Furthermore, the combustion of fossil fuels has a negative impact on the environment, as it contributes to the majority of the emissions of carbon dioxide (CO_2) in a modern society[5]. In recent decades, the cumulative CO_2 concentration in the atmosphere has exceeded 400 ppm[6]. This figure is still increasing with a higher speed (i.e. ~ 20 ppm per decade[7]), which is roughly ten times the average CO_2 concentration increase rate (i.e. per decade) over the last hundreds of thousands of years[7]. One of the concomitant problems of elevated atmospheric CO_2 concentration is global warming. From the end of the 19th century to the early 21st century, the earth's globally averaged temperature has been reported to increase by ~ 0.85 ℃[5]. In order to curb climate change, several remarkable international agreements, such as Kyoto Protocol and Paris Agreement, have operationalised for the purpose of reducing greenhouse gas (GHG) (mainly CO_2) emissions. The environmental concerns have reinforced the need for the development of alternative energies, and also called for the carbon capture, utilisation and storage (CCUS) technologies.

The exploration of renewable energy sources (e.g. solar, wind, biomass, hydro and geothermal energy) and the dissemination of renewable energy technologies (e.g. turning natural renewable energies to electricity, heat or fuels) are rising territories of the current research[8]. In contrast to fossil fuels with an extremely slow generation rate and a limited supply, renewable energy sources could be continuously replenished by nature and, in principle, far outstrips the world's energy demand[8]. Since 2010, the market of renewable energy sources has continued to expand, and several innovative technologies such as wind turbine, hydro and solar photovoltaic systems

have grown vigorously[8]. Global electricity generated from renewable energy has increased by ~1.7 times over the last ten years, and it is expected to climb to ~2.7 times in 2035[8]. In comparison with the intermittent renewable energy resources (i.e. non-dispatchable and fluctuate with conditions), biomass-based electricity generation is more reliable and predictable. Coupled with the abundance of biomass[8], more and more researchers are focusing on bioelectricity production. Microbial fuel cells (MFCs), as a typical example of bioelectricity generation systems, are capable to generate renewable electricity from organic/inorganic matters through biocatalytic processes. As various wastewater can be used to fuel the systems, MFCs also offer an environmentally friendly possibility to meet the water sanitation needs, and to replace the current expensive and energy-intensive wastewater treatments.

Regarding CCUS, it is a collective term that encompasses (i) carbon capture and utilisation (CCU) and (ii) carbon capture and storage (CCS) technologies based on the final destination of the captured CO_2[9]. CO_2 can be captured: (i) before the occurrence of combustion and power generation (also referred to as "pre-combustion/pre-conversion capturing CO_2); (ii) during the combustion processes (known as "oxy-fuel combustion"); or (iii) after the normal combustion (coined as "post-combustion capturing CO_2 ")[2,9,10]. However, the current carbon capture strategies always encounter a series of problems, such as high cost[2], energy intensive[2,11], a higher requirement of CO_2 storage capacity[11] and potential leakage of the aqueous adsorbents/absorbents[10,12]. Following a set of subsequent processes (like dehydration and compression), the captured CO_2 would be eventually (i) converted to valuable fuels/chemicals (corresponding to CCU)[2,9,10], or (ii) stored in places such as underground and ocean (corresponding to CCS). In recent years, CCU technologies have attracted vast attention and wide interests due to their environmental and economic benefits. It has been widely reported that CO_2 can be converted thermally, photochemically, biochemically or electrochemically[2,12,13]. Compared with the traditional thermodynamic CO_2 conversion process[13], the innovative approaches based on photochemical, biochemical and electrochemical processes pave a promising pathway to 'green' products by avoiding the use of fossil fuels to provide energy[2]. Microbial electrosynthesis cells (MESs) and electrochemical CO_2 reduction reaction (ECO2RR) systems incorporating gas diffusion electrode (GDE) are particularly emphasised in this thesis. Both of them are capable of valorising CO_2 to valuable products, and operating under mild operational conditions (i.e. room temperature and ambient pressure). The distinguished difference between the two systems lies in catalysts: the conventional metal catalysts are generally adopted in the electrochemical CO_2 reduction

systems, while autotrophic bacteria function as biocatalysts in MESs. Depending on the operating conditions and type of (bio)catalysts, CO_2 can be converted to different products.

1.2 Motivation and objectives

Although the aforementioned technologies (i.e. MFCs, MESs and ECO2RR systems) are promising, the poor performance limits their industrial applications from an engineering point of view. To date, many efforts have been made to improve their performance.

Regarding MFCs, it has been proven that the synthesised multispecies biofilm exhibits a higher current density and substrate conversion rate[14–17]. In addition, it is preferred for practical use owing to its better stability[17,18]. The spatial heterogeneity together with the anodic extracellular electron transfer mechanisms (AEETs) and the interplays between different microbial species determine the performance of MFCs. Thus, examining the impacts of these factors holds the potential to not only improve MFCs' performance but also provide deeper insights into the complex functionalities in other similar systems.

For MESs, the lower product yield and production rate are the main obstacles to achieving successful industrialisation and commercialisation. Research towards MESs has been intensified in the past decades, albeit mostly by experimental work. There are rather fewer studies shedding light on the cathodic extracellular electron transfer mechanisms (CEETs), which play a pivotal role in systems' output. Mathematical frameworks and numerical simulations could improve the understandings of the nascent MESs technologies, and provide an efficient approach to predict and optimise the systems.

Analogous to MESs' study, despite the numerous investigations of GDE-based ECO2RR systems aiming to intensify the current density and improve the selectivity of the desired product, most of them, however, are of the nature of experimental exploration. The understandings of microscopic interactions in the systems and their impacts on the whole electrolyser performance, which are vital to the system development but hardly accessible through experimental work, still remain unrevealed. A model-based analysis is instrumental to gain a holistic understanding of mechanisms such as kinetic-transport interactions in sophisticated electrochemical systems and can be used as a tool for future development towards successful practical applications.

The overall aims of the research are outlined as follows:

1. To develop novel mathematical models that are capable of capturing the kinetics-transport interactions and complex behaviours of entwined processes, which involves electrochemical, transport (mass transfer) phenomena and, where applicable, biological growth and a complex spatial structure of multispecies biofilm.
2. To apply such advanced models to improve the understanding of other similar (bio)electrochemical systems and guide their optimal design.

1.3 Thesis structure

This thesis is presented in the integrated format and consists of six chapters in total, including introduction (Chapter 1), literature review (Chapter 2), three research chapters (Chapters 3-5) and conclusions (Chapter 6). Note that each of the research chapters is composed of a published peer-reviewed journal paper or a manuscript to be submitted. For consistency, the original terms and the original numbers of sections, figures, tables and equations in the peer-reviewed journal paper/manuscript are re-phrased and re-arranged in this thesis. The outlines for these chapters are enumerated as follows:

1. Chapter 1 provides the background, motivation and aims of the research.
2. Chapter 2 reviews the literature of bioelectrochemical systems (BESs) and ECO2RR systems. Each part addresses its fundamental mechanism, relevant modelling work, research gaps and outlook.
3. Chapter 3 presents the modelling work on MFCs with a two-species anodic biofilm, and focuses on analysing (i) the responses of dynamics and spatial distribution of the two-species anodic biofilm to different individual AEETs (i.e. MET and DET) and operating conditions (i.e. batch and continuous modes); (ii) the influence of the two-species spatial pattern on the MFCs current generation. The performance of the biofilm and current generation with different AEETs and operating conditions are compared and discussed. The modelling of bioelectrochemical kinetics lays the foundation for the work in Chapter 4.
4. Chapter 4 describes the numerical study of the cathodic biofilm with multiple types of CEETs in MESs. The qualitatively validated model is employed to identify the governing CEET, and analyse the impact of several important parameters on product yield and production rate.

5. Chapter 5 moves onto the GDE-based ECO2RR systems, for which a two-dimensional multiphase model capturing the details of the catalyst layer is established. Specific electrical energy consumption (SEEC) and product yield (PY) are used as indicators to examine the GDE scalability and evaluate the system's performance under various conditions.
6. Chapter 6 concludes the studies presented in this thesis, which emphases the contributions of each project. The limitations of this research are also pointed out, followed by possible future research directions.

References

(1) Ganesh, I. Electrochemical Conversion of Carbon Dioxide into Renewable Fuel Chemicals - The Role of Nanomaterials and the Commercialization. *Renew. Sustain. Energy Rev.* **2016**, *59*, 1269–1297.

(2) Mustafa, A.; Guene, B.; Shuai, Y.; Wang, Z.; Tan, H. Current Technology Development for CO2 Utilization into Solar Fuels and Chemicals : A Review. *J. Energy Chem.* **2020**, *49*, 96–123.

(3) White, M. T.; Bianchi, G.; Chai, L.; Tassou, S. A.; Sayma, A. I. Review of Supercritical CO2 Technologies and Systems for Power Generation. *Appl. Therm. Eng.* **2021**, *185*, 116447.

(4) Razmjoo, A.; Kaigutha, L. G.; Rad, M. A. V.; Marzband, M.; Davarpanah, A.; Denai, M. A Technical Analysis Investigating Energy Sustainability Utilizing Reliable Renewable Energy Sources to Reduce CO2 Emissions in a High Potential Area. *Renew. Energy* **2021**, *164*, 46–57.

(5) Pachauri, R. K.; Meyer, L. *Climate Change 2014: Synthesis Report*; Geneva, 2014.

(6) Dáder, B.; Fereres, A.; Moreno, A.; Trębicki, P. Elevated CO2 Impacts Bell Pepper Growth with Consequences to Myzus Persicae Life History, Feeding Behaviour and Virus Transmission Ability. *Sci. Rep.* **2016**, *6*, 19120.

(7) Nwabara, U. O.; Cofell, E. R.; Verma, S.; Negro, E.; Kenis, P. J. A. Durable Cathodes and Electrolyzers for the Efficient Aqueous Electrochemical Reduction of CO2.

ChemSusChem **2020**, *13*, 855–875.

(8) Ellabban, O.; Abu-Rub, H.; Blaabjerg, F. Renewable Energy Resources: Current Status, Future Prospects and Their Enabling Technology. *Renew. Sustain. Energy Rev.* **2014**, *39*, 748–764.

(9) Cuéllar-Franca, R. M.; Azapagic, A. Carbon Capture, Storage and Utilisation Technologies: A Critical Analysis and Comparison of Their Life Cycle Environmental Impacts. *J. CO2 Util.* **2015**, *9*, 82–102.

(10) Yaashikaa, P. R.; Senthil Kumar, P.; Varjani, S. J.; Saravanan, A. A Review on Photochemical, Biochemical and Electrochemical Transformation of CO2 into Value-Added Products. *J. CO2 Util.* **2019**, *33*, 131–147.

(11) Baena-Moreno, F. M.; Rodríguez-Galán, M.; Vega, F.; Alonso-Fariñas, B.; Vilches Arenas, L. F.; Navarrete, B. Carbon Capture and Utilization Technologies: A Literature Review and Recent Advances. *Energy Sources, Part A Recover. Util. Environ. Eff.* **2019**, *41* (12), 1403–1433.

(12) Lu, X.; Leung, D. Y. C.; Wang, H.; Leung, M. K. H.; Xuan, J. Electrochemical Reduction of Carbon Dioxide to Formic Acid. *ChemElectroChem* **2014**, *1*, 836–849.

(13) Snoeckx, R.; Bogaerts, A. Plasma Technology-a Novel Solution for CO2 Conversion? *Chem. Soc. Rev.* **2017**, *46*, 5805–5863.

(14) Liu, H.; Hu, H.; Chignell, J.; Fan, Y. Microbial Electrolysis: Novel Technology for Hydrogen Production from Biomass. *Biofuels* **2010**, *1* (1), 129–142.

(15) Logan, B. E. Exoelectrogenic Bacteria That Power Microbial Fuel Cells. *Nat. Rev. Microbiol.* **2009**, *7* (5), 375–381.

(16) Yang, Y.; Wu, Y.; Hu, Y.; Cao, Y.; Poh, C. L.; Cao, B.; Song, H. Engineering Electrode-Attached Microbial Consortia for High-Performance Xylose-Fed Microbial Fuel Cell. *ACS Catal.* **2015**, *5* (11), 6937–6945.

(17) Liu, T.; Yu, Y. Y.; Chen, T.; Chen, W. N. A Synthetic Microbial Consortium of Shewanella and Bacillus for Enhanced Generation of Bioelectricity. *Biotechnol. Bioeng.*

2017, *114* (3), 526–532.

(18) Anna Prokhorova, A.; Katrin Sturm-Richter, a Andreas Doetsch, B.; Johannes Geschera, C. Resilience, Dynamics, and Interactions within a Model Multispecies Exoelectrogenic-Biofilm Community. *Appl. Environ. Microbiol.* **2017**, *83* (6).

Chapter 2 Literature review

Greenhouse gases (GHGs) refer to the gases which are capable of trapping the heat from the sun into the earth's atmosphere. They primarily consist of water vapour (H_2O), carbon dioxide (CO_2), methane (CH_4), nitrous oxide (N_2O) and ozone (O_3). The nature GHG effect leads to an appropriate increase in temperature, allowing life to be able to survive. However, since the start of the industrial revolution[1], the GHG effect is much pronounced by human activities and becomes a daunting challenge. Anthropogenic CO_2 from burning fossil fuels accounts for about 70% of the GHG emissions[2]. Driven by the concerns about depletion of available fossil fuels and associated environmental issues, research interests in exploring (i) the renewable energy options to leave fossil fuels on the ground and (ii) the carbon capture and utilisation (CCU) technologies have been proliferated in the past decades[2]. Moreover, with the population growth and society development, wastewater and solid waste have become 'societal burden'. The exploration of a sustainable approach is highly desirable to treat them properly[3].

2.1 Bioelectrochemical systems (BESs)

As one of emerging technologies, bioelectrochemical systems (BESs) are capable to convert chemical energy into green electricity and other value-added products (such as hydrogen, hydrogen peroxide, methane, acetate, longer chain organics and their corresponding alcohols)[4] through a series of biochemical and electrochemical processes[4–7] (see Figure 2.1). In a BES, living microorganisms are responsible to catalyse electrochemical reactions[5,7].

Strictly speaking, a catalyst is defined as the substance not consumed or changed in the reaction, nor affecting the net-energy balance of reaction. The living microorganisms in BESs need to consume certain energy to support itself for growth and cell maintenance, and thus it does not strictly obey the definition of catalyst[5,8,9]. More rigorously, biocatalysis processes should be called biotransformation processes[8]. Nevertheless, the microorganisms, which act as catalysts, accelerate reactions by decreasing overpotential[5]. Therefore, for the sake of convenience, the term 'biocatalyst' is used in this thesis, which is in line with its most frequently used definition in the literature.

2.1.1 Mechanisms and types of BESs

2.1.1.1 Overview of BESs mechanisms

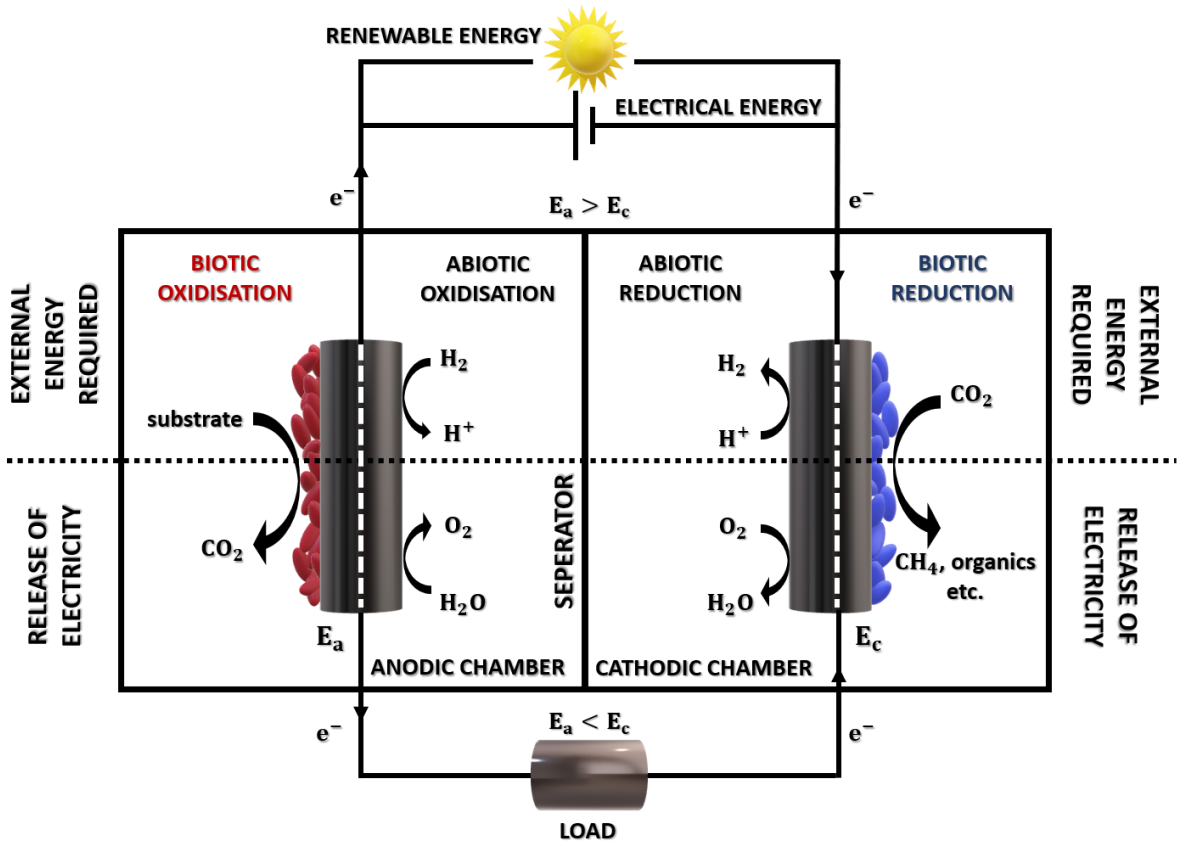

Figure 2.1 Schematic illustration of a bioelectrochemical system (BES).

Generally, a BES consists of anodic and cathodic chambers where the respective anode and cathode are immersed in, an external circuit, and a separator (typically an ion exchange membrane or a salt bridge)[5,6,10–12] (see Figure 2.1). BESs comprise oxidation reactions occurring in the anodic chamber and reduction reactions occurring in the cathodic chamber[5]. During the operation, electrons are liberated in the anodic chamber and transferred through an external circuit to the cathode[6,11].

The specific anodic and cathodic reactions determine the operation scenarios: BESs could operate as (i) a 'galvanic cell' with the spontaneous release of electricity; and (ii) an 'electrolysis/electrosynthesis cell' which requires external energy to trigger non-spontaneous redox reactions for the generation of the value-added products[5,6,8]. Even for an identical anodic reaction, BESs combined with various cathodic reactions could operate in the opposite direction (i.e. generation or consumption of electricity)[5,8]. Theoretically, the negative free

reaction energy leads to a spontaneous redox reaction (implying that BESs output electricity), whereas the positive free reaction energy means that a redox reaction is non-spontaneous (implying that external energy is required). The free reaction energy, ΔG^r, can be either derived from thermodynamics or linked to anodic and cathodic potential electrochemically[6,8,13]:

$$\Delta G^r = -nF(E_c - E_a) \quad (2.1)$$

where n represents the number of electrons transferred per redox reaction; F is the Faraday constant; E_c and E_a represent the cathode and anode potential, respectively.

According to Eq. (2.1) and Figure 2.1, the redox reactions take place spontaneously and BESs deliver an electric power output when the cathode potential is higher than the anode potential. Otherwise, additional energy should be provided[6,8] (see Figure 2.1).

Apart from powering BESs by using the conventional electricity sources, the same systems could be used to harvest renewable energies (such as solar, wind and geothermal energy) to drive the non-spontaneous reactions to produce high heating value chemicals, which can be viewed as a means for renewable energy storage in the form of value-added chemicals[14]. Note that all the discussions above are without regard to the occurrence of overpotentials (electrochemical losses). In reality, a variety of BESs' overpotentials cannot be neglected and would lead to additional positive free reaction energy[5]. This passive effect for 'galvanic cell' means that there would be less electricity output than the theoretical value while for 'electrolysis/electrosynthesis cell' more external energy would be required compared with the thermodynamical need[5,8].

Depending on the reaction spontaneity[6] and function, BESs are further classified into different systems such as microbial fuel cells (MFCs), microbial electrolysis cells (MECs), microbial electrosynthesis systems (MESs), microbial solar cells (MSCs), microbial remediation cells (MRCs) and microbial desalination cells (MDCs)[4,11]. In the following sections, we will give a higher-level overview of the application niches of BESs and demonstrate them in detail, especially for MFCs and MESs.

2.1.1.2 MFCs

MFCs, as an archetype and the most extensively studied example of BESs[7,8,15], are the only technology to directly convert chemical energy to electricity through a biocatalysed anodic

oxidation process[7,8]. Since pollutants (from various environments, including wastewater, contaminated soils and sediments[6]) can feed MFCs as a substrate, MFCs are promising for wastewater treatment and environment remediation[5,11]. In addition to the aforementioned large-scale applications, MFCs are envisaged as biosensors for monitoring oxygen[12] or detecting toxicity[7,11,12].

The microorganisms that are able to achieve extracellular electron transfer (EET) are referred to as electrochemically active bacteria (EAB)[16]. Some references also term this type of microorganisms as electroactive bacteria[17]. Anaerobic EAB oxidise the substrate and free electrons and protons. Electrons released by the bacteria are conveyed to the anode via the mechanisms of the anodic extracellular electron transfer (AEET) and then flow through an external circuit to the cathode. The AEET mechanisms between bacteria and an anode are illustrated in Section 2.1.2.1. Typically, the protons would move through the separator and react with oxygen, O_2, to form pure water in the cathodic chamber[5,8,12] (see Figure 2.1).

In comparison with abiotic fuel cells, the employment of the whole microorganisms allows MFCs to work under mild conditions (i.e. ambient operating temperature and pressure) and without the use of highly corrosive media nor the extensive demand for noble metal catalysts, thus entailing inherent environmental benefits[7]. Although the MFCs catalysed by enzymes also possess the aforementioned advantages, the requirement for enzyme isolation and the issues of such as short lifetime and denaturation of enzyme make it disadvantageous[7]. On the other hand, MFCs could eliminate the need for intensive energy input and thus offer a unique possibility for sustainable wastewater treatment to replace the current technologies (for example, conventional aerobic activated sludge)[12]. Research by He et al. (2017)[18] shows more advantages for MFCs as a wastewater treatment unit[12].

2.1.1.3 MECs

As mentioned above, the cathodic chamber in an MFC is aerobic where protons react with O_2 to form water. By the removal of O_2 in the cathodic chamber and the supply of external electricity source, MFCs could switch to another sub-division of BESs, i.e. MECs. Protons can extract the electrons to produce H_2 on the MECs' cathode[19]. In contrast to MFCs which deliver electricity, MECs need an external power source to initiate the thermodynamically unfavourable reaction[5,7,12].

Since a certain amount of energy and electrons could be gained from the anodic substrate oxidisation process, the energy required for MECs is significantly lower in comparison with its counterpart of water electrolysis[45,19–21]. Owing to the complete anaerobic environment, MECs could circumvent O_2 leakage to the anodic chamber[12].

2.1.1.4 MESs

The system with an objective to electrosynthesise chemical compounds through microbially catalysed cathodic reduction processes is called MESs[5]. The microorganisms, as biocatalysts, are potentially capable to upgrade CO_2 to CH_4 or other organic compounds[5,22,23]. In this regard, MESs are the hybrid technologies combining carbon sequestration and valuable biochemicals production[4]. Analogous to MECs, external energy is required for the majority of MESs[24] to initiate the non-spontaneous reactions and/or accelerate reaction rates[5,25–27].

Different from MFCs which draw electrons from microorganisms, MESs typically leverage autotrophic EAB to gain electrons derived from cathode for the synthesis of valuable compounds[3,5]. The EET between the solid cathode and the cathodic EAB is termed as the mechanisms of cathodic EET (CEET), which is discussed in Section 2.1.2.2.

Similar to other applications of BESs, the employment of microorganisms as catalysts in MESs could circumvent the unsustainability, corrosion and expensive use entailed by the conventional metal catlaysts[27–29]. Most importantly, MESs could convert CO_2 to multi-carbon products[22,23], whereas the abiotic electrochemical CO_2 reduction reaction (ECO2RR) systems are limited to reduce CO_2 to lower carbon products, such as formate or carbon monoxide (CO)[23].

2.1.1.5 Others

In this section, other applications of BESs are introduced briefly with a focus on their basic operating principles.

By introducing photosynthetic organisms into MFCs' anodic chamber, MFCs switch to MSCs, and the external addition of substrate is not necessarily required. Organic matter is generated by photosynthetic bacteria or higher plants and then further utilised by the anodic EAB to achieve electron transfer. MSCs offer a possibility to capture solar energy and generate electricity simultaneously[30].

On the basis of two-chamber MFCs, MDCs incorporate another chamber between anodic and cathodic chambers by inserting an anion exchange membrane (AEM) adjacent to the anode and a cation exchange membrane (CEM) next to the cathode. The water that is being desalinated is supplied to the middle chamber. As mentioned in Section 2.1.1.2, electrons and protons would be liberated during the anodic oxidation process. To restore the change balance in the catholyte, anions (i.e. Cl^-) from the middle chamber would orient toward the anode as the AEM prevents cations from leaving the anodic chamber. Similarly, anions (i.e. Na^+) would flow into the cathodic chamber through the CEM[31]. MDCs hold great promise for satisfying the triple purposes of wastewater treatment, electricity generation and water desalination[7]. As no requirement for external energy and pressurisation, MDCs open up a new field of desalination that possibly replace the current expensive and higher energy-consuming technologies[31].

If electron acceptor (EA) in MECs/MESs changes to contaminants, such as nitrate[32], tetrachloroethene (PCE)[33], trichloroethene (TCE)[34,35] and uranium[36], BESs could serve the purpose of environmental remediation, and this type of BESs is coined as 'MRCs'[37].

2.1.2 Extracellular electron transfer mechanisms

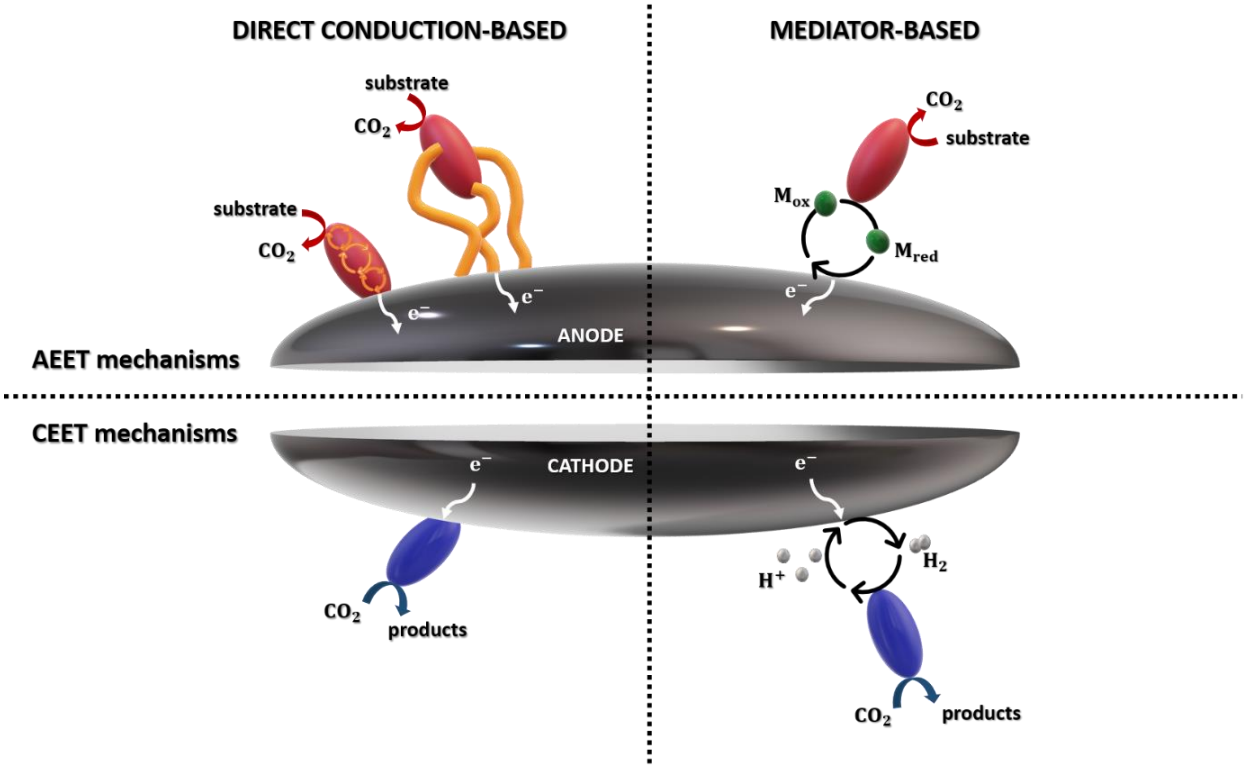

Figure 2.2 Schematic representation of extracellular electron transfer mechanisms (EETs).

As it is stated at the beginning, microorganisms require energy to proliferate and keep themselves alive[8,9]. Energy is generated through redox reactions between an electron donor (ED) and an EA[9]. Therefore, all living organisms including microorganisms need a pair of ED/EA[38]. The solid electrode could play the role of either terminal EA or ED to complete microbial metabolism[38]. The electron transportation between EAB and electrode surfaces is defined as EET[17]. AEET mechanisms mean electrons flow from microorganisms towards the anode surface, whereas CEET mechanisms refer to a cathode pumping electrons to feed microorganisms[5].

EET integrating microbiology and electrochemistry plays a key role in determining the BESs performance[39]. The concept of EET was first proposed in 1910[5]. However, its mechanism is still a subject to debate and the related theoretical studies have not been established unequivocally.

2.1.2.1 AEET mechanisms

For AEET mechanisms, microorganisms extract electrons from a substrate (ED) and then transfer them to the terminal EA, i.e. an insoluble anode.

There are two widely-accepted putative mechanisms of AEET mechanisms (see Figure 2.2), namely direct conduction-based extracellular electron transfer (DET) and mediator-based extracellular electron transfer (MET). Regarding DET, microorganisms are capable of directly donating electrons to an anode, without the assistance of any mobile component[5,17]. DET is enabled by EAB that physically contact with the electrode or form a conductive biofilm[5,7,17]. The participation of outer membrane complexes in DET has been widely studied and clearly demonstrated in *Shewanella oneidensis* and *Geobacter sulfurreducens*[5,7,17]. Take *S. oneidensis* MR1 as an example: the electrons liberated by substrate oxidation are transferred from the inner membrane to periplasmic c-type cytochrome MtrA via a menaquinone pool and c-type cytochrome CymA anchored in the inner membrane. Subsequently, the electrons carried by MtrA are transferred to the outer membrane-embedded c-type cytochromes MtrC and OmcA through scaffolding protein, MtrB. Eventually, electrons are released extracellularly[5,40,41]. Recently, another interaction way between microorganisms and insoluble EA was proposed[42]. It has been indicated that electrons might be directly conveyed to the external EA – aided by conductive extracellular appendages (which are known as pili or pili-like nanowires) instead

of outer membrane c-type cytochromes[5,7,42]. DET is reckoned as an elegant and appealing route to transport electrons[38].

In contrast to DET, MET means that microorganisms donate electrons towards the anode surface by virtue of mediators (also known as 'electron shuttles'). Mediators could be from an artificial supplement or the natural (mainly secondary[5]) metabolites generated by the cells themselves[5]. Nevertheless, the requirement of the regular addition of mediators is a great challenge in a long-run practical operation. Thus, it is necessary to exploit the microorganisms which are capable of producing mediators endogenously. There are several microorganisms that have been found to be capable of secreting mediators; for instance, phenazines by *Pseudomonas aeruginosa* and flavin by *S. oneidensis*[5,17]. The above is a typical description for MET. However, a more rigorous definition should be given for mediators here: mediators referred to in MET should undergo a completed reversible redox process that involves two steps, one is the intracellular reduction reaction of mediators with a substrate and the other is the extracellular oxidisation reaction of mediators on the insoluble EA (i.e. anode) surface[17]. This clarification aims to distinguish from the scenario where, for example, fermentative bacteria produce H_2 firstly and then H_2 is oxidised at the anode surface to generate electricity[7,43]. H_2 is not recognised as a mediator in the true sense due to its failure of carrying out multiple cyclic redox processes. This type of electricity generation is excluded from this thesis[44]. Compared with DET, MET relaxes the restriction of close contact of the living bacteria with the anode; hence electricity generation would not be limited by the bacteria-colonised surface area. Moreover, MET allows more electrons from the distal region to be carried by mediators, which in turn transfer electrons to the anode surface through the diffusion process.

All the above discussion concerns the independent EET, while some microorganisms such as *S. oneidensis* have been found to be able to transfer electrons by both pathways (i.e. DET and MET)[44]. Therefore, researchers start to look beyond individual EET and turn to investigate the dual EET integrating both DET and MET. Relevant numerical work is introduced in Section 2.1.3.1.

2.1.2.2 CEET mechanisms

In comparison with the numerous literature reporting AEET mechanisms in MFCs, only a few studies have shed light on CEET mechanisms thus far[5,23,38]. CEET mechanisms are determined by medium culture and cathodic potential, and can vary for different types of microorganisms[45].

Analogous to AEET mechanisms, electrons are hypothesised to be transferred between microorganisms and the cathode directly[5,38] or assisted by mediators[35,46–53] (see Figure 2.2). To distinguish from the terms used for anodic processes, the process of microorganisms directly seizing electrons from the cathode is defined as cathodic direct conduction-based extracellular electron transfer (CDET) and the pathway of cathode feeding electrons to microorganisms via mediators is called cathodic mediator-based extracellular electron transfer (CMET).

CDET was firstly supported by the work on *Geobacter* species in 2004[32]. In 2010, the first non-*Geobacter* species, *Anaeromyxobacter dehalogenans*, was reported to be able to dechlorinate 2-chlorophenol to phenol via CDET[54]. After that, several proof-of-concept studies were carried out for several types of acetogens. Biocathode inoculated with a pure culture of *Sporomusa ovata*[55] and other species belonging to *Clostridium phylum*[56] (i.e. including *Sporomusa sphaeroides*, *Sporomusa silvacetica*, *Clostridium ljungdahlii*, *Clostridium aceticum* and *Moorella thermoacetica*) was showed to be capable of reducing CO_2 to multi-carbon products (primarily acetate) via CDET. The possibility of H_2 carrying electrons was ruled out by setting a relatively higher (i.e. more positive than $-0.6\ V_{SHE}$) cathodic potential[55,56]. The CDET was further corroborated by the observations of (i) close contact of microorganisms with an electrode, and (ii) no visible turbidity existing in the cathode chamber, coinciding with several prior CDET-proved studies[55]. Yet, it is worthy to note here that not all acetogens could directly take up electrons from an electrode. For example, *Acetobacterium woodii* only grows with H_2 as an ED[56]. In 2015, another separate study[57] demonstrated that for *C. ljungdahlii*, CO_2 reduction (to acetate) was assisted by H_2 as an ED when more negative cathode potential was imposed (i.e. $-0.9\ V_{Ag/AgCl}$). This conclusion was supported by several lines of evidence: (i) no biofilm formed or attached acetogens were observed; (ii) acetate production ceased upon removal of planktonic acetogens. Moreover, this work indicated that both the presence of H_2 bubbles and the change of local pH would be deleterious to biofilm formation and eventually prevent acetogens growth through CDET. Successive studies[45,58] also stated that CMET with H_2 could play a role for acetogens to acquire electrons from cathode imposed at more positive potential. Very recently, both CDET and CMET were considered to exist in the acetogens-dominating multispecies cathodic biofilm[23].

2.1.3 Modelling work

Although Section 2.1.1 has shown that BESs is a promising technology, its advantages are usually masked by several challenges, especially the systems' poor performance (more details can be found in Section 2.1.4). Comprehensive understanding of EET and the impacts of numerous entwined parameters is of paramount importance for the design and optimisation of the system. In comparison with experimental explorations, the model-based analysis offers an economical and efficient solution but receives less attention.

There are different criteria for the classification of BESs models; for instance, (i) BESs models can be divided into such as those of MFCs, MESs, MECs and MDCs based on the function of the modelled system[59,60]; (ii) adhering to various requirements and researchers' background, a BES model falls into mechanism-based or application-based models[59]; (iii) according to investigation objectives, BESs models are classified into half-cell model (either anode- or cathode-based), and fuel-cell models comprising both anodic and cathodic chambers (if modelled MFC is two-chamber configuration)[59]; or (iv) in terms of the microbial community, BESs models would be constructed with either single-species or multispecies culture[60].

Generally, mathematical models of BESs are constructed by incorporating mass and charge conservations, coupling with a set of kinetic equations and laws such as the commonly used Monod (Monod-type) equation, Butler-Volmer equation, Ohm's law and others. In terms of model implementation, the numerical computing tools including COMSOL Multiphysics[61], C/C++[62], Matlab[63], Java codes[61] and others could be employed either individually or collectively[61] to provide solutions in an efficient way.

Existing MFCs and MECs/MESs models, with a focus on EET are discussed and represented in Sections 2.1.3.1 and 2.1.3.2, respectively. Figure 2.3 shows the selected representative BESs models.

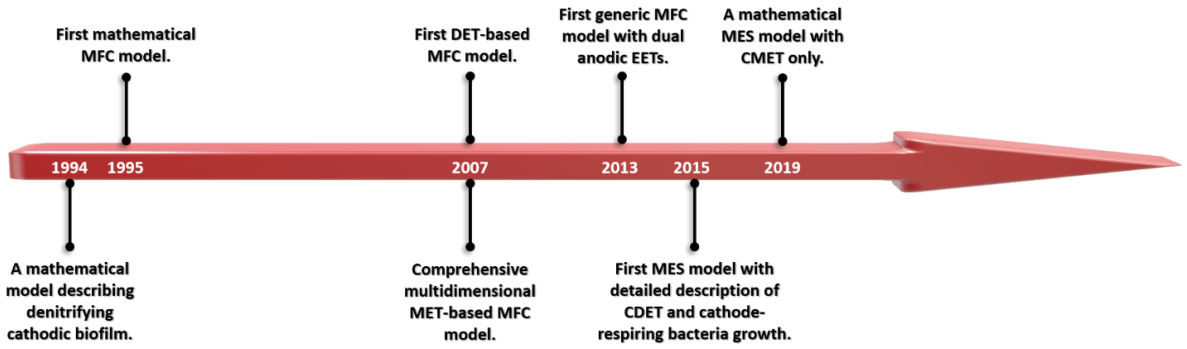

Figure 2.3 Evolution of BESs models.

2.1.3.1 MFCs

Zhang and Halme[63] established the first MFC model, i.e. a one-dimensional (1D) dynamic model of a batch MFC with both planktonic cells[62] and exogenous chemical mediators of HNQ (2-hydroxy-1,4-naphtboquinone). This work could quantitively predict the MFC's current output with various concentrations of mediator and substrate. Although this model is rather simple (compared with the later studies) and preliminary (as plenty of variables and parameters were oversimplified), it still offers a good start for MFC modelling as the first attempt[64].

However, this line of research has not been further pursued significantly until 2007 when Picioreanu et al. offered a multidimensional (i.e. one-, two- and three-dimensional) computational model for MFCs[62]. This modelling framework still focused on the anodic compartment of an MFC, with externally added soluble redox mediators and operated in a batch mode, but incorporated both suspended and biofilm cells and more processes with detailed mathematical descriptions. In their work, the dynamic evolution of several operating variables (including current output, biofilm thickness and formation, concentrations for biomass, and several soluble components) was represented. Additionally, it also discussed two types of competition: (i) that between the single microbial species located at different regions (i.e. suspended and entrapped inside biofilm cells) and (ii) that between two competing species (i.e. acetoclastic EAB and acetoclastic methanogens) within the same biofilm. Given that this model was developed in a general form, it is versatile to various biofilm-based MFCs regardless of biofilm age, bacteria species and so on[59,64]. Later on, the same research group expanded the prior model[62] by substituting the pure substrate of acetate with wastewater (i.e. a mixture of various substrates), introducing a multispecies microbial community[65] and further considering

the convection of liquid flow and the migration of ions[61]. These changes allow the constructed model to reflect the practical phenomena more realistically and have broader applications.

While Picioreanu et al. dedicated to developing MET-only MFC models, Marcus et al.[66] presented another dynamic multispecies model in parallel, in which the direct conduction was assumed as the only mode for anodic electron transfer. Through combining the double-Monod equation and Nernst equation, the expression called 'Nernst-Monod' is derived and functions in relating insoluble EA of anode together with the soluble substrate (ED) to biomass growth. The novel 'Nernst-Monod' formulation is one of the most significant contributions of their work and could be adaptable to many other cases, including the MES model, which is introduced in the following section (see Section 2.1.3.2). Moreover, this model took biomass endogenous respiration and inactivation processes, as well as the consequent biofilm thickness variation into consideration. The effects of biofilm conductivity, biofilm thickness and inert biomass have also been studied by this model. Despite the lack of experimental validation, the work of Marcus et al. is regarded as a key milestone in the progress of understanding EET, especially DET.

All the models above have laid a good foundation for the further development of more advanced MFCs models; however, the nature of the early stage models (such as 1D, anode-based half-cell model) precludes themselves from carrying out more investigations and making more credible predictions. Numerous successive studies have devoted efforts to construct more comprehensive and realistic models, which are very helpful to provide more detailed insights and have a wide applicability[64,67].

However, no one integrated multiple EET mechanisms into a single model until 2013 when Renslow et al.[39] put forward a generic model combing DET and MET with *S. oneidensis* as the EAB and studied different proportions of the two electron transfer mechanisms under different conditions. The authors proposed two cases in terms of the dual EET model: (1) the isolated case, which means DET and MET are independent and no interactions; and (2) the interacting case, where DET interacts with the biofilm matrix and both electron pathways have a mutual influence on each other. Although this model is remarkable, it is rather coarse due to the assumption of unlimited ED and mediators supply, as well as ignoring the biofilm growth. In addition, Renslow et al. only obtained some results about the isolated case; interacting-dual mechanisms were only presented at the conceptual level. More processes need to be included in the model in order to make simulation closer to reality.

2.1.3.2 MECs/MESs

Up to now, most BESs models mainly focus on MFCs, and the numerical research towards other BESs is rather limited and still in an infant stage. A mathematical model describing the denitrifying cathodic biofilm was proposed as early as 1994, in which the reduction of nitrate was assisted by the intermediately generated H_2. The established 1D steady-state model was primarily used to distinguish the different responses of denitrification rate to the applied current under various designed conditions[68]. However, the modelling of MECs/MESs has taken longer time to receive the researchers' attention, and only in the past few years relevant numerical studies were intensified. In 2011, a relatively simple space-independent (i.e. 0D) dynamic model describing the flow-by mode MEC that inoculated by four microorganisms – fermentative, electricigenic, methanogenic acetoclastic and methanogenic hydrogenophilic – was proposed. The assumption of layered biofilm structure together with other simplifications (such as the homogeneous distribution of carbon source and products within the biofilm, well-mixed anodic bulk liquid, constant total amount of mediators, constant pH value and temperature) significantly reduce the model complexity. These simplifications also improve the computational efficiency when it comes to the prediction of product H_2 yield and substrate removal efficiency at different applied potential and inlet substrate concentrations. This work still primarily focused on the modelling of the anodic biofilm, which comprised the first three aforementioned microorganisms (i.e. fermentative, electricigenic and methanogenic acetoclastic). The description for the cathodic biofilm composed of the single species of methanogenic hydrogenophilic was simplified by setting zero-order growth kinetics for methanogenic hydrogenophilic[69]. After that, this model was modified and adopted to explore the optimal state, including microorganism concentration, applied potential and current density for achieving the maximum rate of H_2 production in the real pilot plant-scale fed batch reactor. The control design was also integrated and discussed in this study[70]. In 2015, a generalised mathematical framework for both MFCs and MECs with identical inoculum[71] was developed on the basis of the previous models: (1) the spatial distribution of multispecies anodic biofilm (i.e. composed of electricigenic and methanogenic acetoclastic) was captured in the developed 1D sub-model based on the MFC model of Marcus et al. [66]; (2) fermentative bacteria were assumed to exist in the anolyte only and the conversion process from the organic substrate to acetate was modelled based on the Bernard's anaerobic digestion model[72]; (3) for single-species cathodic biofilm in the MEC, the generalised framework set more rigorous and reasonable constraints for the methanogenic hydrogenophilic growth in terms of H_2 utilisation.

This experimentally validated modelling work achieved the shift from MFCs to MECs by changing the anode potential boundary condition and proposed a convenient and reliable way to approximate anode potential through the applied cell potential in the MECs. However, the bottlenecks for cathodic biofilm such as (i) the oversimplified description of the growth kinetic for CEET mechanisms, and (ii) the lack of the detailed description of the spatial distribution of microorganism and product were not addressed in this work. To address the gaps, Kazemi et al.[73] presented the MES modelling work regarding the pure cathodic culture with the single species of *S. ovata*, which is capable of transforming CO_2 and water to organic matters[60]. *S. ovata* was assumed to capture electrons via CDET only and its metabolism kinetics was much similar to Marcus et al.'s anodic DET theory[66]. The established 1D model was employed to monitor the dynamic and spatial evolutions for several vital parameters, and explore the effects of bulk substrate concentration and cathode potential. While several points in this study (e.g. electric potential equation, substrate mass balance in the catholyte) are still debatable, this model was the first attempt to offer a detailed mathematical description for the cathode-respiring microorganism growth. Very recently (2020), the modified 'Nernst-Monod' equation derived by Kazemi et al.[73] was employed by another research group[74] to investigate the electron transfer kinetics of the cathodic immobilized bacteria which are capable of achieving Fe(III)EDTA reduction.

In contrast to the CDET, Gadkari et al.[75] presented a dynamic fed-batch MES model with CMET only. The extracellular electron transportation within both the conceptual two-species anodic and cathodic biofilm was supposed to be achieved by relying on the redox mediators. The MES performance with various operating parameters including cycling time was examined and both chambers (i.e. anodic and cathodic) were considered in this study; however, the spatial analysis was not included since a homogeneous microorganism distribution and a well-mixed substrate concentration were assumed. Besides the aforementioned models, the succeeding modelling work[76] incorporating temperature, pH and different growth types for planktonic microorganism in the MESs was established and used to guide the design and operation for the system of transforming CO_2 to formate.

2.1.4 Current bottlenecks and perspectives

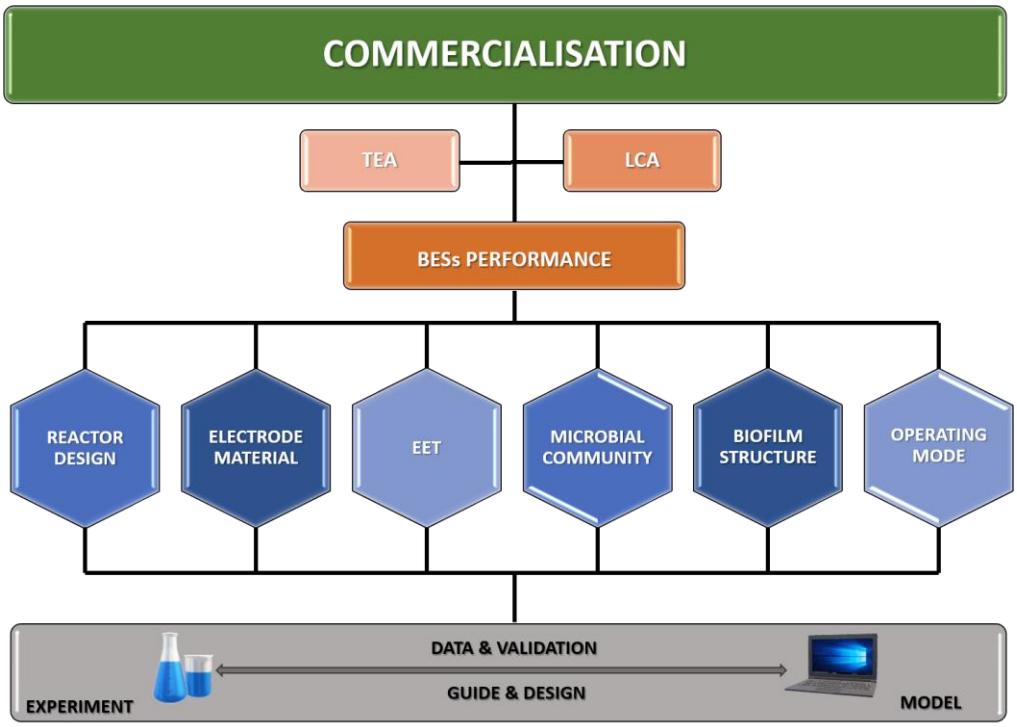

Figure 2.4 Overview of BESs from research tools to commercialisation.

In the previous section, it has been demonstrated that BESs are a versatile technology that is capable of serving multiple functions. The advantages related to different applications have also been outlined above. However, there are still numerous existing hindering factors, which prevent BESs from transforming to practical applications. The summary of BESs technology from research tools to commercialisation is shown in Figure 2.4.

The current over-arching challenge for BESs technology is its poor performance. For the 'galvanic cell' type BESs, the poor performance typically refers to a low electricity output[12]. It has been reported that the electricity generated by MFCs is too low even to support the continuous operation of a sensor[12]. As for the type of 'electrolysis/electrosynthesis cell', the low product yield[55,57,77,78] is the main issue. Additionally, the higher cost is another key barrier for BESs to move out of the lab[12].

Research groups working in various fields have made many efforts to address these challenges. As electrode would be closely related to microbe-electrode interactions[5], numerous material scientists are dedicated to exploring better electrode materials with suitable surface properties since the last decades[5,12,14]. Modification of electrode surface is proposed to be an attractive

possibility to improve the BESs performance. Compared with the untreated carbon cloth cathode in the MESs, at least two-fold improvements were achieved for the product (i.e. acetate) generation rate by either generating a positively-charged cathode surface with chitosan/cyanuric chloride or treating cathode surface with metal nanoparticles[78]/carbon nanotubes (CNTs)[79]. A higher power output was also observed for the composite anode with CNTs in the MFCs[12]. Nevertheless, the use of metal nanoparticles of gold/palladium or CNTs would be economically infeasible and therefore not suitable for further upscaling[79]. Thus, further research should be oriented to develop more scalable electrode[5]. In the field of reactor engineering, although separators in the two-chamber BESs could effectively eliminate reactant crossover between the anodic and cathodic chambers[8], it significantly increases the internal resistance and the capital cost of a system[12,14]. Therefore, exploration of rational designs is required. Currently, membrane-less single-chamber MECs have been successfully implemented in the experiments[14], but there are still many obstacles that need to be overcome when this configuration is adopted in larger-scale operations[14]. Most studies mentioned above are of a nature of experimental exploration. As mentioned in Section 2.1.3, numerical studies could also be as a powerful tool for system optimisation and to gain in-depth understandings. Although considerable progresses in BESs models have been made, securing the essential parameters (e.g. internal resistance, separator permeability[62]) is still the biggest challenge for almost all BESs modellers. Carrying out the relevant experiment would be much helpful for data acquisition and model validation, which warrants further predictions[60,62]. In turn, a legitimate model could provide useful insights to guide the experimental design and operation. Other aspects, such as the manipulation of microbial community and the control of operating mode, would be worthy to be investigated towards better BESs performance.

Once the performance of BESs reaches a higher level, a techno-economic analysis (TEA) and life cycle analysis (LCA) should follow up to assess the economic feasibility and the environmental impact of this technology[60] before commercialisation.

2.2 Electrical CO_2 reduction reaction (ECO2RR) systems

Besides BESs, electrical CO_2 reduction reaction (ECO2RR) is another attractive and potentially practical CCU strategy to alleviate the GHG effect by upgrading CO_2 to valuable chemicals[80,81]. Analogous to MESs introduced previously, the ECO2RR system could be powered by either conventional electricity or other renewable electricity generation approaches.

In this vein, the ECO2RR system would be a potential reservoir for the storage of intermittent renewable energy (e.g. solar and wind[80,81]).

Although it has been recognised that both anode and cathode are pivotal for the whole system, this thesis mainly focuses on the cathodic part as the cathode is the main driver for CO_2 conversion.

2.2.1 Fundamentals

The overall operating mechanism for ECO2RR is much similar to that of MESs, i.e. CO_2 is reduced to the desired product cathodically, while a typical oxygen evolution reaction (OER) takes place anodically[1,80,81].

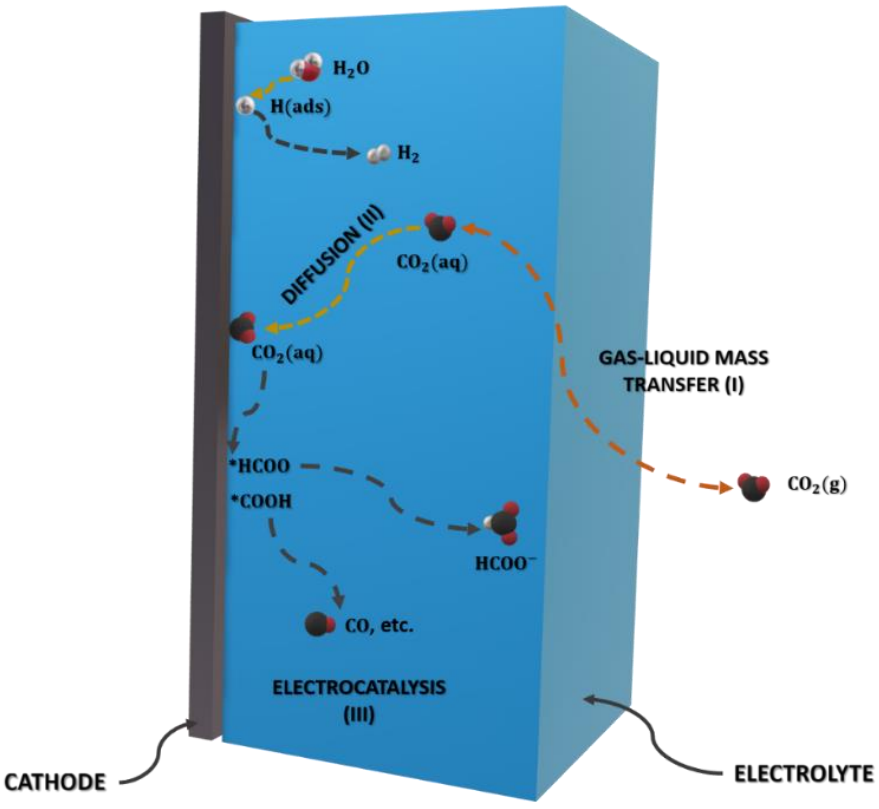

Figure 2.5 Key processes involved in an ECO2RR system.

Unlike the microorganisms employed in the MESs where CO_2 is delicately converted to the desired products by cell metabolisms, different products would be formed in the ECO2RR system depending on the catalyst type and local reaction condition[80]. As shown in Figure 2.5, when the dissolved $CO_2(aq)$ reaches the catalyst surface, it is firstly adsorbed and activated.

After that, intermediate products (such as *HCOO and *COOH) are generated through multiple proton-coupled electron transfer processes and then further reduced or desorbed to form different final products (e.g. CO and formate)[80–82]. It is widely accepted that the dissolved $CO_2(aq)$ is the only active reactant for electrochemical reactions, rather than HCO_3^-, CO_3^{2-}or $CO_2(g)$[83–87].

The first and foremost issue in the two-chamber ECO2RR system is the lower concentration of $CO_2(aq)$ near the catalyst surface[1,80,81,88,89], which is attributed to the lower solubility[1,88], large mass transfer resistance[89] and longer diffusion distance of CO_2[1,80]. This problem would be magnified and significantly limit the overall reaction rate if a system has a higher current density[81]. Despite some measurements that can increase the CO_2 solubility, such as increasing operating pressure, lowering operating temperature and employment of ionic/organic liquid[81,88], these approaches would have a higher requirement for facilities and potentially increase the cost[88] and energy consumption[81]. Rational designs for reactor and electrode suggest a research direction to the improvement of the overall performance of an ECO2RR electrolyser under mild operating conditions (i.e. room temperature and ambient pressure)[80,88], which is discussed in the following sections.

Figure 2.5 also implies that the involvement of various intermediates and diverse synthesis pathways leads to the lower selectivity for the target product in the ECO2RR system[80]. The undesirable hydrogen evolution reaction (HER) is another key aspect that causes a lower selectivity (see Figure 2.5). This is attributed to two reasons: (i) owing to sharing the similar standard potential, HER would occur simultaneously with ECO2RR[81,82,88]; (ii) the smaller activation energy and relatively abundant reactant concentration of HER make H_2 to be generated preferentially than the carbonaceous chemicals[82,88]. A catalyst is able to control synthesis pathways[80] by changing the stability of intermediates[88] and the adsorption energy for different species . Thus, selecting a proper catalyst is instrumental for gaining the desired products efficiently. In terms of CO production, the catalysts of Ag and Au exhibit excellent electrocatalysis[1,80], while formate would be the predominant product when Sn and Pd are used as catalysts[1,80]. Cu and Cu-based (such as Cu_xO, a mixture of Cu_2O, CuO and Cu[88]) catalysts have the unique capability to produce multi-carbon products, which is not possible with any other known elemental catalysts[1,80].

2.2.2 Configurations

The background discussion in the previous section has mentioned that the overall performance of an ECO2RR electrolyser would be affected by its setup. The table below lists several choices for ECO2RR electrolysers regarding (i) operating mode, (ii) electrolyser configuration, (iii) type of electrode and separator (if applicable). These options can be flexibly combined according to the requirements. In the following sections, we focus on two configurations: (i) a two-chamber electrolyser with a planar electrode and (ii) a three-chamber electrolyser with a gas diffusion electrode (GDE).

Table 2.1 Design options for an ECO2RR electrolyser.

Operating mode			
	Batch	Semi-batch	Continuous
Electrolyser configuration			
	Two-chamber	Three-chamber	Microfluidic
Electrode type			
	Planar		GDE
Separator type			
	AEM	CEM	Bipolar exchange membrane (BPM)

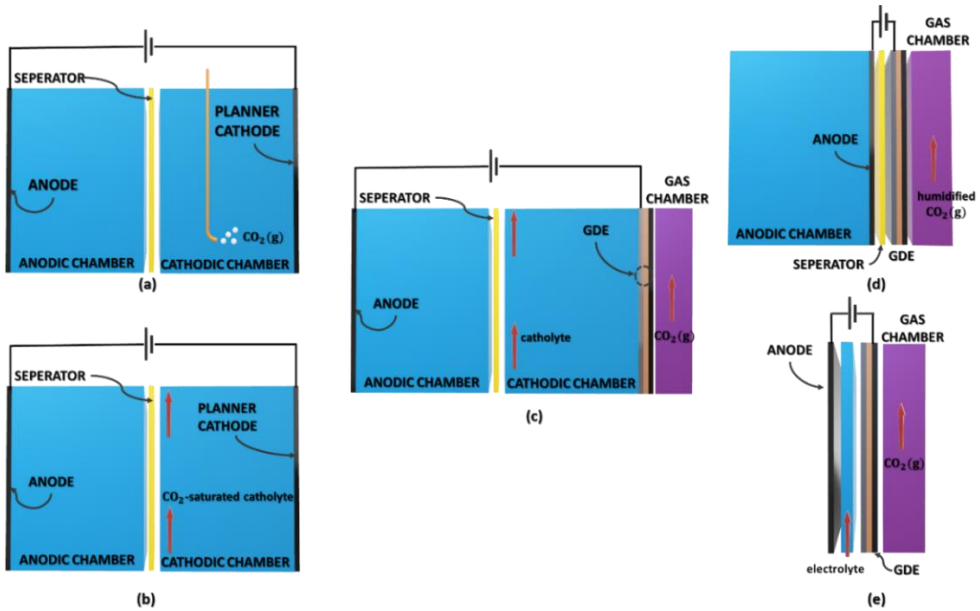

Figure 2.6 Selected types of ECO2RR setup.

2.2.2.1 Two-chamber electrolyser with a planar electrode

In a conventional batch-operated two-chamber electrolyser with a planar electrode (see Figure 2.6(a)), CO_2 is pumped into electrolyte as in gaseous form[81,88] followed by the series of steps demonstrated above (see Figure 2.5). This setup is frequently adopted for most lab-scale ECO2RR studies[1,81,88], since it is cheap, simple and convenient for rapid testing[81]. However, as mentioned above, the lower solubility and poor mass transport of CO_2 would greatly impede the system (even with vigorously stirred catholyte) from obtaining higher current density (i.e. typically $< 100\ \text{mA cm}^{-2}$) [81]. In this regard, a two-chamber electrolyser with a planar electrode under batch mode is not suitable for the scale-up of commercial operations. In contrast to the batch-operated reactors, the reactors under a continuous mode are well-developed and widely adopted in many studies[82]. Thus, all reactors discussed below are under a continuous mode.

Several studies have shown that the continuous supply of the CO_2-saturated catholyte[90] (see Figure 2.6(b)) would improve the performance of an ECO2RR system (i.e. higher overall reaction rates and lower ohmic loss)[81]; however, potential additional costs would be incurred due to an external auxiliary unit for CO_2 capture.

2.2.2.2 Three-chamber electrolyser with a GDE

The configuration of a three-chamber electrolyser with a GDE (see Figure 2.6(c)) provides an alternative way to achieve better performance without altering the operating environment. CO_2 gas is supplied to the system from the bottom of the additional chamber (i.e. gas chamber) and escapes together with other gaseous products at the other side. The current collector, gas diffusion layer (GDL) and catalyst layer (CL) collectively constitute a GDE. The current collector[88] between the gas chamber and the GDL serves the purpose of providing electrons. The GDL acts as a backbone, on which catalysts are immobilised to form a CL. CO_2 and electrons are transported via diffusion and conduction respectively through the porous conductive GDL, and then meet the catholyte in the CL. CO_2 conversion takes place at the liquid-solid interface in the CL.

The implementation of GDE successfully separates the gas and liquid phase[1], which could efficiently address the problems encountered in a two-chamber electrolyser. The distance of CO_2 diffusion to the catalyst surface is significantly reduced[1,80], which is beneficial for

maintaining a higher reactant concentration[80]. Moreover, GDE avoids the bubble formation at the electrode surface, which results in a larger active electrode area and smaller ohmic losses[81,89]. Owing to the multiple benefits of a GDE, the current density is amplified to larger than $100\ \mathrm{mA\ cm^{-2}}$ [1], meaning that the CO_2 conversion process in this arrangement is commercially feasible[91]. Aside from the favourable economics, the three-chamber setup also carries its own issues – among others, these include GDL flooding[80,92] and salt precipitation[1,93]. GDL flooding means that the aqueous catholyte would penetrate through the CL and go into the GDL over time. Salt precipitation is another negative factor affecting the overall ECO2RR system, particularly for the alkaline electrolysers. Take the ECO2RR electrolyser pumped with KOH catholyte as an example: carbonate/bicarbonate salts, such as $KHCO_3/K_2CO_3$, would be formed through the following set of reactions[94]:

$$CO_2 + KOH \rightarrow KHCO_3 \quad \text{(R2.1)}$$

$$KHCO_3 + KOH \rightarrow H_2O + K_2CO_3 \quad \text{(R2.2)}$$

$$K_2CO_3 \cdot 1.5H_2O + CO_2 \rightarrow 2KHCO_3 + 0.5H_2O \quad \text{(R2.3)}$$

$$K_2CO_3 + H_2O + CO_2 \rightarrow 2KHCO_3 \quad \text{(R2.4)}$$

Due to the lower solubility of $KHCO_3$ and K_2CO_3 [94], they would precipitate and eventually block the pores in a GDE. Both GDL flooding and salt precipitation would hinder CO_2 mass transportation, which in turn debases the system's performance and causes the instability issues[1,94].

2.2.2.3 Other configurations

Other configurations for the ECO2RR system could be derived from the two aforementioned setups.

Membrane electrode assembly (MEA)[1,91] (see Figure 2.6(d)) is a novel configuration based on a traditional three-chamber electrolyser with a GDE (see Figure 2.6(c)). As the aqueous catholyte is responsible for the problems of GDL flooding and salt precipitation, the cathodic chamber (where catholyte flowing through) is removed in a MEA. Additionally, for the purpose of minimising ohmic loss, two electrodes are arranged closely on the opposite sides of the separator (i.e. ion exchange membrane)[81,91]. The humidified reactant gas is required in such a setup in order to provide pathways for ions[90] and keep separator moisture[1,95] and reactants active (e.g. for CO_2)[90].

Microfluidic electrolyser (see Figure 2.6(d)) is established by removing the physical membrane separator in a traditional three-chamber electrolyser with a GDE (see Figure 2.6(c)) but creating a thin electrolyte channel (with a thickness < 1 mm) between the two electrodes[81,82]. Anolyte and catholyte are merged and not distinguished from each other, resulting in a more compact design.

2.2.3 Scale-up

To deliver the ECO2RR system on a larger scale, most research on ECO2RR is dedicated to the development of stable, efficient and selective catalysts[96]. Some exploration has also been made to the optimisation of electrode configuration and operational conditions[92,97]. However, fewer studies have focused on the scale-up[98–102] to date. In 2007, a seven-fold scaled-up continuous trickle-bed reactor for the electrochemical conversion of CO_2 to formate was successfully established[99]. Several pilot-scale experiments towards the electrochemical CO_2 conversion were carried out afterwards, which all adopted the traditional CO_2 supply approach of immersing electrodes into the aqueous electrolyte[100]. Not until 2018 did literature report the first scale-up exploration on the ECO2RR with a silver GDE for CO_2 conversion to CO. In this work, the electrode geometrical surface area of the GDE was scaled up by one order of magnitude starting with $10\ cm^2$. The scalability of the GDE was shown by the improved CO yield and the comparable specific energy consumption of the larger device. Still, a need for further optimisation was recognised to obtain higher selectivity for the product[101]. Very recently, a similar ECO2RR system[102] (i.e. with the silver GDE for CO_2 conversion to CO) was further scaled up (with the electrode geometrical surface area of the GDE reaching $300\ cm^2$). The selectivity for CO was improved by adopting the parameter values which are suitable for industrial applications. Although the operational settings, such as temperature, current density and CO_2 feed flowrate, are mostly determined empirically instead of through a systematic analysis, this study represents an important step further to the industrialisation of ECO2RR.

In addition to the experimental studies, model-based analysis is instrumental to gain a deeper understanding of the kinetics-transport interactions in such sophisticated electrochemical systems and eventually promote the transition from bench-scale research to industrial-scale applications. The first GDE model for the CO_2 reduction process (i.e. a two-dimensional model of the cathode GDE in a continuous CO_2 electrolyser for formate production) was constructed on the basis of Li & Oloman cathodic model[99] by introducing fluid dynamics and more

sophisticated electrochemical kinetics[103]. Subsequently, a full-cell model comprising both anode and cathode GDEs for converting CO_2 to CO[104] and that to formic acid in ionic electrolyte[105] was proposed. All the aforementioned studies performed parametric tests and identified the limiting factors with respect to current density. Yet, they treated the whole GDE as a single porous medium and assumed that gaseous CO_2 was able to be adsorbed onto the catalysts and react with the electrolyte directly, which does not reflect the experimental findings that only dissolved $CO_2(aq)$ is the active reactant for electrochemical reactions[83–87]. In 2016, the previously developed full-cell model for electrochemical conversion of CO_2 to formate/formic acid[105] was extended in a separate study to integrate (i) the multiphase flow in the catholyte, (ii) the CO_2 adsorption process and (iii) transportation through a membrane. The extended mode was then used in a scale-up analysis to assess the impact of cell height[106]. Nevertheless, the CL (the main site where the three phases, i.e. solid, gas and liquid, are in close contact and where electrochemical reactions occur) was still treated as an infinitely thin porous surface without considering its internal mass transfer and internal distribution of chemical species and potential.

A general and detailed mathematical framework for the porous electrode was proposed as early as 1975, in which the pores of a solid matrix were assumed to be completely flooded with the electrolyte but no presence of the gas phase[107]. In 1991, this porous electrode theory was further developed by including the gas transportation region and the active catalyst layer[108]. Recently, a GDE model accounting for the local details of the CL (such as the aqueous phase reactions and CL hydrophobicity) was developed[90]. The evaluation of several variables (such as CO_2 concentration, pH value, current density) in the CL and the effects of several operating settings were presented. Further work extended the model to include (i) the anode (which was treated as an interface); and (ii) an investigation of the temperature and water variation for the MEAs[91,93]. However, restricted by the one-dimensional (1D) nature, the electrolyte channel and gas chamber (where the aqueous electrolyte and mixture gas flow through in the GDE) in these studies[90,91] were assumed isotropic, which ignored the spatial variation along the direction of the feed gas flow. This assumption may introduce inaccuracy in the predicted current density distribution, which is recognised in the previous work[90]. Moreover, these proposed multiphysics models generally require further experimental validation. The deficiency of model validation and the oversimplified model would restrict the application of mathematical modelling in systematically supporting the future development (including up-scaling) of the GDE-based ECO2RR system.

2.2.4 Current bottlenecks and perspectives

Despite the fact that numerous pioneering studies have made significant strides to boost the overall system performance, concentrated efforts are still needed to accomplish successful commercialisation. We would like to discuss future development avenues from three levels.

The first one would be the electrode level, as the cathode is the heart of an ECO2RR electrolyser and plays a decisive role. Section 2.2.2 has demonstrated that the GDE could achieve moderate-to-high current densities[109] and avoid the affiliated cost and stability issues thanks to its mild operating conditions[109]. Nevertheless, in addition to higher current density, higher selectivity for target product, lower energy consumption and longer lifetime of electrolyser ($> 30{,}000$ h[101]) are also required in practical applications[100,110]. Stability is still the unsolved issue for the GDE. Currently reported ECO2RR systems cannot maintain a higher current density for a longer time and the performance of the GDE would be declining after a few tens of hours[80]. In the future, the experimental exploration for the superior electrode materials, which is more hydrophobic and highly conductive, may help address this problem. From the modelling point of view, the construction of a dynamic multi-scale framework embracing sufficient details could aid us to answer several timely questions, such as 'how long is the operation time until the GDL to be totally flooded' and 'how does the catalyst degrade over time'[111].

The second level is in terms of the completed electrolyser. As we stated at the very beginning, the anodic chamber is also a critical part in an ECO2RR system and worthy to be optimised. Currently, OER is the only anodic reaction considered in most of the ECO2RR studies[82]. Strategies such as the employment of cheap but efficient anode catalysts and the use of wastewater alternative to pure water, could lead to a more cost-effective and environmental-friendly unit[81,82].

The highest level goes beyond the scope of the ECO2RR system itself. For example, by integrating with renewable energy, an ECO2RR system could serve as a tool for storing and utilising intermittent energy. Similar to other processes, relevant LCA and TEA could also be carried out for holistic performance analyses.

2.3 Rationale for the scope of this PhD project

As stated in Section 2.1.4, the dauting challenge of BESs lies in their poor performance. For MFCs, it has been reported that, compared with the pure culture of a single type of EAB, a multispecies biofilm can boost substrate conversion, electron transfer and electricity output[10,112–114]. Till now, most work of the multispecies MFCs are experiments-based, and all the existing numerical studies are yet to be extended to support the systematic analysis of the anodic multispecies consortia. Several questions – such as how the multispecies anodic biofilm evolve with various AEET mechanisms under different operating conditions, and how the multispecies anodic biofilm relate to the eventual power output – are still yet to be unveiled. Regarding MESs, the lower product yield is one of the primary obstacles preventing it from achieving successful commercialisation. Despite that the numerous attempts have been made to increase the product yield and production rate, most of them are empirical explorations. It is essential to have a holistic understanding of CEET mechanisms to effectively improve the performance of MESs.

For the ECO2RR system, most research has focused on experimentally mining effective catalysts to improve the yield of the target product. Limited attention has been paid to the optimisation of electrode configuration and operational conditions[92,97], and even fewer numerical studies have focused on upscaling[98–102]. Further work is required to fill these research gaps to achieve the successful transition for the ECO2RR system from laboratory studies to practical applications.

References

(1) Nwabara, U. O.; Cofell, E. R.; Verma, S.; Negro, E.; Kenis, P. J. A. Durable Cathodes and Electrolyzers for the Efficient Aqueous Electrochemical Reduction of CO2. *ChemSusChem* **2020**, *13*, 855–875.

(2) Johnsson, F.; Kjärstad, J.; Rootzén, J. The Threat to Climate Change Mitigation Posed by the Abundance of Fossil Fuels. *Clim. Policy* **2019**, *19* (2), 258–274.

(3) Jiang, Y.; May, H. D.; Lu, L.; Liang, P.; Huang, X.; Ren, Z. J. Carbon Dioxide and Organic Waste Valorization by Microbial Electrosynthesis and Electro-Fermentation. *Water Res.* **2019**, *149*, 42–55.

(4) Kumar, G.; Saratale, R. G.; Kadier, A.; Sivagurunathan, P.; Zhen, G.; Kim, S. H.; Saratale, G. D. A Review on Bio-Electrochemical Systems (BESs) for the Syngas and Value Added Biochemicals Production. *Chemosphere* **2017**, *177*, 84–92.

(5) Rabaey, K.; Rozendal, R. A. Microbial Electrosynthesis - Revisiting the Electrical Route for Microbial Production. *Nat. Rev. Microbiol.* **2010**, *8* (10), 706–716.

(6) Zhang, X.; Li, X.; Zhao, X.; Li, Y. Factors Affecting the Efficiency of a Bioelectrochemical System: A Review. *RSC Adv.* **2019**, *9* (34), 19748–19761.

(7) Santoro, C.; Arbizzani, C.; Erable, B.; Ieropoulos, I. Microbial Fuel Cells: From Fundamentals to Applications. A Review. *J. Power Sources* **2017**, *356*, 225–244.

(8) Harnisch, F.; Schroder, U. From MFC to MXC: Chemical and Biological Cathodes and Their Potential for Microbial Bioelectrochemical Systems. *Chem. Soc. Rev.* **2010**, *39* (11), 4433–4448.

(9) Smolke, C. *The Metabolic Pathway Engineering Handbook: Fundamentals*; CRC Press, 2009.

(10) Logan, B. E. Exoelectrogenic Bacteria That Power Microbial Fuel Cells. *Nat. Rev. Microbiol.* **2009**, *7* (5), 375–381.

(11) Ivase, T. J. P.; Nyakuma, B. B.; Oladokun, O.; Abu, P. T.; Hassan, M. N. Review of the Principal Mechanisms, Prospects, and Challenges of Bioelectrochemical Systems. *Environ. Prog. Sustain. Energy* **2020**, *39*, e13298.

(12) Do, M. H.; Ngo, H. H.; Guo, W. S.; Liu, Y.; Chang, S. W.; Nguyen, D. D.; Nghiem, L. D.; Ni, B. J. Challenges in the Application of Microbial Fuel Cells to Wastewater Treatment and Energy Production: A Mini Review. *Sci. Total Environ.* **2018**, *639*, 910–920.

(13) Logan, B.; Hamelers, B.; Rozendal, R.; Schröder, U.; Keller, J.; Freguia, S.; Alterman, P.; Verstraete, W.; Rabaey, K. Microbial Fuel Cells Methodology and Technology. *Environ. Sci. Technol.* **2006**, *40* (17), 5181–5192.

(14) Zhang, Y.; Angelidaki, I. Microbial Electrolysis Cells Turning to Be Versatile

Technology: Recent Advances and Future Challenges. *Water Res.* **2014**, *56*, 11–25.

(15) Yu, Y. Y.; Zhai, D. D.; Si, R. W.; Sun, J. Z.; Liu, X.; Yong, Y. C. Three-Dimensional Electrodes for High-Performance Bioelectrochemical Systems. *Int. J. Mol. Sci.* **2017**, *18* (1).

(16) Yang, Z.; Yang, A. Modelling the Impact of Operating Mode and Electron Transfer Mechanism in Microbial Fuel Cells with Two-Species Anodic Biofilm. *Biochem. Eng. J.* **2020**, *158* (107560).

(17) Sydow, A.; Krieg, T.; Mayer, F.; Schrader, J.; Holtmann, D. Electroactive Bacteria—Molecular Mechanisms and Genetic Tools. *Appl. Microbiol. Biotechnol.* **2014**, *98* (20), 8481–8495.

(18) He, L.; Du, P.; Chen, Y.; Lu, H.; Cheng, X.; Chang, B.; Wang, Z. Advances in Microbial Fuel Cells for Wastewater Treatment. *Renew. Sustain. Energy Rev.* **2017**, *71*, 388–403.

(19) Jafary, T.; Daud, W. R. W.; Ghasemi, M.; Kim, B. H.; Md Jahim, J.; Ismail, M.; Lim, S. S. Biocathode in Microbial Electrolysis Cell; Present Status and Future Prospects. *Renew. Sustain. Energy Rev.* **2015**, *47*, 23–33.

(20) Call, D. F.; Wagner, R. C.; Logan, B. E. Hydrogen Production by Geobacter Species and a Mixed Consortium in a Microbial Electrolysis Cell. *Appl. Environ. Microbiol.* **2009**, *75* (24), 7579–7587.

(21) Lim, S. S.; Yu, E. H.; Daud, W. R. W.; Kim, B. H.; Scott, K. Bioanode as a Limiting Factor to Biocathode Performance in Microbial Electrolysis Cells. *Bioresour. Technol.* **2017**, *238*, 313–324.

(22) Prévoteau, A.; Carvajal-Arroyo, J. M.; Ganigué, R.; Rabaey, K. Microbial Electrosynthesis from CO2: Forever a Promise? *Curr. Opin. Biotechnol.* **2020**, *62*, 48–57.

(23) Izadi, P.; Fontmorin, J.; Godain, A.; Yu, E. H.; Head, I. M. Parameters Influencing the Development of Highly Conductive and Efficient Biofilm during Microbial Electrosynthesis: The Importance of Applied Potential and Inorganic Carbon Source.

npj Biofilms Microbiomes **2020**, *6* (40).

(24) Logan, B. E.; Rossi, R.; Ragab, A.; Saikaly, P. E. Electroactive Microorganisms in Bioelectrochemical Systems. *Nat. Rev. Microbiol.* **2019**, *17* (5), 307–319.

(25) Lovley, D. R. Powering Microbes with Electricity: Direct Electron Transfer from Electrodes to Microbes. *Environ. Microbiol. Rep.* **2011**, *3* (1), 27–35.

(26) Logan, B. E.; Call, D.; Cheng, S.; Hamelers, H. V. M.; Sleutels, T. H. J. A.; Jeremiasse, A. W.; Rozendal, R. A. Microbial Electrolysis Cells for High Yield Hydrogen Gas Production from Organic Matter. *Environ. Sci. Technol.* **2008**, *42* (23), 8630–8640.

(27) Rosenbaum, M.; Aulenta, F.; Villano, M.; Angenent, L. T. Cathodes as Electron Donors for Microbial Metabolism: Which Extracellular Electron Transfer Mechanisms Are Involved? *Bioresour. Technol.* **2011**, *102* (1), 324–333.

(28) Aulenta, F.; Catapano, L.; Snip, L.; Villano, M.; Majone, M. Linking Bacterial Metabolism to Graphite Cathodes: Electrochemical Insights into the H2-Producing Capability of Desulfovibrio Sp. *ChemSusChem* **2012**, *5* (6), 1080–1085.

(29) Villano, M.; Aulenta, F.; Ciucci, C.; Ferri, T.; Giuliano, A.; Majone, M. Bioelectrochemical Reduction of CO2 to CH4 via Direct and Indirect Extracellular Electron Transfer by a Hydrogenophilic Methanogenic Culture. *Bioresour. Technol.* **2010**, *101* (9), 3085–3090.

(30) Strik, D. P. B. T. B.; Timmers, R. A.; Helder, M.; Steinbusch, K. J. J.; Hamelers, H. V. M.; Buisman, C. J. N. Microbial Solar Cells: Applying Photosynthetic and Electrochemically Active Organisms. *Trends Biotechnol.* **2011**, *29* (1), 41–49.

(31) Cao, X.; Huang, X.; Liang, P.; Xiao, K.; Zhou, Y.; Zhang, X.; Logan, B. E. A New Method for Water Desalination Using Microbial Desalination Cells. *Environ. Sci. Technol.* **2009**, *43* (18), 7148–7152.

(32) Gregory, K. B.; Bond, D. R.; Lovley, D. R. Graphite Electrodes as Electron Donors for Anaerobic Respiration. *Environ. Microbiol.* **2004**, *6* (6), 596–604.

(33) Strycharz, S. M.; Woodard, T. L.; Johnson, J. P.; Nevin, K. P.; Sanford, R. A.; Löffler,

F. E.; Lovley, D. R. Graphite Electrode as a Sole Electron Donor for Reductive Dechlorination of Tetrachlorethene by Geobacter Lovleyi. *Appl. Environ. Microbiol.* **2008**, *74* (19), 5943–5947.

(34) Aulenta, F.; Catervi, A.; Majone, M.; Panero, S.; Reale, P.; Rossetti, S. Electron Transfer from a Solid-State Electrode Assisted by Methyl Viologen Sustains Efficient Microbial Reductive Dechlorination of TCE. *Environ. Sci. Technol.* **2007**, *41* (7), 2554–2559.

(35) Aulenta, F.; Canosa, A.; Reale, P.; Rossetti, S.; Panero, S.; Majone, M. Microbial Reductive Dechlorination of Trichloroethene to Ethene With Electrodes Serving as Electron Donors Without the External Addition of Redox Mediators. *Biotechnol. Bioeng.* **2009**, *103* (1), 85–91.

(36) Gregory, K. B.; Lovley, D. R. Remediation and Recovery of Uranium from Contaminated Subsurface Environments with Electrodes. *Environ. Sci. Technol.* **2005**, *39* (22), 8943–8947.

(37) Wang, H.; Ren, Z. J. A Comprehensive Review of Microbial Electrochemical Systems as a Platform Technology. *Biotechnol. Adv.* **2013**, *31* (8), 1796–1807.

(38) Thrash, J. C.; Coates, J. D. Review: Direct and Indirect Electrical Stimulation of Microbial Metabolism. *Environ. Sci. Technol.* **2008**, *42* (11), 3921–3931.

(39) Renslow, R.; Babauta, J.; Kuprat, A.; Schenk, J.; Ivory, C.; Fredrickson, J.; Beyenal, H. Modeling Biofilms with Dual Extracellular Electron Transfer Mechanisms. *Phys. Chem. Chem. Phys.* **2013**, *15* (44), 19262–19283.

(40) Coursolle, D.; Baron, D. B.; Bond, D. R.; Gralnick, J. A. The Mtr Respiratory Pathway Is Essential for Reducing Flavins and Electrodes in Shewanella Oneidensis. *J. Bacteriol.* **2010**, *192* (2), 467–474.

(41) Szeinbaum, N.; Burns, J. L.; DiChristina, T. J. Electron Transport and Protein Secretion Pathways Involved in Mn(III) Reduction by Shewanella Oneidensis. *Environ. Microbiol. Rep.* **2014**, *6* (5), 490–500.

(42) Reguera, G.; McCarthy, K. D.; Mehta, T.; Nicoll, J. S.; Tuominen, M. T.; Lovley, D. R.

Extracellular Electron Transfer via Microbial Nanowires. *Nature* **2005**, *435*, 1098–1101.

(43) Berk, R. S.; Canfield, J. H. Bioelectrochemical Energy Conversion. *Appl. Microbiol.* **1964**, *12* (1), 10–12.

(44) Philips, J.; Verbeeck, K.; Rabaey, K.; Arends, J. B. A. *Microbial Electrochemical and Fuel Cells: Fundamentals and Applications*; Keith Scott, E. H. Y., Ed.; Woodhead Publishing, 2016.

(45) Tremblay, P. L.; Angenent, L. T.; Zhang, T. Extracellular Electron Uptake: Among Autotrophs and Mediated by Surfaces. *Trends Biotechnol.* **2017**, *35* (4), 360–371.

(46) Lithgow, A. M., Romero, L., Sanchez, I. C., Souto, F. A.; Vega, C. A. Interception of the Electron-Transport Chain in Bacteria with Hydrophilic Redox Mediators. I: Selective Improvement of the Performance of Biofuel Cells with 2, 6-Disulphonated Thionine as Mediator. *J. Chem. Res.* **1986**, *5*, 178–179.

(47) Hongo, M.; Iwahara, M. Application of Electro-Energizing Method to L-Glutamic Acid Fermentation. *Agric. Biol. Chem.* **1979**, *43* (10), 2075–2081.

(48) Park, D. H.; Laivenieks, M.; Guettler, M. V.; Jain, M. K.; Zeikus, J. G. Microbial Utilization of Electrically Reduced Neutral Red as the Sole Electron Donor for Growth and Metabolite Production. *Appl. Environ. Microbiol.* **1999**, *65* (7), 2912–2917.

(49) Park, D. H.; Zeikus, J. G. Utilization of Electrically Reduced Neutral Red by Actinobacillus Succinogenes: Physiological Function of Neutral Red in Membrane-Driven Fumarate Reduction and Energy Conservation. *J. Bacteriol.* **1999**, *181* (8), 2403–2410.

(50) Kim, T. S.; Kim, B. H. Electron Flow Shift in Clostridium Acetobutylicum Fermentation by Electrochemically Introduced Reducing Equivalent. *Biotechnol. Lett.* **1988**, *10* (2), 123–128.

(51) Sakakibara, Y.; Kuroda, M. Electric Prompting and Control of Denitrification. *Biotechnol. Bioeng.* **1993**, *42*, 535–537.

(52) Clauwaert, P.; Tolêdo, R.; van der Ha, D.; Crab, R.; Verstraete, W.; Hu, H.; Udert, K.

M.; Rabaey, K. Combining Biocatalyzed Electrolysis with Anaerobic Digestion. *Water Sci. Technol.* **2008**, *57* (4), 575–579.

(53) Ohmura, N.; Matsumoto, N.; Sasaki, K.; Saiki, H. Electrochemical Regeneration of Fe(III) to Support Growth on Anaerobic Iron Respiration. *Appl. Environ. Microbiol.* **2002**, *68* (1), 405–407.

(54) Strycharz, S. M.; Gannon, S. M.; Boles, A. R.; Franks, A. E.; Nevin, K. P.; Lovley, D. R. Reductive Dechlorination of 2-Chlorophenol by Anaeromyxobacter Dehalogenans with an Electrode Serving as the Electron Donor. *Environ. Microbiol. Rep.* **2010**, *2* (2), 289–294.

(55) Kelly P. Nevin; Trevor L. Woodard; Franks, A. E.; Summers, Z. M.; Derek R. Lovley. Microbial Electrosynthesis: Feeding Microbes Electricity To Convert Carbon Dioxide and Water to Multicarbon Extracellular Organic Compounds. *MBio* **2010**, *1* (2).

(56) Nevin, K. P.; Hensley, S. A.; Franks, A. E.; Summers, Z. M.; Ou, J.; Woodard, T. L.; Snoeyenbos-West, O. L.; Lovley, D. R. Electrosynthesis of Organic Compounds from Carbon Dioxide Is Catalyzed by a Diversity of Acetogenic Microorganisms. *Appl. Environ. Microbiol.* **2011**, *77* (9), 2882–2886.

(57) Bajracharya, S.; Ter Heijne, A.; Dominguez Benetton, X.; Vanbroekhoven, K.; Buisman, C. J. N.; Strik, D. P. B. T. B.; Pant, D. Carbon Dioxide Reduction by Mixed and Pure Cultures in Microbial Electrosynthesis Using an Assembly of Graphite Felt and Stainless Steel as a Cathode. *Bioresour. Technol.* **2015**, *195*, 14–24.

(58) Deutzmann, J. S.; Sahin, a M.; Spormann, A. M. Extracellular Enzymes Facilitate Electron Uptake in Biocorrosion and Bioelectrosynthesis. *MBio* **2015**, *6* (2), e00496-15.

(59) Xia, C.; Zhang, D.; Pedrycz, W.; Zhu, Y.; Guo, Y. Models for Microbial Fuel Cells: A Critical Review. *J. Power Sources* **2018**, *373*, 119–131.

(60) Gadkari, S.; Gu, S.; Sadhukhan, J. Towards Automated Design of Bioelectrochemical Systems: A Comprehensive Review of Mathematical Models. *Chem. Eng. J.* **2018**, *343*, 303–316.

(61) Picioreanu, C.; van Loosdrecht, M. C. M.; Curtis, T. P.; Scott, K. Model Based Evaluation of the Effect of PH and Electrode Geometry on Microbial Fuel Cell Performance. *Bioelectrochemistry* **2010**, *78* (1), 8–24.

(62) Picioreanu, C.; Head, I. M.; Katuri, K. P.; van Loosdrecht, M. C. M.; Scott, K. A Computational Model for Biofilm-Based Microbial Fuel Cells. *Water Res.* **2007**, *41* (13), 2921–2940.

(63) Zhang, X.; Halme, A. Modelling of a Microbial Fuel Cell Process. *Biotechnol. Lett.* **1995**, *17* (8), 809–814.

(64) Ortiz-martínez, V. M.; Salar-garcía, M. J.; Ríos, A. P. D. L.; Hernández-fernández, F. J.; Egea, J. A. Developments in Microbial Fuel Cell Modeling. *Chem. Eng. J.* **2015**, *271*, 50–60.

(65) Picioreanu, C.; Katuri, K. P.; Head, I. M.; Van Loosdrecht, M. C. M.; Scott, K. Mathematical Model for Microbial Fuel Cells with Anodic Biofilms and Anaerobic Digestion. *Water Sci. Technol.* **2008**, *57* (7), 965–971.

(66) Marcus, A. K.; Torres, C. I.; Rittmann, B. E. Conduction-Based Modeling of the Biofilm Anode of a Microbial Fuel Cell. *Biotechnol. Bioeng.* **2007**, *98* (6), 1171–1182.

(67) Jadhav, D. A.; Carmona-Martínez, A. A.; Chendake, A. D.; Pandit, S.; Pant, D. Modeling and Optimization Strategies towards Performance Enhancement of Microbial Fuel Cells. *Bioresour. Technol.* **2021**, *320* (124256).

(68) Sakakibara, Y.; Flora, J. R. V.; Suidan, M. T.; Kurodo, M. Modeling of Electrochemically-Activated Denitrifying Biofilms. *Water Res.* **1994**, *28* (5), 1077–1086.

(69) Pinto, R. P.; Srinivasan, B.; Escapa, A.; Tartakovsky, B. Multi-Population Model of a Microbial Electrolysis Cell. *Environ. Sci. Technol.* **2011**, *45* (11), 5039–5046.

(70) Yahya, A. M.; Hussain, M. A.; Wahab, A. K. A. Modeling, Optimization, and Control of Microbialelectrolysis Cells in a Fed-Batch Reactor for Production of Renewable Biohydrogen Gas. *Int. J. ENERGY Res.* **2015**, *39*, 557–572.

(71) Karimi Alavijeh, M.; Mardanpour, M. M.; Yaghmaei, S. A Generalized Model for Complex Wastewater Treatment with Simultaneous Bioenergy Production Using the Microbial Electrochemical Cell. *Electrochim. Acta* **2015**, *167*, 84–96.

(72) Bernard, O.; Hadj-Sadok, Z.; Dochain, D.; Genovesi, A.; Steyer, J. P. Dynamical Model Development and Parameter Identification for an Anaerobic Wastewater Treatment Process. *Biotechnol. Bioeng.* **2001**, *75* (4), 424–438.

(73) Kazemi, M.; Biria, D.; Rismani-Yazdi, H. Modelling Bio-Electrosynthesis in a Reverse Microbial Fuel Cell to Produce Acetate from CO2 and H2O. *Phys. Chem. Chem. Phys.* **2015**, *17*, 12561–12574.

(74) Zhao, J.; Feng, K.; Liu, S. H.; Lin, C. W.; Zhang, S.; Li, S.; Li, W.; Chen, J. Kinetics of Biocathodic Electron Transfer in a Bioelectrochemical System Coupled with Chemical Absorption for NO Removal. *Chemosphere* **2020**, *249*, 126095.

(75) Gadkari, S.; Shemfe, M.; Modestra, J. A.; Mohan, S. V.; Sadhukhan, J. Understanding the Interdependence of Operating Parameters in Microbial Electrosynthesis: A Numerical Investigation. *Phys. Chem. Chem. Phys.* **2019**, *21*, 10761–10772.

(76) Abel, A. J.; Clark, D. S. A Comprehensive Modeling Analysis of Formate-mediated Microbial Electrosynthesis. *ChemSusChem* **2020**, *13*.

(77) Zaybak, Z.; Pisciotta, J. M.; Tokash, J. C.; Logan, B. E. Enhanced Start-up of Anaerobic Facultatively Autotrophic Biocathodes in Bioelectrochemical Systems. *J. Biotechnol.* **2013**, *168* (4), 478–485.

(78) Nie, H.; Zhang, T.; Cui, M.; Lu, H.; Lovley, D. R.; Russell, T. P. Improved Cathode for High Efficient Microbial-Catalyzed Reduction in Microbial Electrosynthesis Cells. *Phys. Chem. Chem. Phys.* **2013**, *15* (34), 14290–14294.

(79) Zhang, T.; Nie, H.; Bain, T. S.; Lu, H.; Cui, M.; Snoeyenbos-West, O. L.; Franks, A. E.; Nevin, K. P.; Russell, T. P.; Lovley, D. R. Improved Cathode Materials for Microbial Electrosynthesis. *Energy Environ. Sci.* **2013**, *6* (1), 217–224.

(80) Nguyen, T. N.; Dinh, C.-T. Gas Diffusion Electrode Design for Electrochemical Carbon

Dioxide Reduction. *Chem. Soc. Rev.* **2020**, *49*, 7488–7504.

(81) Garg, S.; Li, M.; Weber, A. Z.; Ge, L.; Li, L.; Rudolph, V.; Wang, G.; Rufford, T. E. Advances and Challenges in Electrochemical CO2 Reduction Processes: An Engineering and Design Perspective Looking beyond New Catalyst Materials. *J. Mater. Chem. A* **2020**, *8*, 1511–1544.

(82) Endrődi, B.; Bencsik, G.; Darvas, F.; Jones, R.; Rajeshwar, K.; Janáky, C. Continuous-Flow Electroreduction of Carbon Dioxide. *Prog. Energy Combust. Sci.* **2017**, *62*, 133–154.

(83) Zhong, H.; Fujii, K.; Nakano, Y.; Jin, F. Effect of CO2 Bubbling into Aqueous Solutions Used for Electrochemical Reduction of CO2 for Energy Conversion and Storage. *J. Phys. Chem. C* **2015**, *119*, 55–61.

(84) Hori, Y.; Murata, A.; Takahashi, R. Formation of Hydrocarbons in the Electrochemical Reduction of Carbon Dioxide at a Copper Electrode in Aqueous Solution. *J. Chem. Soc. Faraday Trans. 1 Phys. Chem. Condens. Phases* **1989**, *85* (8), 2309–2326.

(85) Hori, Y.; Suzuki, S. Electrolytic Reduction of Bicarbonate Ion at a Mercury Electrode. *J. Electrochem. Soc.* **1983**, *130*, 2387.

(86) Kumar, B.; Llorente, M.; Froehlich, J.; Dang, T.; Sathrum, A.; Kubiak, C. P. Photochemical and Photoelectrochemical Reduction of CO2. *Annu. Rev. Phys. Chem.* **2012**, *63*, 541–569.

(87) Haas, T.; Krause, R.; Weber, R.; Demler, M.; Schmid, G. Technical Photosynthesis Involving CO2 Electrolysis and Fermentation. *Nat. Catal.* **2018**, *1*, 32–39.

(88) Xiang, H.; Rasul, S.; Scott, K.; Portoles, J.; Cumpson, P.; Yu, E. H. Enhanced Selectivity of Carbonaceous Products from Electrochemical Reduction of CO2 in Aqueous Media. *J. CO2 Util.* **2019**, *30*, 214–221.

(89) Yang, Z.; Li, D.; Xing, L.; Xiang, H.; Xuan, J.; Cheng, S.; Yu, E. H.; Yang, A. Modeling and Upscaling Analysis of Gas Diffusion Electrode-Based Electrochemical Carbon Dioxide Reduction Systems. *ACS Sustain. Chem. Eng.* **2021**, *9*, 351–361.

(90) Weng, L. C.; Bell, A. T.; Weber, A. Z. Modeling Gas-Diffusion Electrodes for CO2 Reduction. *Phys. Chem. Chem. Phys.* **2018**, *20*, 16973–16984.

(91) Weng, L. C.; Bell, A. T.; Weber, A. Z. Towards Membrane-Electrode Assembly Systems for CO2 Reduction: A Modeling Study. *Energy Environ. Sci.* **2019**, *12*, 1950–1968.

(92) Gabardo, C. M.; O'Brien, C. P.; Edwards, J. P.; McCallum, C.; Xu, Y.; Dinh, C. T.; Li, J.; Sargent, E. H.; Sinton, D. Continuous Carbon Dioxide Electroreduction to Concentrated Multi-Carbon Products Using a Membrane Electrode Assembly. *Joule* **2019**, *3*, 2777–2791.

(93) Weng, L.-C.; Bell, A. T.; Weber, A. Z. A Systematic Analysis of Cu-Based Membrane-Electrode Assemblies for CO2 Reduction through Multiphysics Simulation. *Energy Environ. Sci.* **2020**, *13*, 3592–3606.

(94) Hernandez-Aldave, S.; Andreoli, E. Fundamentals of Gas Diffusion Electrodes and Electrolysers for Carbon Dioxide Utilisation: Challenges and Opportunities. *Catalysts* **2020**, *10* (713).

(95) Liang, H.; Xu, R.; Chen, K.; Shen, C.; Yin, S. Self-Humidifying Membrane Electrode Assembly with Dual Cathode Catalyst Layer Structure Prepared by Introducing Polyvinyl Alcohol into the Inner Layer. *RSC Adv.* **2016**, *6*, 1333–1338.

(96) García de Arquer, F. P.; Dinh, C. T.; Ozden, A.; Wicks, J.; McCallum, C.; Kirmani, A. R.; Nam, D. H.; Gabardo, C.; Seifitokaldani, A.; Wang, X.; Li, Y. C.; Li, F.; Edwards, J.; Richter, L. J.; Thorpe, S. J.; Sinton, D.; Sargent, E. H. CO2 Electrolysis to Multicarbon Products at Activities Greater than 1 A cm−2. *Science.* **2020**, *367*, 661–666.

(97) Tan, Y. C.; Lee, K. B.; Song, H.; Oh, J. Modulating Local CO2 Concentration as a General Strategy for Enhancing C−C Coupling in CO2 Electroreduction. *Joule* **2020**, *4*, 1104–1120.

(98) De Mot, B.; Hereijgers, J.; Duarte, M.; Breugelmans, T. Influence of Flow and Pressure Distribution inside a Gas Diffusion Electrode on the Performance of a Flow-by CO2 Electrolyzer. *Chem. Eng. J.* **2019**, *378*, 122224.

(99) Li, H.; Oloman, C. Development of a Continuous Reactor for the Electro-Reduction of Carbon Dioxide to Formate - Part 2: Scale-Up. *J. Appl. Electrochem.* **2007**, *37*, 1107–1117.

(100) Lee, M. Y.; Park, K. T.; Lee, W.; Lim, H.; Kwon, Y.; Kang, S. Current Achievements and the Future Direction of Electrochemical CO2 Reduction: A Short Review. *Crit. Rev. Environ. Sci. Technol.* **2020**, *50* (8), 769–815.

(101) Jeanty, P.; Scherer, C.; Magori, E.; Wiesner-Fleischer, K.; Hinrichsen, O.; Fleischer, M. Upscaling and Continuous Operation of Electrochemical CO2 to CO Conversion in Aqueous Solutions on Silver Gas Diffusion Electrodes. *J. CO2 Util.* **2018**, *24*, 454–462.

(102) Krause, R.; Reinisch, D.; Reller, C.; Eckert, H.; Hartmann, D.; Taroata, D.; Wiesner-Fleischer, K.; Bulan, A.; Lueken, A.; Schmid, G. Industrial Application Aspects of the Electrochemical Reduction of CO2 to CO in Aqueous Electrolyte. *Chemie-Ingenieur-Technik* **2020**, *92*, 53–61.

(103) Wang, H.; Leung, D. Y. C.; Xuan, J. Modeling of a Microfluidic Electrochemical Cell for CO2 Utilization and Fuel Production. *Appl. Energy* **2013**, *102*, 1057–1062.

(104) Wu, K.; Birgersson, E.; Kim, B.; Kenis, P. J. A.; Karimi, I. A. Modeling and Experimental Validation of Electrochemical Reduction of CO2 to CO in a Microfluidic Cell. *J. Electrochem. Soc.* **2015**, *162* (1), F23–F32.

(105) Offong, A. C.; Anthony, E. J.; Manovix, V. Modelling and Simulating CO2 Electro-Reduction to Formic Acid Using Microfluidic Electrolytic Cells: The Influence of Bi-Sn Catalyst and 1-Ethyl-3-Methyl Imidazolium Tetra-Fluoroborate Electrolyte on Cell Performance. *Int. J. energy power Eng.* **2019**, *13* (8), 603–610.

(106) Georgopoulou, C.; Jain, S.; Agarwal, A.; Rode, E.; Dimopoulos, G.; Sridhar, N.; Kakalis, N. On the Modelling of Multidisciplinary Electrochemical Systems with Application on the Electrochemical Conversion of CO2 to Formate/Formic Acid. *Comput. Chem. Eng.* **2016**, *93*, 160–170.

(107) Newman, J.; Tiedemann, W. Porous-electrode Theory with Battery Applications. *AIChE J.* **1975**, *21* (1), 25–41.

(108) Bernardi, Dawn M., Verbrugge, M. W. Mathematical Model of a Gas Diffusion Electrode Bonded to a Polymer Electrolyte. *AIChE J.* **1991**, *37* (8), 1151–1163.

(109) Whipple, D. T.; Kenis, P. J. A. Prospects of CO2 Utilization via Direct Heterogeneous Electrochemical Reduction. *J. Phys. Chem. Lett.* **2010**, *1*, 3451–3458.

(110) Sridhar, N.; Hill, D. *Carbon Dioxide Utilization: Electrochemical Conversion of CO2 – Opportunities and Challenges*; 2011.

(111) Jhong, H. R. M.; Ma, S.; Kenis, P. J. Electrochemical Conversion of CO2 to Useful Chemicals: Current Status, Remaining Challenges, and Future Opportunities. *Curr. Opin. Chem. Eng.* **2013**, *2* (2), 191–199.

(112) Habermann, W.; Pommer, E. H. Biological Fuel Cells with Sulphide Storage Capacity. *Appl. Microbiol. Biotechnol.* **1991**, *35* (1), 128–133.

(113) Yang, Y.; Wu, Y.; Hu, Y.; Cao, Y.; Poh, C. L.; Cao, B.; Song, H. Engineering Electrode-Attached Microbial Consortia for High-Performance Xylose-Fed Microbial Fuel Cell. *ACS Catal.* **2015**, *5* (11), 6937–6945.

(114) Liu, T.; Yu, Y. Y.; Chen, T.; Chen, W. N. A Synthetic Microbial Consortium of Shewanella and Bacillus for Enhanced Generation of Bioelectricity. *Biotechnol. Bioeng.* **2017**, *114* (3), 526–532.

Chapter 3 Modelling the impact of operating mode and electron transfer mechanism in microbial fuel cells with two-species anodic biofilm

Published as: ***Z. Yang****, A. Yang* (2020), Biochemical Engineering Journal, 158, 107560.*

Among all authors contributed to the published article, ***Z. Yang*** *designed and performed the modelling work, analysed and interpreted the results, and wrote the manuscript. A. Yang designed and supervised the study, analysed and interpreted the results, and revised the manuscript.*

Summary

This chapter addresses the electricity-generating BESs, which is the first one of the two types of BESs studied in this thesis. With a focus on improving the understanding of multi-species biofilms, mathematical models are developed for a microbial fuel cell (MFC) with a 'fermenter-electrochemically active bacteria (EAB)' type, two-species biofilm, governed by mediator-based extracellular electron transfer (MET) or direct conduction-based extracellular electron transfer (DET), and operating under a batch or continuous mode. Numerical simulations have been carried out to test the impact of a range of physical and biochemical parameters on biofilm composition and current generation.

The results reveal the contrast between two operating modes, caused by the difference in the length of time available and in the substrate supply for the evolution of the biofilm, and the contrast between systems governed by MET and DET, arising primarily from the difference between the role of the mediator and that of the electrical potential played in the two systems, respectively. Many observations, including several counter-intuitive occasions, stem from the trade-offs between the impacts of the process parameters on bioelectrochemical kinetics, mass transfer, and electrical resistance. The simulation results also predict the existence of optimal parameter settings in various cases for the purpose of electricity generation. These findings provide potentially useful insights to guide the design and operation of MFCs or other types of bioelectrochemical devices that employ multi-species biofilms.

The framework of modelling bioelectrochemical processes developed in this chapter lays the foundation for the work in Chapter 4, where the second type of BESs is studied.

3.1 Introduction

In recent decades, climate change and other environmental issues associated with the use of fossil fuels make it urgent to explore green and renewable energy options. Bioelectrochemical systems (BESs), which generate electricity or valuable products[1–3] (such as hydrogen[4,5], hydrogen peroxide[6] and methane[7,8]) from low-cost substrates by the use of microorganisms, hold great potential in a wide range of energy, environmental and other biological applications. As an important example of BESs, microbial fuel cells (MFCs) are able to generate electricity from microbially catalysed anodic oxidation processes in the absence of conventional metal catalysts, with potential applications in several areas such as energy recovery, water purification, and biosensors for oxygen and pollutants[2,9,10].

MFCs rely on microorganisms to harvest energy and harness electrons from substrate. The microorganisms that are able to oxidise substrates and achieve extracellular electron transfer (EET) are often referred to as electrochemically active bacteria (EAB). To date, two prevailing types of anodic extracellular electron transfer (AEET) have been considered, namely mediator-based extracellular electron transfer (MET) and direct conduction-based extracellular electron transfer (DET). MET relies on soluble mediators as electron shuttles to convey electrons from bacteria cells to the anode surface. Oxidised mediators act as the primary electron acceptor (EA) to extract electrons from substrate, and reduced mediators subsequently diffuse to the anode surface, where electrons are released and the mediator is re-oxidised. In DET, electrons are supplied to the anode directly via exchange with conductive biofilm in this type[11–13].

While a single species of EAB can be capable of completing the conversion of certain types of substrate to electrons on its own, it has been shown that synergy may exist in a multispecies biofilm compared to pure culture which enhances substrate conversion, electron transfer and power output[9,14–16]. For example, the ‘fermenter-EAB’ community of *Shewanella oneidensis* (*S. oneidensis*) and *Escherichia coli* (*E. coli*) was investigated, with the latter acting as a fermenter to convert the primary substrate (glucose) into what the former (acting as the EAB) could utilise[17,18]. More recently, a microbial consortium comprising *S. oneidensis* MR-1 and *Bacillus subtilis* RH33 was utilised, in which the latter, nonelectrogenic microbe produced a high amount of mediators (riboflavin) to boost bioelectricity generation of the former, which

is an EAB[16]. Both of the two studies found that the maximum voltage output, substrate utilisation and electron transfer efficiency of the mixture consortia were higher than the pure culture. In addition, it was reported by several studies that a synthesised mixture community was capable to sustain high diversity by avoiding one species dominating and to resist external environmental disturbances, hence improving the overall stability of the system[16,19].

Up to now, most studies on the multispecies BESs (and MFCs in particular) are of a nature of experimental exploration[16–18,20]. On mathematical modelling, only a handful of modelling studies address multispecies systems. An earlier work simulated anodic biofilms with anaerobic digestion (AD), where the microbial community involved EAB and the typical microbial populations of AD, with MET as the modelled AEET mechanism. The dynamic evolution of several variables (solute concentration in the bulk liquid, distribution of current density and biomass on the anode) were evaluated and the effect of external resistance was considered, which however did not focus on the interplay between various mechanisms[21]. Later, the model of multispecies AD biofilm was extended to include further details such as the pH variation in the liquid flow at the anodic chamber, yet without revealing the spatial distribution of multiple species in the biofilm[22]. A very recent study presented the modelling of four microbial groups in a bioanode which carried out fermentation, electroactivity and methanogenesis, with DET as the assumed AEET mechanism[23]. All these existing modelling studies are yet to be extended to support further systematic analysis of multi-species bioanodes, particularly on the evolution and stability of the microbial communities in anodic biofilms in connection with various internal mechanisms and operating conditions.

In this work, new insights are sought with respect to (i) the spatial distribution and dynamics of a multi-species biofilm hosting bioelectrochemical processes, and (ii) their impact on electricity generation in a MFC. Adopting a relatively simple, 1D biofilm model and a two-species "fermenter-EAB" consortium, the focus of this work is to analyse in detail the change in the composition of the biofilm resulting from the interplay between electrochemical kinetics, mass transport and AEET mechanisms, under the influence of (i) biofilm characteristics such as maximum thickness, conductivity, and seeding ratio of the initial populations, (ii) operating mode, i.e. batch or continuous, and (iii) operating settings such as substrate supply, dilution rate and external electrical resistance. The purpose of this study is to develop an understanding of the impact of these key factors and their trade-offs, hence offering insights for the future engineering of multi-species biofilms in MFCs and other similar BESs.

3.2 Model description

The constructed model focuses on the anodic chamber of a MFC operating with an external electrical resistance. The anodic chamber comprises an electrode with biofilm attachment and a bulk liquid phase in which the electrode is embedded. The biofilm is based on a two-species community, with a fermenter to convert a primary substrate to an intermediate substrate to feed an EAB. The biofilm is assumed to only grow in the x-axis direction which is perpendicular to the impenetrable anode surface (i.e. the direction in which the biofilm heterogeneity is typically dominant[24]). The biofilm inner surface (i.e. that next to the supporting electrode base) is located at $x = 0$; the interface with the bulk liquid phase (where x = biofilm thickness) is referred to as the outer surface. As illustrated in Figure 3.1, the whole model for the anodic chamber is divided into three sub-models: electrode, biofilm and bulk liquid sub-models. Their formulations with two different operating modes (batch and continuous) and two AEET mechanisms (MET and DET) are presented below. In "fermenter-EAB" type of multispecies system, the soluble components consist of primary substrate (i.e. the substrate directly added to the MFC), intermediate substrate (i.e. the product generated by the fermenter to feed the EAB) and two forms of mediator (i.e. oxidised and reduced).

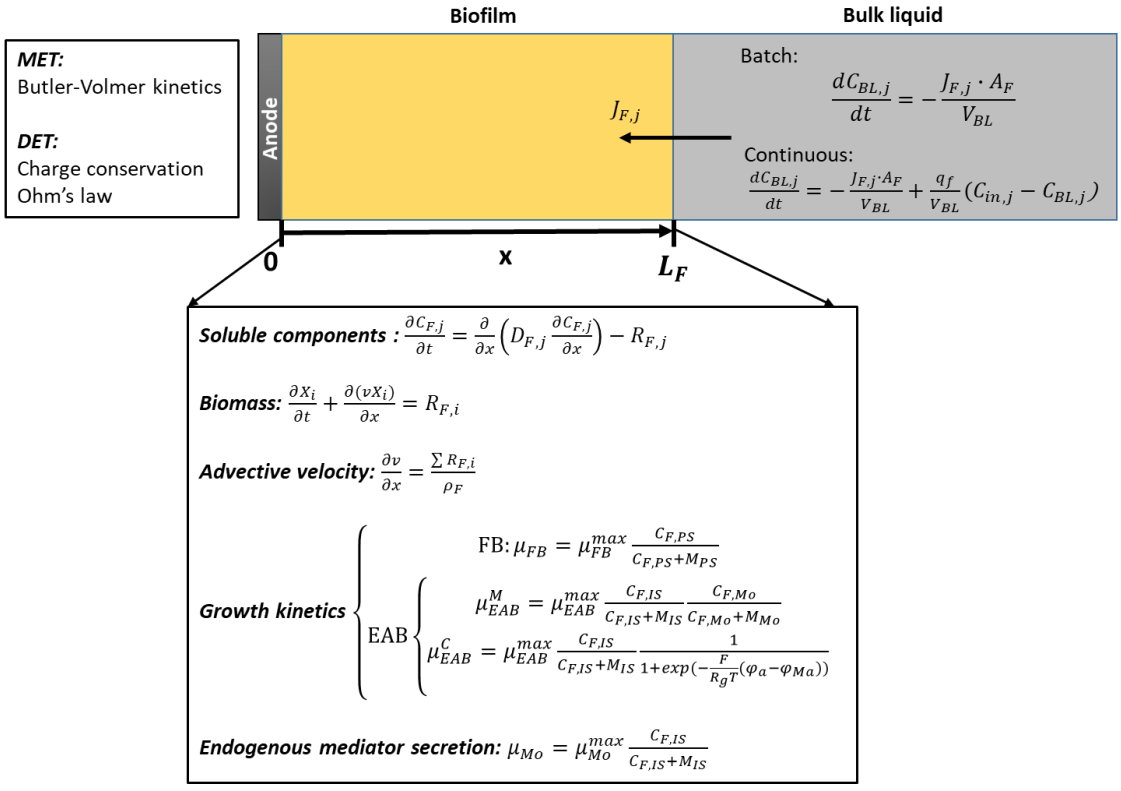

Figure 3.1 Schematic model and equations applied in the MFC model.

3.2.1 Electrode sub-models

3.2.1.1 MET-based model

The current generation via the MET pathway relies on the conversion of the two forms of a mediator at the anode surface. This reversible chemical process is depicted as:

$$C_{F,Mr}|_{x=0} \underset{r_{ox}}{\overset{r_{red}}{\leftrightharpoons}} C_{F,Mo}|_{x=0} + ne^- \quad \text{(R3.1)}$$

$C_{F,Mr}|_{x=0}$ and $C_{F,Mo}|_{x=0}$ represent the concentrations of the reduced and oxidised forms of the mediator (Mr and Mo) at the anode surface, respectively. For a given reversible redox reaction and given concentrations of the involved chemical species, the anode potential (φ_a) (which determines the overpotential) is the decisive factor of the reaction direction. A higher (lower) potential increases the rate of the oxidation (reduction) process per unit electrode surface area, r_{ox} (r_{red}). The oxidation and reduction rates of the mediator at the anode surface, are governed by the Butler-Volmer kinetics as commonly adopted in MFC models[11,12,25,26]:

$$r_{ox} = k_{ox} C_{F,Mr}|_{x=0} exp\left(\frac{(1-\beta)nF}{R_g T}\varphi_a\right) \quad (3.1)$$

$$r_{red} = k_{red} C_{F,Mo}|_{x=0} exp\left(\frac{-\beta nF}{R_g T}\varphi_a\right) \quad (3.2)$$

where k_{ox}, k_{red} are the oxidation and reduction rate constants, respectively; β is the transfer coefficient; n is the number of electrons transferred per redox mediator reaction; R_g is the ideal gas constant; T is the operating temperature. Note that resolving φ_a involves Eq. (3.8) which is to introduce later. The net redox reaction rate, r^M equals to $(r_{ox} - r_{red})$, and the current density, i^M is:

$$i^M = nFr^M \quad (3.3)$$

where F is the Faraday constant.

3.2.1.2 DET-based model

With DET, electrons liberated from the (intermediate) substrate oxidation process (assuming no endogenous respiration) are conducted to the anode surface through the biofilm matrix with

an assumed constant effective biofilm conductivity, k_s^{eff}. Electron transfer via DET is considered as an irreversible process (similar to enzymatic reactions), meaning electrons only have the oxidation current (i.e. electrons flow towards anode) and cannot be sent back to the cells due to irreversibility of the microbial metabolic processes[12,13,27]. However, in order to include non-soluble electrodes into the kinetics, it is assumed here that the transfer of electrons between the bacteria and the conductive biofilm are fast and reversible.

The change in current (i^C) in the biofilm matrix is caused by the production of electrons via DET[13]. The charge conservation is applied[12,13,28,29]:

$$\frac{\partial i^C}{\partial x} = -FR^C \tag{3.4}$$

where R^C is the electron generation rate via DET. R^C is obtained according to the Pirt model[30]:

$$R^C = \frac{\gamma_{IS} f_e^o X_{EAB} \mu_{EAB}^C}{Y_{IS/EAB}} \tag{3.5}$$

where γ_{IS} is the degree of reduction (i.e. electron equivalence) of EAB's substrate[31]; f_e^o is the fraction of the EAB's substrate used for energy generation[13]; $Y_{IS/EAB}$ is the (apparent) yield of EAB on its substrate; X_{EAB} and μ_{EAB}^C are the EAB's biomass concentration in the biofilm and the specific growth rate associated with the DET mechanism, respectively. X_{EAB} and μ_{EAB}^C will be described further in the following sections.

Ohm's law defines the relationship between the anode potential, φ_a and current density, corresponding to an assumed electron hopping process within the biofilm adjacent to the anode[13,32]:

$$k_s^{eff} \frac{\partial \varphi_a}{\partial x} + i^C = 0 \tag{3.6}$$

Collectively, Eqs. (3.4) to (3.6) can lead to the governing Eq. (3.7) used for simulating potential changes in the anodic biofilm:

$$k_s^{eff} \frac{\partial^2 \varphi_a}{\partial x^2} = \frac{F \gamma_{IS} f_e^o X_{EAB} \mu_{EAB}^C}{Y_{IS/EAB}} \tag{3.7}$$

The following equation, which is also derived from Ohm's law acts as the boundary condition at the biofilm inner surface to solve Eq. (3.7)[33]:

$$\varphi_a = \varphi_c - |i^C| A_E (R_{int} + R_{ext}) \tag{3.8}$$

where φ_c is the cathode potential; A_E is the electrode surface area; R_{int} and R_{ext} represent the internal and external resistance, respectively. Note that Eq. (3.8) is also used in the MET-based model for resolving φ_a. A non-flux boundary condition is adopted for Eq. (3.7) at the biofilm outer surface, since electrons cannot conduct outside the biofilm[13]. Focusing on the simulation of the anodic chamber, φ_c, is assumed to be fixed to a specific value while φ_a is predicted[26].

3.2.2 Biofilm sub-models

3.2.2.1 Mass balance of soluble components

In the anodic chamber considered in this work, soluble components are present in the biofilm (modelled here) and in the bulk liquid phase (modelled in Section 3.2.3). These components include the primary substrate, the intermediate substrate, and, in the case of MET, the oxidised form and the reduced form of the mediator. Concentrations of soluble components in the biofilm are a function of time and location. Mass balance for any soluble component, j, can be expressed as:

$$\frac{\partial C_{F,j}}{\partial t} = \frac{\partial}{\partial x}\left(D_{F,j}\frac{\partial C_{F,j}}{\partial x}\right) - R_{F,j} \tag{3.9}$$

where $C_{F,j}$ is the concentration of a soluble component, j, in the biofilm; $D_{F,j}$ is the diffusion coefficient for the soluble component, j, in the biofilm; $R_{F,j}$ denotes the net consumption rate of the soluble component. Eq. (3.9) states that the concentration of a dissolved component in the biofilm changes in response to the molecular diffusion (first term on the right hand side) and reactions (second term on the right hand side) in the biofilm. For most practical applications, the advective flux[34,35] and molecular turbulent dispersion[28] are shown to be negligible small compared with the diffusion process and thus not included in Eq. (3.9).

Based on Fick's first law and continuity of the flux at biofilm/bulk liquid interface, the flux of a soluble component across the interface, $J_{F,j}$, (defined as per unit cross-sectional area of the entire biofilm) is given below, assuming a constant concentration gradient in the diffusion layer

on the bulk liquid side adjacent to the biofilm outer surface (where $x = L_F$, the biofilm thickness).

$$J_{F,j} = D_{F,j} \frac{\partial C_{F,j}}{\partial x}|_{x=L_F} = \frac{D_{BL,j}}{L_{LBL}} (C_{BL,j}\epsilon - C_{F,j}|_{x=L_F}) \quad (3.10)$$

where $D_{BL,j}$ is the diffusion coefficient in the bulk liquid; L_{LBL} is the thickness of the liquid boundary layer (LBL) between the bulk liquid phase and the biofilm; ϵ is the porosity of the biofilm, introduced into the equation to account for the nature of the concentrations in the biofilm being per unit volume of the entire biofilm (i.e. solid matrix plus void space occupied by fluid). Eq. (3.10) serves as the boundary condition for Eq. (3.9) at the biofilm outer surface.

At the inner surface of the biofilm (i.e. the anode surface), the following mass balance applies[26,28]:

$$D_{F,j} \frac{\partial C_{F,j}}{\partial x}|_{x=0} + r_j = 0 \quad (3.11)$$

where r_j is the production rate of the soluble component, j, per unit surface area. For components not involved in reactions at this surface (i.e. primary and intermediate substrates), the consumption rate becomes zero.

3.2.2.2 Mass balance of biomass

Mass balance of the biomass of each microbial species considers biomass production and advective movement due to biofilm growth[13,36]. Because the advective flux plays the dominating role, therefore, other types of flux are negligible[28,34]:

$$\frac{\partial X_i}{\partial t} + \frac{\partial (v X_i)}{\partial x} = R_{F,i} \quad (3.12)$$

where X_i is the concentration of the biomass, i, in the biofilm; v is the advective velocity (i.e. the velocity at which the biofilm grows along the x-axis); $R_{F,i}$ denotes the net production rate for the biomass, i, in the biofilm.

As a simplifying assumption, inactivation of biomass is ignored. The advective velocity is modelled as below, with the value of zero applied at the anode/biofilm[13,36]:

$$\frac{\partial v}{\partial x} = \frac{\sum R_{F,i}}{\rho_F} \tag{3.13}$$

where ρ_F is the biofilm biomass density, which is defined as the ratio of dry biomass weight and biofilm volume.

3.2.2.3 Growth kinetics

Growth of the fermentative bacteria (FB) is modelled according to the Monod Equation:

$$\mu_{FB} = \mu_{FB}^{max} \frac{C_{F,PS}}{C_{F,PS} + M_{PS}} \tag{3.14}$$

where μ_{FB} is the specific growth rate; μ_{FB}^{max} is the maximum specific growth rate; $C_{F,PS}$ is the primary substrate concentration in the biofilm; M_{PS} is the half-saturation (Monod) constant.

The specific growth rate of the EAB is controlled by both its substrate and the EA. With MET, the oxidised mediator plays the role of EA. During the reaction with the intermediate substrate that feeds the EAB, the soluble mediator is reduced by capturing electrons from the intermediate substrate and then diffused towards the anode surface, discharging its electrons there and converted (re-generated) to the oxidised form. The rate of EAB's specific growth rate with the MET mechanism, μ_{EAB}^{M} can be modelled by the double Monod kinetic equation, which is frequently used to represent the dual limitation[12,13,26,37–40]:

$$\mu_{EAB}^{M} = \mu_{EAB}^{max} \frac{C_{F,IS}}{C_{F,IS} + M_{IS}} \frac{C_{F,Mo}}{C_{F,Mo} + M_{Mo}} \tag{3.15}$$

where μ_{EAB}^{max} is the maximum specific growth rate; $C_{F,IS}$ and $C_{F,Mo}$ represent the concentration of the intermediate substrate and that of the EA (i.e. Mo), respectively; M_{IS}, M_{Mo} are the half-saturation (Monod) constants corresponding to the intermediate substrate and the EA.

In the case of DET, the biofilm-modified anode is assumed to be the only EA which accepts the electrons generated by the EAB through the biofilm matrix comprising extracellular polymeric substances and biomass[41]. Modifying the double Monod equation and using anode potential, φ_a, as the driving force of electrons transfer, the rate of EAB's specific growth rate in DET mechanism (μ_{EAB}^{C}) can be modelled by the Nernst-Monod Equation, commonly adopted in previous modelling work[13,23,27,33].

$$\mu_{EAB}^{C} = \mu_{EAB}^{max} \frac{C_{F,IS}}{C_{F,IS} + M_{IS}} \frac{1}{1 + exp\left(-\frac{F}{R_g T}(\varphi_a - \varphi_{Ma})\right)} \quad (3.16)$$

where φ_{Ma} denotes the anode potential corresponding to half-maximum specific growth rate.

The growth of FB leads to the conversion of the primary substrate to the intermediate substrate. The growth of the EAB with either AEET mechanism causes the consumption of the intermediate substrate in the biofilm. In the MET case, it also causes the consumption of the oxidised mediator and the production of the reduced mediator. These chemical conversion rates are modelled through links with the growth kinetics via respective yield coefficients (see Appendix A, Section I for details).

3.2.2.4 Endogenous mediator secretion

Cell proliferation of the *Shewanella* species was previously shown to be clearly accompanied by the secretion of the mediator in its oxidised form (Mo)[42]. Here, the specific Mo secretion rate (μ_{Mo}) is modelled by a Monod-type equation:

$$\mu_{Mo} = \mu_{Mo}^{max} \frac{C_{F,IS}}{C_{F,IS} + M_{IS}} \quad (3.17)$$

where μ_{Mo}^{max} represents the maximum specific Mo secretion rate. The abundance of Mo in the anodic chamber is determined by the initial concentration of the mediator (which is assumed to be all in the oxidised form) and the endogenous secretion; no external mediator addition is considered.

3.2.3 Bulk liquid sub-models

The bulk liquid phase plays a role of supplying nutrients to the biofilm. Through diffusion, other soluble components can also be exchanged between the bulk liquid phase and the biofilm. The bulk liquid compartment is treated as a well-mixed volume. As this work focuses on the biofilm, no planktonic biomass is modelled in the bulk liquid, unless stated otherwise. Moreover, detached biomass from the biofilm is also neglected.

In a batch system, the mass balance of a soluble component in the bulk liquid is described as below:

$$\frac{dC_{BL,j}}{dt} = -\frac{A_F \cdot J_{F,j}}{V_{BL}} \tag{3.18}$$

where $C_{BL,j}$ is the concentration of a soluble component, j, in the bulk liquid; A_F is the area of the liquid-biofilm interface, i.e. the cross-sectional area of the biofilm, identical to the area of anode substratum, A_E.

In a continuous system where the bulk liquid volume is connected with an inlet flow and an outlet flow with the same volumetric flowrate, q_f, the mass balance of a soluble component is written as:

$$\frac{dC_{BL,j}}{dt} = -\frac{A_F \cdot J_{F,j}}{V_{BL}} + \frac{q_f}{V_{BL}}(C_{in,j} - C_{BL,j}) \tag{3.19}$$

where $C_{in,j}$ is the concentration of the soluble component in the inlet flow.

3.2.4 Biofilm thickness

Referring to the advective velocity of the biofilm as introduced earlier in Eq. (3.13), the biofilm thickness changes as follows:

$$\frac{dL_F}{dt} = v|_{x=L_F} \tag{3.20}$$

The above equation ignores the detachment loss of biomass from the biofilm at its outer surface, and ceases to be active once the biofilm thickness has reached a pre-defined maximum level. To avoid dealing with the moving outer boundary of the biofilm due to its growth, a converted coordination is constructed by introducing ζ, which is defined as[13,36]:

$$\zeta = \frac{x}{L_F} \tag{3.21}$$

This treatment allows the above-mentioned boundary to be fixed at $\zeta = 1$. This conversion requires the previously introduced functions $f(x,t)$ to be converted to $f(\zeta,t)$ in accordance with the following rules in which $\frac{dL_F}{dt}$ is termed as u_L[36]:

$$\frac{\partial f(x,t)}{\partial x} = \frac{1}{L_F}\frac{\partial f(\zeta,t)}{\partial \zeta} \tag{3.22}$$

$$\frac{\partial f(x,t)}{\partial t} = \frac{\partial f(\zeta,t)}{\partial t} - \frac{\zeta u_L}{L_F}\frac{\partial f(\zeta,t)}{\partial \zeta} \tag{3.23}$$

Biofilm growth has been modelled in all the simulations of a batch system. For continuous systems, preliminary tests in this work showed that the simulation results were affected to a negligible extent by the inclusion of the phase where the biofilm grows from its initial thickness to its maximum thickness, and this phase also turned out to be rather short compared to the time needed for the system to reach a steady state. Therefore, when a continuous system was simulated, this phase of growth was neglected, and a constant biofilm thickness was applied.

3.3 Model implementation and application

All constructed models have been implemented in the COMSOL Multiphysics Software (5.3a Version COMSOL Inc., Burlington, MA, USA).

We have applied the models to an anodic biofilm with *S. oneidensis, (as known as* MR1) as the EAB and *E. coli* as the FB. For *S. oneidensis*, the existence of multiple electron transfer pathways including MET and DET has been confirmed by several studies[12,27,43,44]. The same consortium was used in a previously reported experimental study[17], where *E. coli* metabolised glucose to lactate, formate and acetate, and *S. oneidensis* utilised intermediate metabolites to generate and transport electrons. It was suggested that formate was the main substrate for *S. oneidensis*, and AEET was assumed to be via MET. It was also suggested that part of the electricity generation was by *E. coli*. In the present theoretical study, we have followed the divide between the roles of the fermenter (only producing the intermediate substrate, not electricity) and the EAB (being the only electricity producer) as presented earlier in model description section, and have taken formate as the only intermediate substrate to be consumed by the EAB (i.e. *S. oneidensis*). It is worthy to note here that the impacts of the energy content of various substrates on cell growth should be considered (if more than one substrate is utilised). Besides, both AEET mechanisms have been simulated. Given the key differences between the experiments reported and the systems to be simulated in this work, the physical and biochemical parameters were obtained from literature sources with no re-calibration to experimental data, although we have adopted, where information is available and applicable, the design and operational settings reported[17]. All parameters adopted in our simulation study

are listed in Table A.1 (see Appendix A, Section II), with items that deserve an explanation being described below.

For the mediator, flavin mononueleotide (FMN) is assumed in this work, which has previously been characterised[12,45,46]. The rate constants of the mediator oxidisation and reduction reactions, k_{ox} and k_{red} can be determined by the reference exchange current density, i_o^{ref} and the standard mediator redox potential, E^0. The i_o^{ref} in the mediator redox reaction is determined by assuming that reactant and oxidant concentrations are 1 mM and the reaction transfer coefficient is 0.5:

$$i_o^{ref} = nF {k_{ox}}^{0.5} {k_{red}}^{0.5} \tag{3.24}$$

Furthermore, the equilibrium potential in the reference condition is identical to the standard mediator redox potential. Therefore, according to the Nernst equation, the relationship between the standard mediator redox reaction and the oxidisation and reduction reaction constants can be developed:

$$E^0 = \frac{R_g T}{nF} \ln \frac{k_{red}}{k_{ox}} \tag{3.25}$$

Combining Eqs. (3.24) and (3.25), the values of k_a and k_c can be obtained with given values of i_o^{ref} and E^0.

3.4 Results

In this section, we present and interpret simulation results, to analyse the variation in the predicted biofilm composition and the corresponding power generation performance of the simulated MFC, under batch and continuous operating modes, two different AEET mechanisms (MET and DET), and a range of chemical, biological and physical conditions. Note that in all the simulation studies reported here, when different values of a specific parameter are tested, all other parameters retain their default values as given in Table A.1 (see Appendix A, Section II), unless stated otherwise. As mentioned earlier, it is assumed that the biomass would 'disappear' (i.e. not exist as planktonic cells in the bulk liquid) if it is excluded from the biofilm. A summary of the key results is provided in Table A.3(a) and (b) (see Appendix A, Section IX) for the batch mode and the continuous mode, respectively.

3.4.1 Batch mode

Here, we are interested in the impact of the two key initial conditions of a batch run, namely the concentrations of glucose and *Mo* and the MR1:*E. coli* seeding ratio in the initial biofilm. Besides, the maximum thickness reachable by the biofilm affects the absolute amount of biomass accommodated by the biofilm and the resistance to mass transfer and current. The external electrical resistance, on the other hand, may change the growth condition of the EAB through affecting the anode potential[47]. Therefore, these two parameters are also studied.

3.4.1.1 Effect of initial concentration of primary substrate (glucose), $C^0_{BL,PS}$

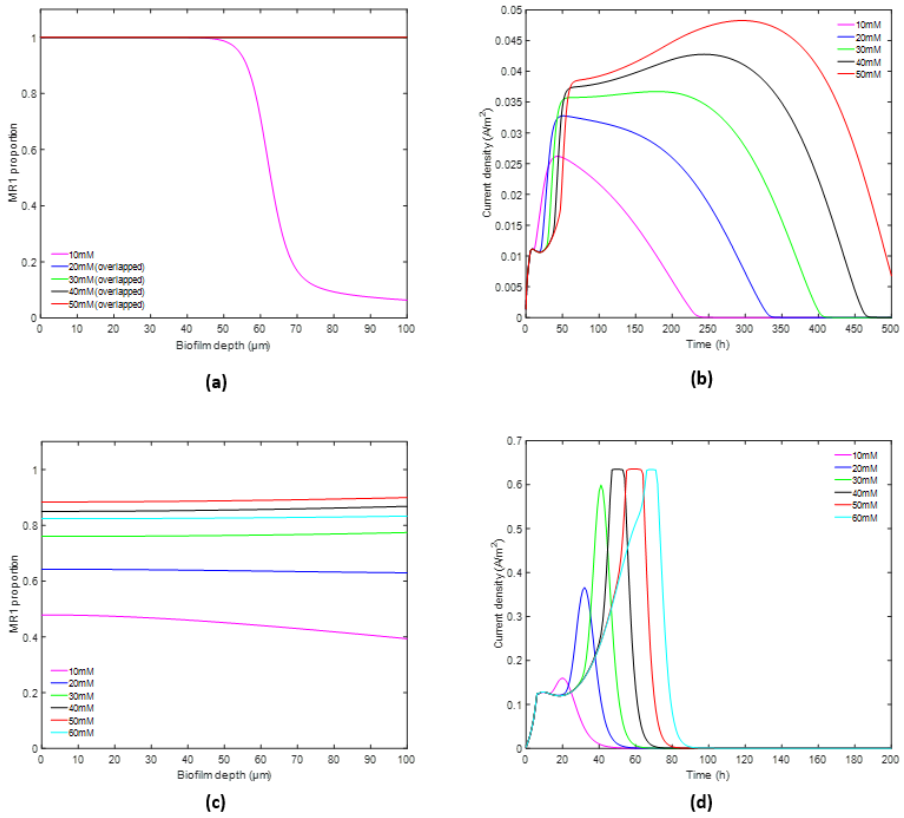

Figure 3.2 Model outputs of the batch MFC at different values of initial glucose concentration, $C^0_{BL,PS}$. (a) and (c): batch-end MR1 proportion in the biofilm with MET and DET, respectively; (b) and (d): current density profile with MET and DET, respectively.

In the case of MET, the co-existence of the two species can be maintained at the end of batch, only when the initial glucose concentration is the lowest among the tested levels (i.e. 10 mM, as shown in Figure 3.2(a)), while all the higher initial glucose concentrations lead to an 'MR1-

only' biofilm. The lower initial glucose supply means lower formate availability, which restricts the growth of MR1. In this case, formate is also depleted sooner and therefore MR1 stops growing within a shorter period. The combination of these two effects prevents MR1 from repelling *E. coli* completely during the batch, whereas in the cases with higher glucose supply both effects manifest in the opposite direction, leading to the exclusion of *E. coli* from the biofilm. Even in the case of sustained co-existence, the region of the biofilm closer to the anode surface is still fully occupied by MR1 thanks to its high specific growth rate in that location. The fraction of *E. coli* gradually increases towards the outer surface next to the bulk liquid phase, which is due to the combination of the decrease in the concentration of Mo (which restricts the growth of MR1) and the increase in the concentration of glucose (which promotes the growth of *E. coli*). Comparing the batch-end species distribution with the initial seeding ratio (MR1: *E. coli* $=$ 6: 4), one can see that over the batch MR1 and *E. coli* have been enriched close to the anode surface and to the bulk liquid, respectively.

It is worthy to note here that, in the cases of higher glucose supply, *E. coli* accomplishes complete glucose conversion before being repelled from the biofilm, consequently higher overall current generation is predicted with higher initial glucose concentrations (as shown in Figure 3.2(b)) which essentially imply greater availability of formate. However, in the early stage of the batch, a run with a higher glucose concentration is shown to produce a lower current density over a certain period of time. This is due to the less restricted initial growth of *E. coli* in that period, which leads to a lower fraction of the current-generating MR1. After that period, the increase in the availability of formate starts to become a dominating driver in the system, gradually turning MR1 to the dominant species, and hence greater current generation.

The results with DET (Figure 3.2(c)) show rather noticeable differences with those with MET. In terms of biofilm composition, the co-existence of the two species is maintained in all the tested cases. This is an outcome of a number of inter-connected factors. Firstly, there is less limitation to the growth of MR1 by potential (see Eq. (3.16)) in DET than that by M_o (see Eq. (3.15)) in MET. Besides, the predicted variation of potential across the biofilm is insignificant at the assumed biofilm thickness and electrical resistance, which is in sharp contrast with the rather uneven distribution of M_o in MET as its recovery (from its reduced form) occurs only at the anode surface. The above two factors mean that compared to the MET case, the predicted growth of MR1 over the entire biofilm is significantly greater during most part of a batch (see Appendix A, Figure A.1), and is spread relatively evenly across the biofilm resulting in a rather

sizable MR1 fraction even at its outer surface. The consequence is that a significant amount of MR1 biomass is produced (before formate is depleted), a noticeable proportion of which however leaves the biofilm through detachment at the outer surface (after the biofilm reaches its assumed maximum thickness). Besides, the faster exhaustion of formate (compared to the MET cases) also means that in all the tested DET cases, MR1 is not able to completely occupy the inner part of the biofilm before the depletion of formate (see Appendix A, Figure A.2), and the biomass composition cross the biofilm varies rather insignificantly (see Figure 3.2(c)), which are both in contrast with the results of the MET model. When the initial glucose concentration increases from 10 mM to 50 mM, the fraction of MR1 increases, as the benefit of a greater concentration of formate (converted from glucose, favouring the growth of MR1) outweighs that of a greater glucose concentration, favouring the growth *E. coli*. The relativity of benefits eventually changes when the initial glucose concentration increases further to 60 mM, leading to a reduced MR1 fraction in the biofilm.

On the predicted current density (Figure 3.2(d)), the impacts of glucose concentration on current density in DET are qualitatively similar to MET. However, the maximum current density achieved with DET is significantly higher than with MET, and the batch duration (marked by the time at which the current density becomes zero) of the former is much shorter than the latter. These are results of the DET case having greater averaged specific growth rate of MR1 (see Appendix A, Figure A.1) and greater consumption of formate by the stronger growth of MR1 (see Appendix A, Figure A.2).

3.4.1.2 Effect of seeding ratio (MR1:*E. Coli*)

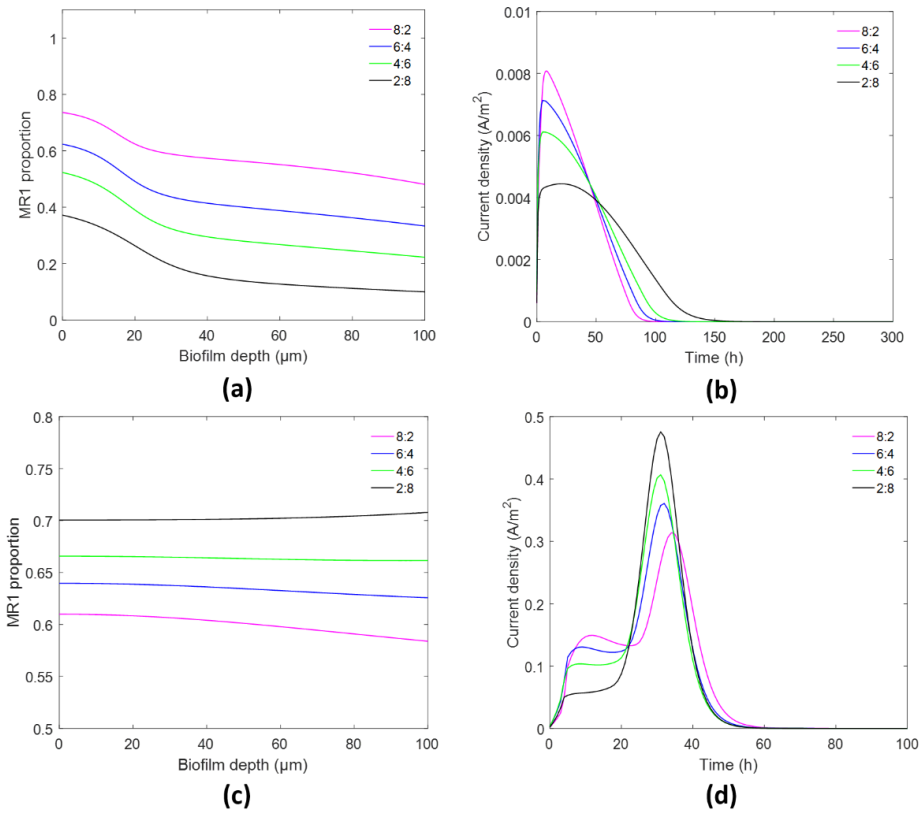

Figure 3.3 Model outputs of the batch MFC at different values of seeding ratios. (a) and (c): batch-end MR1 proportion with MET when $C^0_{BL,PS}$=1 mM and when with DET $C^0_{BL,PS} = 20$ mM, respectively; (b) and (d): current density profile with MET when $C^0_{BL,PS}$=1 mM and with DET when $C^0_{BL,PS} = 20$ mM.

Setting the initial glucose concentration to 20 mM, the variation in seeding ratio did not change the dominance of the high glucose (and hence formate) availability in the predicted dynamics of the system, as confirming the similar observation described in Section 3.4.1.1. However, at 10 mM, a level shown earlier (magenta line in Figure 3.2(a)) to lead to co-existence (at the default seeding ratio, 6: 4), the tested seeding ratios result in qualitatively similar batch-end species distribution profiles. If we continue to decrease the initial glucose concentration $C^0_{BL,PS}$ to 1 mM, the MR1 proportion at the anode surface changes significantly with seeding ratio, as shown in Figure 3.3(a). In this case, higher seeding ratios still lead to higher batch-end MR1 proportions in the biofilm, however in the case of the highest seeding ratio (8: 2), MR1 proportion at the anode surface reduces from 80% to ~ 75% during the batch (while an increase in predicted for the other ratios). This reduction is the victim of rapid consumption of formate by the large initial fraction of MR1 in the biofilm which causes a low formate

concentration and reduces the specific growth rate of MR1. In terms of current generation, higher seeding ratios generally lead to higher peaks of current density and shorter batches, when the seeding ratio can actually affect the biofilm composition, i.e. when the system starts with a sufficiently low glucose concentration, as illustrated in Figure 3.3(b) for the case of $C_{BL,PS}^{0} = 1$ mM.

In the case of DET, it turns out that the order of batch-end biofilm compositions between different batches completely reverses the order of the initial seeding ratios (Figure 3.3(c); see Figure A.3 in Appendix A, Section V for further details). When explaining the 1 mM $C_{BL,PS}^{0}$ case with MET (Figure 3.3(a)), we pointed out the negative effect on the specific growth rate of MR1 at the low formate concentration caused by the "over" consumption of a high initial fraction of MR1. In the cases tested with DET, this negative effect becomes much more pronounced, and leads to the observed reversion. Essentially, this means that a batch with a higher seeding ratio experiences a higher amount of MR1 in the biofilm (compared to a batch with a lower seeding ratio) in the early stage of the batch, and then moves to a biofilm composition with a lower amount of MR1. This is also reflected by the trends of current generation, as shown in Figure 3.3(d): a batch with a higher (lower) seeding ratio has a higher (lower) level of current density initially, and then transits to a lower (higher) level.

3.4.1.3 Effect of maximum biofilm thickness, L_F^{max}

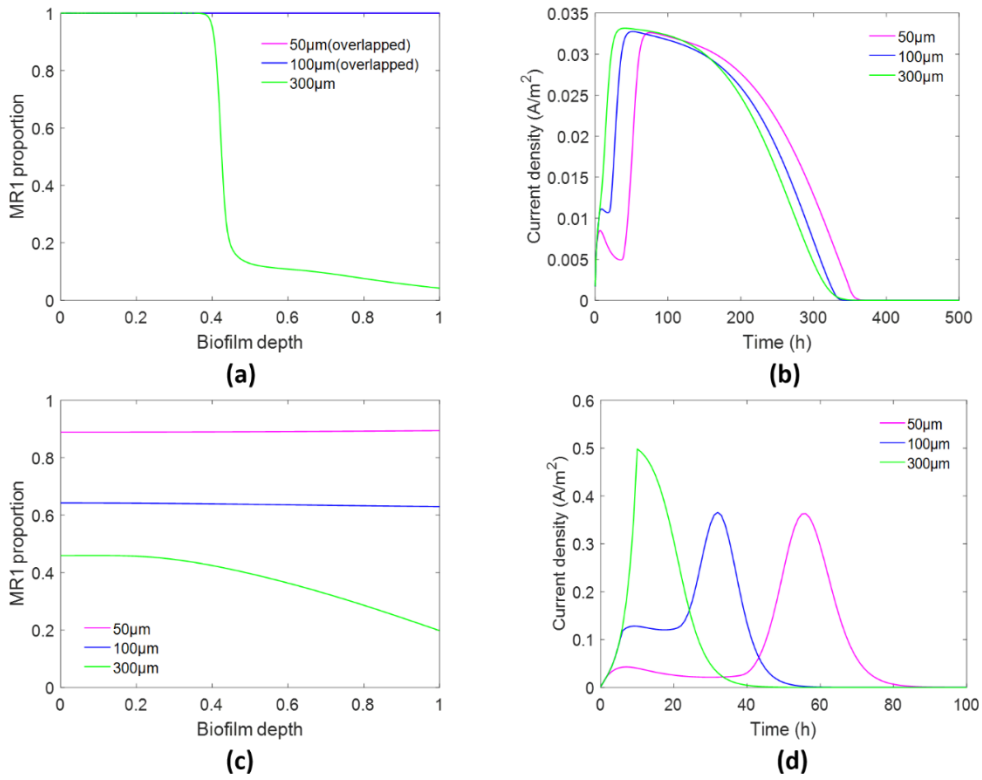

Figure 3.4 Model outputs of the batch MFC at different values of maximum biofilm thickness, L_F^{max}. (a) and (c): batch-end MR1 proportion in the biofilm with MET and DET, respectively; (b) and (d): current density profile with MET and DET, respectively.

With MET, the increase in biofilm thickness causes the biofilm type to shift from 'MR1-only' to 'MR1-*E. coli* co-existing' (see Figure 3.4(a)). The biofilm composition is closely related to Mo and formate concentration profiles within the biofilm. As the biofilm is set to greater thickness, the concentrations of formate and Mo are more hindered by diffusion resistance. Subsequently, the specific growth rate of MR1 is limited and MR1 cannot occupy the entire biofilm. On current generation, one can see from Figure 3.4(b) that the change in biofilm thickness causes little difference in the maximum current density. However, the two batches with lower thickness experience an apparent dip in current density after the biofilm grows to its maximum thickness. This is caused by the longer period of repulsion by *E. coli* to MR1 in these thinner biofilms which itself is due to longer availability of glucose.

In the case of DET, co-existence of the two species is predicted with all the three thickness levels; the overall proportion of MR1 is lower in a thicker biofilm (Figure 3.4(c)). Analogous

to the effect of a thicker biofilm on formate and Mo concentrations with MET, formate concentration and electrical potential are lower with a thicker biofilm in the case of DET, leading to slower growth of MR1. The more obvious change of MR1 proportion with location in the thickest biofilm is attributed to the increasing variation of electrical potential and formate concentration across the biofilm. The trend of current density with DET is similar as MET, but with stronger initial decrease in the two thinner biofilm. This is because of the faster formate consumption (hence weaker competitiveness of MR1) with DET, compared to the corresponding batch with MET, during the "dipping" period (Figure 3.4(d)).

3.4.1.4 Effect of external resistance, R_{ext}

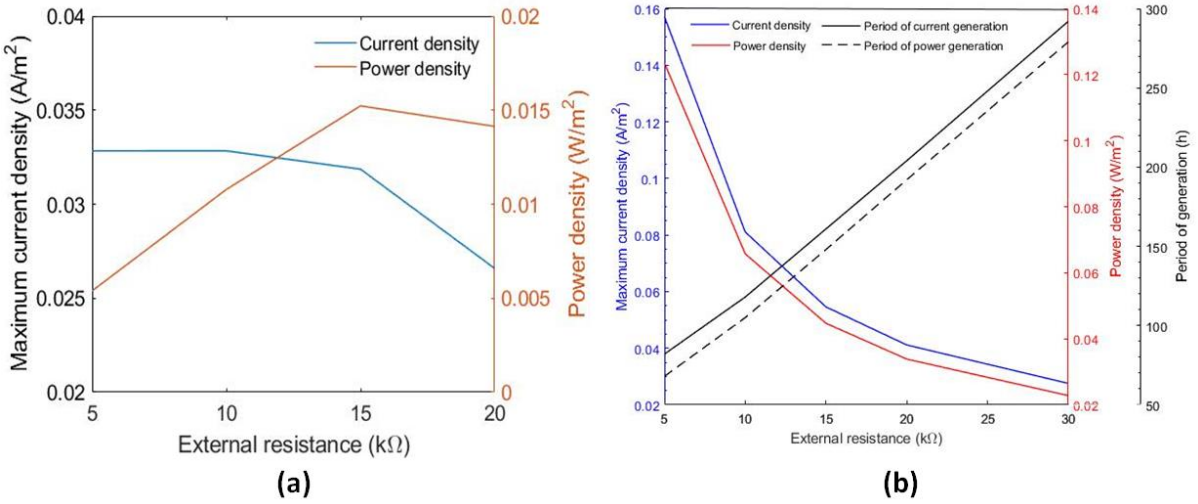

Figure 3.5 Model outputs of the batch MFC at different values of external resistance, R_{ext}. (a) with MET; (b) with DET.

The effect of R_{ext} on biofilm composition in the batches modelled with MET turns out to be insignificant, as a 'MR1-only' biofilm is always obtained at the end (results not shown). Besides, the simulation results suggest that the current density is insensitive to R_{ext} when R_{ext} is smaller ($< 10\ \text{k}\Omega$) (see Figure 3.5(a)). There are two factors that determine current generation in the case of MET: anode potential and M_r concentration at the anode surface. The anode potential is higher when R_{ext} is smaller, which has a direct positive impact on the rate of M_r oxidation ($M_r \rightarrow M_o$) at the anode surface. However, this also makes M_r harder to accumulate (see Appendix A, Figure A.4), which limits the oxidation process. The combined effect of the above two factors is that the difference in current density between different R_{ext} is rather insignificant at the lower range of R_{ext}. However, when R_{ext} becomes larger ($>$

10 kΩ), the influence of a lower anode potential is more significant and dictates the slower rate of the M_r oxidation process. Therefore, the peak current density decreases noticeably. In terms of power density, as the product of current density and R_{ext}, it shows a peak at $R_{ext} = 15$ kΩ (Figure 3.5(a)).

With DET, higher R_{ext} is beneficial for MR1 to occupy the biofilm by the end of a batch, with MR1 occupying the entire biofilm when R_{ext} exceeds 30 kΩ (see Appendix A, Figure A.5). We find that electrical potential in the biofilm drops significantly with a higher R_{ext}, which limits the specific growth rate of MR1. On the other hand, the restricted growth of MR1 also means lower consumption and therefore more sustained availability of formate, which enables MR1 to continue its growth for a longer period (corresponding to the period of current generation, see Appendix A, Figure A.6). Consequently, the fraction of MR1 is able to eventually recover and even dominates the biofilm. In terms of current generation, the batches with higher electrical resistance are predicted to have a lower peak current (and power) density but a longer period of active current (and power) generation, as shown in Figure 3.5(b). Note that the period of generation is defined as the length of time during the system generates current (and power).

3.4.1.5 Effect of initial concentration of the oxidised form of the mediator in the bulk liquid, $C^0_{BL,Mo}$

In the case of MET, the batch-end biofilm composition changes from 'MR1-only' to 'MR1-*E. coli* co-existing' type with M_o increase (see Appendix A, Figure A.7(a)). In Section 3.4.1.2, we have pointed out that a higher MR1:*E.coli* seeding ratio can lead to faster formate consumption which hinders the occupation of the biofilm by MR1. A similar effect is caused here by a higher M_o. With respect to current generation, faster formate consumption caused by a higher initial concentration of M_o leads to an earlier and higher peak current density, and a shorter duration of current production, as shown in Figure A.7(b) (see Appendix A, Section VII).

3.4.2 Continuous mode

With the continuous mode, our interest lies in the longer-term behaviour and performance of the MFC, which appeared from the conducted simulation runs to be insensitive to the initial glucose concentration $C^0_{BL,PS}$ in the bulk liquid and the seeding ratio, therefore the results of

the simulations aimed to show their influence are not reported here. Besides, the effect of external resistance on the biofilm composition was shown to be negligible. The predicted power generation showed the same characteristics in simulations with the two different AEET mechanisms: the current density decreases with the increasing external resistance, and an optimal value of external resistance exists and corresponds to a maximum power density, both of which are in accordance with the previously reported experimental finding[47]. As no insights manifested additionally to those already revealed by the batch mode with respect to the impact of external resistance, the simulation results pertaining to this parameter are not further discussed. The rest of this section will thus focus on the impact of two important parameters for a continuous bioreactor, namely flowrate (which determines dilution) and inlet substrate (i.e. glucose in this case) concentration, as well as biofilm thickness which shows multiple effects in the earlier analysis of the batch mode. Besides, one initial condition, namely the initial Mo concentration in the bulk liquid, was shown to affect the long-term composition of the biofilm, hence the relevant results are presented here. Unless stated otherwise, the results shown are of a steady state reached by the continuous reactor.

3.4.2.1 Effect of flowrate, q_f

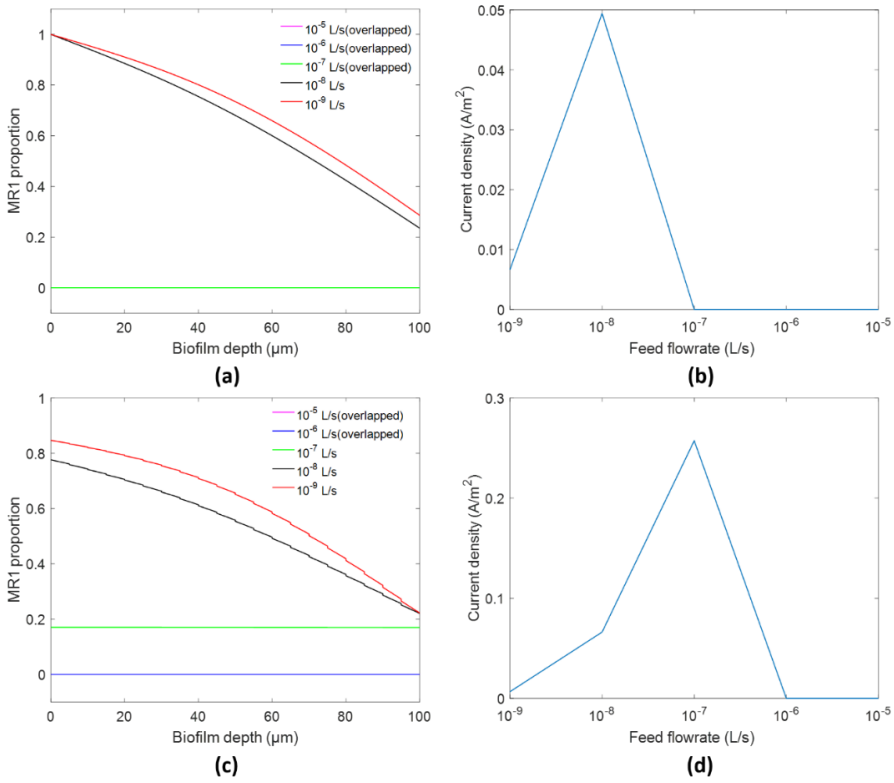

Figure 3.6 Model outputs of the continuous MFC at different values of flowrate, q_f. (a) and (c): MR1 proportion in the biofilm at the steady state with MET and DET, respectively; (b) and (d): current density profile with MET and DET, respectively.

The results for the MET model are shown in Figure 3.6(a) and (b). With the feeding flowrate being 1×10^{-7} L/s or higher, MR1 is shown to be completely repelled from the biofilm, which is due to the significant dilution impact leading to a low formate concentration that causes severe restrictions to the growth of MR1. This means collapse of the 'fermenter-EAB' consortium, and hence the failure of the system to produce current. When the flowrate is reduced to 1×10^{-8} L/s, the anodic chamber becomes able to accumulate formate to a level that allows MR1 to compete with *E. coli* for the space in the biofilm, leading to a biofilm composition profile similar to those observed earlier in the batch reactor (with MET). As the two-species consortium is stably present, continuous current generation is sustained. Further reduction of the flowrate improves the competitiveness of MR1 in the biofilm, however the lower supply of glucose leads to the reduction of current density.

For DET, Figure 3.6(c) and (d) show that in general, biofilm composition and current generation follow a tendency of changes with flowrate similar to the case of MET. It is noticeable, however, the biofilm transfer from '*E. coli*-only' to '*E. coli*-MR1 co-existing' via a special occasion with unvaried distribution of the two species cross the biofilm, at a flowrate of 1×10^{-7} L/s. In this occasion, the formate concentration is high enough to increase the specific growth rate of MR1 (compared to the cases with higher flowrates) to the same level of *E. coli* before *E.coli* completely occupies the biofilm. At steady state, this identical specific growth rate of MR1 and *E.coli* dictates a zero spatial gradient of the biomass fractions in the biofilm (see Appendix A, Section VIII for a proof).

3.4.2.2 Effect of inlet concentration of primary substrate (glucose), $C_{in,PS}$

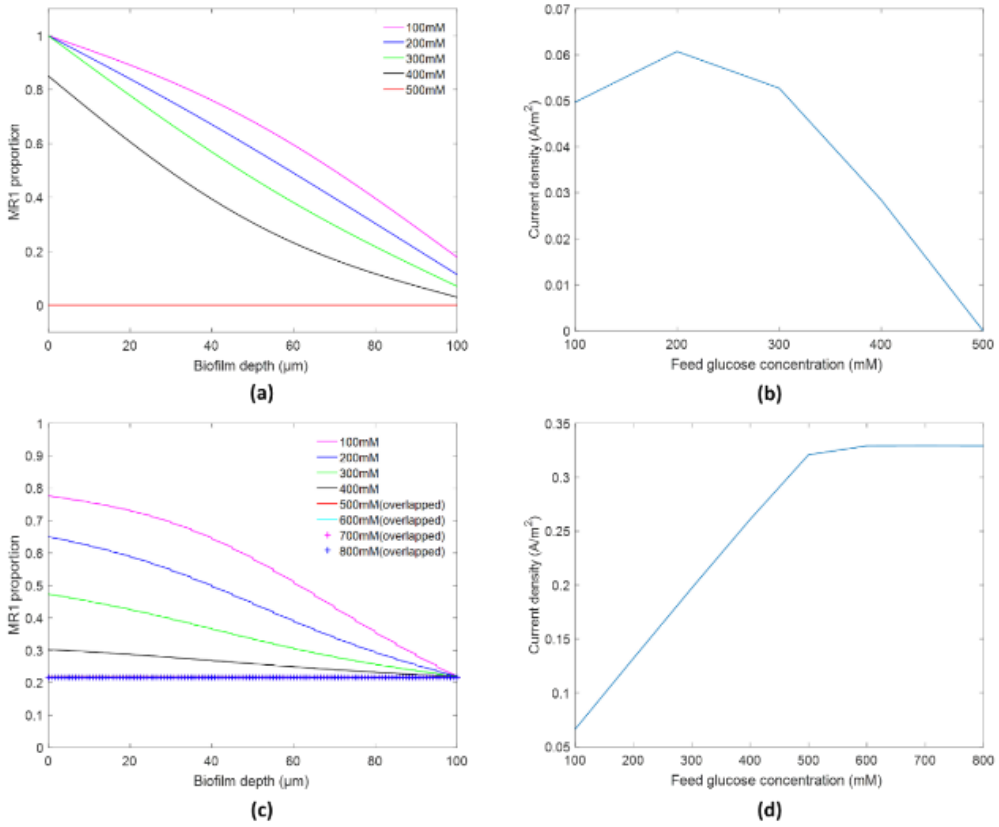

Figure 3.7 Model outputs of the continuous MFC at different values of inlet glucose concentration, $C_{in,PS}$. (a) and (c): MR1 proportion in the biofilm at the steady state with MET and DET, respectively. (b) and (d): current density profile with MET and DET, respectively.

As shown in the Figure 3.7(a), a continuous MFC governed by MET is predicted to have *E. coli* repelling MR1 from the biofilm strongly when the system is fed with more concentrated

glucose, with *E. coli* occupying the biofilm completely when $C_{in,PS}$ increases to 500 mM. At the biofilm inner surface, the specific growth rate of *E. coli* rises significantly when $C_{in,PS}$ is increased to 400 mM as it to a large extent reduces the glucose limitation to the growth of *E. coli* even at this most remote location for glucose supply. Although the increased *E. coli* growth also means better supply of formate, the specific growth rate of MR1 starts to decline at a certain point due to the limitation by M_o following the fast initial consumption resulting from the abundant substrate supply. These two causes collectively lead to the predicted decline and eventual exclusion of MR1 from the biofilm as $C_{in,PS}$ increases. On current generation, Figure 3.7(b) shows that the current density boosts firstly as the greater supply of the substrate plays a more dominant role. After that, it decreases, dictated by the decline of the fraction of MR1 in the biofilm.

In the case of DET, the fraction of MR1 in the biofilm also shows a declining trend as $C_{in,PS}$ increases. However, unlike the case of MET where MR1 is eventually repelled completely, here an upper limit ($\sim 80\%$) is predicted for the proportion of *E. coli* (Figure 3.7(c)). This is because, compared to the significant influence of the reduction in M_o concentration in the case of MET, the level of the anode potential in the case of DET allows the specific growth rate of MR1 to eventually stabilise at a level equal to that of *E. coli*, resulting in the co-existing, even distribution of the two species across the biofilm. On current generation, the case of DET is shown (Figure 3.7(d)) to be dominated by the supply of the substrate (via the specific growth rate of MR1, as opposed to the fraction of MR1 in the biofilm) with increase in current density until the substrate supply reaches a saturated level.

3.4.2.3 Effect of maximum biofilm thickness, L_F^{max}

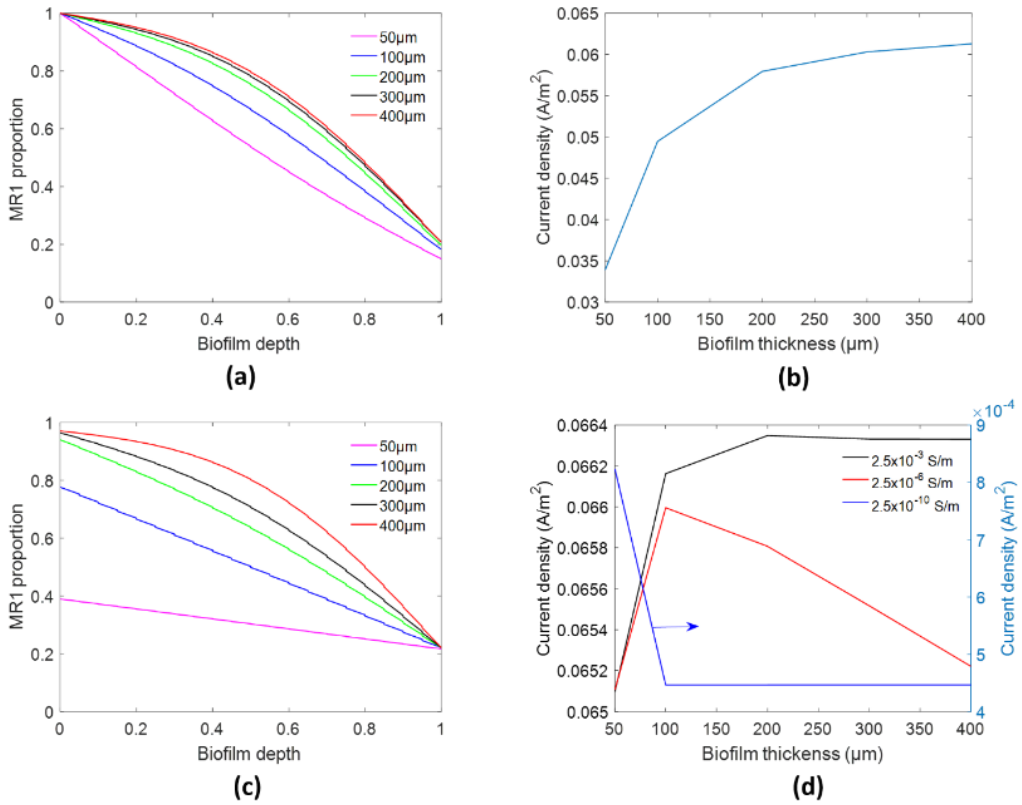

Figure 3.8 Model outputs of the continuous MFC at different values of the maximum biofilm thickness, L_F^{max}. (a) and (c): MR1 proportion in the biofilm at the steady state with MET and DET, respectively; (b) and (d): current density with MET and DET, respectively.

In the case of MET, it can be seen from Figure 3.8(a) that the proportion of MR1 in the biofilm increases with the thickness of the biofilm, which is due to the negative effect of a thicker biofilm on the growth of *E. coli* via the impediment of the diffusion of glucose from the bulk liquid. The gain in the fraction of MR1 in a thicker biofilm however decreases as the thickness increases, because of the negative impact of the impeded diffusion of glucose on the supply of formate. Accordingly, the current density shows an increasing trend with the biofilm thickness, but at a reduced increment, as presented in Figure 3.8(b).

Compared to MET, the DET case is affected by the biofilm thickness via another factor additional to the impediment on glucose diffusion: electrical resistance (and hence potential) within the biofilm matrix. However, the results shown in Figure 3.8(c), similar to that of MET, are primarily dictated by glucose diffusion, since at the default electrical conductivity of the biofilm (2.5×10^{-3} S/m) the potential gradient within the biofilm is negligible. With

hypothetical lower conductivity values, the impact of potential becomes more predominant, as can be seen in Figure 3.8(d). The figure shows that, with a higher conductivity (2.5×10^{-3} S/m), the current density increases with biofilm thickness when the biofilm is thinner than 200 μm, due to the dominating effect of the increased fraction of MR1 in the biofilm. Beyond this thickness, the current density has no obvious further improvement, because of the combined effect of the two factors that generally affect the current density, namely the increase in MR1 fraction and the decrease in the specific growth rate of MR1 (mainly due to the reduction in formate availability at this particular level of conductivity). With lower conductivities, overall the biofilm generates smaller current densities, which is not surprising as higher electrical resistance causes lower electrical potential and hence slower growth of MR1.

Figure 3.8(d) also shows that when the biofilm conductivity is 2.5×10^{-6} S/m, there is an optimal biofilm thickness within the tested range, which corresponds to a maximum current density, suggesting that the disadvantage of a thicker biofilm (causing potential drop across the biofilm) becomes increasingly pronounced and eventually overweighs the advantage of the increase in MR1 fraction. When the biofilm conductivity is the lowest, i.e. 2.5×10^{-10} S/m, the lower MR1 specific growth rate (now significantly caused by the reduction of potential across the biofilm) is the major determinant of current generation: the current density decreases first as the biofilm thickness increases and then sustains a constant level by the compensation of a higher MR1 biomass fraction in the thicker biofilm.

3.4.2.4 Effect of initial concentration of the oxidised form of the mediator in the bulk liquid, $C^0_{BL,Mo}$

Both initial Mo concentration, $C^0_{BL,Mo}$ and inlet concentration of primary substrate (glucose), $C_{in,PS}$ would vary in different practical applications (for example, treating the wastewater from various sources, intending to boost performance by artificially increasing $C^0_{BL,Mo}$). In this section, the effect of $C^0_{BL,Mo}$ coupled with $C_{in,PS}$ is discussed. It turns out that the impact of initial Mo concentration, $C^0_{BL,Mo}$ on the steady-state biofilm composition, in MET-based systems, is dependent of inlet concentration of primary substrate (glucose), $C_{in,PS}$, as shown in Table 3.1.

Table 3.1 Variation of biofilm composition with $C^0_{BL,Mo}$ and $C_{in,PS}$.

$C^0_{BL,Mo}$	$C_{in,PS} = 100$ mM	$C_{in,PS} = 300$ mM	$C_{in,PS} = 500$ mM
0 mM	*E. coli*-MR1 co-existence	*E. coli* only	*E. coli* only
1×10^{-5} mM			
1×10^{-3} mM		*E. coli*-MR1 co-existence	
1×10^{-1} mM			

The steady-state biofilm composition does not change with the initial Mo concentration when $C_{in,PS}$ is as either 100 mM or 500 mM. At the lower $C_{in,PS}$, the Mo concentration in the biofilm is able to sustain the specific growth rate of MR1 and is not consumed rapidly, hence allowing for the two species to co-exist. At the higher $C_{in,PS}$, none of the tested Mo values can sustain the consumption by the growth of MR1 and will become depleted eventually. Together with the fact that a higher $C_{in,PS}$ is also beneficial for *E. coli* growth, an '*E. coli*-only' biofilm results with all the tested initial Mo concentrations, and this result is consistent with the earlier discussion on the impact of $C_{in,PS}$ (see Section 3.4.2.2). When $C_{in,PS}$ equals to 300 mM, however, the increase in the initial Mo concentration appears to be able to cause changes to the stable biofilm composition, with the biofilm shifts from '*E. coli*-MR1 co-existing' to '*E. coli*-only'. Among the tested levels of the initial Mo concentration, the "middle" value of 1×10^{-3} mM appears to mark the transition in the ability of the available Mo to sustain MR1 in the biofilm. As an effective approach to produce helpful simplification of a mathematical model, the dimensional analysis/non-dimensionalisation is encouraged to be introduced in the future.

3.5 Discussion

3.5.1 Batch vs. Continuous reactors

The nature of a batch reactor means that the evolution of its dynamics terminates once all the substrates are completely consumed, whereas a continuous reactor has the chance to unfold its dynamics without such a time limitation. Due to this difference, the initial conditions significantly affect the biofilm composition and current generation in the batch mode, which however often do not have an impact on the long-term state of the continuous reactor (with the exception of the initial M_o concentration in the case of MET). Taking seeding ratio as an

example, our simulation results show that the initial setting clearly influence the end state of the batch reactor through distinct mechanisms and dynamics with MET and DET. In a continuous reactor, such dynamics could also be experienced in the early stage of the operation, yet the further evolution of the dynamics would eventually eliminate the influence of the difference in the initial setting. On the impact of other parameters settings, the theoretically infinitely long period of operation, together with the continued supply of substrate, could lead to rather different outcomes in the continuous reactor than its batch counter-part. In fact, it was the case of the maximum biofilm thickness: MR1 proportion decreases with biofilm thickness in the batch mode, while an opposite trend manifests in the continuous mode with both AEET mechanisms.

In both batch and continuous reactors, optimal parameter settings could be identified from the simulation results, although in different senses. With a continuous reactor, steady-state power output can be used as a clear objective, which can only be delivered by parameter settings that result in a stable consortium. From Table A.3(b) (see Appendix A, Section IX), one can see such parameter settings, which are typically those that lead to the "best" composition of the biofilm, i.e. those resulting in the ideal combination of the amount of MR1 in the biofilm and its overall specific growth rate. For a batch reactor, all the tested cases showed complete conversion of the original substrate (glucose) regardless of the final composition of the biofilm. However, in terms of power generation, batches with certain parameter settings are predicted to have a higher peak current density and a shorter period needed for complete conversion (see Appendix A, Table A.3(a)), which may be considered as more desirable than the other parameter settings.

3.5.2 MET vs. DET

From the model description, one can see that with both AEET mechanisms, current generation is primarily determined by the growth of MR1, either directly as with DET or indirectly as with MET (which is through affecting the generation of the reduced mediator). In the case of MET, the specific growth rate of MR1 is affected by the concentration of M_o, which is replaced by the potential in the biofilm in the case of DET. In the results section, we have already stated one important implication of this difference: As M_o is regenerated by oxidation only at the anode surface, its concentration declines rapidly in the biofilm towards the outer surface. In contrast, the electrical potential tends to have minor variation across the biofilm except when

its electrical resistance is extremely high. This difference underlies several general observations relating to the comparison of DET with MET, including a lesser degree of spatial variation in the fractions of the two species, greater overall growth of MR1 in the biofilm, and higher attainable current density. There is yet another aspect of the difference between the role of M_o in MET and that of potential in DET: A positive feedback loop exists with M_o and the growth of MR1, in that a higher M_o concentration can escalate the proportion of MR1 in the biofilm; the increased amount of MR1 in turn produces more M_o. In contrast, a higher potential can improve the growth of MR1 and hence current generation, which however would lead to the increase of the potential loss by the external load, i.e. to a reduction to the potential at the anode surface and hence across the biofilm, hence forming a negative feedback loop. None of these two loops would function in isolation with other aspects of the dynamics of the reactor, yet the difference between them means that temporal variation of M_o could bring influence more significantly to an MET system than that of the potential to a DET system.

In this work, these two AEET mechanisms have been studied separately. There is experimental evidence that shows the co-functioning of MET and DET in certain systems[48]. It would be interesting for the future work to model a multi-species anodic biofilm with dual AEET mechanisms, building on an existing model[12].

3.5.3 Trade-offs and their implications

It is noticeable that biofilm composition response and current generation performance are often the result of various trade-offs between multiple impacts of individual factors. For example, the initial glucose concentration in a batch reactor and the feed glucose concentration in a continuous reactor affect both the growth rate of *E. coli* (directly) and that of MR1 (via formate concentration). In a continuous reactor, its flowrate affects both substrate supply and dilution. In both types of reactors, biofilm thickness impacts on the amount of biomass the biofilm can accommodate and on the resistances to mass transfer and current conduction. In each pair of such trade-off impacts, their relevant dominance determines the "net" impact of the impacting factor, which however may shift with the variation in the magnitude of some other parameter settings, as observed, for example, in the predicted variation of the steady-state current density against biofilm thickness in the continuous reactor with DET and an intermediate level of biofilm conductivity (see Section 3.4.2.3). The trade-offs and their shifts have shown in several cases to lead to the existence of an optimal parameter value, such as 15 kΩ for the external

resistance in batch with MET; 1×10^{-8} and 1×10^{-7} $\mathrm{L/s}$ for the flowrate in the continuous MFCs with MET and DET, respectively; and 100 μm for the biofilm thickness with moderate conductivity (i.e.2.5×10^{-6} $\mathrm{S/m}$) in the continuous MFC with DET. It should be mentioned that biofilm composition and current generation may show different trends from the impact of the various factors and trade-offs, as the former is primarily affected by the comparative specific growth rate of the two microbes at different locations of the biofilm, while the latter is largely affected by the overall amount of MR1 biomass in the biofilm and its overall (or average) specific growth rate.

3.6 Conclusions

Detailed simulation studies were carried in this work on MFCs with an anodic biofilm populated with a 'fermenter-EAB' two-species microbial consortium. The results reveal the responses of biofilm composition and current generation to a range of chemical, biological and physical factors via two different AEET mechanisms (MET and DET) and under two operating modes (batch and continuous). The outcome of a batch MFC was shown to be significantly influenced by all the initial conditions, while the oxidised mediator concentration appeared to be the only initial condition that affects the steady state of a continuous MFC (with MET). The two operating modes also showed contrasting responses to the maximum biofilm thickness, while the continuous mode additionally showed critical impacts of flowrate and the inlet substrate concentration on the stability of the consortium and on the relative species abundance across the biofilm. Between MET and DET, the different roles and spatial distribution profiles of oxidised mediator concentration (relevant to MET) and electrical potential (relevant to DET) were shown to dictate a number of key differences in the predicted outcomes of the two AEET mechanisms. Generally, biofilm composition and current generation in the simulated MFCs are shaped by the trade-offs that exist between multiple impacts of individual factors in all the simulated cases, reflecting the interplay between microbial growth, mass transfer, and electrical conduction. Our simulation results also suggested that optimal settings exist with several parameters leading to reduced batch duration or enhanced continuous power generation.

References

(1) Allen, R. M.; Bennetto, H. P. Microbial Fuel-Cells: Electricity Production from Carbohydrates. *Appl. Biochem. Biotechnol.* **1993**, *39*, 27–40.

(2) Harnisch, F.; Schroder, U. From MFC to MXC: Chemical and Biological Cathodes and Their Potential for Microbial Bioelectrochemical Systems. *Chem. Soc. Rev.* **2010**, *39* (11), 4433–4448.

(3) Yu, Y. Y.; Zhai, D. D.; Si, R. W.; Sun, J. Z.; Liu, X.; Yong, Y. C. Three-Dimensional Electrodes for High-Performance Bioelectrochemical Systems. *Int. J. Mol. Sci.* **2017**, *18* (1).

(4) Cheng, S.; Logan, B. E. Sustainable and Efficient Biohydrogen Production via Electrohydrogenesis. *Proc. Natl. Acad. Sci. U. S. A.* **2007**, *104* (47), 18871–18873.

(5) Rozendal, R. A.; Jeremiasse, A. W.; Hamelers, H. V. M.; Buisman, C. J. N. Hydrogen Production With a Microbial Biocathode. *Environ. Sci. Technol.* **2008**, *42*, 629–634.

(6) Rozendal, R. A.; Leone, E.; Keller, J.; Rabaey, K. Efficient Hydrogen Peroxide Generation from Organic Matter in a Bioelectrochemical System. *Electrochem. commun.* **2009**, *11* (9), 1752–1755.

(7) Villano, M.; Aulenta, F.; Ciucci, C.; Ferri, T.; Giuliano, A.; Majone, M. Bioelectrochemical Reduction of CO2 to CH4 via Direct and Indirect Extracellular Electron Transfer by a Hydrogenophilic Methanogenic Culture. *Bioresour. Technol.* **2010**, *101* (9), 3085–3090.

(8) Cheng, S.; Xing, D.; Call, D. F.; Logan, B. E. Direct Biological Conversion of Electrical Current into Methane by Electromethanogenesis. *Environ. Sci. Technol.* **2009**, *43* (10), 3953–3958.

(9) Logan, B. E. Exoelectrogenic Bacteria That Power Microbial Fuel Cells. *Nat. Rev. Microbiol.* **2009**, *7* (5), 375–381.

(10) Do, M. H.; Ngo, H. H.; Guo, W. S.; Liu, Y.; Chang, S. W.; Nguyen, D. D.; Nghiem, L. D.; Ni, B. J. Challenges in the Application of Microbial Fuel Cells to Wastewater Treatment and Energy Production: A Mini Review. *Sci. Total Environ.* **2018**, *639*, 910–920.

(11) Okamoto, A.; Hashimoto, K.; Nealson, K. H.; Nakamura, R. Rate Enhancement of

Bacterial Extracellular Electron Transport Involves Bound Flavin Semiquinones. *Proc. Natl. Acad. Sci.* **2013**, *110* (19), 7856–7861.

(12) Renslow, R.; Babauta, J.; Kuprat, A.; Schenk, J.; Ivory, C.; Fredrickson, J.; Beyenal, H. Modeling Biofilms with Dual Extracellular Electron Transfer Mechanisms. *Phys. Chem. Chem. Phys.* **2013**, *15* (44), 19262–19283.

(13) Marcus, A. K.; Torres, C. I.; Rittmann, B. E. Conduction-Based Modeling of the Biofilm Anode of a Microbial Fuel Cell. *Biotechnol. Bioeng.* **2007**, *98* (6), 1171–1182.

(14) Habermann, W.; Pommer, E. H. Biological Fuel Cells with Sulphide Storage Capacity. *Appl. Microbiol. Biotechnol.* **1991**, *35* (1), 128–133.

(15) Yang, Y.; Wu, Y.; Hu, Y.; Cao, Y.; Poh, C. L.; Cao, B.; Song, H. Engineering Electrode-Attached Microbial Consortia for High-Performance Xylose-Fed Microbial Fuel Cell. *ACS Catal.* **2015**, *5* (11), 6937–6945.

(16) Liu, T.; Yu, Y. Y.; Chen, T.; Chen, W. N. A Synthetic Microbial Consortium of Shewanella and Bacillus for Enhanced Generation of Bioelectricity. *Biotechnol. Bioeng.* **2017**, *114* (3), 526–532.

(17) Wang, V. B.; Sivakumar, K.; Yang, L.; Zhang, Q.; Kjelleberg, S.; Loo, S. C. J.; Cao, B. Metabolite-Enabled Mutualistic Interaction between Shewanella Oneidensis and Escherichia Coli in a Co-Culture Using an Electrode as Electron Acceptor. *Sci. Rep.* **2015**, *5*, 1–11.

(18) Ren, Z.; Ward, T. E.; Regan, J. M. Electricity Production from Cellulose in a Microbial Fuel Cell Using a Defined Binary Culture. *Environ. Sci. Technol.* **2007**, *41* (13), 4781–4786.

(19) Anna Prokhorova, A.; Katrin Sturm-Richter, a Andreas Doetsch, B.; Johannes Geschera, C. Resilience, Dynamics, and Interactions within a Model Multispecies Exoelectrogenic-Biofilm Community. *Appl. Environ. Microbiol.* **2017**, *83* (6), e03033-16.

(20) Tong Lin, Xue Bai, Yidan Hu, Bingzhi Li, Ying-Jin Yuan, H. S. Synthetic

Saccharomyces Cerevisiae-Shewanella Oneidensis Consortium Enables Glucose-Fed High-Performance Microbial Fuel Cell. *AIChE J.* **2017**, *63* (6), 1830–1838.

(21) Picioreanu, C.; Katuri, K. P.; Head, I. M.; Van Loosdrecht, M. C. M.; Scott, K. Mathematical Model for Microbial Fuel Cells with Anodic Biofilms and Anaerobic Digestion. *Water Sci. Technol.* **2008**, *57* (7), 965–971.

(22) Picioreanu, C.; van Loosdrecht, M. C. M.; Curtis, T. P.; Scott, K. Model Based Evaluation of the Effect of PH and Electrode Geometry on Microbial Fuel Cell Performance. *Bioelectrochemistry* **2010**, *78* (1), 8–24.

(23) Belleville, P.; Merlin, G.; Ramousse, J.; Deseure, J. Two-Dimensional Modelling of Syntrophic Glucose Conversion in Bioanodes for Coulombic Efficiency Optimization. *Bioresour. Technol. Reports* **2019**, *6*, 15–25.

(24) Zhou, X.-H.; Qiu, Y.-Q.; Shi, H.-C.; Yu, T.; He, M.; Cai, Q. A New Approach to Quantify Spatial Distribution of Biofilm Kinetic Parameters by in Situ Determination of Oxygen Uptake Rate (OUR). *Environ. Sci. Technol.* **2009**, *43* (3), 757–763.

(25) John, N.; Karen, E. T.-A. *Electrochemical Systems*, Third.; John Wiley & Sons: Hoboken, New Jersey, US, 2004.

(26) Picioreanu, C.; Head, I. M.; Katuri, K. P.; van Loosdrecht, M. C. M.; Scott, K. A Computational Model for Biofilm-Based Microbial Fuel Cells. *Water Res.* **2007**, *41* (13), 2921–2940.

(27) Torres, I.; Marcus, A. K.; Lee, H.; Parameswaran, P.; Krajmalnik-brown, R.; Rittmann, B. E. A Kinetic Perspective on Extracellular Electron Transfer by Anode-Respiring Bacteria. *FEMS Microbiol. Rev.* **2010**, *34*, 3–17.

(28) Wanner, O.; Eberl, H. J.; Morgenroth, E.; Noguera, D. R.; Picioreanu, C.; Rittmann, B. E.; Loosdrecht, M. C. M. van. *Mathematical Modeling of Biofilms*; IWA Task Group on Biofilm Modeling, 2006.

(29) Kazemi, M.; Biria, D.; Rismani-Yazdi, H. Modelling Bio-Electrosynthesis in a Reverse Microbial Fuel Cell to Produce Acetate from CO2 and H2O. *Phys. Chem. Chem. Phys.*

2015, *17*, 12561–12574.

(30) Beeftink, H. H.; Heijden, van der R. T. J. M.; Heijnen, J. J. Maintenance Requirements: Energy Supply from Simultaneous Endogenous Respiration and Substrate Consumption. *FEMS Microbiol. Ecol.* **1990**, *73*, 203–209.

(31) Smolke, C. *The Metabolic Pathway Engineering Handbook: Fundamentals*; CRC Press, 2009.

(32) Bernardi, Dawn M., Verbrugge, M. W. Mathematical Model of a Gas Diffusion Electrode Bonded to a Polymer Electrolyte. *AIChE J.* **1991**, *37* (8), 1151–1163.

(33) Karimi Alavijeh, M.; Mardanpour, M. M.; Yaghmaei, S. A Generalized Model for Complex Wastewater Treatment with Simultaneous Bioenergy Production Using the Microbial Electrochemical Cell. *Electrochim. Acta* **2015**, *167*, 84–96.

(34) Wanner, O.; Reichert, P. Mathematical Modeling of Mixed-Culture Biofilms. *Biotechnol. Bioeng.* **1996**, *49*, 172–184.

(35) Sakakibara, Y.; Flora, J. R. V.; Suidan, M. T.; Kurodo, M. Modeling of Electrochemically-Activated Denitrifying Biofilms. *Water Res.* **1994**, *28* (5), 1077–1086.

(36) Wanner, O.; Gujer, W. A Multispecies Biofilm Model. *Biotechnol. Bioeng.* **1986**, *28* (3), 314–328.

(37) Velasquez-orta, S. B.; Head, I. M.; Curtis, T. P.; Scott, K.; Lloyd, J. R.; Canstein, H. Von. The Effect of Flavin Electron Shuttles in Microbial Fuel Cells Current Production. **2010**, *85*, 1373–1381.

(38) Zhang, X.; Halme, A. Modelling of a Microbial Fuel Cell Process. *Biotechnol. Lett.* **1995**, *17* (8), 809–814.

(39) Bae, W.; Rittmann, B. E. A Structured Model of Dual-Limitation Kinetics. *Biotechnol. Bioeng.* **1996**, *49* (6), 683–689.

(40) Tsompanas, M. A.; Adamatzky, A.; Ieropoulos, I.; Phillips, N.; Sirakoulis, G. C.;

Greenman, J. Modelling Microbial Fuel Cells Using Lattice Boltzmann Methods. *IEEE/ACM Trans. Comput. Biol. Bioinforma.* **2019**, *16* (6), 2035–2045.

(41) Laspidou, C. S.; Rittmann, B. E. Modeling the Development of Biofilm Density Including Active Bacteria, Inert Biomass, and Extracellular Polymeric Substances. *Water Res.* **2004**, *38*, 3349–3361.

(42) Canstein, H. Von; Ogawa, J.; Shimizu, S.; Lloyd, J. R. Secretion of Flavins by Shewanella Species and Their Role in Extracellular Electron Transfer. *Appl. Environ. Microbiol.* **2008**, *74* (3), 615–623.

(43) Myers, C. R.; Myers, J. M. Localization of Cytochromes to the Outer Membrane of Anaerobically Grown Shewanella Putrefaciens MR-1. *J. Bacteriol.* **1992**, *174* (11), 3429–3438.

(44) Newman, D. K.; Kolter, R. A Role for Excreted Quinones in Extracellular Electron Transfer. *Nature* **2000**, *405*, 94–97.

(45) Pinto, D.; Coradin, T.; Laberty-Robert, C. Effect of Anode Polarization on Biofilm Formation and Electron Transfer in Shewanella Oneidensis/Graphite Felt Microbial Fuel Cells. *Bioelectrochemistry* **2018**, *120*, 1–9.

(46) Choi, S.; Kim, B.; Chang, I. S. Tracking of Shewanella Oneidensis MR-1 Biofilm Formation of a Microbial Electrochemical System via Differential Pulse Voltammetry. *Bioresour. Technol.* **2018**, *254*, 357–361.

(47) Zhang, L.; Zhu, X.; Li, J.; Liao, Q.; Ye, D. Biofilm Formation and Electricity Generation of a Microbial Fuel Cell Started up under Different External Resistances. *J. Power Sources* **2011**, *196*, 6029–6035.

(48) Uria, N.; Ferrera, I.; Mas, J. Electrochemical Performance and Microbial Community Profiles in Microbial Fuel Cells in Relation to Electron Transfer Mechanisms. *BMC Microbiol.* **2017**, *17* (208).

Chapter 4 Modelling cathodic biofilms with interacting dual extracellular electron transfer mechanisms in a microbial electrosynthesis cell for the production of acetate from carbon dioxide

To be submitted to Biotechnology and Bioengineering

Summary

This chapter delivers the numerical work of microbial electrosynthesis cells (MESs), which is the second type of BESs in this thesis. MESs are capable of sustainably upgrading CO_2 to various valuable chemicals. In this work, a dynamic model describing the conversion process of CO_2 to acetate in an MES is presented and quantitively validated against experimental data. This comprehensive model introduces the interactive dual-cathodic extracellular electron transfer mechanism (dual-CEET), and incorporates the details of the biofilm metabolism and pH effects.

Following successive identification of the dominating CEET, the impact of several parameters on acetate yield and production rate is evaluated. The numerical results suggest an optimal value for applied cathode potential, which results in the maximum acetate yield and production rate. A compromise between acetate yield and production rate is predicted when the initial pH value changes. Additionally, a larger thickness and a larger specific surface area of the biofilm are shown to be instrumental for achieving a higher acetate production rate. At last, a range of the specific gas-liquid interfacial area that could effectively improve acetate production rate is predicted. This study enables us to gain a deeper insight into the interactions between microorganisms and cathode electrode. The developed model could be a critical tool for the further design and optimisation of similar systems.

The understanding of the cathodic kinetics and transport phenomena, which is gained in this chapter, paves the way to the development of the mathematical model for electrochemical CO_2 reduction in Chapter 5.

4.1 Introduction

Electrochemical conversion of CO_2 to multi-carbon products, as one of the most attractive CO_2 capture and utilisation (CCU) technologies[1–4], is capable of reducing CO_2 by using simpler processes[5] operated at ambient conditions (i.e. 298 K and absolute pressure of 100 kPa)[6]. However, the practical application of conventional (i.e. abiotic) electrochemical CO_2 reduction reaction (ECO2RR) systems are limited by several factors, including poor stability and high expense of cathode materials, poor selectivity of products, sluggish CO_2 reduction reactions, and competition with hydrogen evolution process[7]. Additionally, ECO2RR is typically limited to reduce CO_2 to lower carbon products, such as formate or carbon monoxide (CO)[8].

The microorganisms, acting as biocatalysts, hold great promise for generating multi-carbon products[1,8] and have been proven to be able to accelerate the cathodic reaction by significantly reducing cathodic overpotential[9,10] and charge transfer resistance[11–13]. In addition to versatility and high specificity[14], the employment of microorganisms as catalysts could circumvent the unsustainability of material supply, corrosion and expensive use caused by the conventional metal cathode[12,15,16]. The systems with an objective to electrosynthesise chemical compounds through microbially catalysed cathodic reduction processes are referred to as microbial electrosynthesis cells (MESs)[14]. Unlike microbial fuel cells (MFCs) which generate power, externally supplied conventional or renewable electrical energy is required for the majority of MESs[2] to proceed with non-spontaneous reactions and/or accelerate reaction rates[14,15,17,18]. In this regard, MESs also offer a possibility to harvest and store intermittent renewable sources.

Acetate is the centre product of the current CO_2 electrochemical process[1,19] owing to its higher economic value[7,20], efficient production process (compared with other multiple carbon products, such as butanol)[14], and easy transportation and storage[14,21]. Moreover, it can be a precursor for other higher-value products (including ethyl alcohols, esters and alkanes[22]). Although MESs hold great promise, lower yield of acetate[7,23–25] (i.e. $< 0.1\ g\ L^{-1}\ h^{-1}$[19,26]) – stemming from smaller current density[2,10] – makes it less competitive than its counterparts (such as conventional electrolysers with metal catalysts)[10], and also hinders its successful transition from the laboratories to practical industrial applications[15,27,28]. In order to achieve successful commercialization, the production rate should reach at least several $g\ L^{-1}\ h^{-1}$ (or $g\ L^{-1}$in titre)[19], and current density is required to be boosted to $10^3\ A\ m^{-3}_{reactor}$[15,27]. A number of studies have found that the cathode properties[29] (such as surface roughness and biofilm

coverage), material[30,31] and type[32] would correlate to microbial electrosynthesis rate. Modification of cathode surface was proposed to be an attractive way to promote microbe-electrode interactions and eventually elevate microbial electrosynthesis rate[24,33]. However, these attempts were empirical due to the limited understanding of the electron transfer mechanism from an electrode to microbes[33]. Moreover, several approaches, such as using the carbon cloth modified with the metal nanoparticles, would be economically infeasible and therefore not suitable for further upscaling[33]. Supplement of the inhibitors restricting the growth of unfavourable microorganism offers another possibility to improve product yield[28], but the need for regular addition hinders its application in larger and long-term systems[28]. These existing developments in this area suggest that a better understanding of the mechanisms of cathodic extracellular electron transfer (i.e. cathode donating electrons to microorganisms, which is abbreviated to CEET), and rational design and optimisation of systems are required to improve system performance stably and sustainably[14,28,33,34].

In comparison with the numerous literature reporting the mechanisms of anodic extracellular electron transfer (i.e. electrons being transferred from microorganisms to the anode, which is abbreviated to AEET) in MFCs, only a few studies have shed light on CEET thus far[8,35]. The mechanisms of CEET are determined by medium culture and cathodic potential, and can vary for different types of microorganisms[34]. Analogous to the mechanisms of AEET, there are two putative mechanisms of CEET, namely cathodic mediator-based extracellular electron transfer (CMET) and cathodic direct conduction-based extracellular electron transfer (CDET)[14,35]. CMET means that the cathode feeds electrons to microorganisms by virtue of the mediators (or called 'electron shuttles'). There is a range of molecules that can act as mediators, such as thionine[36], neutral red[37–39], methyl viologen[40], self-secreted redox mediators[41], and hydrogen (H_2)[42–44]. The mediators are capable of accepting electrons from the cathode and then donating electrons to microorganisms[35]. CDET means that microorganisms draw electrons from the cathode directly[14,35]. Recently, our experiment[8] proposed that cathodic microorganisms can take up electrons either indirectly (i.e. CMET) or directly (i.e. CDET). In this case, the conductive biofilm is like the extension of the cathode. Both microorganisms and the mediators can interact with the conductive biofilm by means of exchanging electrons. The type of CEET that consists of interactive CMET and CDET is coined as 'dual-CEET'[45]. As mentioned earlier, a comprehensive understanding of CEET mechanisms is of paramount importance for the design and optimisation of a MES system to improve product yield. Model-based analyses

could offer an economical and efficient approach to improved solutions but, as indicated in Section 2.1.3.2, they have received limited attention to date.

In this study, a comprehensive one-dimensional (1D) dynamic model for an acetogens-dominating biofilm with interacting dual CEET mechanisms is established. Our experimentally validated model is used to explore the effects of several key parameters on the system's performance and give guidance for the potential process optimisation. To the best of our knowledge, this is the first modelling framework for the cathodic biofilm in the MESs with a detailed description of the interacting dual CEETs, and a detailed account of stoichiometry calculation and pH influence. This proposed work could advance the knowledge of CEET mechanisms and provide useful strategies for further practical design and operation.

4.2 Model description

Our modelling work is dedicated to a dual-chamber MES, which is fed with gaseous CO_2 and operated in the (semi-) batch mode. The constructed dynamic model focuses on the cathodic half-cell with a potentiostat maintaining the constant cathodic potential. The cathodic half-cell consists of the bio-cathode inoculated with active sludge[8], and the bulk liquid phase of catholyte in which cathode is immersed. Acetogens refer to the species that are capable of upgrading CO_2 to acetate via a reduction reaction[8,46]. As (i) the acetogens dominate in the biofilm (i.e. they occupy $\sim 50\%$ of the biofilm based on the experimental observation[8]) and (ii) the CEET mechanisms of acetogens are the topic of our interest, the other species are ignored in our model. Therefore, the proposed biofilm model is assumed to comprise active acetogens and inert components (i.e. solid matrix and inactivated acetogens) only. Owing to the relatively higher coulombic efficiency (which corresponds to a slower growth rate) of the current-consuming bacteria, it has been extensively reported that the cathodic biofilm is much thinner than the anodic biofilm[7,8,25,47–52]. Hence, same to the treatment in the prior MESs' modelling studies[53–55], the biofilm with a constant thickness is modelled. For computational efficiency, a 1D biofilm model is established by assuming that the biofilm only grows in the x-axis direction (i.e. perpendicular to the cathode substratum); thus, all quantities represent the average value over the plane parallel to the cathode substratum. As illustrated in Figure 4.1, the cathode substratum is located at $x = 0$, while the outer surface of the biofilm (i.e. the interface facing the bulk liquid phase) is at $x = L_F$.

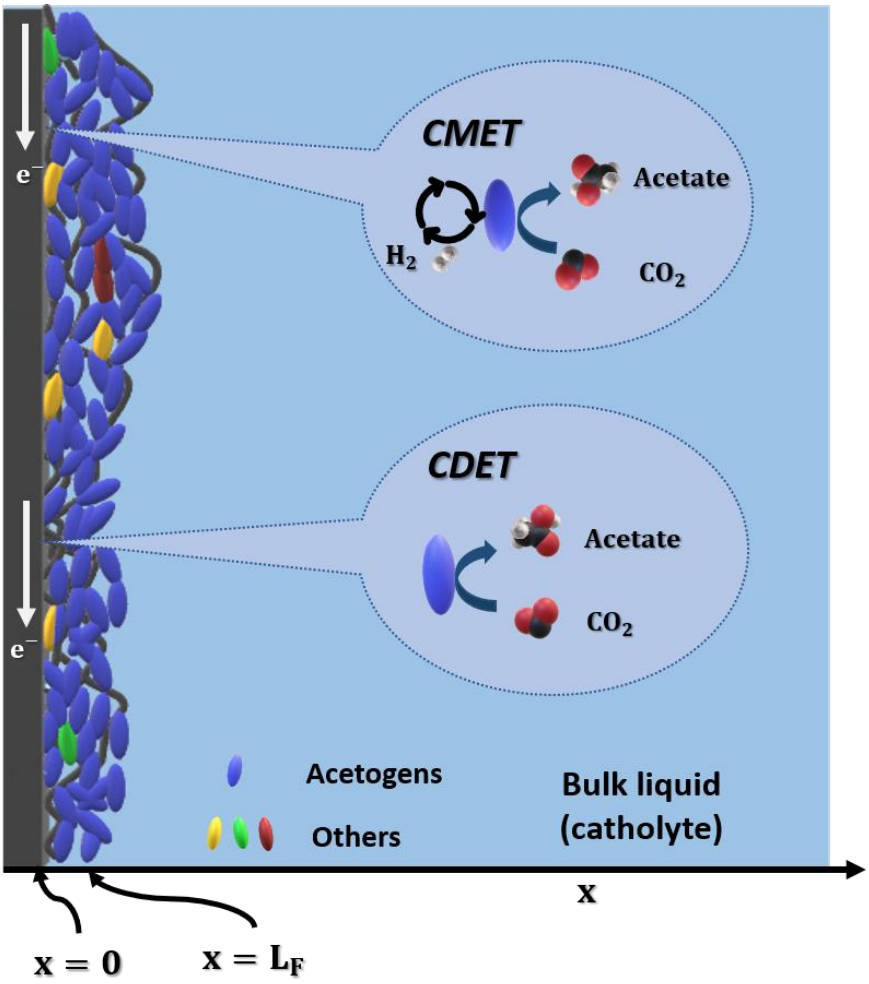

Figure 4.1 Schematic representation of individual CMET and CDET; and constructed mathematical model for an MES.

4.2.1 Mass conservation in the biofilm

The biofilm can be treated as a porous medium consisting of a solid phase (i.e. biomass) plus the void space occupied by the fluid[46,56]. The void space in the biofilm is assumed to be fully occupied by the liquid phase (i.e. catholyte), based on the experimental observation of no detection of any gaseous species[8] and our assumption of no suspended biomass within the pores[21]. The ratio of the total volume of the void space to the entire volume of biofilm is defined as the porosity, ϵ.

4.2.1.1 Soluble components

For any soluble component in the biofilm, its concentration (versus the liquid phase), $C_{F,j}$, varying with time and location is governed by mass conservation:

$$\frac{\partial(\epsilon C_{F,j})}{\partial t} + \frac{\partial(J_{F,j})}{\partial x} = R_{F,j} \tag{4.1}$$

$$J_{F,j} = -D_j^{eff} \frac{\partial(C_{F,j})}{\partial x} \tag{4.2}$$

where $J_{F,j}$ is the flux (with respect to biofilm cross-sectional area) of the soluble component, j[57]; D_j^{eff} is the effective diffusion coefficient for the soluble component, j, in the biofilm[57]; $R_{F,j}$ denotes the net production rate (per unit biofilm volume) for the soluble component, j, in the biofilm and can be found in Appendix B Table B.1. Herein, we only account for the diffusive flux across the biofilm outer surface for the soluble component, j, which is described by Fick's law (see Eq. (4.2)). Given the relatively higher conductivity of the catholyte[1,58] and the small current density produced by the system[8], the migration of ionic species is not considered[59]. For most practical applications, the advective flux[54,60] and molecular turbulent dispersion[57] are shown to be negligibly small compared with the diffusive process and thus not included.

Considering that (i) the $C_{F,j}$ is defined in terms of the biofilm's liquid phase and (ii) the diffusion process is normally regarded as taking place in the liquid phase only[57,60], the value of the D_j^{eff} should be obtained as:

$$D_j^{eff} = f_j D_{W,j} \tag{4.3}$$

where f_j is the relative diffusion coefficient[56] (or called correction factor[57,61]) for the soluble component, j—accounting for the reduction due to the existence of the solid phase in the biofilm[56,57,61–63]. The value of the constant f_j depends on the soluble components, biofilm type and specific operating condition[61]. $D_{W,j}$ denotes the diffusion coefficient for the soluble component, j, in pure water.

The cathode substratum is regarded as an impermeable surface, hence zero flux for the soluble component, j, at $x = 0$. At the outer surface of the biofilm (i.e. $x = L_F$), the flux continuity through the liquid phase of the interface should be fulfilled in the absence of reactions[56]:

$$J_{F,j}|_{x=L_F} = -\frac{\epsilon D_{W,j}}{L_{LBL}}(C_{BL,j} - C_{F,j}|_{x=L_F}) \tag{4.4}$$

where $C_{BL,j}$ is the concentration for the soluble component, j, in the bulk liquid phase; L_{LBL} is the thickness of the liquid boundary layer (LBL) between the bulk liquid phase and the biofilm. The ratio of $D_{W,j}$ and L_{LBL} represents the mass transfer coefficient. It is assumed that the diffusion coefficients in the bulk liquid phase are identical to those in pure water[57].

4.2.1.2 Biomass

For the biomass of interest (i.e. active and inactive acetogens)[57], the advective flux plays a dominating role; hence the other types of flux are negligible[57,60]. The mass conservation for the biomass, i, is expressed as:

$$\frac{\partial(X_i)}{\partial t} + \frac{\partial(\boldsymbol{v}X_i)}{\partial x} = R_{F,i} \tag{4.5}$$

where X_i is the concentration of the biomass, i, in the biofilm; $R_{F,i}$ denotes the net production rate for the biomass, i, in the biofilm and can be found in Table 4.1. v is the advective velocity, representing the biofilm expansion or shrink along the x-axis, which is induced by the net growth of all types of biomass[46,56,57,60]:

$$\frac{\partial v}{\partial x} = \frac{1}{\theta_b}\sum_i \frac{R_{F,i}}{\rho_i} \tag{4.6}$$

where ρ_i is the intrinsic density for the biomass, i, defined as the mass of the biomass divided by its own volume. The value of v at the cathode substratum (i.e. $x = 0$) equals zero (0)[56,64]. θ_b is the volume fraction of the total biomass in the biofilm and its value would change with respect to the biomass growth[21]:

$$\theta_b = \sum_i \frac{X_i}{\rho_i} \tag{4.7}$$

The value of ϵ would vary based on the following relationship:

$$\epsilon = 1 - \theta_b \tag{4.8}$$

4.2.2 Mass conservation in the bulk liquid

4.2.2.1 Soluble components

The bulk liquid phase serves the role of supplying substrate (i.e. $CO_2(aq)$) and other components used for biomass growth (such as H^+) to the biofilm through diffusion. Given the much larger volume of the bulk liquid phase, V_{BL}, compared with the biofilm, the bulk liquid phase is regarded as well-mixed. Therefore, the concentration for any soluble component, j, in the bulk liquid phase, $C_{BL,j}$, varies with time only. Note that the flux across the cation exchange membrane (CEM) for H^+ (the only cation that we are interested in) is negligible here. It has been reported by several studies that (i) H^+ transportation is much hindered by the CEM, and (ii) the transfer rate of H^+ is much smaller compared with the anodic generation and cathodic consumption rate[65]. Additionally, in our modelled experiment, the concentrations of other cations (such as Na^+, K^+, Ca^{2+} and Mg^{2+}) are several orders of magnitude higher when compared with the relatively lower concentration of H^+. This means that those cations with higher concentrations would transfer more predominantly[66] and strongly impede H^+ transportation across the membrane that we adopted[67]. The mass conservation for $C_{BL,j}$ is given by:

$$\frac{dC_{BL,j}}{dt} = \frac{A_F \cdot J_{F,j}|_{x=L_F}}{V_{BL}} + R_{BL,j} \tag{4.9}$$

where A_F denotes the area of the biofilm/bulk liquid interface; the value of A_F is assumed as identical to that of the area of cathode substratum; $R_{BL,j}$ is the net production rate for the soluble component, j, in the bulk liquid phase.

4.2.2.2 Biomass

The planktonic acetogens in the bulk liquid phase are not taken into account in this model, given the fact that (i) no detection of H_2 was shown in the experiment[8], which suggest almost no H_2 was present in the bulk liquid phase; and (ii) the biofilm/bulk liquid interface (i.e. $x = L_F$) is electrically insulated. The first reason greatly limits the acetogens growth via CMET, while the second factor makes it almost impossible for acetogens to grow via CDET.

4.2.3 Dual cathodic electron transfer mechanism (dual-CEET)

The mathematical modelling framework for acetogens with dual-CEET is represented in this section. For CMET (see Figure 4.1), the conductive biofilm acts as an extension of the cathode. Firstly, electrons that are derived from the cathode would be conducted through the biofilm and used to generate the mediator (i.e. H_2). Then, H_2 (as the electron donor, ED) reduces $CO_2(aq)$ to acetate and sustains the microorganism growth. Based on the experimental observation of no detection of any gaseous species[8], all produced H_2 is assumed to be dissolved in the liquid phase, most of which would be rapidly utilised by acetogens (a very low concentration of $H_2(aq)$ is predicted by our simulation). The specific growth rate of active autotrophic acetogens with CMET, μ_A^M, is given by the double Monod equation[68,69]:

$$\mu_A^M = \mu_A^{max}\left(\frac{C_{F,H_2}}{C_{F,H_2} + M_{H_2}}\right)\left(\frac{C_{F,CO_2}}{C_{F,CO_2} + M_{CO_2}}\right) \tag{4.10}$$

where μ_A^{max} is the maximum specific growth rate for the active autotrophic acetogens; M_{H_2} and M_{CO_2} are the Monod (half-saturation) constants for H_2 and CO_2, respectively.

In the case of CDET (see Figure 4.1), the insoluble cathode serves as the ED to feed electrons to acetogens directly. The transfer of electrons from the cathode to the acetogens through conductive biofilm is assumed to be fast and reversible. Analogous to the Nernst-Monod equation employed for the electron-producing bacteria in MFCs, the specific growth rate of the active autotrophic acetogens with CDET, μ_A^C, is derived by combining the double Monod kinetics and the Nernst equation[46,64]:

$$\mu_A^C = \mu_A^{max}\left(\frac{1}{1 + exp\left(-\frac{F\eta}{R_g T}\right)}\right)\left(\frac{C_{F,CO_2}}{C_{F,CO_2} + M_{CO_2}}\right) \tag{4.11}$$

where F is the Faraday constant; $\eta = \varphi_{M_c} - \varphi_s$, φ_{M_c} denotes the cathode potential corresponding to the half-maximum specific growth rate, φ_s is the local electric potential (see Eq. (4.25)). R_g is the ideal gas constant, and T is the operating temperature.

It has been shown by the experiment that the acetate growth is affected by pH (i.e. $\mathrm{pH} = -\log C_{\mathrm{H}^+}$)[8]. This phenomenon is mathematically described as[70]:

$$\mu_A^{max} = \mu_{A,opt}^{max}\vartheta(\mathrm{pH}) \tag{4.12}$$

where $\mu_{A,opt}^{max}$ denotes the maximum specific growth rate for the active autotrophic acetogens under the optimal condition. The value of $\mu_{A,opt}^{max}$ is estimated based on Heijin's theory[71,72] (see Appendix B Section V). Note that $\mu_{A,opt}^{max}$ is assumed to be constant regardless of the CEETs. The function of pH, $\vartheta(\mathrm{pH})$ is given by the piecewise function[70]:

$$\vartheta(\mathrm{pH}) = 0 \quad \text{if } \mathrm{pH} < \mathrm{pH}^{\min} \text{ or } \mathrm{pH} > \mathrm{pH}^{\max} \tag{4.13}$$

$$\vartheta(\mathrm{pH}) = \frac{(\mathrm{pH} - \mathrm{pH}^{\min})(\mathrm{pH} - \mathrm{pH}^{\max})}{(\mathrm{pH} - \mathrm{pH}^{\min})(\mathrm{pH} - \mathrm{pH}^{\max}) - (\mathrm{pH} - \mathrm{pH}_{\mathrm{opt}})^2} \quad \text{if } \mathrm{pH}^{\min} \le \mathrm{pH} \le \mathrm{pH}^{\max} \tag{4.14}$$

where $\mathrm{pH}_{\mathrm{opt}}$, $\mathrm{pH}^{\min}$ and $\mathrm{pH}^{\max}$ represent the optimal, minimal and maximal values of pH feasible for acetogens growth, respectively.

Our proposed dual-CEET for acetogens is similar to the prior study[45], in which CMET and CDET are assumed to occur simultaneously. This means that the apparent (i.e. observed) specific growth rate for active autotrophic acetogens, μ_A, is the sum of μ_A^M and μ_A^C. In order to avoid the predicted μ_A (after combining μ_A^M and μ_A^C) exceeding the theoretical maximal value[45], the following sigmoid function $S(\tau)$ is employed:

$$S(\tau) = \frac{1}{1 + exp(-1000\tau)} \tag{4.15}$$

where $\tau = (\mu_A^M + \mu_A^C) - \mu_A^{max}\left(\frac{C_{F,CO_2}}{C_{F,CO_2}+M_{CO_2}}\right)$. Using this function, the modified μ_A^{M*} and μ_A^{C*} are given by:

$$\mu_A^{M*} = \mu_A^M\big(1 - S(\tau)\big) + \mu_A^{max}\left(\frac{C_{F,CO_2}}{C_{F,CO_2} + K_{CO_2}}\right)\left(\frac{\mu_A^M}{\mu_A^M + \mu_A^C}\right)S(\tau) \tag{4.16}$$

$$\mu_A^{C*} = \mu_A^C\big(1 - S(\tau)\big) + \mu_A^{max}\left(\frac{C_{F,CO_2}}{C_{F,CO_2} + K_{CO_2}}\right)\left(\frac{\mu_A^C}{\mu_A^M + \mu_A^C}\right)S(\tau) \tag{4.17}$$

4.2.4 Biofilm metabolism and microbial kinetics

All the biotic processes, microbial kinetics and stoichiometry for the acetogens-dominating biofilm have been summarised in Table 4.1. The details are presented in the following sections.

4.2.4.1 Stoichiometry of autotrophic growth with cell maintenance

Given the fact that most microorganisms have a similar composition, a typical formula ($CH_{1.8}O_{0.5}N_{0.2}$) for the organic/dry part of biomass is adopted[58,72]. In our work, $CO_2(aq)$ is utilised as the inorganic carbon source for the growth of the autotrophic acetogens (X_A). The ammonium, NH_4^+, is considered as the nitrogen source[8]. $CO_2(aq)$ is selected as the carbon source for two reasons: (i) the experiment revealed that the acetogens are in favour of utilising $CO_2(aq)$, rather than other forms of inorganic carbon (such as bicarbonate)[8]; (ii) a prior study has shown that, compared with bicarbonate as the carbon source, the protein synthesis process for acetogens would be faster with $CO_2(aq)$[8,73].

For the CMET with H_2 as the ED, the general form of the complete autotrophic growth process including cell maintenance is expressed as:

$$-\frac{1}{Y^M_{H_2/X_A}}H_2 + Y^M_{X_A/CO_2}CO_2 + Y^M_{X_A/NH_4^+}NH_4^+ + Y^M_{X_A/H^+}H^+ + CH_{1.8}O_{0.5}N_{0.2}(X_A) + Y^M_{X_A/Ac}CH_3COOH\ (Ac) + Y^M_{X_A/H_2O}H_2O \quad \text{(R4.1)}$$

The values of the stoichiometry (i.e. yield coefficient, negative value for reactants and positive value for products) above can be obtained through a series of the balances (including the degree of reduction, element and charge), and the relationships of energies. If heat production is involved, the values for enthalpy are also required. Considering that the constant operating temperature is maintained in our experiment, the heat effect is neglected. The detailed calculation method is outlined in Appendix B Section IV.

The complete autotrophic growth process with the CDET is analogous to the reaction with the CMET above. However, it is not easy to obtain the stoichiometry theoretically due to the insoluble cathode. Therefore, the values for the stoichiometry in the autotrophic growth process with the CDET are estimated. The values for the unknown parameters are fitted to the experimental data (i.e. measured acetate concentration and pH value within $0\sim7$ days[8]). It is

worthy to note that the stoichiometry for the insoluble ED (i.e. cathode) is expressed as the number of electrons required to form 1 Cmol X_A (n), as the electrons from the cathode are supposed to feed acetogens directly.

4.2.4.2 Cell death

Active biomass would convert to inert species, X_I, during the cell death process[68]. The rate of cell death is described by the first-order kinetics with a death coefficient for active biomass (b_{dea})[57,64] (see Table 4.1).

4.2.5 Homogeneous reactions

In our proposed model, the following types of homogeneous reactions within the catholyte are considered[74]. Although both phosphate ions and hydrogen phosphate ions are the strongly hydrolysed salt ions[75], their hydrolysis reactions are neglected here due to a lack of sufficient kinetic data.

$$CO_2(aq) + H_2O \xrightarrow{k_{HR4.2}} H^+ + HCO_3^- \quad \text{(R4.2)}$$

$$HCO_3^- \xrightarrow{k_{HR4.3}} H^+ + CO_3^{2-} \quad \text{(R4.3)}$$

$$CO_2(aq) + OH^- \xrightarrow{k_{HR4.4}} HCO_3^- \quad \text{(R4.4)}$$

$$HCO_3^- + OH^- \xrightarrow{k_{HR4.5}} H_2O + CO_3^{2-} \quad \text{(R4.5)}$$

$$CH_3COOH\ (Ac) \xrightarrow{k_{HR4.6}} H^+ + CH_3COO^-(Ac^-) \quad \text{(R4.6)}$$

$$H_2PO_4^- \xrightarrow{k_{HR4.7}} H^+ + HPO_4^{2-} \quad \text{(R4.7)}$$

$$HPO_4^{2-} \xrightarrow{k_{HR4.8}} H^+ + PO_4^{3-} \quad \text{(R4.8)}$$

$$H_2O \xrightarrow{k_{HR4.9}} H^+ + OH^- \quad \text{(R4.9)}$$

The homogeneous reaction rate, $R_{H,j}$, is expressed as[76]:

$$R_{H,j} = \sum_{Hn} S_{Hn,j}\left(k_{Hn} \prod_{S_{Hn,q}<0} C_q - \frac{k_{Hn}}{K_{Hn}} \prod_{S_{Hn,q}>0} C_q\right)\ (n = R4.2, R4.3 \ldots R4.9) \quad (4.18)$$

where $S_{Hn,j(q)}$ the stoichiometric coefficient of soluble component, j (q), in homogeneous reaction Hn (negative means reactants and positive values for products); k_{Hn} and K_{Hn} are the

forward reaction constant and the equilibrium constant of the homogeneous reaction Hn, respectively. Water is assumed to be always abundant and its concentration is treated as 1. Note that, for the porous biofilm, all the homogeneous reaction rates should be scaled by ϵ, as the homogenous reactions only take place in the liquid phase[77,78].

The equilibrium constants can be obtained thermodynamically from the following equation[70,79]:

$$K_{Hn} = exp\left(\frac{\Delta S_{Hn}}{R_g}\right) exp\left(-\frac{\Delta H_{Hn}}{R_g T}\right) \quad (n = R4.2, R4.3 \dots R4.9) \tag{4.19}$$

where ΔS_{Hn} and ΔH_{Hn} denote the change of entropy and heat of the homogeneous reaction, respectively. Required data can be found in Appendix B Section II.

4.2.6 Gas-liquid mass transfer

Based on the experimental operation[8], the gas-liquid mass transfer for CO_2 in the cathodic chamber should be taken into account, and its rate is expressed as:

$$R_{P,CO_2(aq)} = -\frac{V_g}{V_{BL}} R_{P,CO_2(g)} = a_{gl} K_{GL} \left(\frac{P_{CO_2(g)}}{H_{CO_2}} - C_{BL,CO_2(aq)}\right) \tag{4.20}$$

where V_g is the volume of the gaseous phase; a_{gl} is the specific gas-liquid interfacial area (in terms of the bulk liquid); K_{GL} is the overall mass transfer coefficient; $P_{CO_2(g)}$ is the partial pressure of CO_2(g); H_{CO_2} is Henry's constant for CO_2.

The details of the calculation of K_{GL} can be found in Appendix B Section VI. Since the dilute microbial compatible catholyte is used[1,8], the value of H_{CO_2} is assumed as a constant (identical to the value in the pure water for simplification). The value of H_{CO_2} at our operating temperature is corrected by the Van't Hoff equation[80,81]:

$$\frac{1}{H_{CO_2}} = \frac{1}{H_{CO_2}^{ref}} exp\left(-\frac{\Delta_{sol} H}{R_g}\left(\frac{1}{T} - \frac{1}{T^{ref}}\right)\right) \tag{4.21}$$

where $\Delta_{sol} H$ is the enthalpy of dissolution. Given the narrow difference between T and T^{ref}, $\Delta_{sol} H$ is assumed to be a constant; thus, the value of $\Delta_{sol} H$ at T^{ref} is adopted.

$P_{CO_2(g)}$ is calculated by assuming that all gases are ideal:

$$\frac{dP_{CO_2(g)}}{dt} = R_g T R_{P,CO_2(g)} \tag{4.22}$$

4.2.7 Electrochemical reactions

Considering the highly conductive biofilm[8], the hydrogen evolution reaction (HER) is assumed to take place not only at the surface of the cathode substratum but everywhere in the biofilm:

$$2H^+ + 2e^- \leftrightarrow H_2 \ (pH \leq 7) \tag{R4.10}$$

$$2H_2O + 2e^- \leftrightarrow H_2 + 2OH^- \ (pH > 7) \tag{R4.11}$$

The magnitude of current density generated by HER, i_{HER}, is described by the Butler-Volmer kinetics[79,82]:

$$i_{HER} = -i_{o,HER}^{a(b),ref}\left(\frac{C_{F,H^+}}{C_{F,H^+}^{ref}}\right)^{\psi} exp\left(-\frac{\alpha_{HER}^{a(b)}F}{R_g T}\left(\varphi_s - \varphi_{eq,HER}^{a(b),ref}\right)\right) \tag{4.23}$$

where the superscripts a and b correspond to reactions (R4.10) and (R4.11), respectively; $i_{o,HER}^{a(b),ref}$ is the exchange current density; ψ is the reaction order with respect to H^+; C_{F,H^+}^{ref} is the reference concentration of H^+; $\alpha_{HER}^{a(b)}$ is the charge transfer coefficient; $\varphi_{eq,HER}^{a(b),ref}$ is the equilibrium potential for the HER in the reference condition and operating temperature. The catholyte potential is set to zero (versus standard hydrogen electrode) and not shown in the Eq. (4.23)[76,83–85].

The charge balance is applied[45,46,57,64]:

$$\frac{\partial i^C}{\partial x} + a_V i_{HER} - \frac{FnX_A\mu_A^{C*}}{W_A} = 0 \tag{4.24}$$

where a_V is the specific surface area for the biofilm matrix, W_A is the molar weight for the active biomass.

The local electric potential, φ_s, is resolved by coupling with Ohm's law[45,46,57,64]:

$$i^C = -k_s^{eff} \frac{\partial \varphi_s}{\partial x} \tag{4.25}$$

where k_s^{eff} is the effective biofilm conductivity.

Two boundary conditions for φ_s are: (i) a constant applied cathode potential, V_{app}, is imposed at $x = 0$; and (ii) zero-flux is applied at the biofilm/bulk liquid interface (i.e. $x = L_F$).

Electrochemical reaction rate, $R_{E,j}$, is given based on Faraday's law[76]:

$$R_{E,j} = -\frac{S_{E,j} a_V i_{HER}}{2F} \tag{4.26}$$

where $S_{E,j}$ is the stoichiometry in the electrochemical reactions (negative means reactants and positive values for products).

Table 4.1 Key microbial kinetics and the stoichiometry for the acetogens-dominating biofilm.

Process	Soluble components				Biomass		Process rate
	$R_{B,CO_2(aq)}$	$R_{B,H_2(aq)}$	$R_{B,Ac}$	R_{B,H^+}	$R_{F,A}$	$R_{F,I}$	
Autotrophic growth (CMET)	$\frac{Y^M_{X_A/CO_2}}{W_A}$	$-\frac{1}{W_A Y^M_{H_2/X_A}}$	$\frac{Y^M_{X_A/Ac}}{W_A}$	$\frac{Y^M_{X_A/H^+}}{W_A}$	$+1$	$-$	$R^M_{gro} = \mu^{M*}_A X_A$
Autotrophic growth (CDET)	$\frac{Y^C_{X_A/CO_2}}{W_A}$	$-$	$\frac{Y^C_{X_A/Ac}}{W_A}$	$\frac{Y^C_{X_A/H^+}}{W_A}$	$+1$	$-$	$R^C_{gro} = \mu^{C*}_A X_A$
Cell death	$-$	$-$	$-$	$-$	-1	$+1$	$R_{dea} = b_{dea} X_A$

4.2.8 Model implementation and evaluation

Initial conditions, key parameters and calculations have been listed in Appendix B. The model is solved by COMSOL Multiphysics 5.4 with the MUMPS general solver.

The production rate, as the most vital indicator for the evaluation of the MESs' performance[86], is calculated through dividing the accumulated acetate concentration by the running period, t (day) (i.e. from the beginning to the time when CO_2 has run out)[86]. The production rate

together with the product yield (defined as the batch-end acetate concentration), is used for the evaluation. Note that acetate refers to the sum of acetic acid (CH_3COOH, Ac) and acetic anions (CH_3COO^-, Ac^-).

4.3 Model validation

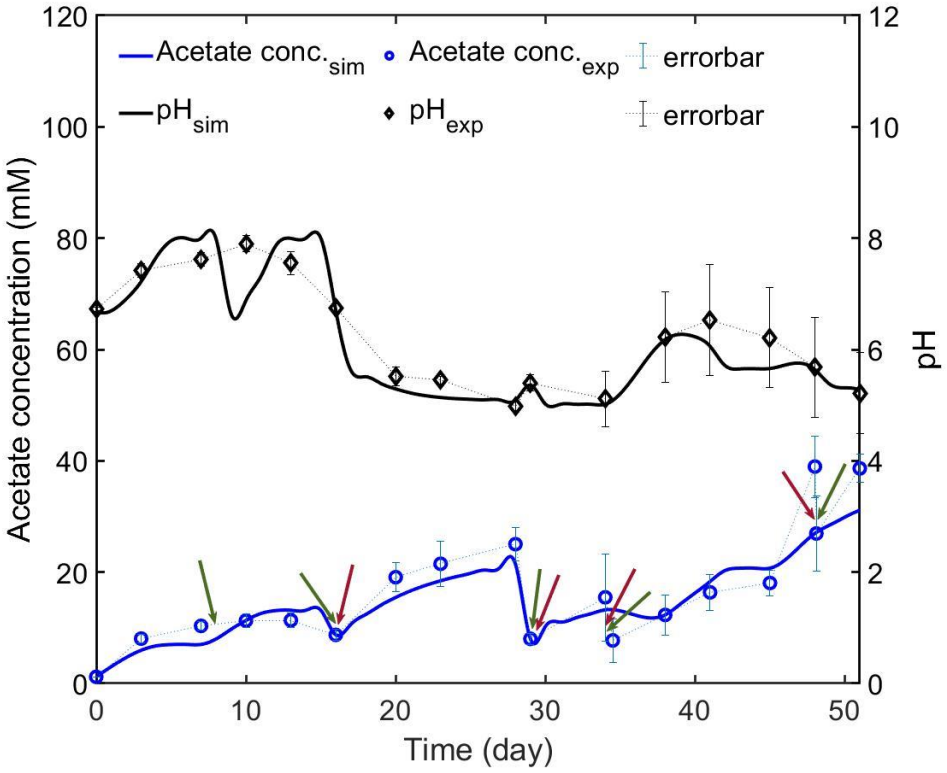

Figure 4.2 Predicted acetate concentration and catholyte pH (by subscript 'sim'), compared with the experimental measurements (by superscript 'exp'). The red and green arrows indicate when fresh medium and CO_2 were provided, respectively.

Figure 4.2 represents the numerical and the experimental results[8] in terms of the pH value and the acetate concentration. The relevant experimental information can be found in the reference[8]. As indicated in Figure 4.2, our model could predict the acetate concentration and pH with good fidelity. The departure (for both the acetate concentration and the pH value) could be attributed to the following factors: (i) there are many other types of microorganisms that exist in the biofilm, mainly including the methanogenic CO_2 -reduction microorganisms (i.e. *Methanobrevibacter* and *Rhodobacter*[8]), the acetate-producing microorganisms (i.e. *Pullulanibacillus* and *Rummeliibacillus* in the catholyte and *Sporomusa* and *Clostridium sensu*

in the biofilm[8]) and the acetate-consuming microorganisms (i.e. acetoclastic methanogens[8]); the effect of these microorganisms on the acetate concentration and pH would be pronounced when the inhibitors (i.e. the substance used to inhibit methanogens growth) have not been added in the system (before day 30)[8]; (ii) the enzymic extracellular H_2 generation process (i.e. formation of H_2 catalysed by the extracellular exoenzymes/coenzymes secreted from acetogens or other microorganisms)[8] and the sophisticated interactions between multiple species in the cathodic inoculum[8] cannot be reflected precisely in this work due to a lack of adequate data; (iii) the initial cathode colonisation and the slow MESs start-up[8] could play important roles in both the acetogens growth and the pH; however, these phenomena are hard to capture and have not been considered in the numerical study; (iv) as observed in the experiment[8], the content of the longer chain organic compounds (such as butyrate and isovalerate) would not be negligible with the accumulation of acetate; these acids can potentially affect the acetate concentration and the pH value (through, for example, their dissociation reactions); (v) the errors of the measured data (including the pH value and the acetate concentration) in the experiment are relatively large (i.e. reflected by the error bars in Figure 4.2)[8].

Our numerical study suggests that the CDET is the dominant electron transfer mechanism for the modelled acetogen-dominating cathodic biofilm[8]. The mathematical framework that we proposed is also capable of being adopted for other MESs to identify their CEETs.

4.4 Results and discussion

We show and interpret simulation results with the variation of several parameters in this section. The default and varied parameter values are listed in Appendix B Table B.4. All simulated systems are operated in the batch mode, and all the (cathode) potential values mentioned below are versus the Ag/AgCl reference electrode.

4.4.1 Effect of the applied cathode potential, V_{app}

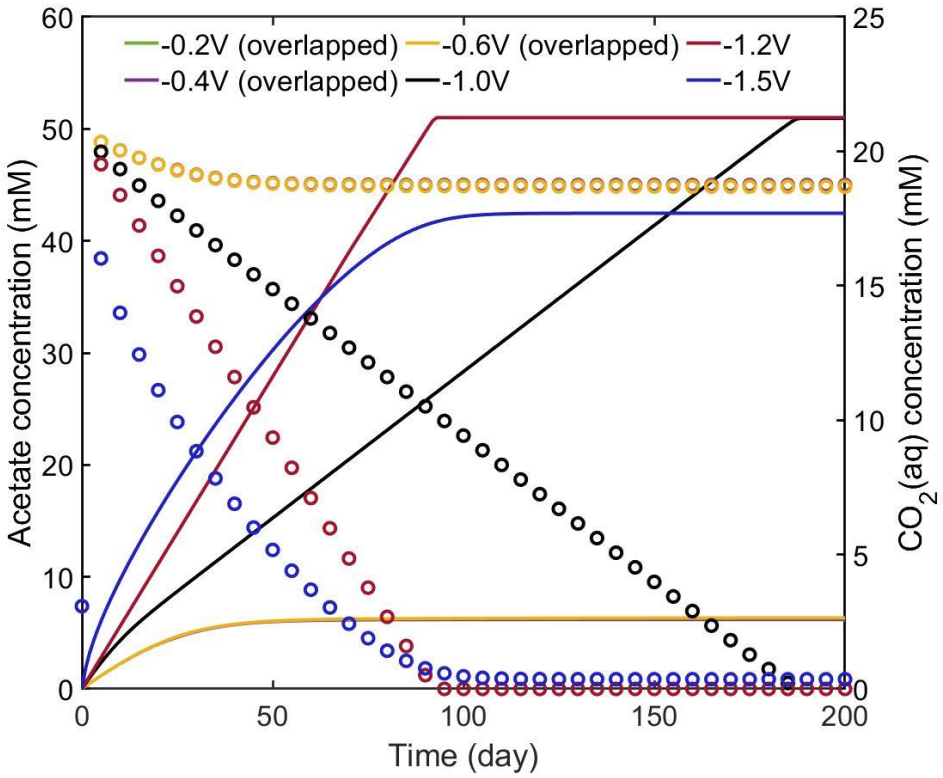

Figure 4.3 Evolution of acetate (solid lines) and dissolved CO_2(aq) concentration (circles) with various levels of applied cathode potential, V_{app}.

We exam the system performance at various levels of the applied cathode potential, V_{app}, ranging from -0.2 V to -1.5 V. It can be seen from Figure 4.3 that when the value of V_{app} is lower (i.e., more positive) than -0.6 V, there are lower acetate accumulation and lower acetate production rate in the system. This phenomenon is expected, as the acetogens growth with CDET – the dominating electron transfer mechanism in our case— is much limited (see Eq. (4.11)). In addition, when V_{app} equals -0.2 V, the acetogens growth with CMET would cease due to a lack of H_2 (see Eq. (4.10); proved by the simulation results). Therefore, under the circumstance with the lower value of V_{app}, active acetogens (X_A) concentration would be reduced due to the continuous cell death process, and no longer exist (and hence no further acetate production) before CO_2 depletion (suggested by the simulation results).

As V_{app} increases to -1.2 V, the acetogens growth rate with both CMET and CDET increases significantly, and hence acetate production rate becomes greater.

When V_{app} further increases to -1.5 V, the faster consumption of CO_2 and the amplified HER rate would accelerate the consumption of H^+. As a consequence, the system becomes more alkaline, which in turn results in more carbonate/bicarbonate. As mentioned above, in our model, only $CO_2(aq)$ is reckoned as the inorganic carbon source for acetogens growth and acetate formation. Therefore, the acetate yield would drop in the more alkaline environment.

From our tests, an optimal value of V_{app} (-1.2 V) exists, corresponding to the highest acetate production rate and the highest acetate yield.

4.4.2 Effect of the initial pH value

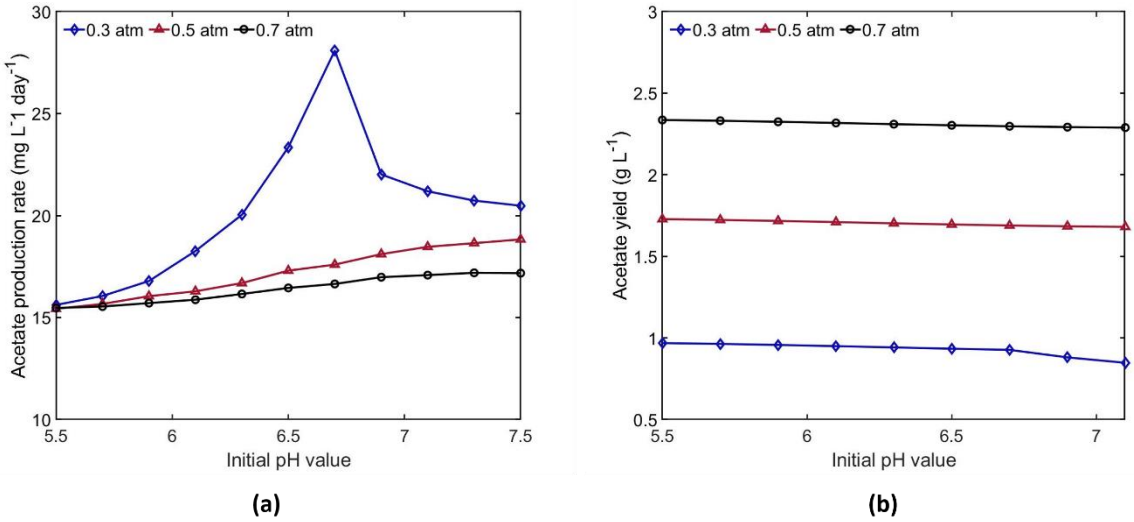

Figure 4.4 (a) Acetate production rate; (b) acetate yield as a function of the initial pH value and the initial CO_2 partial pressure.

pH, as a vital parameter, affects the inorganic carbon form and the growth of the microorganisms. In this section, the effect of the initial pH value is discussed. Figure 4.4(a) and (b) respectively show the acetate production rate (i.e. time-averaged value) and the acetate yield with various initial pH values.

For the system with an initial CO_2 partial pressure, $P^0_{CO_2(g)}$, of 0.7 atm, pH would drop initially, regardless of the its initial value. This is attributable to the transfer of CO_2 from the gas phase to the liquid phase (see Eq. (4.20); proved by simulation). As for the systems with lower initial pH values (i.e. initial pH < 6), the decrease of the pH makes it (further) deviate from its optimal value (i.e. $pH_{opt} = 6$) for the acetogens growth. Consequently, the maximum specific

growth rate (see Eqs. (4.12) to (4.14)) becomes lower, hence the decrease in the acetogens specific growth rate with CDET (μ_A^{C*}). In contrast, the acetogens specific growth rate with CMET (μ_A^{M*}) is accelerated as more H_2 would be produced (via HER) under the more acidic conditions. Owing to the dominance of the CDET in our case, the overall acetogens growth rate decreases, which follows the trend of μ_A^{C*} (from the simulation results). When the initial pH is higher than 6, a higher initial pH (within the tested range) would lead to a less deviation from pH_{opt} during the batch due to the dropping of pH caused by the transfer of CO_2 from the gas phase to the liquid phase. The reasons above could explain the phenomenon of the lower acetate production rate in the system with lower initial pH values, whereas the acetate yield shows an opposite trend: the systems with lower initial pH values would be beneficial to produce more acetate. Analogous to the analysis in Section 4.4.1, acetate yield is closely related to the form of inorganic carbon. Under the more acidic conditions, more inorganic carbon would be presented in the form of dissolved $CO_2(aq)$; and subsequently be utilised for the acetogens growth and the acetate production. Similar trajectories for the acetate production rate and the acetate yield can also be observed when $P^0_{CO_2(g)}$ decreases to 0.5 atm.

When $P^0_{CO_2(g)}$ further decreases to 0.3 atm, a lower initial pH value still positively influences the acetate yield, but the profile of the acetate production rate changes at the higher range of pH values. An extremely high value of the initial pH (i.e. $pH > 6.7$) would be the least favourable choice for both the acetate production rate and the acetate yield. As discussed above, pH would drop at the beginning. For the systems with the higher initial pH value (i.e. initial $pH > 6$), the decline of pH would make it closer to pH_{opt}. Consequently, acetogens grow faster and CO_2 is consumed rapidly. However, the CO_2 supply is limited in this case (due to the relatively low $P^0_{CO_2(g)}$), and hence the lower CO_2 concentration would take the system back to higher pH levels which deviate from pH_{opt}. Both the lower CO_2 concentration and the overly alkaline condition are detrimental to the acetogens growth, resulting in a lower acetogens production rate along with a lower acetate yield. At the given $P^0_{CO_2(g)}$ of 0.3 atm, an optimal value of 6.7 for the initial pH exists for the acetate production rate.

4.4.3 Effect of specific surface area of the biofilm matrix, a_V

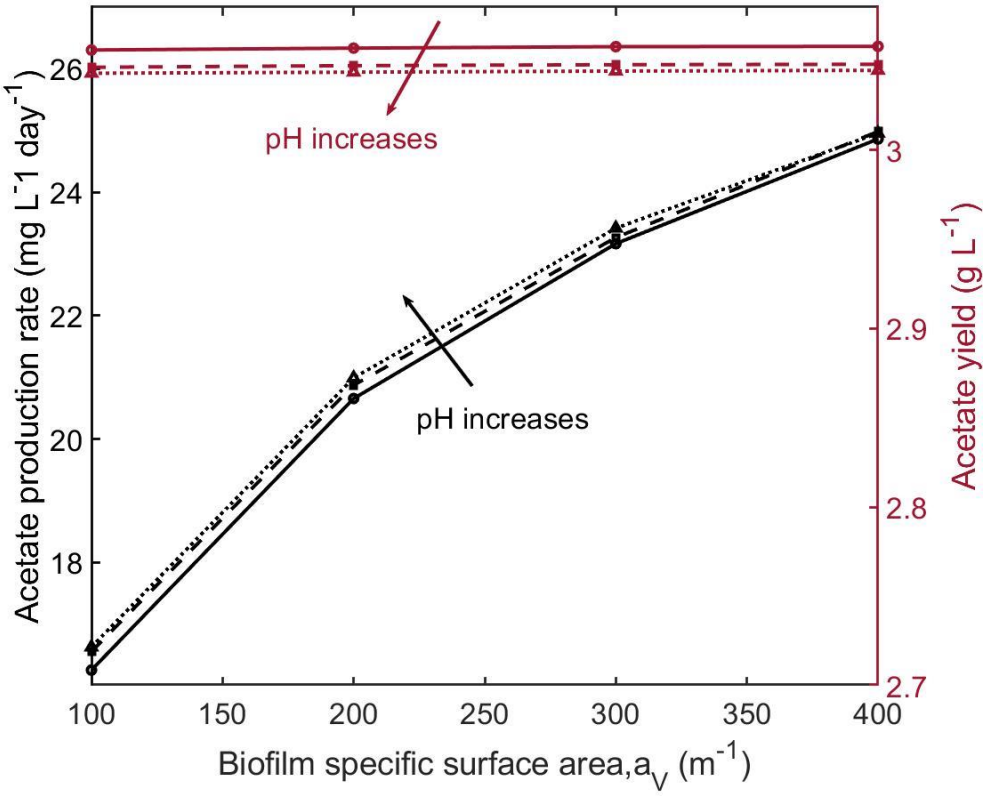

Figure 4.5 The effect of the specific surface area of the biofilm matrix, a_V, on the acetate production rate (i.e. time-averaged value) and the acetate yield with various initial pH values. Black lines represent the acetate production rate; red lines represent the acetate yield; solid lines with circles, dashed lines with squares and dotted lines with triangles denote the system started with the pH value of 6.7, 7.1 and 7.9, respectively.

The specific surface area of the biofilm matrix, a_V, is critical for the electrochemical reactions and would potentially affect the systems' performance. Screening of the impact of a_V is carried out and outlined in this section. There are two implications that can be drawn from Eq. (4.26): (i) on the one hand, a larger value of a_V would accelerate the consumption of H^+, which would prevent the pH values from rapidly dropping to a very low level. As stated previously, overly acidic conditions would impede the acetogens growth with CDET. Note that owing to the higher biofilm conductivity, k_s^{eff}, the local electric potential, φ_s, has a negligible change with increasing current; (ii) on the other hand, a larger a_V would generate more H_2, which is beneficial for the acetogens growth with CMET (see Eq. (4.10)). Therefore, the biofilm with a larger value of a_V is instrumental for the acetogens growth with both types of CEETs, and thus

it is able to lead to a higher acetate production rate. This trend holds for all the three different initial pH values, as shown in Figure 4.5. It should be noted that, as illustrated in Section 4.4.2 and Figure 4.5, a compromise between the acetate yield and the acetate production rate for a given value of a_V should be considered. The choice of the optimal value of the initial pH should be integrated with other additional information, such as operating cost and acetate price, which will be considered in future work.

4.4.4 Effect of the biofilm thickness and the specific gas-liquid interfacial area, a_{gl}

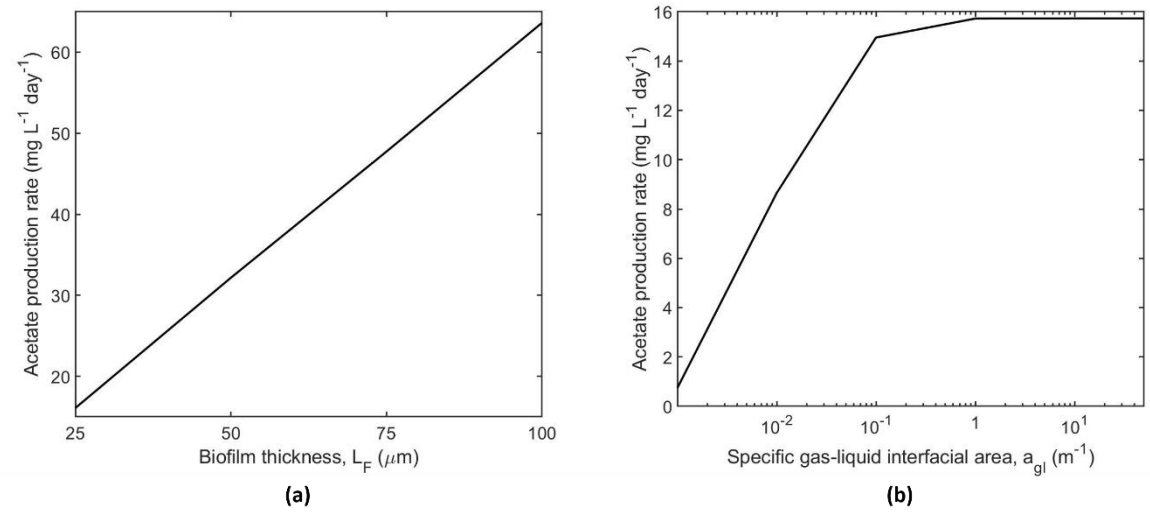

Figure 4.6 The effect of (a) the biofilm thickness, L_F, and (b) the specific gas-liquid interfacial area, a_{gl}, on the acetate production rate.

The influences of the biofilm thickness, L_F, and the specific gas-liquid interfacial area, a_{gl}, both as factors that affect mass transfer in the system, are also tested in this study; the results are presented in Figure 4.6(a) and (b), respectively.

It can be seen from Figure 4.6(a) that the acetate production rate always increases with the greater biofilm thickness. A thicker biofilm could accommodate more acetogens, but it would also lead to a longer distance for (i) the electron conduction and (ii) the soluble component diffusion. Both of these two factors would negatively affect acetogens growth. Thanks to the higher value of k_s^{eff} and the lower value of the half-saturation constants for CO_2 (M_{CO_2}), the negative effects (i.e. the more positive electric potential and the lower CO_2 concentration)

induced by the thicker biofilm turn out to be negligible. Therefore, the total amount of the active acetogens hosted by the biofilm dominates the acetate production rate.

CO_2 plays a pivotal role in (i) providing feedstock for the acetate synthesis (by the acetogens) and (ii) regulating the system's pH. Among the operational parameters controlling the CO_2 supply, the specific gas-liquid interfacial area, a_{gl}, is easy to manipulate and therefore it is investigated here. The drastic increase in acetate production rate can be observed when the value of a_{gl} climbs to $0.1\ \mathrm{m}^{-1}$ (see Figure 4.6(b)). This is because that the resulting acceleration of CO_2 gas-liquid mass transfer (see Eq. (4.20)) leads to the elevated overall CO_2 (aq) concentration and also makes the system's pH closer to $\mathrm{pH}_{\mathrm{opt}}$ (proved by the simulation results). Nevertheless, it would become less effective to improve the acetate production rate by further increasing a_{gl} (i.e. $> 1\ \mathrm{m}^{-1}$) after the growth of acetogens becomes saturated with CO_2(aq) concentration. In practice, the optimal value of a_{gl} should be determined together with other analyses; for example, the cost for creating the larger a_{gl}.

4.5 Conclusions

In this work, a comprehensive mathematical framework for the acetogens-dominating cathodic biofilm in the microbial electrosynthesis cell (MES) was established. In addition to considering the transport phenomena and electrochemical kinetics, the proposed dynamic model also incorporates the detailed descriptions of (i) two types of cathodic extracellular electron transfer mechanisms (CEETs); (ii) biofilm metabolism and microbial kinetics; (iii) homogeneous reactions in the pH-buffered catholyte; and (iv) the effects of pH. This model was quantitatively validated by comparing the predicted acetate concentration and pH value with the experimental data. The simulation results reveal that the cathodic direct conduction-based extracellular electron transfer (CDET) is dominating in the modelled biofilm. However, it is highly desirable to carry out the relevant experiment with pure culture of acetogens and higher (i.e. more positive) cathodic potential in the further to verify this numerical prediction.

The simulation results have suggested that, for the system modelled in this work, the applied cathode potential of -1.2 V is the optimal value to gain a higher value of acetate production rate and acetate yield simultaneously. Regarding the initial pH, while a lower value generally increases the acetate yield, it would reduce the acetate production rate for the systems with the moderate-to-high CO_2 supply (i.e. $P^0_{CO_2(g)} = 0.5$ and 0.7 atm). For the systems with limited

CO_2 supply (i.e. $P^0_{CO_2(g)} = 0.3\,\text{atm}$), there is an optimal initial pH value of 6.7, which corresponds to the highest acetate production rate. On the impact of the specific surface area of the biofilm matrix and the biofilm thickness, a larger value for both factors is preferable to obtain a higher acetate production rate. For the specific gas-liquid interfacial area, the acetate production rate can be improved when the area increases to a certain level ($\sim 1\ \text{m}^{-1}$), beyond which the improvement will diminish. Generally, these effects are shaped by the multiple entwined factors, such as pH, acetogens growth kinetics, CO_2 supply and H_2 generation.

To conclude, the model constructed in this work provides a numerical approach to assessing the contribution of each CEET (from a theoretical perspective) and serves as a tool for an evaluation of the impact of different parameters, which could eventually improve the system's performance (from a practical perspective). The integration with other studies, such as techno-economic analysis and life cycle analysis, is of interest for future work.

References

(1) Prévoteau, A.; Carvajal-Arroyo, J. M.; Ganigué, R.; Rabaey, K. Microbial Electrosynthesis from CO2: Forever a Promise? *Curr. Opin. Biotechnol.* **2020**, *62*, 48–57.

(2) Logan, B. E.; Rossi, R.; Ragab, A.; Saikaly, P. E. Electroactive Microorganisms in Bioelectrochemical Systems. *Nat. Rev. Microbiol.* **2019**, *17* (5), 307–319.

(3) Nguyen, T. N.; Dinh, C.-T. Gas Diffusion Electrode Design for Electrochemical Carbon Dioxide Reduction. *Chem. Soc. Rev.* **2020**, *49*, 7488–7504.

(4) García de Arquer, F. P.; Dinh, C. T.; Ozden, A.; Wicks, J.; McCallum, C.; Kirmani, A. R.; Nam, D. H.; Gabardo, C.; Seifitokaldani, A.; Wang, X.; Li, Y. C.; Li, F.; Edwards, J.; Richter, L. J.; Thorpe, S. J.; Sinton, D.; Sargent, E. H. CO2 Electrolysis to Multicarbon Products at Activities Greater than 1 A cm−2. *Science.* **2020**, *367*, 661–666.

(5) Gattrell, M.; Gupta, N.; Co, A. A Review of the Aqueous Electrochemical Reduction of CO2 to Hydrocarbons at Copper. *J. Electroanal. Chem.* **2006**, *594* (1), 1–19.

(6) Oloman, C.; Li, H. Electrochemical Processing of Carbon Dioxide. *ChemSusChem* **2008**, *1*, 385–391.

(7) Kelly P. Nevin; Trevor L. Woodard; Franks, A. E.; Summers, Z. M.; Derek R. Lovley. Microbial Electrosynthesis: Feeding Microbes Electricity To Convert Carbon Dioxide and Water to Multicarbon Extracellular Organic Compounds. *MBio* **2010**, *1* (2).

(8) Izadi, P.; Fontmorin, J.; Godain, A.; Yu, E. H.; Head, I. M. Parameters Influencing the Development of Highly Conductive and Efficient Biofilm during Microbial Electrosynthesis: The Importance of Applied Potential and Inorganic Carbon Source. *npj Biofilms Microbiomes* **2020**, *6* (40).

(9) Rabaey, K.; Read, S. T.; Clauwaert, P.; Freguia, S.; Bond, P. L.; Blackall, L. L.; Keller, J. Cathodic Oxygen Reduction Catalyzed by Bacteria in Microbial Fuel Cells. *ISME J.* **2008**, *2* (5), 519–527.

(10) Rozendal, R. A.; Jeremiasse, A. W.; Hamelers, H. V. M.; Buisman, C. J. N. Hydrogen Production With a Microbial Biocathode. *Environ. Sci. Technol.* **2008**, *42*, 629–634.

(11) You, S. J.; Ren, N. Q.; Zhao, Q. L.; Wang, J. Y.; Yang, F. L. Power Generation and Electrochemical Analysis of Biocathode Microbial Fuel Cell Using Graphite Fibre Brush as Cathode Material. *Fuel Cells* **2009**, *9* (5), 588–596.

(12) Aulenta, F.; Catapano, L.; Snip, L.; Villano, M.; Majone, M. Linking Bacterial Metabolism to Graphite Cathodes: Electrochemical Insights into the H2-Producing Capability of Desulfovibrio Sp. *ChemSusChem* **2012**, *5* (6), 1080–1085.

(13) Yu, L.; Duan, J.; Zhao, W.; Huang, Y.; Hou, B. Characteristics of Hydrogen Evolution and Oxidation Catalyzed by Desulfovibrio Caledoniensis Biofilm on Pyrolytic Graphite Electrode. *Electrochim. Acta* **2011**, *56* (25), 9041–9047.

(14) Rabaey, K.; Rozendal, R. A. Microbial Electrosynthesis - Revisiting the Electrical Route for Microbial Production. *Nat. Rev. Microbiol.* **2010**, *8* (10), 706–716.

(15) Rosenbaum, M.; Aulenta, F.; Villano, M.; Angenent, L. T. Cathodes as Electron Donors for Microbial Metabolism: Which Extracellular Electron Transfer Mechanisms Are Involved? *Bioresour. Technol.* **2011**, *102* (1), 324–333.

(16) Villano, M.; Aulenta, F.; Ciucci, C.; Ferri, T.; Giuliano, A.; Majone, M.

Bioelectrochemical Reduction of CO2 to CH4 via Direct and Indirect Extracellular Electron Transfer by a Hydrogenophilic Methanogenic Culture. *Bioresour. Technol.* **2010**, *101* (9), 3085–3090.

(17) Lovley, D. R. Powering Microbes with Electricity: Direct Electron Transfer from Electrodes to Microbes. *Environ. Microbiol. Rep.* **2011**, *3* (1), 27–35.

(18) Logan, B. E.; Call, D.; Cheng, S.; Hamelers, H. V. M.; Sleutels, T. H. J. A.; Jeremiasse, A. W.; Rozendal, R. A. Microbial Electrolysis Cells for High Yield Hydrogen Gas Production from Organic Matter. *Environ. Sci. Technol.* **2008**, *42* (23), 8630–8640.

(19) May, H. D.; Evans, P. J.; LaBelle, E. V. The Bioelectrosynthesis of Acetate. *Curr. Opin. Biotechnol.* **2016**, *42*, 225–233.

(20) Drake, H. L.; Gößner, A. S.; Daniel, S. L. Old Acetogens, New Light. *Ann. N. Y. Acad. Sci.* **2008**, *1125*, 100–128.

(21) Cheng, S.; Xing, D.; Call, D. F.; Logan, B. E. Direct Biological Conversion of Electrical Current into Methane by Electromethanogenesis. *Environ. Sci. Technol.* **2009**, *43* (10), 3953–3958.

(22) Matemadombo, F.; Puig, S.; Ganigué, R.; Ramírez-García, R.; Batlle-Vilanova, P.; Dolors Balaguer, M.; Colprim, J. Modelling the Simultaneous Production and Separation of Acetic Acid from CO2 Using an Anion Exchange Membrane Microbial Electrosynthesis System. *J. Chem. Technol. Biotechnol.* **2017**, *92*, 1211–1217.

(23) Zaybak, Z.; Pisciotta, J. M.; Tokash, J. C.; Logan, B. E. Enhanced Start-up of Anaerobic Facultatively Autotrophic Biocathodes in Bioelectrochemical Systems. *J. Biotechnol.* **2013**, *168* (4), 478–485.

(24) Nie, H.; Zhang, T.; Cui, M.; Lu, H.; Lovley, D. R.; Russell, T. P. Improved Cathode for High Efficient Microbial-Catalyzed Reduction in Microbial Electrosynthesis Cells. *Phys. Chem. Chem. Phys.* **2013**, *15* (34), 14290–14294.

(25) Bajracharya, S.; Ter Heijne, A.; Dominguez Benetton, X.; Vanbroekhoven, K.; Buisman, C. J. N.; Strik, D. P. B. T. B.; Pant, D. Carbon Dioxide Reduction by Mixed and Pure

Cultures in Microbial Electrosynthesis Using an Assembly of Graphite Felt and Stainless Steel as a Cathode. *Bioresour. Technol.* **2015**, *195*, 14–24.

(26) LaBelle, E. V.; Marshall, C. W.; Gilbert, J. A.; May, H. D. Influence of Acidic PH on Hydrogen and Acetate Production by an Electrosynthetic Microbiome. *PLoS One* **2014**, *9* (10), 1–10.

(27) Foley, J. M.; Rozendal, R. A.; Hertle, C. K.; Lant, P. A.; Rabaey, K. Life Cycle Assessment of High-Rate Anaerobic Treatment, Microbial Fuel Cells, and Microbial Electrolysis Cells. *Environ. Sci. Technol.* **2010**, *44*, 3629–3637.

(28) Patil, S. A.; Arends, J. B. A.; Vanwonterghem, I.; Van Meerbergen, J.; Guo, K.; Tyson, G. W.; Rabaey, K. Selective Enrichment Establishes a Stable Performing Community for Microbial Electrosynthesis of Acetate from CO2. *Environ. Sci. Technol.* **2015**, *49*, 8833–8843.

(29) Pons, L.; Délia, M. L.; Bergel, A. Effect of Surface Roughness, Biofilm Coverage and Biofilm Structure on the Electrochemical Efficiency of Microbial Cathodes. *Bioresour. Technol.* **2011**, *102*, 2678–2683.

(30) Dumas, C.; Basseguy, R.; Bergel, A. Microbial Electrocatalysis with Geobacter Sulfurreducens Biofilm on Stainless Steel Cathodes. *Electrochim. Acta* **2008**, *53* (5), 2494–2500.

(31) Dumas, C.; Mollica, A.; Féron, D.; Basséguy, R.; Etcheverry, L.; Bergel, A. Marine Microbial Fuel Cell: Use of Stainless Steel Electrodes as Anode and Cathode Materials. *Electrochim. Acta* **2007**, *53* (2), 468–473.

(32) Pons, L.; Délia, M. L.; Basséguy, R.; Bergel, A. Effect of the Semi-Conductive Properties of the Passive Layer on the Current Provided by Stainless Steel Microbial Cathodes. *Electrochim. Acta* **2011**, *56* (6), 2682–2688.

(33) Zhang, T.; Nie, H.; Bain, T. S.; Lu, H.; Cui, M.; Snoeyenbos-West, O. L.; Franks, A. E.; Nevin, K. P.; Russell, T. P.; Lovley, D. R. Improved Cathode Materials for Microbial Electrosynthesis. *Energy Environ. Sci.* **2013**, *6* (1), 217–224.

(34) Tremblay, P. L.; Angenent, L. T.; Zhang, T. Extracellular Electron Uptake: Among Autotrophs and Mediated by Surfaces. *Trends Biotechnol.* **2017**, *35* (4), 360–371.

(35) Thrash, J. C.; Coates, J. D. Review: Direct and Indirect Electrical Stimulation of Microbial Metabolism. *Environ. Sci. Technol.* **2008**, *42* (11), 3921–3931.

(36) Lithgow, A. M., Romero, L., Sanchez, I. C., Souto, F. A.; Vega, C. A. Interception of the Electron-Transport Chain in Bacteria with Hydrophilic Redox Mediators. I: Selective Improvement of the Performance of Biofuel Cells with 2, 6-Disulphonated Thionine as Mediator. *J. Chem. Res.* **1986**, *5*, 178–179.

(37) Hongo, M.; Iwahara, M. Application of Electro-Energizing Method to L-Glutamic Acid Fermentation. *Agric. Biol. Chem.* **1979**, *43* (10), 2075–2081.

(38) Park, D. H.; Laivenieks, M.; Guettler, M. V.; Jain, M. K.; Zeikus, J. G. Microbial Utilization of Electrically Reduced Neutral Red as the Sole Electron Donor for Growth and Metabolite Production. *Appl. Environ. Microbiol.* **1999**, *65* (7), 2912–2917.

(39) Park, D. H.; Zeikus, J. G. Utilization of Electrically Reduced Neutral Red by Actinobacillus Succinogenes: Physiological Function of Neutral Red in Membrane-Driven Fumarate Reduction and Energy Conservation. *J. Bacteriol.* **1999**, *181* (8), 2403–2410.

(40) Kim, T. S.; Kim, B. H. Electron Flow Shift in Clostridium Acetobutylicum Fermentation by Electrochemically Introduced Reducing Equivalent. *Biotechnol. Lett.* **1988**, *10* (2), 123–128.

(41) Aulenta, F.; Canosa, A.; Reale, P.; Rossetti, S.; Panero, S.; Majone, M. Microbial Reductive Dechlorination of Trichloroethene to Ethene With Electrodes Serving as Electron Donors Without the External Addition of Redox Mediators. *Biotechnol. Bioeng.* **2009**, *103* (1), 85–91.

(42) Sakakibara, Y.; Kuroda, M. Electric Prompting and Control of Denitrification. *Biotechnol. Bioeng.* **1993**, *42*, 535–537.

(43) Clauwaert, P.; Tolêdo, R.; van der Ha, D.; Crab, R.; Verstraete, W.; Hu, H.; Udert, K.

M.; Rabaey, K. Combining Biocatalyzed Electrolysis with Anaerobic Digestion. *Water Sci. Technol.* **2008**, *57* (4), 575–579.

(44) Ohmura, N.; Matsumoto, N.; Sasaki, K.; Saiki, H. Electrochemical Regeneration of Fe(III) to Support Growth on Anaerobic Iron Respiration. *Appl. Environ. Microbiol.* **2002**, *68* (1), 405–407.

(45) Renslow, R.; Babauta, J.; Kuprat, A.; Schenk, J.; Ivory, C.; Fredrickson, J.; Beyenal, H. Modeling Biofilms with Dual Extracellular Electron Transfer Mechanisms. *Phys. Chem. Chem. Phys.* **2013**, *15* (44), 19262–19283.

(46) Kazemi, M.; Biria, D.; Rismani-Yazdi, H. Modelling Bio-Electrosynthesis in a Reverse Microbial Fuel Cell to Produce Acetate from CO2 and H2O. *Phys. Chem. Chem. Phys.* **2015**, *17*, 12561–12574.

(47) Nevin, K. P.; Hensley, S. A.; Franks, A. E.; Summers, Z. M.; Ou, J.; Woodard, T. L.; Snoeyenbos-West, O. L.; Lovley, D. R. Electrosynthesis of Organic Compounds from Carbon Dioxide Is Catalyzed by a Diversity of Acetogenic Microorganisms. *Appl. Environ. Microbiol.* **2011**, *77* (9), 2882–2886.

(48) Lovley, D. R. Electromicrobiology. *Annu. Rev. Microbiol.* **2012**, *66*, 391–409.

(49) Strycharz, S. M.; Woodard, T. L.; Johnson, J. P.; Nevin, K. P.; Sanford, R. A.; Löffler, F. E.; Lovley, D. R. Graphite Electrode as a Sole Electron Donor for Reductive Dechlorination of Tetrachlorethene by Geobacter Lovleyi. *Appl. Environ. Microbiol.* **2008**, *74* (19), 5943–5947.

(50) Beese-Vasbender, P. F.; Grote, J. P.; Garrelfs, J.; Stratmann, M.; Mayrhofer, K. J. J. Selective Microbial Electrosynthesis of Methane by a Pure Culture of a Marine Lithoautotrophic Archaeon. *Bioelectrochemistry* **2015**, *102*, 50–55.

(51) Strycharz, S. M.; Gannon, S. M.; Boles, A. R.; Franks, A. E.; Nevin, K. P.; Lovley, D. R. Reductive Dechlorination of 2-Chlorophenol by Anaeromyxobacter Dehalogenans with an Electrode Serving as the Electron Donor. *Environ. Microbiol. Rep.* **2010**, *2* (2), 289–294.

(52) Park, H. Il; Kim, D. K.; Choi, Y. J.; Pak, D. Nitrate Reduction Using an Electrode as Direct Electron Donor in a Biofilm-Electrode Reactor. *Process Biochem.* **2005**, *40* (10), 3383–3388.

(53) Picioreanu, C.; Kreft, J. U.; Van Loosdrecht, M. C. M. Particle-Based Multidimensional Multispecies Biofilm Model. *Appl. Environ. Microbiol.* **2004**, *70* (5), 3024–3040.

(54) Sakakibara, Y.; Flora, J. R. V.; Suidan, M. T.; Kurodo, M. Modeling of Electrochemically-Activated Denitrifying Biofilms. *Water Res.* **1994**, *28* (5), 1077–1086.

(55) Zhao, J.; Feng, K.; Liu, S. H.; Lin, C. W.; Zhang, S.; Li, S.; Li, W.; Chen, J. Kinetics of Biocathodic Electron Transfer in a Bioelectrochemical System Coupled with Chemical Absorption for NO Removal. *Chemosphere* **2020**, *249*, 126095.

(56) Yang, Z.; Yang, A. Modelling the Impact of Operating Mode and Electron Transfer Mechanism in Microbial Fuel Cells with Two-Species Anodic Biofilm. *Biochem. Eng. J.* **2020**, *158*, 107560.

(57) Wanner, O.; Eberl, H. J.; Morgenroth, E.; Noguera, D. R.; Picioreanu, C.; Rittmann, B. E.; Loosdrecht, M. C. M. van. *Mathematical Modeling of Biofilms*; IWA Task Group on Biofilm Modeling, 2006.

(58) Picioreanu, C.; Head, I. M.; Katuri, K. P.; van Loosdrecht, M. C. M.; Scott, K. A Computational Model for Biofilm-Based Microbial Fuel Cells. *Water Res.* **2007**, *41* (13), 2921–2940.

(59) Batstone, D. J.; Keller, J.; Blackall, L. L. The Influence of Substrate Kinetics on the Microbial Community Structure in Granular Anaerobic Biomass. *Water Res.* **2004**, *38* (6), 1390–1404.

(60) Wanner, O.; Reichert, P. Mathematical Modeling of Mixed-Culture Biofilms. *Biotechnol. Bioeng.* **1996**, *49*, 172–184.

(61) Giraldo-Gomez, E. Kinetics of Anaerobic Treatment: A Critical Review. *Crit. Rev. Environ. Control* **1991**, *21* (5–6), 411–490.

(62) Horn, H.; C.Hempel, D. Modeling Mass Transfer and Substrate Utilization in the Boundary Layer of Biofilm Systems. *Water Sci. Technol.* **1998**, *37* (4–5), 139–147.

(63) Philip S. Stewart. Diffusion in Biofilm. *J. Bacteriol.* **2003**, *185* (5), 1485–1491.

(64) Marcus, A. K.; Torres, C. I.; Rittmann, B. E. Conduction-Based Modeling of the Biofilm Anode of a Microbial Fuel Cell. *Biotechnol. Bioeng.* **2007**, *98* (6), 1171–1182.

(65) Zhang, X.; Li, X.; Zhao, X.; Li, Y. Factors Affecting the Efficiency of a Bioelectrochemical System: A Review. *RSC Adv.* **2019**, *9* (34), 19748–19761.

(66) Cao, X.; Huang, X.; Liang, P.; Xiao, K.; Zhou, Y.; Zhang, X.; Logan, B. E. A New Method for Water Desalination Using Microbial Desalination Cells. *Environ. Sci. Technol.* **2009**, *43* (18), 7148–7152.

(67) Chae, K. J.; Choi, M.; Ajayi, F. F.; Park, W.; Chang, I. S.; Kim, I. S. Mass Transport through a Proton Exchange Membrane (Nafion) in Microbial Fuel Cells. *Energy and Fuels* **2008**, *22*, 169–176.

(68) Horn, H.; Hempel, D. C. Substrate Utilization and Mass Transfer in an Autotrophic Biofilm System: Experimental Results and Numerical Simulation. *Biotechnol. Bioeng.* **1997**, *53* (4), 363–371.

(69) Gadkari, S.; Shemfe, M.; Modestra, J. A.; Mohan, S. V.; Sadhukhan, J. Understanding the Interdependence of Operating Parameters in Microbial Electrosynthesis: A Numerical Investigation. *Phys. Chem. Chem. Phys.* **2019**, *21*, 10761–10772.

(70) Abel, A. J.; Clark, D. S. A Comprehensive Modeling Analysis of Formate-mediated Microbial Electrosynthesis. *ChemSusChem* **2020**, *13*.

(71) J.J. Heijnen. Bioenergetics of Microbial Growth. In *Encyclopedia of Bioprocess Technology: Fermentation, Biocatalysis, and Bioseparation*; John Wiley & Sons: New York, 1999.

(72) Smolke, C. *The Metabolic Pathway Engineering Handbook: Fundamentals*; CRC Press, 2009.

(73) Tomlinson, N.; Barker, H. A. Carbon Dioxide and Acetate Utilization by Clostridium Kluyveri. *J. Biol. Chem.* **1953**, *209* (2), 595–595.

(74) Hashiba, H.; Weng, L. C.; Chen, Y.; Sato, H. K.; Yotsuhashi, S.; Xiang, C.; Weber, A. Z. Effects of Electrolyte Buffer Capacity on Surface Reactant Species and the Reaction Rate of CO2 in Electrochemical CO2 Reduction. *J. Phys. Chem. C* **2018**, *122* (7), 3719–3726.

(75) Leaist, D. G. Coupled Diffusion Produced by Hydrolysis of Aqueous Potassium Phosphate. *J. Solution Chem.* **1985**, *14* (10), 709–721.

(76) Weng, L. C.; Bell, A. T.; Weber, A. Z. Modeling Gas-Diffusion Electrodes for CO2 Reduction. *Phys. Chem. Chem. Phys.* **2018**, *20*, 16973–16984.

(77) Mo, Z.; Friedly, J. C. Local Reaction and Diffusion in Porous Media Transport Models. *Water Resour. Res.* **2000**, *36* (2), 431–438.

(78) Yang, Z.; Li, D.; Xing, L.; Xiang, H.; Xuan, J.; Cheng, S.; Yu, E. H.; Yang, A. Modeling and Upscaling Analysis of Gas Diffusion Electrode-Based Electrochemical Carbon Dioxide Reduction Systems. *ACS Sustain. Chem. Eng.* **2021**, *9*, 351–361.

(79) Weng, L. C.; Bell, A. T.; Weber, A. Z. Towards Membrane-Electrode Assembly Systems for CO2 Reduction: A Modeling Study. *Energy Environ. Sci.* **2019**, *12*, 1950–1968.

(80) Valderrama, J. O.; Campusano, R. A.; Forero, L. A. A New Generalized Henry-Setschenow Equation for Predicting the Solubility of Air Gases (Oxygen, Nitrogen and Argon) in Seawater and Saline Solutions. *J. Mol. Liq.* **2016**, *222*, 1218–1227.

(81) Sander, R. Compilation of Henry's Law Constants (Version 4.0) for Water as Solvent. *Atmos. Chem. Phys.* **2015**, *15*, 4399–4981.

(82) Weber, A. Z.; Newman, J. Modeling Transport in Polymer-Electrolyte Fuel Cells. *Chem. Rev.* **2004**, *104* (10), 4679–4726.

(83) Björnbom, P. Influence of Diffusion Resistances on Gas Diffusion Electrodes. *J. Electrochem. Soc.* **1986**, *133* (9), 1874–1875.

(84) Buck, R. P. Kinetics of Bulk and Interfacial Ionic Motion: Microscopic Basis and Limits for the Nernst-Planck Equation Applied to Membrane Systems. *J. Memb. Sci.* **1984**, *17*, 1–62.

(85) Baker, D. R. Reducing Nonlinear Systems of Transport Equations to Laplace's Equation. *SIAM J. Appl. Math.* **1993**, *53* (2), 419–439.

(86) A., Mieke C. A. Van Eerten-Jansen, A. T. H.; Hamelers, C. J. N. B.; M., H. V. Microbial Electrolysis Cells for Production of Methane from CO2: Long-Term Performance and Perspectives. *Int. J. ENERGY Res.* **2012**, *36*, 809–819.

Chapter 5 Modelling and upscaling analysis of gas diffusion electrode based electrochemical carbon dioxide reduction systems

Published as: ***Z. Yang****, D. Li, L. Xing, H. Xiang, J. Xuan, S. Cheng, E. H. Yu*, A. Yang*, ACS Sustainable Chemistry & Engineering, 2021, 9, 1, 351-361.*

Among all authors contributed to the published article, ***Z. Yang*** *designed and performed the modelling work, analysed and interpreted the results, and wrote the manuscript. A. Yang supervised the study, analysed and interpreted the results, and revised the manuscript. D. Li, H. Xiang and E. H. Yu carried out the relevant experimental work, provided the required data and revised the manuscript. L. Xing, J. Xuan and S. Cheng revised the manuscript.*

Summary

Following the study of CO_2 reduction through bioelectrochemical processes in Chapter 4, this chapter addresses another emerging technology for CO_2 utilisation – electrochemical CO_2 reduction reaction (ECO2RR) systems incorporating gas diffusion electrodes (GDE). The GDE-based ECO2RR systems have the potential to transform CO_2 to valuable products efficiently and environment-friendly. A two-dimensional multiphase model capturing the details of the catalyst layer in a GDE that produces formate with by-products is established and quantitatively validated against experimental data. This model is capable of describing the mixture gas and aqueous species transportation, electron conduction processes and a series of interrelated chemical and electrochemical reactions. Specific electrical energy consumption (SEEC) and product yield (PY) have been introduced and used to examine the GDE scalability and evaluate the system performance. The results predict the optimal values for applied cathode potential and catalyst loading and porosity. The effect of inlet gas composition and velocity is also evaluated. Moreover, this study predicts that the GDE is scalable as it retains a stable performance as its geometrical surface area varies. This model together with the simulation findings contributes to the improved understanding of GDE-based CO_2 conversion as needed for the future development towards successful industrial applications.

5.1 Introduction

Electrochemical CO_2 reduction reaction (ECO2RR) has recently emerged as one of the carbon capture and utilisation (CCU) technologies, which transforms CO_2 to valuable chemicals by consuming water and electricity[1,2]. Depending on the catalyst type, CO_2 can be reduced to different products such as syngas, methane (CH_4), formate ($HCOO^-$) and ethyl alcohol (C_2H_5OH) in the cathodic compartment[1,3]. Currently, its application is significantly limited by the low current density, mainly owing to the large CO_2 mass transfer resistance and the undesirable competitive hydrogen evolution reaction (HER)[1–5]. Gas diffusion electrode (GDE) offers a prospect to the improvement of the overall performance of an ECO2RR electrolyser under mild operating conditions (i.e. room temperature and ambient pressure)[1,4].

Different from the most frequently adopted conventional two-chamber electrolyser with planar electrodes, where CO_2 is purged into the cathode chamber[4] or supplied via the CO_2-saturated catholyte[3], the reactant gaseous CO_2 is directly fed into the gas chamber (GASC) and diffused through the gas diffusion layer (GDL) into the catalyst layer (CL). Compared to the planar electrode, the CL remarkably enlarges the specific area for ECO2RR reaction, alleviates the mass transfer constraint of dissolved CO_2, and reduces the ohmic loss by shortening the distance of reactant to the reaction sites and avoiding bubble appearance[1–3,6–9]. Despite the moderate-to-high current densities achieved[10], there is much room for GDEs to become more competitive than their traditional counterparts (i.e. electrolyser for water splitting), eventually accomplishing successful commercialisation and industrilisation[1,2,11].

To date, most research on ECO2RR is dedicated to experimentally developing stable, efficient and selective catalysts[2]. Limited attention has been paid to the optimisation of electrode configuration and operational conditions[9,12], and even fewer studies focus on upscaling[8,11,13–15]. In this paper, a two-dimensional steady-state multiphase GDE model describing inter- and intra-phase mass transfer, electrochemical kinetics and aqueous-phase reactions is reported. The modelled system converts CO_2 to CO and formate with the latter selected as our target product due to its industrial importance and commercial potential[5]. Here, we present an experimental validation of our model, and subsequently use the model for predicting the scalability of the GDE and the influence of several key parameters on the system's performance. To the best of our knowledge, this is the first report of a GDE model for multiple CO_2-reduction products with a detailed account of reaction kinetics and mass transfer. This model is applied

to investigate the GDE scalability and selectivity, which are both important for the industrial application of this technology.

5.2 Model development and model-based evaluation

5.2.1 Description of the GDE

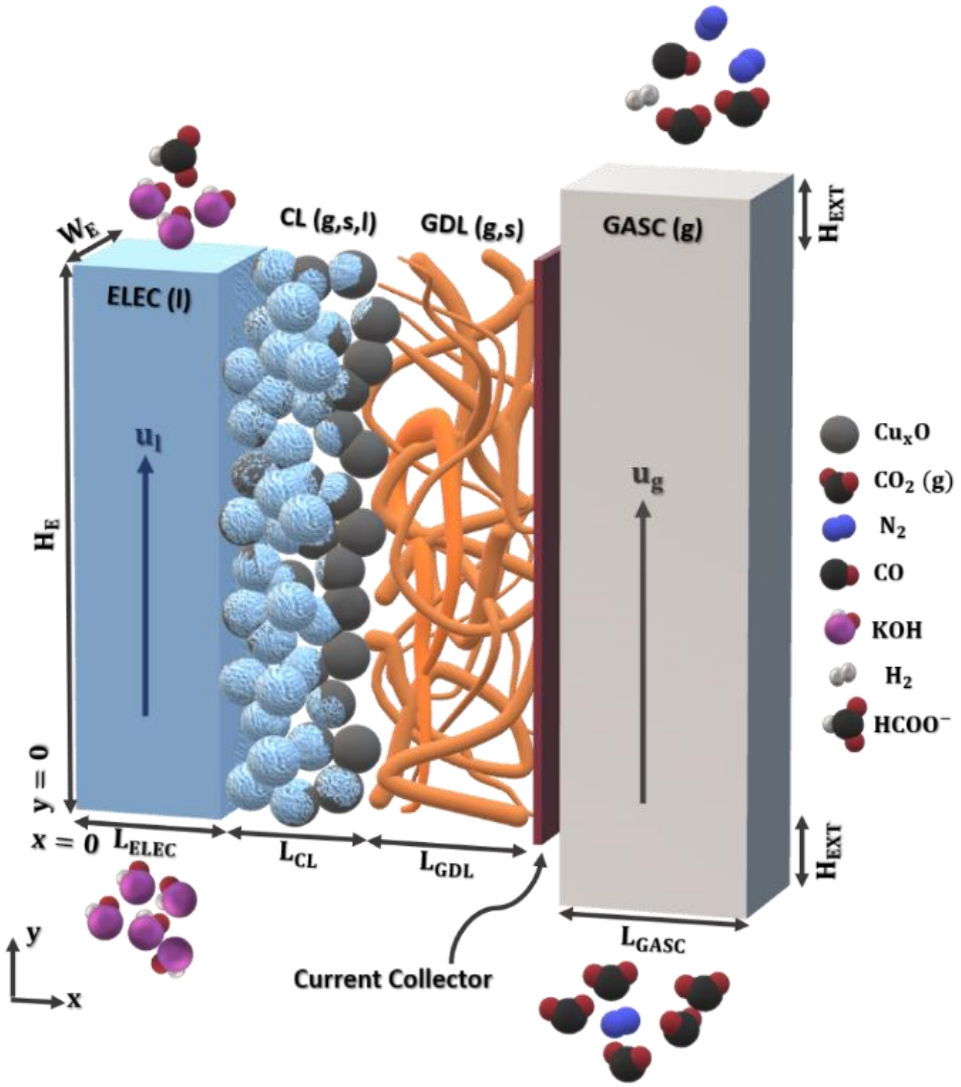

Figure 5.1 Schematic GDE model.

As shown in Figure 5.1, our GDE model comprises, from left to right, electrolyte channel (ELEC), CL, GDL and GASC. They are parallel rectangular compartments with identical heights (y-axis) and widths but different thicknesses (x-axis). The feed gas is supplied into the system from the bottom of the GASC and escapes together with other gaseous products (i.e. CO, H_2) at the other side. The current collector[4] between the GASC and the GDL, with

negligible ohmic loss compared to the GDL and the CL, serves the purpose of providing electrons. CO_2 and electrons are transported via diffusion and conduction respectively through the porous hydrophobic GDL and react in the CL. The GDL in our case is treated as a single-layer GDL[16]. As mentioned earlier, it is widely accepted that the dissolved $CO_2(aq)$ is the only active reactant for electrochemical reactions, rather than HCO_3^-, CO_3^{2-}or $CO_2(g)$[17–21]. Thus, the gas-liquid mass transfer for CO_2 and homogeneous (aqueous-phase) reactions which consume $CO_2(aq)$ in the CL should be considered. The CL is a layer coated with the granular catalyst of Cu_xO (a mixture of Cu_2O, CuO and Cu), a non-toxic and abundant choice attractive for upscaling and also with a promise for the generation of multi-carbon products[4,22,23]. The electrolyte (potassium hydroxide, KOH) and the aqueous products (i.e. formate) flow through the ELEC. In our case, two competing CO_2 electrochemical reduction reactions occur in the CL:

$$CO_2(aq) + H_2O + 2e^- \leftrightarrow HCOO^- + OH^- \quad \text{(R5.1)}$$

$$CO_2(aq) + H_2O + 2e^- \leftrightarrow CO + 2OH^- \quad \text{(R5.2)}$$

In addition to CO_2 reduction reactions, as mentioned earlier, an unwanted parasitic HER also takes place in the CL simultaneously. The HER in the alkaline condition is represented as:

$$2H_2O + 2e^- \leftrightarrow H_2 + 2OH^- \quad \text{(R5.3)}$$

The established two-dimensional, steady-state model simulates a multiphase GDE which is assumed isothermal since the level of current density[24,25] means moderate generation of heat, which, on the other hand, is continuously carried away by the electrolyte flow[24,25]. The x- and y- dimensions of the model are illustrated in Figure 5.1. The geometric parameters, which follow the experimental study[4], are tabulated in Appendix C, Table C.2.

5.2.2 Gaseous species

Gaseous species (i.e. $CO_2(g)$, N_2, H_2 and CO) are considered in the GASC, the GDL and the CL; their mass conservation is modelled by Eq. (5.1). The mixture-averaged diffusion model is employed here to evaluate multicomponent diffusive fluxes without an excessive computational cost[3,26–29]. The Soret effect is not considered in the diffusion term due to the isothermal assumption[30].

$$\nabla \cdot \left(-\rho_g D_{i,m} \nabla \omega_i - \rho_g \omega_i D_{i,m} \frac{\nabla M_g}{M_g} \right) + \nabla \cdot (\rho_g u_g \omega_i) = R_{i,m} \tag{5.1}$$

where i denotes the gaseous species; ρ_g represents the mixture gas density; ω_i denotes the mass fraction of gaseous species; M_g is the averaged molar weight of mixture gas, which is calculated by $(\sum_i \frac{\omega_i}{M_i})^{-1}$; M_i is the molar weight of gaseous species; $D_{i,m}$ is the diffusivity of each gaseous species in the medium, m; u_g is mixture gas velocity. The term $R_{i,m}$ for each species in the GASC and the GDL is zero; in the CL it can be found in Appendix C, Table C.1.

The gaseous diffusivity, $D_{i,m}$, is derived from the Maxwell-Stefan equation and simplified by assuming all other gaseous species have same velocities:

$$D_{i,m} = \frac{1 - \omega_i}{\sum_{k \neq i} \frac{x_k}{D_{ik}}} \tag{5.2}$$

where D_{ik} is the binary diffusivities for the species pairs present; x_k denotes the molar fraction of gaseous species, k. In comparison with other mixture gas models such as Maxwell-Stefan, this assumption makes $D_{i,m}$ to be determined by those parameters that are easily obtained[27,28,30].

The gas velocity, u_g is solved by momentum balance together with overall mass balance. It is assumed that the gas mixture flow in the open channel of the GASC is laminar and compressible (Ma < 0.3)[24].

$$\rho_g (u_g \cdot \nabla) u_g = \nabla \cdot \left[-PI + \mu_g \left(\nabla u_g + (\nabla u_g)^T \right) - \frac{2}{3} \mu_g (\nabla \cdot u_g) I \right] + \rho_g g \tag{5.3}$$

$$\nabla \cdot (\rho_g u_g) = 0 \tag{5.4}$$

where P is the total gas pressure; μ_g is dynamic viscosity of the gas mixture; I is the identity tensor and g is the gravitational acceleration.

In porous media of the GDL and the CL, $D_{i,m}$ in Eq. (5.1) is corrected for the effective porosity for gas, $\epsilon_{m,g}^{eff}$ by using the Bruggeman equation[3]:

$$D_{i,m}^{eff} = \frac{1-\omega_i}{\sum_{k\neq i}\frac{x_k}{(\epsilon_{m,g}^{eff})^{1.5}D_{ik}}} \tag{5.5}$$

It is generally assumed that electrochemical reactions can only occur at the active sites in the CL, where the electrolyte, the reactant and the catalyst meet, also regarding as the three-phase interface[3,24,31]. This requires the pores in the CL to be partially or completely wetted. We define S_m as the saturation coefficient, representing the ratio of liquid occupied volume to the total volume of the pores in the medium, m. It is assumed that the factors affecting saturation (e.g. pore hydrophobicity and size distribution, capillary pressure, etc.[3,32]) remain unchanged and therefore the saturation coefficient is constant. The value of 0.5 is applied for the saturation coefficient in the CL, S_{CL} in our case (the detailed calculation method can be found in Appendix C Section III). Same to the treatment in the prior modelling work[3], GDL is assumed as completely dry (i.e. $S_{GDL} = 0$). The relationship between $\epsilon_{m,g}^{eff}$ and S_m is:

$$\epsilon_{m,g}^{eff} = \epsilon_m^o(1-S_m) \tag{5.6}$$

where ϵ_m^o represents the intrinsic porosity in the medium, m , which is defined as the ratio of the total volume occupied by the pores and the total volume of the medium and assumed as constant and isotropic. ϵ_{CL}^o is calculated by:

$$\epsilon_{CL}^o = 1 - \frac{m_{cat}}{\rho_{cat}L_{CL}} \tag{5.7}$$

where m_{cat} is the mass loading of catalyst (mass of catalyst per geometrical electrode surface area); ρ_{cat} denotes the catalyst density. Neglecting any effect of bubbles, the pores in the CL are assumed to be occupied by a static liquid phase and the gas mixture with the effective porosity, $\epsilon_{m,g}^{eff}$[3,31]. Momentum balance for laminar flow in the porous media becomes Darcy's law, in order to model mixture gas transport[3,26,29,33].

$$u_g = -\frac{\kappa_{m,g}^{eff}}{\mu_g}(\nabla P + \rho_g g) \tag{5.8}$$

where $\kappa_{m,g}^{eff}$ is the effective permeability for gas in the porous medium, m. Its value for a Darcian flow in the CL, which is assumed to be occupied by uniform spherical shape catalysts with a mono-disperse size distribution, is estimated by the Kozeny-Carman equation[34,35]:

$$\kappa_{CL,g}^{eff} = \frac{d_{cat}^2}{180} \frac{(\epsilon_{CL,g}^{eff})^3}{(1-\epsilon_{CL,g}^{eff})^2} \tag{5.9}$$

where d_{cat} is the diameter of catalyst particles. The effective permeability for the fibrous media, the GDL depends strongly on the intrinsic porosity and is given by[3,35–37]:

$$\kappa_{GDL,g}^{eff} = \frac{\kappa_{GDL}^{o} {\epsilon_{GDL}^{o}}^3}{(1-\epsilon_{GDL}^{o})^2} (1-S_{GDL})^3 \tag{5.10}$$

It is worth noting that the GDL may face the 'flooding' problem (i.e. electrolyte penetrates through the CL and goes into GDL) and become wetted in reality[1,12]. In this case, the effective gaseous diffusivity (see Eqs. (5.5) and (5.6)) and permeability (see Eq. (5.10)) would decrease, potentially leading to poor GDE performance. Incorporating this detail would require modifications to the affected equations in the future.

The overall mass balance in the GDL and the CL is analogous to that of the GASC:

$$\nabla \cdot (\rho_g u_g) = Q_m \tag{5.11}$$

where Q_m is the source term, which is zero for the GDL and the sum of gaseous reaction rates in the CL (see Appendix C, Table C.1).

N_2 mass fraction is determined by following mass constraint:

$$\sum \omega_i = 1 \tag{5.12}$$

5.2.3 Aqueous species

The mass conservation of aqueous species, j, is modelled by the Nernst-Plank equation Eq. (5.13):

$$\nabla \cdot \left(-\rho_l D_{j,m} \nabla \omega_j - \frac{z_j F \rho_l \omega_j D_{j,m} \nabla V_l}{R_g T} + \rho_l \omega_j u_l \right) = R_{j,m} \tag{5.13}$$

where ρ_l is the density of the liquid mixture; z_j is the valence of ionic species; R_g is the ideal gas constant; T is operating temperature; u_l is the liquid velocity, which is the ratio of

volumetric flowrate to cross section area of the ELEC, q_l/A_{ELEC}; $D_{j,m}$ is the diffusivity of aqueous species and it is also corrected by the Bruggeman relationship in the porous medium, m.[38] The term of $R_{j,m}$ in CL is listed in the Appendix C, Table C.1.

5.2.4 Homogenous reactions

With fresh KOH as the electrolyte being continuously supplied and the CL being sufficiently thin[4], it is assumed that the pH (and hence the concentration of OH^-, C_{OH}) in both the ELEC and the liquid phase in the CL maintain constant at the same value as feed concentration. Hereby we only consider homogeneous reactions under the alkaline condition:

$$CO_2(aq) + OH^- \xrightarrow{k_{HR5.4}} HCO_3^- \quad \text{(R5.4)}$$

$$HCO_3^- + OH^- \xrightarrow{k_{HR5.5}} H_2O + CO_3^{2-} \quad \text{(R5.5)}$$

Reaction rates for (R5.4) and (R5.5) are expressed as:

$$R_{Ha} = k_{HR5.4} C_{CO_2(aq)} C_{OH} - \frac{k_{HR5.4}}{K_{HR5.4}} C_{HCO_3} \quad (5.14)$$

$$R_{Hb} = k_{HR5.5} C_{HCO_3} C_{OH} - \frac{k_{HR5.5}}{K_{HR5.5}} C_{CO_3} \quad (5.15)$$

where $k_{HR5.4}$, $k_{HR5.5}$ are the forward reaction constants; $K_{HR5.4}$, $K_{HR5.5}$ are the equilibrium constants for the homogenous reaction (R5.4) and (R5.5), respectively. It is worthy to note here that, for the partially wetted porous CL, the reaction rate, R_{Ha} and R_{Hb} should be scaled by the $S_{CL}\epsilon_{CL}^0$, according to the volume averaged model[39].

Homogenous reaction rates for $CO_2(aq)$, HCO_3^- and CO_3^{2-} are:

$$R_{H,CO_2(aq)} = -M_{CO_2} R_{Ha};\ R_{H,HCO_3} = M_{HCO_3}(R_{Ha} - R_{Hb});\ R_{H,CO_3} = M_{CO_3} R_{Hb}; \quad (5.16)$$

where M_{CO_2}, M_{HCO_3} and M_{CO_3} are molecular weight for CO_2, HCO_3^- and CO_3^{2-}, respectively.

5.2.5 Gas-liquid mass transfer

For the gas-liquid mass transfer in the CL, we only consider it for CO_2 due to the negligible solubility of CO and H_2[26]. Given the operating temperature[4], water condensation/evaporation is also ignored. The gas-liquid mass transfer rate for CO_2 is written as:

$$R_{P,CO_2(aq)} = -R_{P,CO_2(g)} = a_{gl} K_{GL} M_{CO_2} \left(\frac{P_{CO_2(g)}}{H_{CO_2}} - C_{CO_2(aq)}\right) \tag{5.17}$$

where a_{gl} is the specific gas-liquid interfacial area; K_{GL} is the overall mass transfer coefficient; H_{CO_2} is Henry's constant for CO_2 and has been calculated taking into account the salting-out effect (see Appendix C Section VII); $P_{CO_2(g)}$ is the partial pressure of $CO_2(g)$, which is calculated according to Dalton's law: $P_{CO_2(g)} = P_{CL} x_{CO_2(g)}$; $C_{CO_2(aq)}$ is the concentration of dissolved CO_2 in the electrolyte. a_{gl} is given by (see Appendix C Section III):

$$a_{gl} = 2 \frac{\epsilon_{CL}^0 (r_{p,CL} - \delta_{ele})}{{r_{p,CL}}^2} \tag{5.18}$$

5.2.6 Electrode kinetics

With the understanding that the rate-determining step (RDS) for each of reactions (R5.1) - (R5.3) is that of one-electron transfer[40,41], the current densities corresponding to the reactions (R5.1) - (R5.3), i_{Ea}, i_{Eb} and i_{Ec} are obtained according to the Butler-Volmer equation (written here for cathodic current only):

$$i_{ER5.1} = -i_{o,ER5.1}^{ref} \left(\frac{C_{CO_2(aq)}}{C_{CO_2(aq),ER5.1}^{ref}}\right) exp\left(-\frac{\alpha_{ER5.1} F}{R_g T}\left(\varphi_s - \varphi_l - \varphi_{eq,ER5.1}^{ref}\right)\right) \tag{5.19}$$

$$i_{ER5.2} = -i_{o,ER5.2}^{ref} \left(\frac{C_{CO_2(aq)}}{C_{CO_2(aq),ER5.2}^{ref}}\right) exp\left(-\frac{\alpha_{ER5.2} F}{R_g T}\left(\varphi_s - \varphi_l - \varphi_{eq,ER5.2}^{ref}\right)\right) \tag{5.20}$$

$$i_{ER5.3} = -i_{o,ER5.3}^{ref} exp\left(-\frac{\alpha_{ER5.3} F}{R_g T}\left(\varphi_s - \varphi_l - \varphi_{eq,ER5.3}^{ref}\right)\right) \tag{5.21}$$

where $i_{o,ER5.1}^{ref}$ $i_{o,ER5.2}^{ref}$ and $i_{o,ER5.3}^{ref}$ are the exchange current densities per catalyst surface area at the reference condition; $C_{CO_2(aq),ER5.1}^{ref}$, $C_{CO_2(aq),ER5.2}^{ref}$ are the reference concentrations of CO_2(aq) corresponding to reactions (R5.1) and (R5.2), respectively; $\alpha_{ER5.1}$, $\alpha_{ER5.2}$ and $\alpha_{ER5.3}$

denote the charge transfer coefficient corresponding to the formation of $HCOO^-$, CO and H_2, respectively; F is the Faraday constant; $\varphi_{eq,ER5.1}^{ref}$, $\varphi_{eq,ER5.2}^{ref}$ and $\varphi_{eq,ER5.3}^{ref}$ are the equilibrium potentials for the electrochemical reactions (R5.1) - (R5.3) in the reference condition and the operating temperature, respectively.

The local electric and electrolyte potential, φ_s and φ_l are derived by Ohm's law coupled with the charge conservation[24]:

$$\nabla \cdot \left(-k_{s,m}^{eff} \nabla \varphi_s\right) = Q_{s,m} \tag{5.22}$$

$$\nabla \cdot \left(-k_{l,m}^{eff} \nabla \varphi_l\right) = Q_{l,m} \tag{5.23}$$

where $k_{s,m}^{eff}$ and $k_{l,m}^{eff}$ are effective conductivities for solid material and electrolyte, respectively. Both of them are assumed constant and are corrected for $(1-\epsilon_m^o)$ and $\epsilon_m^o S_m$ respectively in the porous media according to the Bruggeman equation[38,42,43]; $Q_{s,m}$ and $Q_{l,m}$ are the source terms. $Q_{s,GDL}$ and $Q_{l,ELEC}$ are equal to zero due to the absence of electrochemical reactions; in the CL, they have same values but with opposite sign[3,37]:

$$-Q_{s,CL} = Q_{l,CL} = a_{sl}(i_{ER5.1} + i_{ER5.2} + i_{ER5.3}) \tag{5.24}$$

Electrochemical reaction rates for $CO_2(aq)$, $HCOO^-$, CO and H_2 are expressed based on Faraday's law:

$$\begin{gathered} R_{E,CO_2(aq)} = \frac{M_{CO_2} a_{sl}(i_{ER5.1}+i_{ER5.2})}{2F};\ R_{E,HCOO} = -\frac{M_{HCOO} a_{sl} i_{ER5.1}}{2F}; \\ R_{E,CO} = -\frac{M_{CO} a_{sl} i_{ER5.2}}{2F};\ R_{E,H_2} = -\frac{M_{H_2} a_{sl} i_{ER5.3}}{2F} \end{gathered} \tag{5.25}$$

where M_{HCOO}, M_{CO} and M_{H_2} are molecular weight for $HCOO^-$, CO and H_2, respectively.

a_{sl} is the specific solid-liquid interfacial area and expressed as follows (see Appendix C Section III):

$$a_{sl} = 2\frac{\epsilon_{CL}^o}{r_{p,CL}} \tag{5.26}$$

5.2.7 Boundary conditions

The gaseous species in the GASC, the GDL and the CL are modelled collectively. At the inlet of the GASC, the mixture gas composition and velocity are set as identical to those of the inlet mixture gas[24]. Ambient pressure (i.e. $1\,\mathrm{atm}$) with non-diffusive species is set for the outlet mixture gas at the outlet of the GASC. Zero-flux for gaseous species is applied at the ELEC/CL interface by assuming that any gas can only escape from the GASC. The pressure is continuous at the GDL/GASC interface.

For the aqueous species, we model them in the CL and the ELEC collectively. Mass fractions at the ELEC inlet (i.e. $y = 0$) are set according to those of the electrolyte feed. The aqueous mass flux at the CL/GDL interface is set to zero assuming no electrolyte leakage.

For the electric potential, constant applied cathode potential, φ_C at the GDL/GASC interface is imposed for the 'GDL+CL' subdomain. In terms of the electrolyte potential, it is modelled within the 'CL+ELEC' subdomain together. The electrolyte potential, φ_l is set as zero (versus standard hydrogen electrode)[3,44–46] and zero-flux is applied at the CL/GDL boundary.

5.2.8 Model-based performance evaluation

In addition to current density and selectivity, the product yield (PY) and the specific electrical energy consumption (SEEC) should also be considered for scale-up analysis, because they are significant factors for the economic costs of an ECO2RR system[47]. Assuming no losses of $\mathrm{HCOO^-}$, the PY is defined as the mass of formate produced per unit time and is given by:

$$\mathrm{PY} = -\frac{a_{sl} M_{HCOO} W_E \int_0^{H_E} \int_0^{L_{CL}} i_{ER5.1}\, dx dy}{2F} \tag{5.27}$$

For the SEEC calculation, we only account for the electricity energy consumed by the electrolyser itself, excluding the consumption by the $\mathrm{CO_2}$ capture process, product purification and auxiliary units such as peristaltic pumps. The SEEC is defined as electric energy consumption for producing a unit mass of the formate product, and is calculated by:

$$\mathrm{SEEC} = \frac{2FV_{app}}{M_{HCOO}\mathrm{FE_{HCOO}}} \tag{5.28}$$

V_{app} represents the required cell voltage and detailed calculation can be found in Appendix C Section IV.

Key parameters are summarised in Appendix C Section II. The model is solved by COMSOL Multiphysics 5.4 with the MUMPS general solver.

5.3 Model validation

For the purpose of validation, the simulated total current density is converted to the overall superficial (geometrical) current density with respect to the cathode geometrical surface area, i_C by[24]:

$$i_C = \frac{a_{sl}\int_0^{H_E}\int_0^{L_{CL}}(i_{ER5.1} + i_{ER5.2} + i_{ER5.3})dxdy}{H_E} \tag{5.29}$$

The Faraday efficiency (FE) is the important indicator representing the selectivity. The FEs for $HCOO^-$, CO and H_2 are defined as:

$$\mathrm{FE_{HCOO}} = \frac{a_{sl}\int_0^{H_E}\int_0^{L_{CL}} i_{ER5.1}dxdy}{i_C H_E} \times 100\% \tag{5.30}$$

$$\mathrm{FE_{CO}} = \frac{a_{sl}\int_0^{H_E}\int_0^{L_{CL}} i_{ER5.2}dxdy}{i_C H_E} \times 100\% \tag{5.31}$$

$$\mathrm{FE_{H_2}} = \frac{a_{sl}\int_0^{H_E}\int_0^{L_{CL}} i_{ER5.3}dxdy}{i_C H_E} \times 100\% \tag{5.32}$$

The experimental data and the detailed experiment setup can be found in reference[4]. As indicated in Figure 5.2, the effects of electrolyte concentration and cathode potential on the i_C and selectivity are predicted by our model with good fidelity at lower KOH concentrations (i.e. 0.5 M). However, there is considerable departure between predicted values and experimental data at higher KOH concentrations (i.e. > 1.0 M), which could be attributed to: (i) C_2 products (i.e. ethyl alcohol and ethylene) are notably generated at higher KOH concentration[4]; (ii) the random error of total current density in experimental measurements enlarges with the KOH concentration higher than 0.5 M[4]; (iii) our steady-state model does not reflect the dynamic changes, such as the variation of catalyst size, composition, and saturation condition; the effects of these factors tend to be more pronounced with a higher current density (which increases with

KOH concentration)[4]. Nevertheless, our model is adequate to be used as a predictive tool at least for relatively low KOH concentrations (i.e. ≤ 1.0 M), which have been the main choice of existing GDE experiments[48–50]. Besides, an additional validation of the model based on a GDE experiment with $KHCO_3$ as electrolyte[4] has been conducted which further supports the general validity of the model (see Appendix C Section V). In the simulation studies presented below, the system with KOH as the electrolyte has been adopted since it would lead to higher current density and formate yield compared to a system using $KHCO_3$ at the same concentration[4,12].

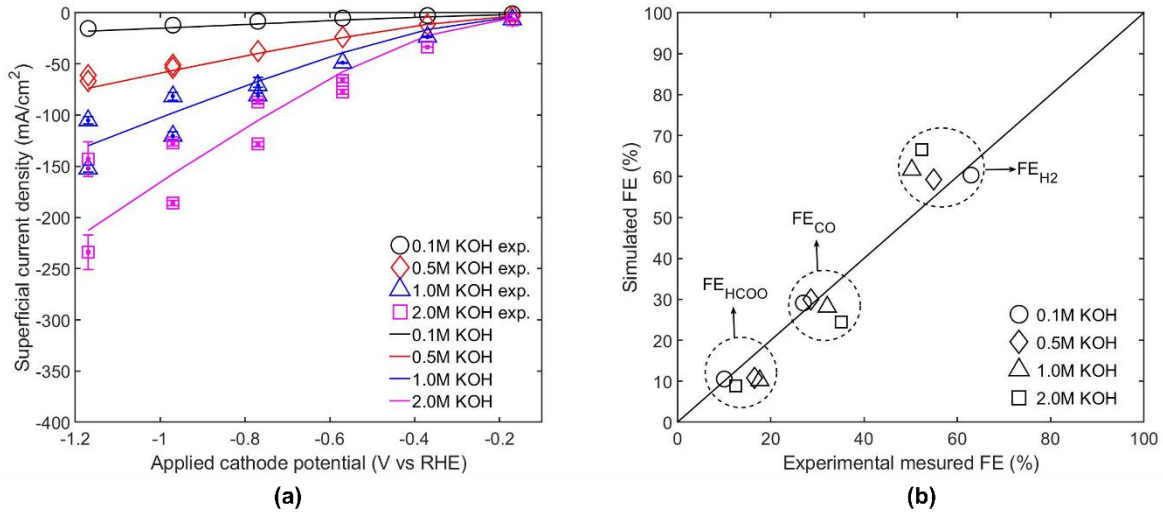

Figure 5.2 (a) Overall superficial current density with respect to the cathode geometrical surface area. The lower bound of experimental data of 0.5 M, 1.0 M and 2.0 M KOH are the measured overall superficial current density; the upper bound experimental data are the current density produced by the reactions (R5.1) - (R5.3) only; (b) Averaged selectivity from data for different cathode potential levels, with various KOH concentrations, compared with calibrated experimental data (excluding products other than H_2, CO and $HCOO^-$).

5.4 Results and discussion

Simulation results with various design and operational parameters are presented and interpreted in this section. In comparison with other KOH concentrations, the system with 0.5M KOH catholyte and at the volumetric flowrate of 0.5 ml/min is selected as it could generate a higher current density and more formate under the same applied cathode potential, without contamination of C2 products. Unless stated otherwise, all other parameters remain as default (see Appendix C, Table C.12) when the parametric study of a specific factor is carried out, and the description of current density change is in terms of its absolute value.

5.4.1 Effect of the applied cathode potential, φ_C

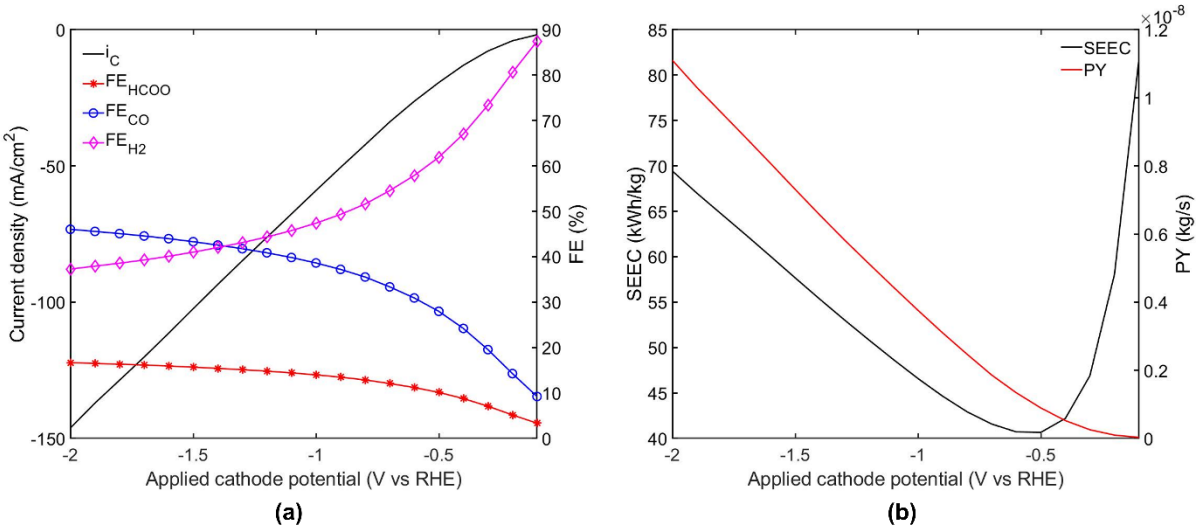

Figure 5.3 The effect of the applied cathode potential, φ_C, on (a) overall superficial current density and selectivity; (b) PY and SEEC.

As shown in Figure 5.3(a), applied cathode potential (φ_C) affects the cathodic overall superficial current density, i_C and selectivity. As φ_C increases, the increases of i_C (shown in Figure 5.3(a)) and partial current density for $HCOO^-$, CO and H_2 (not directly shown in Figure 5.3(a)) are expected (see Eqs. (5.19)-(5.21) and (5.29)). Owing to a smaller charge transfer coefficient and a significantly lower exchange current density of HER, FE_{H_2} continuously decreases with more negative φ_C, which is desirable; however, FE_{CO} increases faster than FE_{HCOO} mainly because less negative φ_C is needed for accelerating CO_2 conversion to CO than to $HCOO^-$ (i.e. $\varphi_{eq,ER5.2}^{ref}$ is more positive than $\varphi_{eq,ER5.1}^{ref}$). Figure 5.3(b) shows that PY is improved as φ_C becomes more negative, which is because of the increase in the partial current density for $HCOO^-$. On SEEC, an optimal value of φ_C of -0.5 V vs RHE exists; more negative φ_C beyond this point would lead to an increase in PY that cannot compensate the increase in the electrical energy consumption (resulting from the increases in both cell voltage and current). The value of -0.5 V vs RHE is selected for other parametric studies use (unless specially mentioned).

5.4.2 GDE scalability

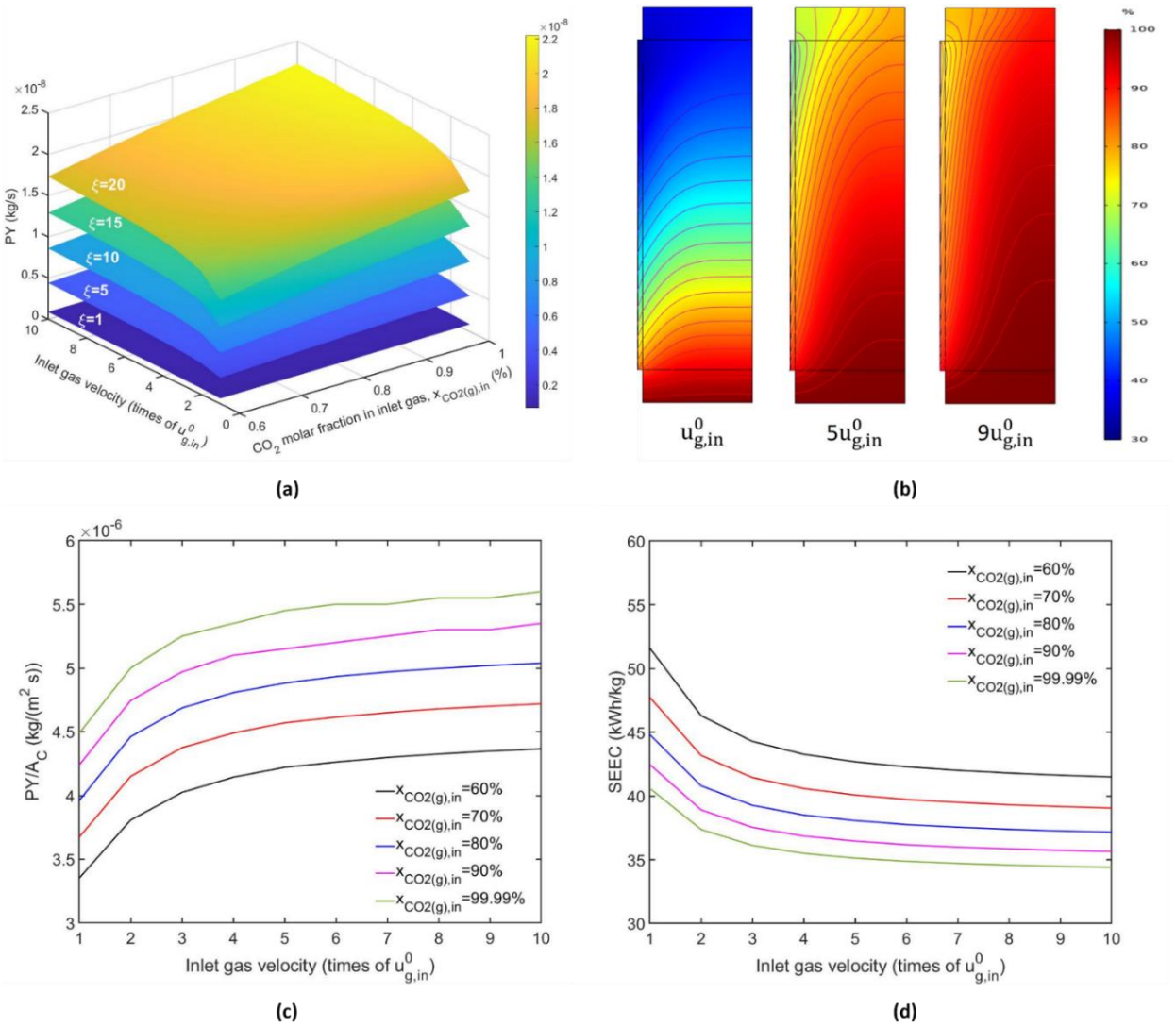

Figure 5.4 (a) PY with various inlet gas composition and velocity; (b) The distribution of CO_2 molar fraction, $x_{CO_2(g)}$ in the 'GASC+GDL+CL' subdomain with inlet gas velocity; (c) PY/A_C and (d) SEEC for the default system (i.e. ξ=1), as the function of inlet gas velocity and composition.

Larger GDEs can provide more reaction sites and therefore improve the PY. To predict the performance of larger-sized GDEs, the cathode geometrical surface area, A_C, is upscaled by increasing electrode height, H_E and width, W_E, while keeping the original aspect ratio (i.e. H_E / W_E). Note that when the thickness of each compartment remains unchanged, the volume of system scales together with A_C. The upscaling factor, ξ, is defined as:

$$\xi = \frac{\text{Upscaled } A_C}{\text{Default } A_C} \tag{5.33}$$

Two key indicators, PY and SEEC, are still employed to evaluate the performance of the upscaled system. The simulation results suggest that the GDE system is scalable for all the tested conditions (i.e. full tested range of gas velocity and molar fraction of CO_2 in feed gas): (i) the PY is approximately scaled by the same factor of ξ (shown in Figure 5.4(a) for illustration); (ii) the SEEC is comparable between the larger and smaller electrolysers (observed from simulation results, not shown here); (iii) the selectivity for each testing cases remains almost unchanged (observed from simulation results, not shown here). The first two observations are in accordance with the recently reported experiment finding[14].

5.4.3 Effect of inlet gas composition and velocity

The impact of the inlet gas velocity, $u_{g,in}$ and the molar fraction of CO_2(g) in feed gas, $x_{CO_2(g),in}$, as two operational settings easy to manipulate, has been discussed in several experimental studies[9,12] and will be examined in this section from the perspective of modelling. For testing, the $u_{g,in}$ is increased up to 10 times of the default value shown in Appendix C, Table C.4, denoted here by $u_{g,in}^0$ and $x_{CO_2(g),in}$ ranges from 60 to 99.99%. Overall, as shown in Figure 5.4(a), increasing CO_2(g) supply, including higher $u_{g,in}$ and $x_{CO_2(g),in}$, is helpful to improve PY for different sizes of the GDE. The PY per A_C, PY/A_C and SEEC with various values of $u_{g,in}$ and $x_{CO_2(g),in}$ for the default size of GDE (i.e. $\xi = 1$) are further plotted in Figure 5.4(c) and (d). One can see that higher $x_{CO_2(g),in}$ always improve both PY/A_C and SEEC. As $u_{g,in}^0$ increases to $5u_{g,in}^0$, both PY/A_C and the SEEC as well as the FE_{HCOO} (not shown) improve remarkably. However, this effect weakens as $u_{g,in}$ increases further. This is due to the trade-off between $x_{CO_2(g)}$ and total pressure in the CL: a larger $u_{g,in}$ elevates the $x_{CO_2(g)}$ (shown in Figure 5.4(b)) but at the same time leads to a reduced total pressure in the CL (see Appendix C, Figure C.5(a)); the combined effect is gradually reduced increments of CO_2(g) partial pressure and hence of the gas-liquid mass transfer rate for CO_2(g) (see Appendix C, Figure C.5(b)), eventually causing diminishing improvements to the production of formate. The effects of $u_{g,in}$ and $x_{CO_2(g),in}$ for other larger systems are similar.

5.4.4 Effect of catalyst loading and arrangement

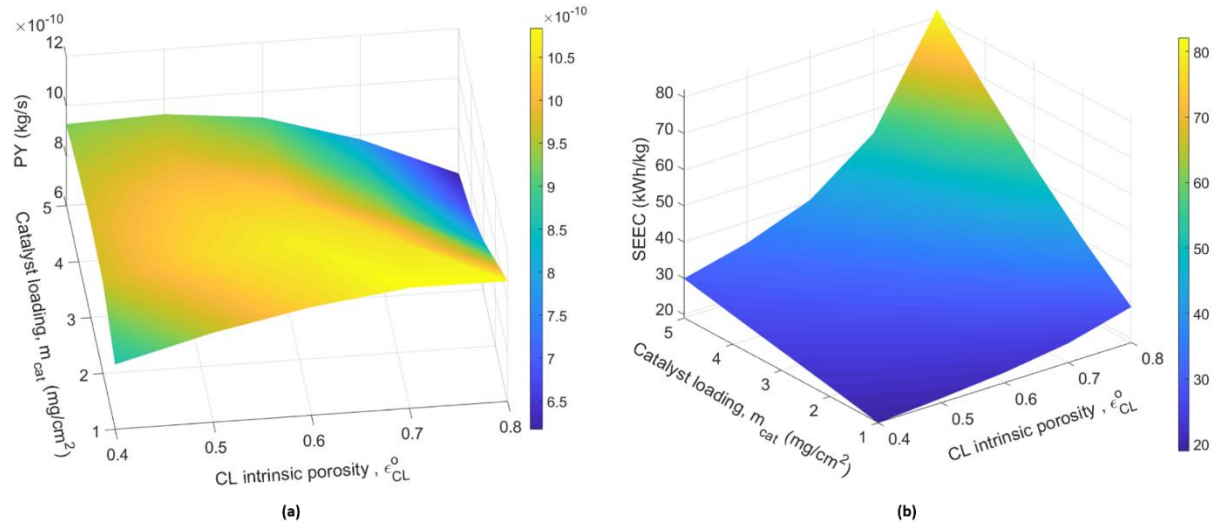

Figure 5.5 (a) PY and (b) SEEC with different catalyst amount and arrangement.

The catalyst amount and its arrangement can potentially affect both the performance and the cost of the ECO2RR system. In this section, the catalyst loading, m_{cat}, and the catalyst arrangement represented by the intrinsic porosity in the CL, ϵ_{CL}^{o}, are discussed. Given the CL manufacture process[4], the parametric study for the intrinsic porosity in the CL, ϵ_{CL}^{o}, is conducted from 0.4 to 0.8, which is in line with the porosity range of random packing arrangements of spherical grains[51].

Figure 5.5(a) shows that the effect of m_{cat} on PY varies for different values of ϵ_{CL}^{o}, which reflects the trade-off between multiple factors including particularly CO_2 supply and the provision of the active surface area for reactions. Based on Eq. (5.7), L_{CL} would increase with m_{cat} when ϵ_{CL}^{o} is kept constant. On the one hand, a larger L_{CL} results in a longer path for gas diffusion (along with a greater ohmic loss of potential), which would lead to a lower $CO_2(g)$ partial pressure in the CL (see Appendix C, Figure C.6) and consequently a negative impact on formate generation. On the other hand, an increase of m_{cat} provides a larger active surface for reactions, which potentially improves product generation (see Eq. (5.27)). For the CL with tighter packing (i.e. $\epsilon_{CL}^{o} < 0.6$), the trade-off of the above factors leads to the occurrence of optimal values of m_{cat} corresponding to the maximum PY (i.e. 3 mg/cm^2 for the CL with $\epsilon_{CL}^{o} = 0.4$ and 2 mg/cm^2 for the CL with $0.4 < \epsilon_{CL}^{o} < 0.6$). However, for the looser packing of the CL (i.e. $\epsilon_{CL}^{o} > 0.6$), the losses associated with the increase thickness of the CL and

outweighs the gains by the increase in the active surface area, therefore PY continuously drops with the increase in catalyst loading.

Analogous to the preceding analysis, the effect of ϵ_{CL}^{o} on PY is also a result of trade-offs. At a given m_{cat}, the change in ϵ_{CL}^{o} leads to a variation in L_{CL} which impacts on CO_2 supply as discussed above. Additionally, the effective diffusivity $D_{CO_2(g),CL}^{eff}$ (see Eqs. (5.5) and (5.6)) and active surface area for gas-liquid mass transfer, a_{gl} (see Eq. (5.18)) augment with the increase in ϵ_{CL}^{o}, which are instrumental to CO_2 supply and subsequently to the PY. Furthermore, the larger active surface area for electrochemical reactions, a_{sl} (see Eq. (5.26)) means more sites available for CO_2 reduction process and can potentially increase PY (see Eq. (5.27)). Besides, ϵ_{CL}^{o} also affects conductivities: the reduced $k_{s,CL}^{eff}$ owing to larger ϵ_{CL}^{o} would lead to a larger voltage drop, although this influence is negligible due to the relatively high value of $k_{s,CL}^{eff}$ in our case (confirmed by the simulation results, not shown here). The $k_{l,CL}^{eff}$ on the other hand increases with a larger ϵ_{CL}^{o}, but the electrolyte potential still drops significantly with the increased L_{CL} and therefore could lead to more positive value of '$\varphi_s - \varphi_l$' (observed from simulation results, not shown here), which is detrimental to CO_2 reduction. With the combined effect of all the factors, the optimal ϵ_{CL}^{o} that leads to the maximum PY shifts from a higher value to a lower value as m_{cat} increases.

To summarise, the effect of m_{cat} and ϵ_{CL}^{o} on PY is shaped by multiple factors, which, in combination, impact on the local value of $i_{ER5.1}$ and the overall surface area or volume of the CL. Overall, as shown in Figure 5.5(a), the distribution of $1\ \mathrm{mg/cm^2}$ catalyst with the intrinsic porosity of 0.7 for the CL, i.e. a design with a low catalyst loading within a "spacious" arrangement, is capable to gain the highest PY (i.e. $1.08 \times 10^{-9}\ \mathrm{kg/s}$) within the tested range of settings.

Different from the PY, Figure 5.5(b) shows that the SEEC always increases with ϵ_{CL}^{o} and m_{cat}, suggesting a more "compact" CL is preferable. The least favourable design in terms of the SEEC (featuring largest ϵ_{CL}^{o} and m_{cat}) coincides with that in terms of the PY, but the optimal setting for the SEEC (featuring lowest ϵ_{CL}^{o} and m_{cat}) corresponds to that leading to an intermediate PY. This is a result of the compromise between the PY and the total energy consumption; the latter is dictated by the larger overpotentials at higher overall currents. The

choice of the optimal design should be integrated with other additional information, such as operating cost and product (formate) price, which will be considered in future work.

5.5 Conclusions

In this paper, gas diffusion electrode (GDE)-based electrochemical conversion of CO_2 to formate together with the by-products (i.e. CO and H_2) was modelled. The two-dimensional steady-state multiphase model was developed by incorporating electrochemical kinetics, the kinetics of homogeneous (aqueous-phase) reactions, and transport phenomena in the cathode compartment. This model demonstrated a good agreement with experimental data of current density and selectivity for the system with lower concentrations of KOH and was employed to investigate the effect of applied cathode potential, inlet gas composition and velocity, and catalyst loading and arrangement on product yield (PY) and specific electrical energy consumption (SEEC).

The simulation results have shown that a more negative cathodic potential results in a higher PY, while the lowest SEEC is reached at an optimal level of -0.5 V vs RHE with the default settings. The GDE was predicted to be scalable in terms of its cathode geometrical surface area, with respect to selectivity, PY and SEEC. On the impact of design and operational parameters, we have shown that both the PY and the SEEC can be improved by better CO_2 supply through a higher CO_2 feed concentration or a greater gas flowrate, although the improvement by the latter becomes insignificant beyond a certain level as the impact of reduced total pressure amplifies. The PY was shown to be shaped by multiple factors when catalyst loading and arrangement are changed. Resulting from the trade-offs between mass transfer resistance, ohmic loss and effective areas available for mass transfer and reactions, dispersion of $1\ mg/cm^2$ catalysts with the porosity of 0.7 in the CL, representing a low loading with a sparse arrangement of catalyst particles, was predicted to be optimal to gain the maximum PY in our study. For the SEEC, its value always becomes larger with m_{cat} and ϵ_{CL}^{o} resulting from the compromise between the increase in the PY and the increase in overpotential losses, suggesting that higher energy efficiencies may prefer a more compact (i.e. thin and dense) catalyst layer.

Overall, our work demonstrates that a GDE-based device for converting CO_2 with formate as a desirable product has good potential for upscaling, and its performance can be significantly improved by choosing the optimal design and operating settings. These learnings may be

applicable to other GDE-based ECO2RR applications. In the future, more efforts could be made to develop a dynamic model to capture further details and integrate with techno-economic analysis and life cycle analysis to gain a holistic understanding of such systems.

References

(1) Nguyen, T. N.; Dinh, C.-T. Gas Diffusion Electrode Design for Electrochemical Carbon Dioxide Reduction. *Chem. Soc. Rev.* **2020**, *49*, 7488–7504.

(2) García de Arquer, F. P.; Dinh, C. T.; Ozden, A.; Wicks, J.; McCallum, C.; Kirmani, A. R.; Nam, D. H.; Gabardo, C.; Seifitokaldani, A.; Wang, X.; Li, Y. C.; Li, F.; Edwards, J.; Richter, L. J.; Thorpe, S. J.; Sinton, D.; Sargent, E. H. CO2 Electrolysis to Multicarbon Products at Activities Greater than 1 A cm−2. *Science.* **2020**, *367*, 661–666.

(3) Weng, L. C.; Bell, A. T.; Weber, A. Z. Modeling Gas-Diffusion Electrodes for CO2 Reduction. *Phys. Chem. Chem. Phys.* **2018**, *20*, 16973–16984.

(4) Xiang, H.; Rasul, S.; Scott, K.; Portoles, J.; Cumpson, P.; Yu, E. H. Enhanced Selectivity of Carbonaceous Products from Electrochemical Reduction of CO2 in Aqueous Media. *J. CO2 Util.* **2019**, *30*, 214–221.

(5) Lu, X.; Leung, D. Y. C.; Wang, H.; Leung, M. K. H.; Xuan, J. Electrochemical Reduction of Carbon Dioxide to Formic Acid. *ChemElectroChem* **2014**, *1*, 836–849.

(6) Newman, J.; Tiedemann, W. Porous-electrode Theory with Battery Applications. *AIChE J.* **1975**, *21* (1), 25–41.

(7) Liang, S.; Altaf, N.; Huang, L.; Gao, Y.; Wang, Q. Electrolytic Cell Design for Electrochemical CO2 Reduction. *J. CO2 Util.* **2020**, *35*, 90–105.

(8) De Mot, B.; Hereijgers, J.; Duarte, M.; Breugelmans, T. Influence of Flow and Pressure Distribution inside a Gas Diffusion Electrode on the Performance of a Flow-by CO2 Electrolyzer. *Chem. Eng. J.* **2019**, *378*, 122224.

(9) Tan, Y. C.; Lee, K. B.; Song, H.; Oh, J. Modulating Local CO2 Concentration as a General Strategy for Enhancing C−C Coupling in CO2 Electroreduction. *Joule* **2020**, *4*,

1104–1120.

(10) Whipple, D. T.; Kenis, P. J. A. Prospects of CO2 Utilization via Direct Heterogeneous Electrochemical Reduction. *J. Phys. Chem. Lett.* **2010**, *1*, 3451–3458.

(11) Lee, M. Y.; Park, K. T.; Lee, W.; Lim, H.; Kwon, Y.; Kang, S. Current Achievements and the Future Direction of Electrochemical CO2 Reduction: A Short Review. *Crit. Rev. Environ. Sci. Technol.* **2020**, *50* (8), 769–815.

(12) Gabardo, C. M.; O'Brien, C. P.; Edwards, J. P.; McCallum, C.; Xu, Y.; Dinh, C. T.; Li, J.; Sargent, E. H.; Sinton, D. Continuous Carbon Dioxide Electroreduction to Concentrated Multi-Carbon Products Using a Membrane Electrode Assembly. *Joule* **2019**, *3*, 2777–2791.

(13) Li, H.; Oloman, C. Development of a Continuous Reactor for the Electro-Reduction of Carbon Dioxide to Formate - Part 2: Scale-Up. *J. Appl. Electrochem.* **2007**, *37*, 1107–1117.

(14) Jeanty, P.; Scherer, C.; Magori, E.; Wiesner-Fleischer, K.; Hinrichsen, O.; Fleischer, M. Upscaling and Continuous Operation of Electrochemical CO2 to CO Conversion in Aqueous Solutions on Silver Gas Diffusion Electrodes. *J. CO2 Util.* **2018**, *24*, 454–462.

(15) Krause, R.; Reinisch, D.; Reller, C.; Eckert, H.; Hartmann, D.; Taroata, D.; Wiesner-Fleischer, K.; Bulan, A.; Lueken, A.; Schmid, G. Industrial Application Aspects of the Electrochemical Reduction of CO2 to CO in Aqueous Electrolyte. *Chemie-Ingenieur-Technik* **2020**, *92*, 53–61.

(16) Garg, S.; Li, M.; Weber, A. Z.; Ge, L.; Li, L.; Rudolph, V.; Wang, G.; Rufford, T. E. Advances and Challenges in Electrochemical CO2 Reduction Processes: An Engineering and Design Perspective Looking beyond New Catalyst Materials. *J. Mater. Chem. A* **2020**, *8*, 1511–1544.

(17) Zhong, H.; Fujii, K.; Nakano, Y.; Jin, F. Effect of CO2 Bubbling into Aqueous Solutions Used for Electrochemical Reduction of CO2 for Energy Conversion and Storage. *J. Phys. Chem. C* **2015**, *119*, 55–61.

(18) Hori, Y.; Murata, A.; Takahashi, R. Formation of Hydrocarbons in the Electrochemical Reduction of Carbon Dioxide at a Copper Electrode in Aqueous Solution. *J. Chem. Soc. Faraday Trans. 1 Phys. Chem. Condens. Phases* **1989**, *85* (8), 2309–2326.

(19) Hori, Y.; Suzuki, S. Electrolytic Reduction of Bicarbonate Ion at a Mercury Electrode. *J. Electrochem. Soc.* **1983**, *130*, 2387.

(20) Kumar, B.; Llorente, M.; Froehlich, J.; Dang, T.; Sathrum, A.; Kubiak, C. P. Photochemical and Photoelectrochemical Reduction of CO2. *Annu. Rev. Phys. Chem.* **2012**, *63*, 541–569.

(21) Haas, T.; Krause, R.; Weber, R.; Demler, M.; Schmid, G. Technical Photosynthesis Involving CO2 Electrolysis and Fermentation. *Nat. Catal.* **2018**, *1*, 32–39.

(22) Ma, S.; Sadakiyo, M.; Luo, R.; Heima, M.; Yamauchi, M.; Kenis, P. J. A. One-Step Electrosynthesis of Ethylene and Ethanol from CO2 in an Alkaline Electrolyzer. *J. Power Sources* **2016**, *301*, 219–228.

(23) Qiao, J.; Fan, M.; Fu, Y.; Bai, Z.; Ma, C.; Liu, Y.; Zhou, X. D. Highly-Active Copper Oxide/Copper Electrocatalysts Induced from Hierarchical Copper Oxide Nanospheres for Carbon Dioxide Reduction Reaction. *Electrochim. Acta* **2015**, *153*, 559–565.

(24) Wu, K.; Birgersson, E.; Kim, B.; Kenis, P. J. A.; Karimi, I. A. Modeling and Experimental Validation of Electrochemical Reduction of CO2 to CO in a Microfluidic Cell. *J. Electrochem. Soc.* **2015**, *162* (1), F23–F32.

(25) Kotb, Y.; Fateen, S. E. K.; Albo, J.; Ismail, I. Modeling of a Microfluidic Electrochemical Cell for the Electro-Reduction of CO2 to CH3OH. *J. Electrochem. Soc.* **2017**, *164* (13), E391–E400.

(26) Weng, L. C.; Bell, A. T.; Weber, A. Z. Towards Membrane-Electrode Assembly Systems for CO2 Reduction: A Modeling Study. *Energy Environ. Sci.* **2019**, *12*, 1950–1968.

(27) J.Kee, R.; Coltrin, M. E.; Glarborg, P.; Zhu, H. *Chemically Reacting Flow*; 2003.

(28) Torstensson, M. A Comparison of the Multicomponent Model and the Mixture

Averaged Approximation, 2014.

(29) Weng, L.-C.; Bell, A. T.; Weber, A. Z. A Systematic Analysis of Cu-Based Membrane-Electrode Assemblies for CO2 Reduction through Multiphysics Simulation. *Energy Environ. Sci.* **2020**, *13*, 3592–3606.

(30) Bongers, H.; De Goey, L. P. H. The Effect of Simplified Transport Modeling on the Burning Velocity of Laminar Premixed Flames. *Combust. Sci. Technol.* **2003**, *175*, 1915–1928.

(31) Wang, H.; Leung, D. Y. C.; Xuan, J. Modeling of a Microfluidic Electrochemical Cell for CO2 Utilization and Fuel Production. *Appl. Energy* **2013**, *102*, 1057–1062.

(32) Balliet, R. J.; Newman, J. Cold Start of a Polymer-Electrolyte Fuel Cell I. Development of a Two-Dimensional Model. *J. Electrochem. Soc.* **2011**, *158* (8), B927–B938.

(33) Serincan, M. F.; Pasaogullari, U.; Sammes, N. M. Effects of Operating Conditions on the Performance of a Micro-Tubular Solid Oxide Fuel Cell (SOFC). *J. Power Sources* **2009**, *192*, 414–422.

(34) Bear, J. *Dynamics of Fluids in Porous Media*; Amerian Elsevier publishing company, 1972.

(35) M. Kaviany. *Principles of Heat Transfer in Porous Media*, Second edi.; Springer: New York, 1999.

(36) Nam, J. H.; Kaviany, M. Effective Diffusivity and Water-Saturation Distribution in Single- and Two-Layer PEMFC Diffusion Medium. *Int. J. Heat Mass Transf.* **2003**, *46*, 4595–4611.

(37) Weber, A. Z.; Newman, J. Modeling Transport in Polymer-Electrolyte Fuel Cells. *Chem. Rev.* **2004**, *104* (10), 4679–4726.

(38) Zhang, B.; Ye, D. D.; Sui, P. C.; Djilali, N.; Zhu, X. Computational Modeling of Air-Breathing Microfluidic Fuel Cells with Flow-over and Flow-through Anodes. *J. Power Sources* **2014**, *259*, 15–24.

(39) Mo, Z.; Friedly, J. C. Local Reaction and Diffusion in Porous Media Transport Models. *Water Resour. Res.* **2000**, *36* (2), 431–438.

(40) Cheng, T.; Xiao, H.; Goddard, W. A. Reaction Mechanisms for the Electrochemical Reduction of CO2 to CO and Formate on the Cu(100) Surface at 298 K from Quantum Mechanics Free Energy Calculations with Explicit Water. *J. Am. Chem. Soc.* **2016**, *138*, 13802–13805.

(41) Wei, J.; Zhou, M.; Long, A.; Xue, Y.; Liao, H.; Wei, C.; Xu, Z. J. Heterostructured Electrocatalysts for Hydrogen Evolution Reaction under Alkaline Conditions. *Nano-Micro Lett.* **2018**, 10:75.

(42) Bernardi, Dawn M., Verbrugge, M. W. Mathematical Model of a Gas Diffusion Electrode Bonded to a Polymer Electrolyte. *AIChE J.* **1991**, *37* (8), 1151–1163.

(43) Xing, L.; Mamlouk, M.; Kumar, R.; Scott, K. Numerical Investigation of the Optimal Nafion® Ionomer Content in Cathode Catalyst Layer: An Agglomerate Two-Phase Flow Modelling. *Int. J. Hydrogen Energy* **2014**, *39*, 9087–9104.

(44) Björnbom, P. Influence of Diffusion Resistances on Gas Diffusion Electrodes. *J. Electrochem. Soc.* **1986**, *133* (9), 1874–1875.

(45) Buck, R. P. Kinetics of Bulk and Interfacial Ionic Motion: Microscopic Basis and Limits for the Nernst-Planck Equation Applied to Membrane Systems. *J. Memb. Sci.* **1984**, *17*, 1–62.

(46) Baker, D. R. Reducing Nonlinear Systems of Transport Equations to Laplace's Equation. *SIAM J. Appl. Math.* **1993**, *53* (2), 419–439.

(47) Spurgeon, J. M.; Kumar, B. A Comparative Technoeconomic Analysis of Pathways for Commercial Electrochemical CO2 Reduction to Liquid Products. *Energy Environ. Sci.* **2018**, *11*, 1536–1551.

(48) Xiang, H.; Miller, H. A.; Bellini, M.; Christensen, H.; Scott, K.; Rasul, S.; Yu, E. H. Production of Formate by CO2 Electrochemical Reduction and Its Application in Energy Storage. *Sustain. Energy Fuels* **2019**, *4*, 277–284.

(49) Endrődi, B.; Bencsik, G.; Darvas, F.; Jones, R.; Rajeshwar, K.; Janáky, C. Continuous-Flow Electroreduction of Carbon Dioxide. *Prog. Energy Combust. Sci.* **2017**, *62*, 133–154.

(50) Xiang, H.; Rasul, S.; Hou, B.; Portoles, J.; Cumpson, P.; Yu, E. H. Copper-Indium Binary Catalyst on a Gas Diffusion Electrode for High-Performance CO2 Electrochemical Reduction with Record CO Production Efficiency. *ACS Appl. Mater. Interfaces* **2020**, *12*, 601–608.

(51) Gueguen, Y.; Victor Palciauskas. *Introduction to the Physics of Rocks*; Princeton university press: Princeton, 1994.

Chapter 6 Conclusions and perspectives

6.1 Summary of research and key contributions

This thesis presents studies towards two types of effective solutions in the fight against the increasing atmospheric CO_2 concentration and the consequential climate change. The first type is to reduce CO_2 emissions from the sources by exploring alternative renewable energies to replace fossil fuels; and another one is to convert the captured CO_2 to value-added chemicals via different routes. There are many hurdles that have to be overcome before these proposed technologies can achieve the desired results and become economically feasible in reality. Numerical studies are critical to (i) obtaining the detailed insights into the underlying mechanisms and the interplays between different processes in the sophisticated systems; and (ii) the design and optimisation of these systems to enable better performance.

Firstly, a one-dimensional (1D) dynamic model was established for a microbial fuel cell (MFC) with a 'fermenter - electrochemically active bacteria (EAB)' type, two-species biofilm, which is governed by the (anodic) mediator-based extracellular electron transfer (MET) or (anodic) direct conduction-based extracellular electron transfer (DET) mechanism. The established model was applied to the '*Escherichia coli* (*E. coli*) - *Shewanella oneidensis* (*S. oneidensis*)' anode-attached consortium, in which *E. coli* acts as a fermenter to convert the primary substrate (i.e. glucose) to formate. The latter EAB, *S. oneidensis*, can utilise the intermediate metabolic (formate) to grow and transport electrons. Through the implementation of the detailed simulation studies on the multispecies biofilm, the impact of the key operating parameters (such as substrate supply and external resistance) and their trade-offs were examined in two operating modes (i.e. batch and continuous mode) with different biofilm characteristics (such as biofilm conductivity and thickness). The results reveal the complex interplays between microbial growth, mass transfer and electrical conduction processes in the multi-species consortium. The simulation outcomes also suggest several optimal settings for the current generation. These findings provide new insights into multi-species biofilms and could guide the design of other similar microbial-electricity-generation devices.

Aside from delivering power, the microorganisms could also be inoculated in the cathodic chamber of microbial electrosynthesis cells (MESs) to convert CO_2. In the second study, CO_2 is reduced to acetate through acetogens in an MES. The proposed mathematical model

incorporates the pH effect and integrates two putative cathodic extracellular electron transfer mechanisms (i.e. cathodic mediator-based extracellular electron transfer (CMET) and cathodic direct conduction-based extracellular electron transfer (CDET)). It was quantitatively validated by the experiments with good fidelity, and then further adopted to (i) identify the governing electron transfer manner; and (ii) analyse system's performance (i.e. acetate yield and production rate) under different operating conditions. The simulation results indicate that in our modelled case, CDET always dominates the cathodic electron transfer, and the ultimate acetate yield/production rate is a combined effect that is induced by multiple coupled processes, even only a single input parameter was changed. In this work, it has also been highlighted that the local pH would significantly affect the system's performance, as pH is closely linked to factors such as the acetogens growth and the content of the inorganic carbon source. This study is the first modelling framework for the cathodic biofilm in the MESs with a detailed description of the interacting dual cathodic extracellular electron transfer mechanisms, biofilm metabolisms, microbial kinetics, and, last but not the least, pH effects. The results of this work advance the knowledge of CEETs and can be applied to give more credible predictions and guidance for further practical design and operation.

The last work of this thesis simulates a gas diffusion electrode (GDE)-based electrochemical CO_2 reduction reaction (ECO2RR) system. CO_2 is transformed to the target product of formate in the cathodic chamber, along with multiple by-products including carbon monoxide and hydrogen. The established two-dimensional (2D), steady-state model captures a series of reaction kinetics and transport phenomena; it focuses on the optimisation of the ECO2RR system and the scale-up of a GDE specifically. The product yield (PY), selectivity and specific electrical energy consumption (SEEC) were introduced as the indicators to examine the scalability of the GDE and evaluate the system's performance. Following the quantitative verification against the experimental data, numerical simulations were carried out. The simulation results demonstrate that GDE is scalable with regard to all the aforementioned aspects. Analogous to the acetate yield in the last project, formate yield and SEEC are shown to be shaped by multiple factors. This work also puts forward several optimal settings and design ideas to improve the system's performance (from an engineering viewpoint). This study can provide a scientific basis for the industrial use of this innovative technology.

6.2 Limitations and future perspectives

For the work on MFCs, a single type of pollutant (i.e. glucose) was considered in this thesis as the feed to the simple 'representative' anodic microorganisms. To be closer to reality, further modelling work is encouraged to treat more complex substrates and expand the spectrum of bacteria species. Also, due to the insufficient experimental information, the constructed MFCs' model was only qualitatively validated. It would be instrumental for the numerical modelling work to collaborate with the relevant experimental studies to make more reliable and accurate predictions. Additionally, it would be helpful for the simplification of a mathematical model to introduce dimensional analysis/non-dimensionalisation in the future.

Regarding the work on MESs, the proposed mathematical model in this thesis only focuses on the cathodic chamber. The development of a full-cell model (i.e. covering both anodic and cathodic chambers) is of paramount importance to understand the MESs' overall working principles and the mutual impacts between the two electrodes. Moreover, it is envisaged that renewable electricity generation (such as wind and solar) could be integrated with the current model in future work. This proposal would not only offer a more sustainable MES system but also provide a practical approach to store intermittent renewable sources.

In addition to the aforementioned product yield, selectivity and specific electrical energy consumption, the stability of a GDE-based ECO2RR system is one of the areas of concern. Nevertheless, limited by the nature of the steady-state model, the saturation condition in the GDE was assumed to be constant in this work without considering the flooding issue. In the future, the research could be focused on the development of dynamic models for GDE-based ECO2RR systems. The life cycle analysis and techno-economic analysis could also be incorporated to promote the industrialisation progress of this technology.

Appendix A

I. Modelling reaction rates

Net reaction rate of biomass in the biofilm, $R_{F,i}$

For the fermentative bacteria, FB:

$$R_{F,FB} = \mu_{FB} X_{FB} \quad \text{(A.1)}$$

where $R_{F,FB}$ is the net reaction rate of FB in the biofilm. X_{FB} is the biomass concentration of FB in the biofilm.

For the electrochemically active bacteria, EAB:

$$R_{F,EAB} = X_{EAB} \mu_{EAB}^{M} \text{ (with MET)} \quad \text{(A.2)}$$

$$R_{F,EAB} = X_{EAB} \mu_{EAB}^{C} \text{ (with DET)} \quad \text{(A.3)}$$

Where $R_{F,EAB}$ is the net reaction rate of EAB in the biofilm. X_{EAB} is the biomass concentration of EAB in the biofilm.

Net consumption rate of a soluble component in the biofilm, $R_{F,j}$

For primary substrate, PS:

$$R_{F,PS} = \frac{X_{FB} \mu_{FB}}{Y_{PS/FB}} \quad \text{(A.4)}$$

where $R_{F,PS}$ is the net consumption rate of primary substrate in the biofilm. $Y_{PS/FB}$ denotes the yield coefficient for FB's growth.

For intermediate substrate, IS:

$$R_{F,IS} = -Y_{PS/IS} R_{F,PS} + \frac{X_{EAB} \mu_{EAB}^{M}}{Y_{IS/EAB}} \text{ (with MET)} \quad \text{(A.5)}$$

$$R_{F,IS} = -Y_{PS/IS} R_{F,PS} + \frac{X_{EAB} \mu_{EAB}^{C}}{Y_{IS/EAB}} \text{ (with DET)} \quad \text{(A.6)}$$

where $R_{F,IS}$ is the net consumption rate of intermediate substrate in the biofilm. $Y_{IS/EAB}$ denotes the yield coefficient for EAB's growth.

For the oxidised form of the mediator, Mo

$$R_{F,Mo} = \frac{\gamma_{IS} f_e^o}{n Y_{IS/EAB}} X_{EAB} \mu_{EAB}^M - X_{EAB} \mu_{Mo} \quad \text{(A.7)}$$

where $R_{F,Mo}$ is the net consumption rate of Mo in the biofilm. μ_{Mo} is the specific Mo secretion rate.

For the reduced form of the mediator, Mr

$$R_{F,Mr} = -\frac{\gamma_{IS} f_e^o}{n Y_{IS/EAB}} X_{EAB} \mu_{EAB}^M \quad \text{(A.8)}$$

where $R_{F,Mr}$ is the net consumption rate of Mr in the biofilm

II. Default values for model parameters

Table A.1 Default values for model parameters.

Symbol	Definition	Value	Reference
Physical and biochemical parameters			
$D_{BL,Mr}$	Diffusion coefficient for Mr (FMNH2) in the bulk liquid	1.72×10^{-9} m^2 s^{-1}	[1]
$D_{BL,IS}$	Diffusion coefficient for intermediate substrate (formate) in the bulk liquid	1.41×10^{-9} m^2 s^{-1}	[1]
$D_{BL,Mo}$	Diffusion coefficient for Mo (FMN) in the bulk liquid	1.72×10^{-9} m^2 s^{-1}	[1]
$D_{BL,PS}$	Diffusion coefficient for primary substrate(glucose) in the bulk liquid	6.70×10^{-10} m^2 s^{-1}	[1]
$D_{F,Mo}$	Diffusion coefficient for Mo (FMN) in the biofilm	4.30×10^{-10} m^2 s^{-1}	[2]
$D_{F,Mr}$	Diffusion coefficient for Mr (FMNH2) in the biofilm	4.30×10^{-10} m^2 s^{-1}	[2]

$D_{F,PS}$	Diffusion coefficient for primary substrate(glucose) in the biofilm	2.01×10^{-10} m^2 s^{-1}	1
$D_{F,IS}$	Diffusion coefficient for intermediate substrate (formate) in the biofilm	3.53×10^{-10} m^2 s^{-1}	1
L_F^0	Initial biofilm thickness	4×10^{-5} m	3*
L_F^{max}	Maximum biofilm thickness	1×10^{-4} m	2
L_{LBL}	Thickness of the liquid boundary layer	1×10^{-5} m	2,4
M_{IS}	Half-saturation constant for EAB's (MR1) substrate	13.2 mM	2
M_{Mo}	Half-saturation constant for Mo (FMN)	1×10^{-4} mM	2
M_{PS}	Half-saturation constant for FB's (*E. coli*) substrate	5.55×10^{-2} mM	10,11
R_g	Ideal gas constant	8.314 J K^{-1} mol^{-1}	
R_{int}	Internal resistance	300 Ω	4–6
$Y_{PS/FB}$	Yield coefficient for FB's (*E. coli*) growth	0.03 kg mol^{-1}	8
$Y_{IS/EAB}$	Yield coefficient for EAB's (MR1) growth	4.95×10^{-3} kg mol^{-1}	7
$Y_{PS/IS}$	Yield coefficient for primary substrate (glucose) conversion	1.73	8
f_e^o	Fraction of the EAB's substrate used for energy generation	0.2	7
k_{ox}	Oxidation reaction rate constant	3.9×10^{-6} m s^{-1}	Calculated[2,9]
k_{red}	Reduction reaction rate constant	2.8×10^{-13} m s^{-1}	Calculated[2,9]
k_s^{eff}	Biofilm conductivity	2.5×10^{-3} S m^{-1}	15,16
γ_{IS}	Electron equivalence of EAB's substrate	2	Calculated 7,18–21
μ_{EAB}^{max}	Maximum growth rate for EAB (MR1)	0.47 h^{-1}	13
μ_{FB}^{max}	Maximum growth rate for FB (*E. coli*)	0.26 h^{-1}	8
μ_{Mo}^{max}	Maximum specific Mo (FMN) secretion rate	4.42×10^{-8} mol kg^{-1}s^{-1}	12**
ρ_F	Biofilm biomass density	27 kg m^{-3}	14

φ_{Ma}	Potential corresponding EAB's half-maximum specific growth rate	-0.155 V vs SHE	[2]
F	Faraday constant	96485 C mol^{-1}	
n	Number of electrons transferred per redox mediator reaction	2	[2,12,17]
β	Transfer coefficient	0.5	Assumed
ϵ	Biofilm porosity	0.6	[22,23]
Design and operational parameters for MFC			
A_E	Electrode surface area	1×10^{-3} m^2	[3]
$C^0_{BL,IS}$	Initial concentration of intermediate substrate (formate) in the bulk liquid	0 mM	[3]
$C^0_{BL,Mo}$	Initial concentration in the bulk liquid for Mo (FMN)	1×10^{-3} mM	[2]
$C^0_{BL,Mr}$	Initial concentration in the bulk liquid for Mr (FMNH2)	0 mM	[2]
$C^0_{BL,PS}$	Initial concentration in the bulk liquid for primary substrate (glucose)	20 mM	[3]
$C_{in,Mo}$	Inlet concentration for Mo (FMN)	0 mM	Assumed
$C_{in,Mr}$	Inlet concentration for Mr (FMNH2)	0 mM	Assumed
$C_{in,IS}$	Inlet concentration for intermediate substrate (formate) concentration	0 mM	Assumed
$C_{in,PS}$	Inlet concentration for primary substrate (glucose)	100 mM	Assumed
R_{ext}	External resistance	1000 Ω	[3]
V_{BL}	Bulk liquid volume	2×10^{-5} m^3	[3]
X^0_{EAB}	Initial biomass concentration in biofilm for EAB (MR1)	16 kg m^{-3}	[3,24]
X^0_{FB}	Initial biomass concentration in biofilm for FB (*E. coli*)	11 kg m^{-3}	[3]
q_f	Inlet/outlet volumetric flowrate	1×10^{-8} L s^{-1}	Assumed
φ_c	Cathode potential	0.68 V vs SHE	[2]
T	Temperature	306 K	[3]

pH	pH	7	Assumed

* Derived from dividing the total mass of seeded biomass given in the literature[3] by biofilm density and anode surface area.

** Calculated by multiplying the maximum Mo secretion per unit mass of protein by the mass fraction of protein in a cell (0.55)[25,26].

III. Calculation of diffusion coefficients

The value of an effective diffusion coefficient in the biofilm is reduced from the corresponding diffusivity in a homogeneous aqueous phase, because of the presence of microbial cells, extracellular polymeric substances, other particles and gas bubbles in the biofilm. The relative effective diffusivity, which is defined as the ratio of the effective diffusivity in the biofilm and that in water is used to describe the reduction of diffusivity in the biofilm. It is assumed in our model that the diffusion coefficient in the bulk liquid is identical to the value of that in water. It is also assumed that the diffusion coefficient in the biofilm is identical to the effective diffusion coefficient. Thus, the relative effective diffusivity is expressed as $D_{F,j}/D_{BL,j}$. The value of relative effective diffusivity for glucose was reported to be 0.3[1]. For other soluble components in our model, a normal value of the relative effective diffusivity, 0.25 is applied[1]. The values of the diffusion coefficients used in our model are summarized in Table A.2.

Table A.2 Values of diffusion coefficients.

Soluble component	Diffusion coefficient in the bulk liquid	Diffusion coefficient in the biofilm
PS	$D_{BL,PS} = 6.70 \times 10^{-10}$ m^2 s^{-1} [1]	$D_{F,PS} = 2.01 \times 10^{-10}$ m^2 s^{-1}
IS	$D_{BL,IS} = 1.41 \times 10^{-9}$ m^2 s^{-1} [1]	$D_{F,IS} = 3.53 \times 10^{-10}$ m^2 s^{-1}
Mo	$D_{BL,Mo} = 1.72 \times 10^{-9}$ m^2 s^{-1}	$D_{F,Mo} = 4.30 \times 10^{-10}$ m^2 s^{-1} [2]
Mr	$D_{BL,Mr} = 1.72 \times 10^{-9}$ m^2 s^{-1}	$D_{F,Mr} = 4.30 \times 10^{-10}$ m^2 s^{-1}[2]

IV. Effect of initial concentration of primary substrate (glucose), $C^0_{BL,PS}$ (batch)

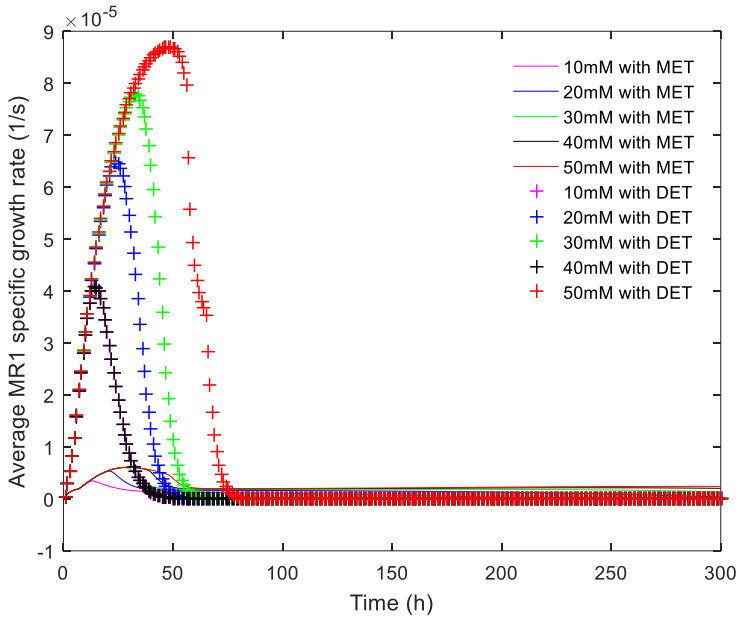

Figure A.1 Average MR1 specific growth rate with MET (solid line) and DET ("+") at different initial concentrations of primary substrate (glucose), $C^0_{BL,PS}$ across the biofilm versus time.

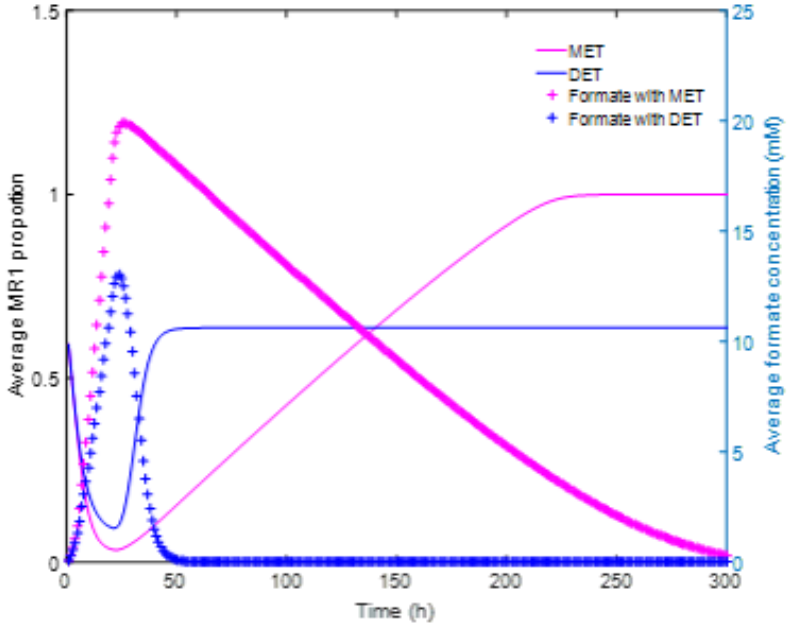

Figure A.2 Average MR1 proportion and formate concentration in the biofilm with two AEETs when $C^0_{BL,PS}$ is 20 mM.

V. Effect of seeding ratio (MR1:*E. coli*) (batch)

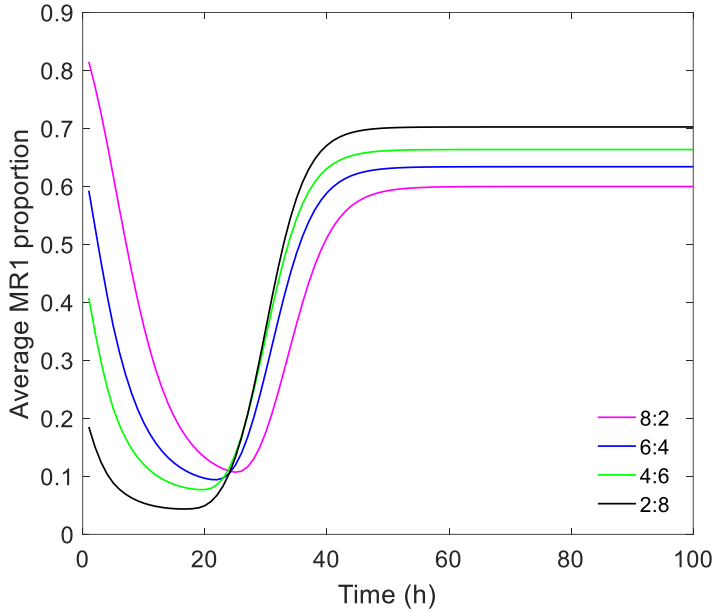

Figure A.3 Average MR1 proportion within the biofilm during the batch with DET at different values of seeding ratio.

VI. Effect of external resistance, R_{ext} (batch)

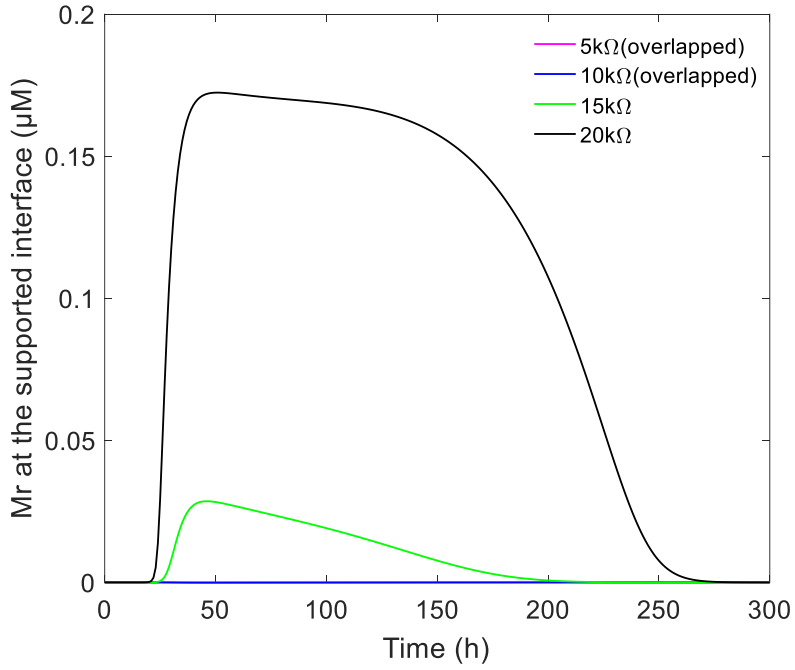

Figure A.4 M_r at the biofilm inner interface concentration (1 μM= 10^{-3} mM).

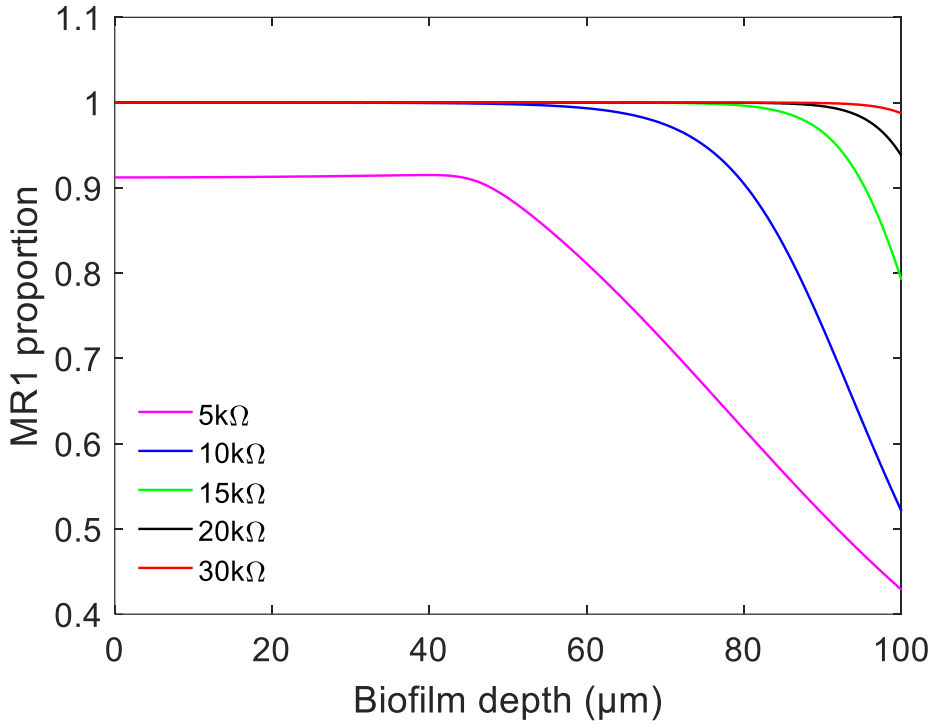

Figure A.5 Batch-end MR1 proportion in the biofilm with DET at different values of external resistance, R_{ext}.

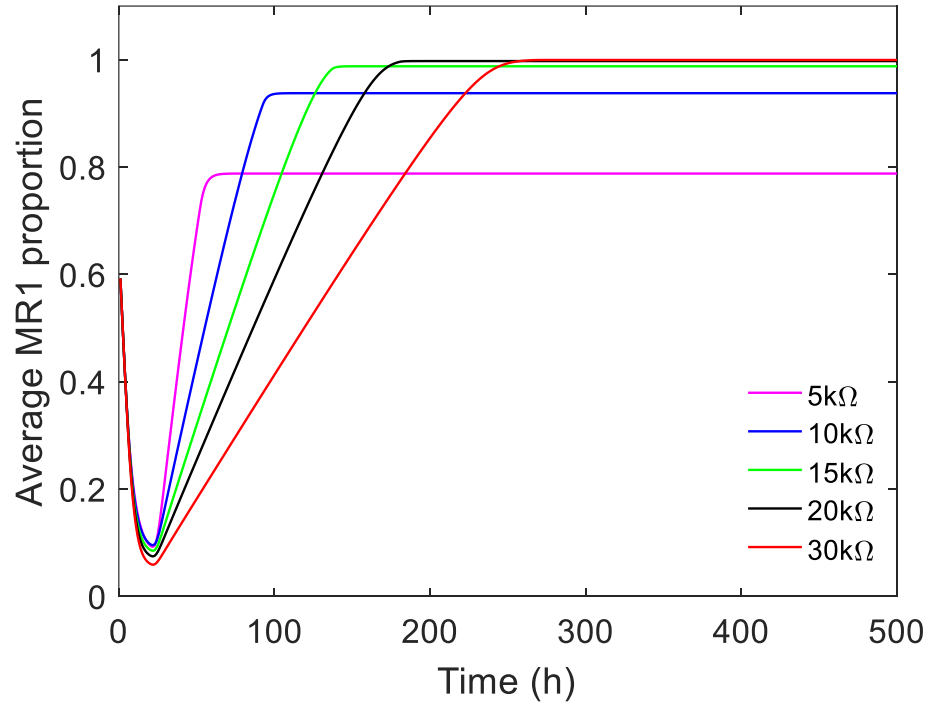

Figure A.6 Average MR1 proportion across the biofilm along time with DET at different values of external resistance, R_{ext}.

VII. Effect of initial concentration of the oxidised form of the mediator in the bulk liquid, $C^0_{BL,Mo}$ (batch)

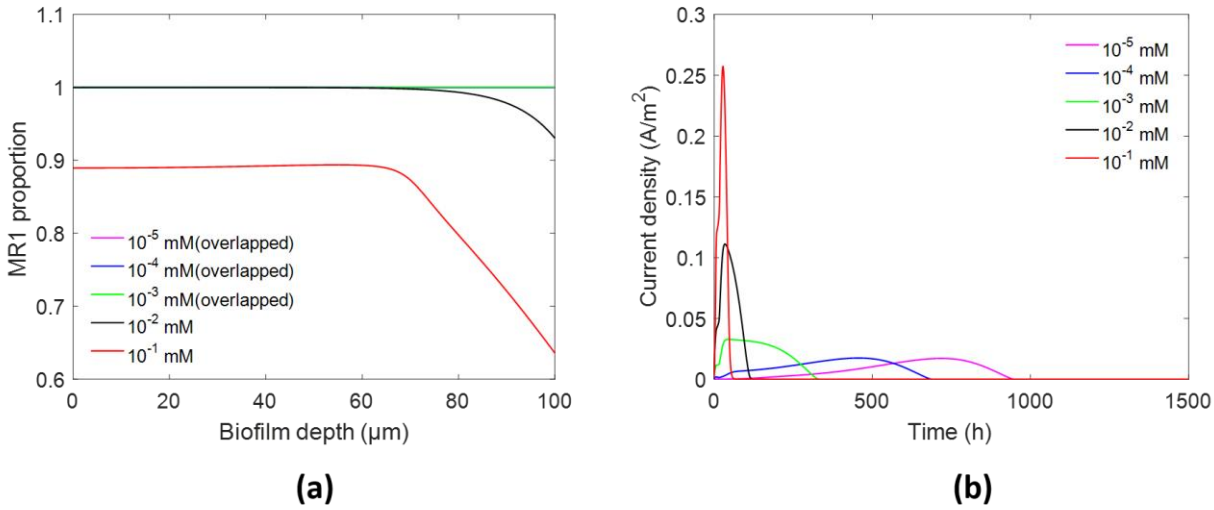

Figure A.7 Model outputs of the batch MFC with MET at different values of initial concentrations of the oxidised form of the mediator in the bulk liquid, $C^0_{BL,Mo}$. (a) batch-end MR1 proportion; (b) current density profile.

VIII. Effect of flowrate, q_f (continuous)

When the biofilm reaches a steady state, Eq. (3.12) becomes:

$$\frac{\partial v}{\partial x} X_{FB} = R_{F,FB} \tag{A.9}$$

$$\frac{\partial v}{\partial x} X_{EAB} = R_{F,EAB} \tag{A.10}$$

Based on Eq. (3.13), the two equations above can be re-written to:

$$\frac{R_{F,FB} + R_{F,EAB}}{\rho_F} X_{FB} = R_{F,FB} \tag{A.11}$$

$$\frac{R_{F,FB} + R_{F,EAB}}{\rho_F} X_{EAB} = R_{F,EAB} \tag{A.12}$$

The following relationship between growth rate and biomass proportion in the biofilm is then obtained:

$$\frac{R_{F,FB}}{R_{F,EAB}} = \frac{X_{FB}}{X_{EAB}} \quad \text{(A.13)}$$

Separately from the fact that growth rate (R) is the product of specific growth rate (μ) and biomass concentration (X):

$$\frac{R_{F,FB}}{R_{F,EAB}} = \frac{\mu_{FB}X_{FB}}{\mu_{EAB}X_{EAB}} \quad \text{(A.14)}$$

Together, these lead to the relationship between the specific growth rates of the two species in an unvaried distribution steady-state biofilm:

$$\frac{\mu_{FB}}{\mu_{EAB}^{M}} = 1 \text{ (with MET)} \quad \text{(A.15)}$$

$$\frac{\mu_{FB}}{\mu_{EAB}^{C}} = 1 \text{ (with DET)} \quad \text{(A.16)}$$

IX. Key simulation results

Table A.3 Summary of key simulation results.*

*Results are described in correspondence to the increase of each controlled parameter, unless stated otherwise.

(a) Simulation results of the batch mode.

Controlled parameter	**AEET mechanism**	
	MET	**DET**
$C_{BL,PS}^{0}$	***Biofilm**:* transferring from 'MR1-*E.coli* co-existing' to 'MR1-only', because of the less restricted growth of MR1 and a longer period of formate availability. ***Current**:* overall higher current density due to improved overall growth of MR1, and longer period of current generation.	***Biofilm**:* always maintaining the co-existence, resulting from the combined effect of stronger and more even growth of MR1 across the biofilm and faster formate exhaustion (hence shorter period available for MR1 to expand). Overall MR1 fraction increases and then drops with $C_{BL,PS}^{0}$, due to the shift in the comparative benefit of higher $C_{BL,PS}^{0}$ to the two species.

		***Current**:* Overall current density benefiting from the increase in $C_{BL,PS}^{0}$ until becoming limited by electrical potential.
Seeding ratio (MR1: *E. coli*)	***Biofilm**:* influence visible only at lower $C_{BL,PS}^{0}$, where initial "head start" of MR1 is retained. ***Current**:* positively affecting the maximum current density thanks to initial higher fraction of MR1.	***Biofilm**:* inversely affecting the batch-end MR1 occupation of the biofilm, due to the 'over' consumption of formate by a larger initial population of MR1. ***Current**:* leading to a higher level of current density initially and then transiting to a lower level, reflecting the dynamics in consumption rate and availability of formate during the batch.
L_F^{max}	***Biofilm**:* shifting from 'MR1-only' to 'MR1-*E.coli* co-existing' due to the increased diffusion resistance to formate and M_o. ***Current**:* densities almost identical but with apparent early-stage dipping in thinner biofilms, which is due to longer *E. coli* repulsion to MR1 in that stage.	***Biofilm**:* co-existence always predicted, but like with MET a thicker biofilm tending to have less MR1, due to increased resistance to current (causing lower electrical potential) and to formate diffusion. ***Current**:* similar to MET, but with longer initial dipping due to greater formate depletion and hence weaker competitiveness of MR1 in that period.
R_{ext}	***Biofilm**:* insignificant impact. ***Current**:* insignificant impact when R_{ext} is low due to the cancellation between the opposite effects of Mr concentration and electrical potential at the anode surface. When R_{ext} exceeds a certain level, further increase causes noticeable reduction of current density as the impact of lower potential outweighs that of higher Mr concentration.	***Biofilm**:* shifting from 'MR1-*E. coli* co-existing' to 'MR1-only', as the reduced specific growth rate of MR1 at a higher resistance allows it to grow for a longer period which helps to expand its occupation. ***Current**:* slower but longer growth of MR1 means a lower maximum current density and a longer period of current generation.

$C^0_{BL,Mo}$	***Biofilm:*** shifting from 'MR1-only' to 'MR1-*E. coli* co-existing', resulting from the shift in the trade-off between MR1's growth and formate exhaustion. ***Current:*** Higher maximum current density and shorter batch obtained in the system with higher M_o, in line with the improved presence of MR1 in the biofilm.	N/A

(b) Simulation results of the continuous mode.

Controlled parameter	**AEET mechanism**	
	MET	**DET**
$C^0_{BL,PS}$ **Seeding ratio (MR1: *E. coli*)**	No impact	No impact
q_f	***Biofilm***: fraction of *E. coli* increasing, eventually changing from 'MR1-*E.coli* co-existing' to '*E.coli*-only', resulting from the trade-off between substrate supply and dilution impact with the latter being more prominent. ***Current***: current density increasing initially and then decreasing, as the dominance shifts from substrate supply to dilution impact.	***Biofilm:*** Similar to MET, with a special case during the transition of the biofilm composition from co-existence to *E. coli* only, where fractions of the two species are invariant across the biofilm as the consequence of their identical specific growth rates. ***Current***: Similar to MET.
$C_{in,PS}$	***Biofilm***: fraction of *E. coli* increasing, eventually changing from 'MR1-*E.coli* co-existing' to '*E.coli*-only', resulting from the reduced restriction to *E.coli* growth by	***Biofilm***: *E.coli* repelling MR1 increasingly and then stabilised at a fraction with MR1 co-existing, as the specific growth rates of two species become identical.

	glucose and the increased restriction to MR1 growth by M_o. ***Current***: current density increasing first as the greater supply of the substrate plays a more dominant role, then decreasing following the decline of the fraction of MR1 in the biofilm.	***Current***: substrate supply playing a dominant role for current generation, with current density increasing until it reaches a saturated level.
L_F^{max}	***Biofilm***: MR1 proportion increasing, caused by the larger negative impact of glucose diffusion resistance on *E. coli* growth, however with a reducing extent as the negative impact of lower formate supply on MR1 becomes increasingly significant. ***Current***: current density increasing following (and in the same fashion of) the increase of MR1 in the biofilm.	***Biofilm***: MR1 proportion increasing similarly to MET. ***Current***: Current density increasing similarly to MET when the conductivity of the biofilm is relatively high, as the potential is affected insignificantly by the increase of biofilm thickness. As the conductivity drops, the influence on potential becomes more prominent and changes the combined effect of increased MR1 proportion and reduced specific growth rate of MR1. This first leads to an increase-then-decline trend of current density as the thickness increases, with further drops in conductivity resulting in a decline-then-flat trend.
$C_{BL,Mo}^0$	Affecting the steady-state biofilm composition at certain levels of inlet glucose concentration.	N/A

References

(1) Philip S. Stewart. Diffusion in Biofilm. *J. Bacteriol.* **2003**, *185* (5), 1485–1491.

(2) Renslow, R.; Babauta, J.; Kuprat, A.; Schenk, J.; Ivory, C.; Fredrickson, J.; Beyenal, H. Modeling Biofilms with Dual Extracellular Electron Transfer Mechanisms. *Phys. Chem.*

Chem. Phys. **2013**, *15* (44), 19262–19283.

(3) Wang, V. B.; Sivakumar, K.; Yang, L.; Zhang, Q.; Kjelleberg, S.; Loo, S. C. J.; Cao, B. Metabolite-Enabled Mutualistic Interaction between Shewanella Oneidensis and Escherichia Coli in a Co-Culture Using an Electrode as Electron Acceptor. *Sci. Rep.* **2015**, *5*, 1–11.

(4) Picioreanu, C.; Head, I. M.; Katuri, K. P.; van Loosdrecht, M. C. M.; Scott, K. A Computational Model for Biofilm-Based Microbial Fuel Cells. *Water Res.* **2007**, *41* (13), 2921–2940.

(5) Min Wang, Zhenhua Yan, Baoxu Huang, Jinsheng Zhao, R. L. Electricity Generation by Microbial Fuel Cells Fuelled with Enteromorpha Prolifera Hydrolysis. *Int. J. Electrochem. Sci.* **2013**, *8*, 2104–2111.

(6) Fan, Y.; Sharbrough, E.; Liu, H. Quantification of the Internal Resistance Distribution of Microbial Fuel Cells. *Environ. Sci. Technol.* **2008**, *42*, 8101–8107.

(7) Luo, S.; Guo, W.; Nealson, K. H.; Feng, X.; He, Z. 13C Pathway Analysis for the Role of Formate in Electricity Generation by Shewanella Oneidensis MR-1 Using Lactate in Microbial Fuel Cells. *Sci. Rep.* **2016**, *6* (20941).

(8) Varma, A.; Boesch, B. W.; Palsson, B. O. Stoichiometric Interpretation of Escherichia Coli Glucose Catabolism under Various Oxygenation Rates. *Appl. Environ. Microbiol.* **1993**, *59* (8), 2465–2473.

(9) Okamoto, A.; Hashimoto, K.; Nealson, K. H.; Nakamura, R. Rate Enhancement of Bacterial Extracellular Electron Transport Involves Bound Flavin Semiquinones. *Proc. Natl. Acad. Sci.* **2013**, *110* (19), 7856–7861.

(10) Hegewald, E.; Knorre, W. A. Kinetics of Growth and Substrate Consumption of Escherichia Coli ML 30 on Two Carbon Sources. *Z. Allg. Mikrobiol.* **1978**, *18* (6), 415–426.

(11) Owens, J. D.; Legan, J. D. Determination of the Monod Substrate Saturation Constant for Microbial Growth. *FEMS Microbiol. Rev.* **1987**, *46*, 419–432.

(12) Canstein, H. Von; Ogawa, J.; Shimizu, S.; Lloyd, J. R. Secretion of Flavins by Shewanella Species and Their Role in Extracellular Electron Transfer. *Appl. Environ. Microbiol.* **2008**, *74* (3), 615–623.

(13) Yinjie J. Tang, Adam L. Meadows, J. D. K. A Kinetic Model Describing Shewanella Oneidensis MR-1 Growth, Substrate Consumption, and Product Secretion. *Biotechnol. Bioeng.* **2007**, *96* (1), 125–133.

(14) Kyoung Sin Ro, J. B. N. Biofilm Density for Biological Fluidized Beds. *Res. J. water Pollut. Control Fed.* **1991**, *63* (5), 815–818.

(15) Malvankar, N. S.; Lau, J.; Nevin, K. P.; Franks, A. E.; Tuominen, M. T.; Lovley, D. R. Electrical Conductivity in a Mixed-Species Biofilm. *Appl. Environ. Microbiol.* **2012**, *78* (16), 5967–5971.

(16) Li, C.; Lesnik, K. L.; Fan, Y.; Liu, H. Redox Conductivity of Current-Producing Mixed Species Biofilms. *PLoS One* **2016**, *11* (5), e0155247.

(17) Ksenzhek, O. S.; Petrova, S. A. Electrochemical Properties of Flavins in Aqueous Solutions. *Bioelectrochemistry Bioenerg.* **1983**, *11*, 105–127.

(18) Bandarenka, A. S.; Ventosa, E.; Maljusch, A.; Masa, J.; Schuhmann, W. Techniques and Methodologies in Modern Electrocatalysis: Evaluation of Activity, Selectivity and Stability of Catalytic Materials. *Analyst* **2014**, *139*, 1274–1291.

(19) Kane, A. L.; Brutinel, E. D.; Joo, H.; Maysonet, R.; Vandrisse, C. M.; Kotloski, N. J.; Gralnick, J. A. Formate Metabolism in Shewanella Oneidensis Generates Proton Motive Force and Prevents Growth without an Electron Acceptor. *J. Bacteriol.* **2016**, *198* (8), 1337–1346.

(20) Kyu, J.; Mayer, F.; Gyun, S.; Müller, V. Energy Conservation by Oxidation of Formate to Carbon Dioxide and Hydrogen via a Sodium Ion Current in a Hyperthermophilic Archaeon. *Proc. Natl. Acad. Sci.* **2014**, *111* (31), 11497–11502.

(21) Smolke, C. *The Metabolic Pathway Engineering Handbook: Fundamentals*; CRC Press, 2009.

(22) Zhang, T. C.; Bishop, P. L. Density, Porosity, and Pore Structure of Biofilms. *Water Res.* **1994**, *28* (11), 2267–2277.

(23) Hu, M.; Zhang, T. C.; Stansbury, J.; Neal, J.; Garboczi, E. J. Determination of Porosity and Thickness of Biofilm Attached on Irregular-Shaped Media. *J. Environ. Eng.* **2013**, *139* (7), 923–931.

(24) Tang, Y. J.; Meadows, A. L.; Kirby, J.; Keasling, J. D. Anaerobic Central Metabolic Pathways in Shewanella Oneidensis MR-1 Reinterpreted in the Light of Isotopic Metabolite Labeling. *J. Bacteriol.* **2007**, *189* (3), 894–901.

(25) Marcus, A. K.; Torres, C. I.; Rittmann, B. E. Conduction-Based Modeling of the Biofilm Anode of a Microbial Fuel Cell. *Biotechnol. Bioeng.* **2007**, *98* (6), 1171–1182.

(26) Whitman, W. B.; Coleman, D. C.; Wiebe, W. J. Prokaryotes: The Unseen Majority. *Proc. Natl. Acad. Sci. U. S. A.* **1998**, *95* (12), 6578–6583.

Appendix B

I. Source terms in the biofilm

Table B.1 Net production rate of the soluble components in the biofilm.

Soluble components, j	Biotic reactions, $R_{B,j}$	Homogenous reactions, $R_{H,j}$	Electrochemical reactions, $R_{E,j}$
CH_3COO^- (Ac^-)	–	R_{H,Ac^-}	–
$H_2PO_4^-$	–	$R_{H,H_2PO_4^-}$	–
PO_4^{3-}	–	$R_{H,PO_4^{3-}}$	–
CO_3^{2-}	–	$R_{H,CO_3^{2-}}$	–
CH_3COOH (Ac)	$R_{B,Ac}$	$R_{H,Ac}$	–
CO_2(aq)	$R_{B,CO_2(aq)}$	$R_{H,CO_2(aq)}$	–
HPO_4^{2-}	–	$R_{H,HPO_4^{2-}}$	–
H^+	R_{B,H^+}	R_{H,H^+}	R_{E,H^+}
H_2(aq)	$R_{B,H_2(aq)}$	–	$R_{E,H_2(aq)}$
HCO_3^-	–	R_{H,HCO_3^-}	–
OH^-	–	R_{H,OH^-}	R_{E,OH^-}

II. Parameters

Table B.2 Key physicochemical parameters in the model.

	Value	Reference
***Soluble components**, j*		
Relative diffusion coefficient for CH_3COOH (Ac), f_{Ac}	0.25	[1]

Relative diffusion coefficient for the species other than CH_3COOH (Ac), $f_{j\neq Ac}$	0.8	2–4
Thickness of the liquid boundary layer, L_{LBL}	1×10^{-5} m	5,6
Biomass, i		
Biofilm thickness, L_F	2.5×10^{-5} m	7
Death coefficient for active biomass, b_{dea}	$0.05/\text{day}$	3
Density of active acetogens, ρ_A	28 kg m^{-3}	8
Density of inactive acetogens, ρ_I	48 kg m^{-3}	8
Electrons required for the acetogens growth with CDET, n	$Y^C_{X_A/Ac}\gamma_{Ac} + \gamma_{X_A}$	Calculated
Half-saturation constants for CO_2, M_{CO_2}	2×10^{-5} M	3
Half-saturation constants for H_2, M_{H_2}	10^{-6} M	9
Initial concentration for active biomass, X_A^0	20 kg m^{-3}	Assumed
Initial concentration for inactive biomass, X_I^0	0 kg m^{-3}	Assumed[10]
Maximal value of pH for acetogen growth, pH^{max}	8.0	10
Minimal value of pH for acetogen growth, pH^{min}	5.0	10
Optimal value of pH for acetogen growth, pH_{opt}	6.0	10
Microbial growth stoichiometry		
Degree of reduction for CH_3COOH (Ac), γ_{Ac}	+8	11
Degree of reduction for H^+, γ_{H^+}	0	11
Degree of reduction for H_2, γ_{H_2}	+2	11
Degree of reduction for H_2O, γ_{H_2O}	0	11
Degree of reduction for $CH_{1.8}O_{0.5}N_{0.2}$ (X_A), γ_{X_A}	+4.2	11
Degree of reduction for CO_2, γ_{CO_2}	0	11

Degree of reduction for NH_4^+, $\gamma_{NH_4^+}$	0	[11]
Factor of reduction to $Y_{H_2/X_A}^{M,max}$, ξ	0.3	Assumed
Gibbs energy of CH_3COOH (Ac) formation under standard condition, $\Delta G_{f,Ac}^{01}$	-94.7 kcal mol^{-1}	[12]
Gibbs energy of H_2 formation under standard condition, $\Delta G_{f,H_2}^{01}$	0 kJ mol^{-1}	[11]
Gibbs energy of H_2O formation under standard condition, $\Delta G_{f,H_2O}^{01}$	-237.18 kJ mol^{-1}	[11]
Gibbs energy of CO_2 formation under standard condition, $\Delta G_{f,CO_2}^{01}$	-394.359 kJ mol^{-1}	[11]
Stoichiometry for CH_3COOH (Ac) in the autotrophic growth process with CDET, $Y_{X_A/Ac}^{C}$	$0.1Y_{X_A/Ac}^{M}$	Assumed
Stoichiometry for H^+ in the autotrophic growth process with CDET, Y_{X_A/H^+}^{C}	0.2	Calculated
Stoichiometry for CO_2 in the autotrophic growth process with CDET, Y_{X_A/CO_2}^{C}	$-2Y_{X_A/Ac}^{C} - 1$	Calculated
Gas-liquid mass transfer		
Reference temperature, T^{ref}	298.15 K	[13]
Specific gas-liquid interfacial area, a_{gl}	29 m^{-1}	[10,14] Calculated
Term of $\frac{-\Delta_{sol}H}{R_g}$ in the Eq. (4.21)	2400 K	[13]
The referenced Henry's constant for CO_2 in the pure water, $H_{CO_2}^{ref}$	29 atm M^{-1}	[13]
Homogeneous reactions		
Change of entropy for the reaction (R4.2), $\Delta S_{HR4.2}$	-96.31 J mol^{-1}K^{-1}	[15–17]

Change of entropy for the reaction (R4.3), $\Delta S_{HR4.3}$	$-148.1\ \mathrm{J\ mol^{-1}K^{-1}}$	15–17
Change of entropy for the reaction (R4.9), $\Delta S_{HR4.9}$	$-80.66\ \mathrm{J\ mol^{-1}K^{-1}}$	15,16
Change of heat for the reaction (R4.2), $\Delta H_{HR4.2}$	$7.64\ \mathrm{kJ\ mol^{-1}}$	15–17
Change of heat for the reaction (R4.3), $\Delta H_{HR4.3}$	$14.85\ \mathrm{kJ\ mol^{-1}}$	15–17
Change of heat for the reaction (R4.9), $\Delta H_{HR4.9}$	$55.84\ \mathrm{kJ\ mol^{-1}}$	15,16
Equilibrium constant for the homogeneous reaction (R4.4), $K_{HR4.4}$	$K_{HR4.2}/K_{Hw}$	15,16,18
Equilibrium constant for the homogeneous reaction (R4.5), $K_{HR4.5}$	$K_{HR4.3}/K_{Hw}$	15,16,18
Equilibrium constant for the homogeneous reaction (R4.6), $K_{HR4.6}$	$1.85 \times 10^{-5}\ \mathrm{M}$	19,20
Equilibrium constant for the homogeneous reaction (R4.7), $K_{HR4.7}$	$10^{-7.21}\ \mathrm{M}$	21,22
Equilibrium constant for the homogeneous reaction (R4.8), $K_{HR4.8}$	$10^{-12.32}\ \mathrm{M}$	21–23
Equilibrium constant for the homogeneous reaction (RB.6), $K_{HRB.6}$	$1.58 \times 10^{-7}\ \mathrm{M}$	21
Equilibrium constant for the homogeneous reaction (RB.7), $K_{HRB.7}$	$2.23 \times 10^{-2}\ \mathrm{M}$	21
Forward rate constant for the reaction (R4.2), $k_{HR4.2}$	$exp\left(1246.98 - \frac{6.19 \times 10^{4}}{T} - 183\ ln(T)\right)\ \mathrm{s^{-1}}$	16,24
Forward rate constant for the reaction (R4.3), $k_{HR4.3}$	$59.44\ \mathrm{s^{-1}}$	16,1823
Forward rate constant for the reaction (R4.4), $k_{HR4.4}$	$2.23 \times 10^{3}\ \mathrm{M^{-1}s^{-1}}$	15,16,23

Forward rate constant for the reaction (R4.5), $k_{HR4.5}$	$6 \times 10^9\ \mathrm{M^{-1}s^{-1}}$	15,16,23
Forward rate constant for the reaction (R4.6), $k_{HR4.6}$	$1 \times 10^5\ \mathrm{s^{-1}}$	22
Forward rate constant for the reaction (R4.7), $k_{HR4.7}$	$1 \times 10^4\ \mathrm{s^{-1}}$	22
Forward rate constant for the reaction (R4.8), $k_{HR4.8}$	$1 \times 10^{-2}\ \mathrm{s^{-1}}$	22
Forward rate constant for the reaction (R4.9), $k_{HR4.9}$	$2.40 \times 10^{-5}\ \mathrm{M\ s^{-1}}$	16
Electrode kinetics		
Apparent activation energy for the HER (pH $\leq$ 7), E^a_{HER}	$(83 + \mathrm{pH})\ \mathrm{kJ\ mol^{-1}}$	15
Cathodic transfer coefficient for the HER (pH $>$ 7), α^b_{HER}	0.36	18
Cathodic transfer coefficient for the HER (pH $\leq$ 7), α^a_{HER}	0.44	15
Effective biofilm conductivity, k_s^{eff}	$0.5\ \mathrm{mS/cm}$	3,10
Equilibrium potential for the HER (pH $>$ 7) in the reference condition and operating temperature, $\varphi^{b,ref}_{eq,HER}$	-0.83 V vs SHE	25–27
Equilibrium potential for the HER (pH $\leq$ 7) in the reference condition and operating temperature, $\varphi^{a,ref}_{eq,HER}$	0 V vs SHE	15
Exchange current density for the HER (pH $>$ 7), $i^{b,ref}_{o,HER}$	$1.16 \times 10^{-6}\ \mathrm{mA\ cm^{-2}}$	18
Exchange current density for the HER (pH $\leq$ 7), $i^{a,ref}_{o,HER}$	$A^a_{HER}\ exp\left(-\frac{E^a_{HER}}{R_g T}\right)$	15
Potential corresponding to the half maximum specific growth rate, φ_{M_c}	-0.6 V vs SHE	Assumed

Pre-exponential factor for the HER (pH $\leq$ 7), A_{HER}^{a}	2.77×10^{19} mA cm^{-2}	15
Reaction order with respect to H^+, ψ	0 (pH $>$ 7) or 2 (pH $\leq$ 7)	
Reference concentration of H^+, C_{F,H^+}^{ref}	1 M	15
Specific surface area for the biofilm matrix, a_V	100 m^{-1}	14
Universal Parameter		
Faraday constant, F	96485 C mol^{-1}	
Ideal gas constant, R_g	8.314 J K^{-1} mol^{-1}	
Molar weight for CO_2, W_{CO_2}	4.4×10^{-2} kg mol^{-1}	
Molar weight for CO_3^{2-}, $W_{CO_3^{2-}}$	6.0×10^{-2} kg mol^{-1}	
Molar weight for OH^- , W_{OH}	1.7×10^{-2} kg mol^{-1}	
Molar weight for $CH_{1.8}O_{0.5}N_{0.2}$ (X_A), W_A	2.46×10^{-2} kg mol^{-1}	
Molar weight for HCO_3^-, $W_{HCO_3^-}$	6.1×10^{-2} kg mol^{-1}	
Operational Setting Parameters		
Applied cathode potential, V_{app}	-1.0 V vs Ag/AgCl	10
Operating temperature, T	308 K	10
Design Parameters		
Area of cathode substratum, A_F	4.9×10^{-4} m^2	10
Volume of the bulk liquid phase, V_{BL}	4×10^{-5} m^3	10
Volume of the gas phase, V_g	1.1×10^{-4} m^3	10

III. Diffusion coefficients for the soluble component, j, in pure water, $D_{w,j}$

The diffusion coefficients for our interested soluble components in pure water at the absolute temperature of T(K) are listed as follows:

Table B.3 The diffusion coefficients for our interested soluble components in pure water.

Soluble component, j	Diffusion coefficient in pure water, $D_{w,j}$	Unit	Reference
CH_3COO^- (Ac^-)	1.43×10^{-5}	cm^2s^{-1}	Assumed[28]
$H_2PO_4^-$	$1 \times 10^{-6}(12.14 - 8.161C_{H_2PO_4^-}^{0.5} + 12.761C_{H_2PO_4^-} - 14.996C_{H_2PO_4^-}^{1.5} + 5.683C_{H_2PO_4^-}^{2})$	cm^2s^{-1}	[29]
PO_4^{3-}	8.0×10^{-10}	m^2s^{-1}	[21]
CH_3COOH (Ac)	1.43×10^{-5}	cm^2s^{-1}	[28]
CO_2(aq)	$2.35 \times 10^{-6} exp\ (\frac{-2119}{T})$	m^2s^{-1}	[30]
HPO_4^{2-}	$1 \times 10^{-6}(12.83 - 11.829C_{HPO_4^{2-}}^{0.5} + 12.870C_{HPO_4^{2-}} - 7.819C_{HPO_4^{2-}}^{1.5} + 1.703C_{HPO_4^{2-}}^{2})$	cm^2s^{-1}	[29]
H^+	$1.56 \times 10^{-10}(T - 273.15) + 5.49 \times 10^{-9}$	m^2s^{-1}	[16]
H_2(aq)	$\frac{2.29 \times 10^{-11}T}{\mu_w^{0.819}}$	m^2s^{-1}	[16]
OH^-	$4.52 \times 10^{-4} exp\ (-1618(\frac{1}{T} + \frac{1}{273.15}))$	m^2s^{-1}	[16]
CO_3^{2-}	$5.447 \times 10^{-9}\left(\frac{T}{210.265} - 1\right)^{2.193}$	m^2s^{-1}	[15,16,31]
HCO_3^-	$7.016 \times 10^{-9}\left(\frac{T}{204.028} - 1\right)^{2.3942}$	m^2s^{-1}	[15,16,31]

where μ_w (centipoise, cP) is the dynamic viscosity of water, which is also the function of T(K)[16]:

$$\mu_w = 10^{(\frac{247.8}{T-140} - 1.6173)} \quad \text{(B.1)}$$

IV. The stoichiometry for autotrophic growth with CMET

The autotrophic anabolic (or called 'biomass synthesis') reaction for the production of 1 C mol biomass is expressed as follows[11]:

$$e\mathrm{CO_2} + a\mathrm{H_2} + b\mathrm{NH_4^+} + c\mathrm{H^+} + d\mathrm{H_2O} + \mathrm{CH_{1.8}O_{0.5}N_{0.2}}\ (\mathrm{X_A}) \qquad \text{(RB.1)}$$

These five stoichiometry coefficients can be solved by the balances for the elemental, charge and degree of reduction, $\gamma_{i(j)}$[11]:

Degree of reduction	
	$\mathrm{a}\gamma_{H_2} + \gamma_{X_A} = 0$
Elemental balances	
C-balance	$e + 1 = 0$
H-balance	$2\mathrm{a} + 4\mathrm{b} + \mathrm{c} + 2\mathrm{d} + 1.8 = 0$
O-balance	$2e + d + 0.5 = 0$
N-balance	$b + 0.2 = 0$

After calculation, the reaction (RB.1) could be re-written as:

$$-\mathrm{CO_2} - 2.1\mathrm{H_2} - 0.2\mathrm{NH_4^+} + 0.2\mathrm{H^+} + 1.5\mathrm{H_2O} + \mathrm{CH_{1.8}O_{0.5}N_{0.2}}(\mathrm{X_A}) \qquad \text{(RB.2)}$$

Charge balance can be applied to check the calculated results.

The anabolic reactions for biomass synthesis are normally endergonic, meaning that energy is required. The catabolic reactions play the role of energy supplement by performing redox reactions between an electron donor (ED) and an electron acceptor (EA). Hence, a certain amount of EA is needed for catabolism. A part of the energy, which is generated by the catabolism, would be utilised to initiate the anabolic reactions. The Gibbs energy released by catabolism varies with different EA/ED couples and specific operating conditions (including temperature, pH, species concentrations, pressure, etc.)[11].

Analogous to the anabolic reaction, the catabolic reaction is first constructed. Note that the catabolic reaction is written on the basis of 1 mol ED consumed[11]:

$$-\mathrm{H_2(ED)} + f\mathrm{CO_2(EA)} + g\mathrm{CH_3COOH\ (Ac)} + h\mathrm{H_2O} \qquad \text{(RB.3)}$$

Perform the following balances for the reaction (RB.3):

Degree of reduction	
	$-\gamma_{H_2} + g\gamma_{Ac} = 0$

Elemental balances

C-balance	$f + 2g = 0$
H-balance	$-2 + 4g + 2h = 0$

After calculation: $f = -0.5; g = 0.25; h = 0.5$. O-balance is used to check the above calculations. Therefore, the complete catabolic reaction is expressed as:

$$-\mathrm{H_2(ED)} - 0.5\mathrm{CO_2(EA)} + 0.25\mathrm{CH_3COOH\ (Ac)} + 0.5\mathrm{H_2O}$$

or (RB.4)

$$\mathrm{H_2(ED)} + 0.5\mathrm{CO_2(EA)} \rightarrow 0.25\mathrm{CH_3COOH\ (Ac)} + 0.5\mathrm{H_2O}$$

Based on the reaction (RB.4) above and the Gibbs energy of formation of the species (i) under standard condition ($\Delta G_{f,i}^{01}$), it is easy to calculate the catabolic energy under the standard conditions(ΔG_{cat}^{01} [11]):

$$\begin{aligned}\Delta G_{cat}^{M} = \Delta G_{cat}^{01} &= -\Delta G_{R}^{01} \\ &= -((-1) \times \Delta G_{f,H_2}^{01} + (-0.5) \times \Delta G_{f,CO_2}^{01} + (+0.25) \times \Delta G_{f,Ac}^{01} \\ &\quad + (+0.5)) \times \Delta G_{f,H_2O}^{01}) = 20.47\mathrm{kJ}\end{aligned} \quad \text{(B.2)}$$

note that it is assumed that only the dissolved $\mathrm{H_2(aq)}$ and $\mathrm{CO_2(aq)}$ can be utilised to form the target product (i.e. acetate). Since the operating temperature in our system is 308 K (35 ℃), the effect of temperature on the catabolic energy must be evaluated. It has been illustrated that temperature would only strongly affect the catabolic reactions involving gases[11]. Considering our system, the impact of temperature on catabolic energy released by the reaction (RB.4) could be negligible . Therefore, ΔG_{cat}^{M} (308 K) is treated as identical to ΔG_{cat}^{M}, which is the value that we calculate above.

Therefore, the value of the Gibbs energy, which is calculated by the Eq. (B.2), implies that the consumption of $1\mathrm{mol\ H_2}$ would release 20.47 kJ of catabolic Gibbs energy in our system.

In 1992, Heijnen et al. proposed several simpler equations to calculate the energy requirement for the heterotrophic and autotrophic growth[11]. In our case, $\mathrm{CO_2/H_2}$ is considered as the redox couple:

$$Y_{X_A/G} = 1000\ kJ/\text{Cmol new } X_A \tag{B.3}$$

$Y_{X_A/G}$ represents that 1000 kJ Gibbs energy is needed to generate 1 Cmol new X_A.

Combining Eqs. (B.2) and (B.3), the required amount of H_2 for the production of 1 Cmol new X_A with CMET, which is term as $Y_{X_A/H_2}^{M,cat}$, is obtained:

$$Y_{X_A/H_2}^{M,cat} = \frac{Y_{X_A/G}}{\Delta G_{cat}^{M}} = 48.85\ (\text{mol } H_2/\text{Cmol new } X_A) \tag{B.4}$$

There are two divisions for ED (i.e. H_2) utilisation: (i) the amount of H_2 (i.e. $Y_{X_A/H_2}^{M,an}$), together with carbon and nitrogen source is utilised for anabolism/cell synthesis. During this anabolism process, EA is not compulsory, and the value of $Y_{X_A/H_2}^{M,an}$ is equal to the absolute value of a in the reaction (RB.1); (ii) the amount of H_2 (i.e. $Y_{X_A/H_2}^{M,cat}$) coupled with EA aims to produce energy via catabolism (see Eq. (B.4)). It is assumed that all the released catabolic Gibbs energy would be used for the anabolism only. The maximum biomass yield, $Y_{H_2/X_A}^{M,max}$, which is defined as the amount of Cmol new X_A produced per mol of H_2, is expressed as:

$$\frac{1}{Y_{H_2/X_A}^{M,max}} = Y_{X_A/H_2}^{M,an} + Y_{X_A/H_2}^{M,cat} = 50.95\ (\text{mol } H_2/\text{Cmol new } X_A) \tag{B.5}$$

Cell maintenance is the innate cell-level endogenous process. It aims for maintaining the homeostasis of cells, including but not limited to the reassembly of denatured proteins. These processes need energy input and therefore a proportion of catabolic Gibbs energy, ΔG_{cat}^{M}, should be assigned to these collective maintenance functions[11,32]. If there is no energy assigned to maintenance, biomass yield would reach the maximum value (Y_{H_2/X_A}^{max}). However, this theoretical maximum value is impossible in reality, as maintenance is innate and inevitable[11]. Thus, the apparent/measured biomass yield in the actual experiment (Y_{H_2/X_A}^{M}) would be smaller than $Y_{H_2/X_A}^{M,max}$[11]. As a simplifying assumption, all the factors are lumped together; and the factor, ξ, is defined to represent the reduction to the $Y_{H_2/X_A}^{M,max}$. Thus, Y_{H_2/X_A}^{M} equls $\xi Y_{H_2/X_A}^{M,max}$.

The complete growth process stoichiometry with cell maintenance can still be obtained through elemental and charge balances[11]. In our case, the general form for acetogens is:

$$-\frac{1}{Y^M_{H_2/X_A}}\mathrm{H_2} + Y^M_{X_A/CO_2}\mathrm{CO_2} + Y^M_{X_A/NH_4^+}\mathrm{NH_4^+} + Y^M_{X_A/H^+}\mathrm{H^+} + \mathrm{CH_{1.8}O_{0.5}N_{0.2}(X_A)} + Y^M_{X_A/Ac}\mathrm{CH_3COOH\ (Ac)} + Y^M_{X_A/H_2O}\mathrm{H_2O} \quad \text{(RB.5)}$$

where:

$$Y^M_{X_A/CO_2} = 0.5\left(-\frac{1}{Y^M_{H_2/X_A}} + 0.1\right);$$

$$Y^M_{X_A/NH_4^+} = -0.2;\ Y^M_{X_A/H^+} = 0.2;$$

$$Y^M_{X_A/Ac} = -0.25\left(-\frac{1}{Y^M_{H_2/X_A}} + 2.1\right)$$

$$Y^M_{X_A/H_2O} = 0.5\left(\frac{1}{Y^M_{H_2/X_A}} + 0.9\right)$$

V. Estimation of the maximum specific growth rate under the optimal condition

As stated in the main text, the maximum specific growth rate under the optimal condition, $\mu^{max}_{A,opt}$, is assumed as a constant regardless of the cathodic electron transfer mechanisms (CEETs). Here we only carry out the theoretical calculations for the acetogens with CMET.

Almost all catabolic Gibbs energy is produced via the electron transportation from ED to EA through the electron transport chain (ETC). The ETC contains the electron-processing proteins that are embedded in the cell membranes. Limited by the area of cell membranes and the amount of ETC proteins, there is a maximal limit for the total amount of electrons transferred per hour per Cmol of total $\mathrm{X_A}$.

According to Heijin's theory[11,33], the maximal biomass specific Gibbs energy production rate, q^{max}_G, can be estimated by coupling the maximal electron transport capacity (i.e. ED's degree of reduction) and the catabolic Gibbs energy released by consuming 1mol ED (see Eq. (B.2)):

$$q^{max}_G = 3exp\left[\frac{-69}{R_g}\left(\frac{1}{T} - \frac{1}{298}\right)\right]\left(\frac{\Delta G^M_{cat}}{\gamma_{H_2}}\right) \quad \text{(B.6)}$$

where R_g is the ideal gas constant; 69 kJ/mol is the energy of activation; γ_{H_2} represents the number of electrons available in the H_2.

As mentioned earlier, cell maintenance should be taken into consideration. Hence, q_G^{max} will be distributed for biomass generation (the first term on the right-had-side, RHS) and cell maintenance (the second term on the RHS):

$$q_G^{max} = Y_{X_A/G}\mu_{A,opt}^{max} + m_G \tag{B.7}$$

where m_G represents kJ Gibbs energy required per hour for 1 Cmol biomass maintenance. It has been reported that the value of m_G is insensitive to cell type and cultivation condition (including EA/ED redox, carbon,nitrogen source, etc). But the temperature does impact m_G, which can be described by[11]:

$$m_G = 4.5exp\left[\frac{-69}{R_g}\left(\frac{1}{T} - \frac{1}{298}\right)\right] \tag{B.8}$$

Combining Eqs. (B.2), (B.3), (B.6), (B.7) and (B.8), the value of $\mu_{A,opt}^{max}$ is obtained, which equals 0.06 h^{-1}.

VI. Overall mass transfer coefficient, K_{GL}

Given our operational condition (i.e. almost base/acid catholyte), it is reasonable to assume the overall gas-liquid mass transfer resistance for CO_2 to be identical to the intrinsic overall CO_2 mass transfer coefficient (without any chemical reactions), K_{GL,CO_2}^0. Additionally, K_{GL,CO_2}^0 is governed by the liquid phase (k_{L,CO_2})[18,34,35] based on the value of CO_2 Henry's constant, H_{CO_2}[34,36].

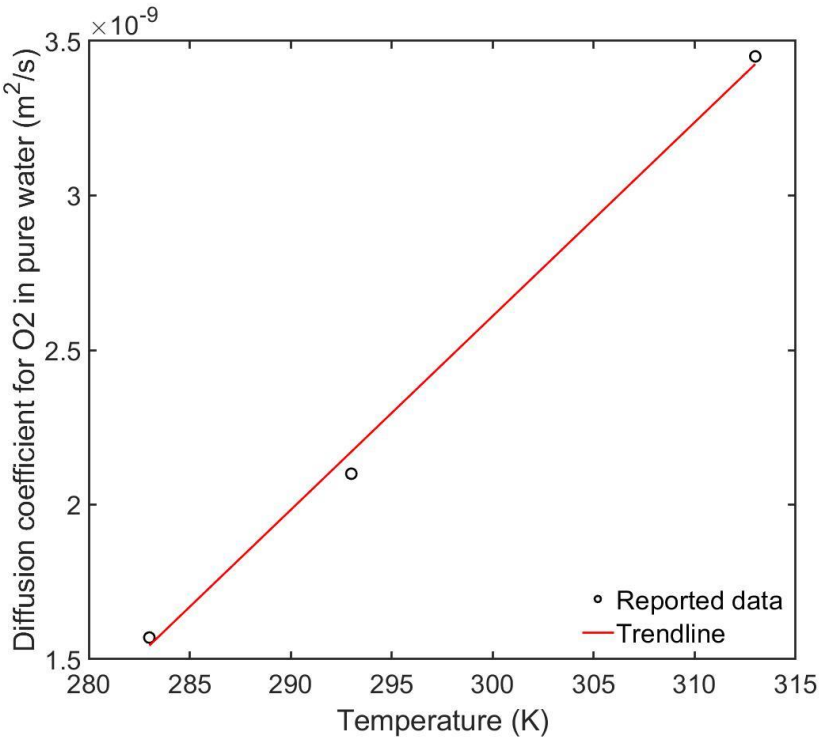

Figure B.1 Diffusion coefficient for O_2 in pure water with respect to temperature.

Two-film theory is commonly adopted for the estimation of k_{L,CO_2}, but it is difficult to find the accurate value for the thickness of a thin film in the literature. Another approach to estimate the value of k_{L,CO_2} is adopted here, which is based on the relationship of the diffusivities between CO_2 and O_2[35,37]:

$$K_{GL,CO_2} = K^0_{GL,CO_2} = k_{L,CO_2} = k_{L,O_2}\left(\frac{D_{W,CO_2(aq)}}{D_{W,O_2(aq)}}\right)^{\zeta} \tag{B.9}$$

where k_{L,O_2} is the liquid-phase specific mass transfer coefficient for O_2; the value of k_{L,O_2} is reported as 0.24 m h^{-1}[37]; $D_{W,O_2(aq)}$ is the diffusion coefficient for O_2 in pure water; ζ is an empirical coefficient ranging from 0.1 to 1[35], which is set as 0.5[37] in our work.

According to the reported values for $D_{W,O_2(aq)}$ with various temperatures[38], we could conclude that the value of $D_{W,O_2(aq)}$ is linearly temperature-dependent, with a slope of 6.27×10^{-11} m^2 s^{-1}(see Figure B.1 and Eq. (B.10)):

$$D_{W,O_2(aq)}\ (\mathrm{m^2\ s^{-1}}) = 6.27 \times 10^{-11} T(\mathrm{K}) - 1.62 \times 10^{-8} \tag{B.10}$$

Therefore, $K_{GL,CO_2} = 0.212\ \text{m h}^{-1} = 5.89 \times 10^{-5}\ \text{m s}^{-1}$.

VII. Initial concentrations (ICs) for the soluble components

It is assumed that all the soluble concentrations are at equilibrium at first (i.e. $t = 0$). According to the experimentally measured data (i.e. pH and the total dissolved inorganic carbon concentration in the catholyte) and the catholyte composition[10], the initial concentrations for all the soluble components can be calculated.

For the systems with the default pH values, we only consider the types of homogeneous reactions under an acidic condition, as the pH was adjusted to < 7 initially[10].

According to (i) the equilibrium homogeneous reactions; (ii) the experimentally measured pH value; (iii) the measured acetate concentration, C^0_{TAc}; (iv) the sum of the initial dissolved inorganic carbon concentration in the catholyte, C^0_{IC}; and (v) the total amount of the initial element of phosphorus (including KH_2PO_4 and K_2HPO_4), C^0_{IP}, the following equations are established[10]:

$$k_{HR4.2}C^0_{B,CO_2(aq)} - \frac{k_{HR4.2}}{K_{HR4.2}}C^0_{B,H^+}C^0_{B,HCO_3^-} = 0 \tag{B.11}$$

$$k_{HR4.3}C^0_{B,HCO_3^-} - \frac{k_{HR4.3}}{K_{HR4.3}}C^0_{B,H^+}C^0_{B,CO_3^{2-}} = 0 \tag{B.12}$$

$$k_{HR4.6}C^0_{B,Ac} - \frac{k_{HR4.6}}{K_{HR4.6}}C^0_{B,H^+}C^0_{B,CH_3COO^-} = 0 \tag{B.13}$$

$$k_{HR4.7}C^0_{B,H_2PO_4^-} - \frac{k_{HR4.7}}{K_{HR4.7}}C^0_{B,H^+}C^0_{B,HPO_4^{2-}} = 0 \tag{B.14}$$

$$k_{HR4.8}C^0_{B,HPO_4^{2-}} - \frac{k_{HR4.8}}{K_{HR4.8}}C^0_{B,H^+}C^0_{B,PO_4^{3-}} = 0 \tag{B.15}$$

$$k_{HR4.9} - \frac{k_{HR4.9}}{K_{HR4.9}}C^0_{B,H^+}C^0_{B,OH^-} = 0 \tag{B.16}$$

$$W_{CO_2(aq)}C^0_{B,CO_2(aq)} + W_{HCO_3^-}C^0_{B,HCO_3^-} + W_{CO_3^{2-}}C^0_{B,CO_3^{2-}} = C^0_{TIC} \tag{B.17}$$

$$C^0_{B,H_2PO_4^-} + C^0_{B,HPO_4^{2-}} + C^0_{B,PO_4^{3-}} = C^0_{TP} \tag{B.18}$$

$$C^0_{B,Ac} + C^0_{B,CH_3COO^-} = C^0_{TAc} \tag{B.19}$$

where $W_{CO_2(aq)}$, $W_{HCO_3^-}$ and $W_{CO_3^{2-}}$ are molecular weight for $CO_2(aq)$, HCO_3^- and CO_3^{2-}, respectively.

It is assumed that the initial concentrations for the soluble component (j) in the biofilm, $C_{F,j}^0$, are identical to the values of $C_{B,j}^0$.

The same calculation procedure would also be applicable to the systems with an initial pH larger than 7. Under this circumstance, the types of homogeneous reactions under an alkaline condition should be considered. Eqs. (B.11) and (B.12) should be substituted by Eqs. (B.20) and (B.21), respectively.

$$k_{HR4.4} C_{B,CO_2(aq)}^0 C_{B,OH^-}^0 - \frac{k_{HR4.4}}{K_{HR4.4}} C_{B,HCO_3^-}^0 = 0 \quad \text{(B.20)}$$

$$k_{HR4.5} C_{B,HCO_3^-}^0 C_{B,OH^-}^0 - \frac{k_{HR4.5}}{K_{HR4.5}} C_{B,CO_3^{2-}}^0 = 0 \quad \text{(B.21)}$$

As for the phosphate ions and hydrogen phosphate ions, their hydrolysis reactions should be considered:

$$HPO_4^{2-} + H_2O \xrightarrow{k_{HRB.6}} H_2PO_4^- + OH^- \quad \text{(RB.6)}$$

$$PO_4^{3-} + H_2O \xrightarrow{k_{HRB.7}} HPO_4^{2-} + OH^- \quad \text{(RB.7)}$$

Corresponding equilibria are written as:

$$k_{HRB.6} C_{B,HPO_4^{2-}}^0 - \frac{k_{HRB.6}}{K_{HRB.6}} C_{B,H_2PO_4^-}^0 C_{B,OH^-}^0 = 0 \quad \text{(B.22)}$$

$$k_{HRB.7} C_{B,PO_4^{3-}}^0 - \frac{k_{HRB.7}}{K_{HRB.7}} C_{B,HPO_4^{2-}}^0 C_{B,OH^-}^0 = 0 \quad \text{(B.23)}$$

VIII. Testing parameter data*

Table B.4 Testing parameter data.

Parameter	Default value	Testing range	Unit
Initial pH	6.7	[5.5: 0.2: 7.5]	N/A
V_{app}	-1.0	$[-1.5, -1.2, -1.0, -0.6, -0.4, -0.2]$	V

L_F	25	$[25, 50, 75, 100]$	μm
a_{gl}	40	$[1 \times 10^{-3}, 1 \times 10^{-2}, 1 \times 10^{-1}, 0.1, 10, 50]$	m^{-1}
a_V	100	$[100: 100: 400]$	m^{-1}

*In all the parametric studies, the initial active biomass concentration, X_A^0, is set as 5 kg m^{-3} and the initial CO_2 partial pressure is set as 1.0 atm.

References

(1) Philip S. Stewart. Diffusion in Biofilm. *J. Bacteriol.* **2003**, *185* (5), 1485–1491.

(2) Horn, H.; C.Hempel, D. Modeling Mass Transfer and Substrate Utilization in the Boundary Layer of Biofilm Systems. *Water Sci. Technol.* **1998**, *37* (4–5), 139–147.

(3) Kazemi, M.; Biria, D.; Rismani-Yazdi, H. Modelling Bio-Electrosynthesis in a Reverse Microbial Fuel Cell to Produce Acetate from CO2 and H2O. *Phys. Chem. Chem. Phys.* **2015**, *17*, 12561–12574.

(4) Wanner, O.; Eberl, H. J.; Morgenroth, E.; Noguera, D. R.; Picioreanu, C.; Rittmann, B. E.; Loosdrecht, M. C. M. van. *Mathematical Modeling of Biofilms*; IWA Task Group on Biofilm Modeling, 2006.

(5) Yang, Z.; Yang, A. Modelling the Impact of Operating Mode and Electron Transfer Mechanism in Microbial Fuel Cells with Two-Species Anodic Biofilm. *Biochem. Eng. J.* **2020**, *158*, 107560.

(6) Picioreanu, C.; Head, I. M.; Katuri, K. P.; van Loosdrecht, M. C. M.; Scott, K. A Computational Model for Biofilm-Based Microbial Fuel Cells. *Water Res.* **2007**, *41* (13), 2921–2940.

(7) Zhao, J.; Feng, K.; Liu, S. H.; Lin, C. W.; Zhang, S.; Li, S.; Li, W.; Chen, J. Kinetics of Biocathodic Electron Transfer in a Bioelectrochemical System Coupled with Chemical Absorption for NO Removal. *Chemosphere* **2020**, *249*, 126095.

(8) Horn, H.; Hempel, D. C. Substrate Utilization and Mass Transfer in an Autotrophic Biofilm System: Experimental Results and Numerical Simulation. *Biotechnol. Bioeng.*

1997, *53* (4), 363–371.

(9) Sakakibara, Y.; Flora, J. R. V.; Suidan, M. T.; Kurodo, M. Modeling of Electrochemically-Activated Denitrifying Biofilms. *Water Res.* **1994**, *28* (5), 1077–1086.

(10) Izadi, P.; Fontmorin, J.; Godain, A.; Yu, E. H.; Head, I. M. Parameters Influencing the Development of Highly Conductive and Efficient Biofilm during Microbial Electrosynthesis: The Importance of Applied Potential and Inorganic Carbon Source. *npj Biofilms Microbiomes* **2020**, *6* (40).

(11) Smolke, C. *The Metabolic Pathway Engineering Handbook: Fundamentals*; CRC Press, 2009.

(12) Fox, R. F. Origin of Life and Energy. In *Encyclopedia of Energy*; Cleveland, C. J., Ed.; Elsevier Science, 2004; pp 781–792.

(13) Sander, R. Compilation of Henry's Law Constants (Version 4.0) for Water as Solvent. *Atmos. Chem. Phys.* **2015**, *15*, 4399–4981.

(14) Batstone, D. J.; Keller, J.; Blackall, L. L. The Influence of Substrate Kinetics on the Microbial Community Structure in Granular Anaerobic Biomass. *Water Res.* **2004**, *38* (6), 1390–1404.

(15) Weng, L. C.; Bell, A. T.; Weber, A. Z. Towards Membrane-Electrode Assembly Systems for CO2 Reduction: A Modeling Study. *Energy Environ. Sci.* **2019**, *12*, 1950–1968.

(16) Abel, A. J.; Clark, D. S. A Comprehensive Modeling Analysis of Formate-mediated Microbial Electrosynthesis. *ChemSusChem* **2020**, *13*.

(17) Ride, D. R. *CRC Handbook of Chemistry and Physics*, 84th ed.; CRC Press, 2004.

(18) Weng, L. C.; Bell, A. T.; Weber, A. Z. Modeling Gas-Diffusion Electrodes for CO2 Reduction. *Phys. Chem. Chem. Phys.* **2018**, *20*, 16973–16984.

(19) James Kendall. The Velocity of the Hydrogen Ion, and a General Dissociation Formula

for Acids. *J. Chem. Soc. Trans.* **1912**, *101*, 1275–1296.

(20) Matemadombo, F.; Puig, S.; Ganigué, R.; Ramírez-García, R.; Batlle-Vilanova, P.; Dolors Balaguer, M.; Colprim, J. Modelling the Simultaneous Production and Separation of Acetic Acid from CO2 Using an Anion Exchange Membrane Microbial Electrosynthesis System. *J. Chem. Technol. Biotechnol.* **2017**, *92*, 1211–1217.

(21) Leaist, D. G. Coupled Diffusion Produced by Hydrolysis of Aqueous Potassium Phosphate. *J. Solution Chem.* **1985**, *14* (10), 709–721.

(22) Shinagawa, T.; Obata, K.; Takanabe, K. Switching of Kinetically Relevant Reactants for the Aqueous Cathodic Process Determined by Mass-Transport Coupled with Protolysis. *ChemCatChem* **2019**, *11*, 5961–5968.

(23) Hashiba, H.; Weng, L. C.; Chen, Y.; Sato, H. K.; Yotsuhashi, S.; Xiang, C.; Weber, A. Z. Effects of Electrolyte Buffer Capacity on Surface Reactant Species and the Reaction Rate of CO2 in Electrochemical CO2 Reduction. *J. Phys. Chem. C* **2018**, *122* (7), 3719–3726.

(24) Schulz, K. G.; Riebesell, U.; Rost, B.; Thoms, S.; Zeebe, R. E. Determination of the Rate Constants for the Carbon Dioxide to Bicarbonate Inter-Conversion in PH-Buffered Seawater Systems. *Mar. Chem.* **2006**, *100*, 53–65.

(25) Li, H.; Oloman, C. Development of a Continuous Reactor for the Electro-Reduction of Carbon Dioxide to Formate - Part 2: Scale-Up. *J. Appl. Electrochem.* **2007**, *37*, 1107–1117.

(26) Jeanty, P.; Scherer, C.; Magori, E.; Wiesner-Fleischer, K.; Hinrichsen, O.; Fleischer, M. Upscaling and Continuous Operation of Electrochemical CO2 to CO Conversion in Aqueous Solutions on Silver Gas Diffusion Electrodes. *J. CO2 Util.* **2018**, *24*, 454–462.

(27) Qiao, J.; Liu, Y.; Zhan, J. *Electrochemical Reduction of Carbon Dioxide: Fundamentals and Technologies*; Taylor & Francis, 2016.

(28) Giraldo-Gomez, E. Kinetics of Anaerobic Treatment: A Critical Review. *Crit. Rev. Environ. Control* **1991**, *21* (5–6), 411–490.

(29) Hatfield, J. D.; Edwards, O. W.; Dunn, R. L. Diffusion Coefficients of Aqueous Solutions of Ammonium and Potassium Orthophosphates at 25°. *J. Phys. Chem.* **1966**, *70* (8), 2555–2561.

(30) Versteeg, G. F.; van Swaal, W. P. M. Solubility and Diffusivity of Acid Gases (CO2, N2O) in Aqueous Alkanolamine Solutions. *J. Chem. Eng. Data* **1988**, *33* (1), 29–34.

(31) Zeebe, R. E. On the Molecular Diffusion Coefficients of Dissolved CO2, HCO3-, and CO32- and Their Dependence on Isotopic Mass. *Geochim. Cosmochim. Acta* **2011**, *75*, 2483–2498.

(32) Hao, X. Di; Wang, Q. L.; Zhu, J. Y.; Van Loosdrecht, M. C. M. Microbiological Endogenous Processes in Biological Wastewater Treatment Systems. *Crit. Rev. Environ. Sci. Technol.* **2010**, *40* (3), 239–265.

(33) J.J. Heijnen. Bioenergetics of Microbial Growth. In *Encyclopedia of Bioprocess Technology: Fermentation, Biocatalysis, and Bioseparation*; John Wiley & Sons: New York, 1999.

(34) A.H.Lincoff;, C. E. C. B. P. E. C. G. J. M. G. *Mass Transfer Coefficients and Henry's Constants for Packed-Tower Air Stripping of Volatile Organics: Measurements and Correlation*; 1985.

(35) Amaral, A.; Gillot, S.; Garrido-Baserba, M.; Filali, A.; Karpinska, A. M.; Plósz, B. G.; de Groot, C.; Bellandi, G.; Nopens, I.; Takács, I.; Lizarralde, I.; Jimenez, J. A.; Fiat, J.; Rieger, L.; Arnell, M.; Andersen, M.; Jeppsson, U.; Rehman, U.; Fayolle, Y.; Amerlinck, Y.; Rosso, D. Modelling Gas–Liquid Mass Transfer in Wastewater Treatment: When Current Knowledge Needs to Encounter Engineering Practice and Vice Versa. *Water Sci. Technol.* **2019**, *80* (4), 607–619.

(36) Han, J.; Eimer, D. A.; Melaaen, M. C. Liquid Phase Mass Transfer Coefficient of Carbon Dioxide Absorption by Water Droplet. *Energy Procedia* **2013**, *37*, 1728–1735.

(37) Yang, A. Modeling and Evaluation of CO2 Supply and Utilization in Algal Ponds. *Ind. Eng. Chem. Res.* **2011**, *50* (19), 11181–11192.

(38) Akita, K.; Yoshida, F. Bubble Size, Interfacial Area, and Liquid-Phase Mass Transfer Coefficient in Bubble Columns. *Ind. Eng. Chem. Process Des. Dev.* **1974**, *13* (1), 84–91.

Appendix C

I. Source terms in the CL

Table C.1 Source terms in the CL.

Species	Gas-liquid mass transfer	Homogenous reactions	Electrochemical reactions
$CO_2(g)$	$R_{P,CO_2(g)}$	–	–
N_2	–	–	–
H_2	–	–	R_{E,H_2}
CO	–	–	$R_{E,CO}$
$CO_2(aq)$	$R_{P,CO_2(aq)}$	$R_{H,CO_2(aq)}$	$R_{E,CO_2(aq)}$
$HCOO^-$	–	–	$R_{E,HCOO}$
${CO_3}^{2-}$	–	R_{H,CO_3}	–
${HCO_3}^-$	–	R_{H,HCO_3}	–

II. Key parameter values

Table C.2 Geometrical parameters in our model.

Geometric parameter	Value
GASC thickness, L_{GASC}	5×10^{-3} m
GDL thickness, L_{GDL}	2.1×10^{-4} m
CL thickness, L_{CL}	2×10^{-5} m
ELEC thickness, L_{ELEC}	1.1×10^{-2} m
Electrode height, H_E	1.5×10^{-2} m
Electrode width, W_E	1.3×10^{-2} m
GASC extension length, H_{EXT}	1.5×10^{-3} m
Cathode geometrical surface area, A_C	2×10^{-4} m^2

Table C.3 Key physicochemical parameter values of the model.

	Value	Reference

Gaseous species		
Binary diffusivity of the component CO_2(g) and H_2, $D_{CO_2H_2}$	6.46×10^{-5} m^2 s^{-1}	[1]
Binary diffusivity of the component CO_2(g) and N_2, $D_{CO_2N_2}$	1.65×10^{-5} m^2 s^{-1}	[1]
Binary diffusivity of the component CO_2(g) and CO, D_{CO_2CO}	1.52×10^{-5} m^2 s^{-1}	[1]
Binary diffusivity of the component H_2 and N_2, $D_{H_2N_2}$	7.79×10^{-5} m^2 s^{-1}	[1]
Binary diffusivity of the component H_2 and CO, D_{H_2CO}	7.43×10^{-5} m^2 s^{-1}	[1]
Binary diffusivity of the component CO and N_2, D_{CON_2}	2.02×10^{-5} m^2 s^{-1}	[1]
Aqueous species		
Diffusivity for CO_3^{2-}, D_{CO_3}	9.23×10^{-10} m^2 s^{-1}	[1]
Diffusivity for CO_2(aq), $D_{CO_2(aq)}$	1.70×10^{-9} m^2 s^{-1} *	Calculated
Diffusivity for HCO_3^-, D_{HCO_3}	1.185×10^{-9} m^2 s^{-1}	[1]
Diffusivity for $HCOO^-$, D_{HCOO}	5×10^{-10} m^2 s^{-1}	[2]
Diffusivity for OH^-, D_{OH}	5.293×10^{-9} m^2 s^{-1}	[1]
Phase change reaction		
Henry's constant for CO_2, H_{CO_2}	See below**	Calculated
Mass transfer coefficient for CO_2, K_{GL}	1×10^{-4} m s^{-1}***	
Homogeneous reactions		
Equilibrium constant for the reaction (R5.4), $K_{HR5.4}$	1×10^{8} M^{-1}	[1]
Equilibrium constant for the reaction (R5.5), $K_{HR5.5}$	4.66×10^{3} M^{-1}	[3]
Forward rate constant for the reaction (R5.4), $k_{HR5.4}$	1×10^{3} M^{-1}s^{-1}	[4]
Forward rate constant for the reaction (R5.5), $k_{HR5.5}$	1×10^{8} M^{-1}s^{-1}	[3]
Electrode kinetics		
Charge transfer coefficient for the reaction (R5.1), $\alpha_{ER5.1}$	0.4***	
Charge transfer coefficient for the reaction (R5.2), $\alpha_{ER5.2}$	0.4***	[1]
Charge transfer coefficient for the reaction (R5.3), $\alpha_{ER5.3}$	0.23 ***	[5]
Exchange current density of the reaction (R5.1),$i_{o,ER5.1}^{ref}$	0.90 A m^{-2} ***	[6]
Exchange current density for the reaction (R5.2), $i_{o,ER5.2}^{ref}$	0.70 A m^{-2}***	[7]
Exchange current density for the reaction (R5.3), $i_{o,ER5.3}^{ref}$	0.015 A m^{-2} ***	[5]

Reference $CO_2(aq)$ concentration of the reaction (R5.1), $C^{ref}_{CO_2(aq),ER5.1}$	1 M	
Reference $CO_2(aq)$ concentration of the reaction (R5.2), $C^{ref}_{CO_2(aq),ER5.2}$	1 M	
Standard potential for the reaction (R5.1), $\varphi^{ref}_{eq,ER5.1}$ in the reference condition (pH=14)	-1.02 V vs SHE	[8,9]
Standard potential for the reaction (R5.2), $\varphi^{ref}_{eq,ER5.2}$ in the reference condition (pH=14)	-0.936 V vs SHE	[10,11]
Standard potential for the reaction (R5.3), $\varphi^{ref}_{eq,ER5.3}$ in the reference condition (pH=14)	-0.83 V vs SHE	[8,9,11]

*See Section VI for calculation details.

**See Section VII for calculation details.

***The values were obtained in this study through parameter fitting by using the experimental data for 0.1M KOH within the range reported in the cited references.

Table C.4 Default values for design and operational parameters.

Definition and symbol	Value	Reference
Universal Parameter		
Density of $CO_2(g)$, $\rho_{CO_2(g)}$	1.83 kg m^{-3}	
Density of H_2, ρ_{H_2}	8.3×10^{-2} kg m^{-3}	
Density of N_2, ρ_{N_2}	1.164 kg m^{-3}	
Density of CO, ρ_{CO}	1.164 kg m^{-3}	
Faraday constant, F	96485 C mol^{-1}	
Ideal gas constant, R_g	8.314 J K^{-1} mol^{-1}	
Molar weight for CO_2, M_{CO_2}	4.4×10^{-2} kg mol^{-1}	
Molar weight for CO_3^{2-}, M_{CO_3}	6.0×10^{-2} kg mol^{-1}	
Molar weight for H_2, M_{H_2}	2×10^{-3} kg mol^{-1}	
Molar weight for $HCOO^-$, M_{HCOO}	4.5×10^{-2} kg mol^{-1}	

Molar weight for OH^- , M_{OH}	1.7×10^{-2} kg mol^{-1}	
Molar weight for CO, M_{CO}	2.8×10^{-2} kg mol^{-1}	
Molar weight of N_2, M_{N_2}	1.4×10^{-2} kg mol^{-1}	
Valence of CO_3^{2-}, z_{CO_3}	-2	
Valence of HCO_3^-, z_{HCO_3}	-1	
Valence of $HCOO^-$, z_{HCOO}	-1	
Operating Setting Parameters		
Electrolyte volumetric flow rate, q_l	For $\varphi_C = -0.17 \sim -0.77$ V vs RHE: 0.25 ml min^{-1} ; For $\varphi_C = -0.77 \sim -1.17$ V vs RHE, 0.5 ml min^{-1}	[7]a
Default feed gas velocity, $u_{g,in}^0$	3.85×10^{-3} m s^{-1}	[7]a
Molar fraction of CO_2(g) in feed gas, $x_{CO_2(g),in}$	99.99%	[7]a
Molar fraction of N_2 in feed gas, $x_{N_2,in}$	0.01%	[7]a
Operating temperature, T	293 K	[7]a
Saturation coefficient in the CL, S_{CL}	0.5	Calculated
Saturation coefficient in GDL, S_{GDL}	0	Assumed
Design Parameters		
Catalyst nanoparticle diameter, d_{cat}	1×10^{-7} m	[7]a
Cathode potential, φ_C	$-0.17 \sim 1.17$ V vs RHE*	[7]a
Cross section area of ELEC, A_{ELEC}	1.43×10^{-4} m^2	b
Cross section area of GASC, A_{GASC}	6.5×10^{-5} m	b
Density of catalyst, ρ_{cat}	6.2×10^3 kg m^{-3}	b
Intrinsic electronic conductivity in the CL, $k_{s,CL}^o$	7.27×10^4 S m^{-1}	[12]
Intrinsic electronic conductivity in the GDL, $k_{s,GDL}^o$	6.8×10^3 S m^{-1}	b
Intrinsic porosity in the GDL, ϵ_{GDL}^0	0.8	[1]
Mass loading of catalyst, m_{cat}	5 mg cm^{-2}	a
Mean CL porous radius, $r_{p,CL}$	3.5×10^{-8} m	[13]
Mean GDL porous radius, $r_{p,GDL}$	7.5×10^{-6} m	[14]

Standard/intrinsic permeability for the GDL, κ_{GDL}^{o}	1.34×10^{-12} m^2	[1,15]
Gaseous species		
Dynamic viscosity of mixture gas, μ_g	1.47×10^{-5} Pa s	
Aqueous species		
Electrolyte density, ρ_l	See below**	[16]
Electrolyte potential in the bulk, φ_{b}	0 V vs SHE	[1]
Intrinsic electrolyte conductivity, k_l^o	See below**	[7]a

a. Provided by our experiment collaborator;
b. Calculated by experimental data;

* The reversible hydrogen electrode (RHE) potential is obtained by bulk catholyte pH based on the Nernst equation (see Section VIII)

** The value varies with electrolyte KOH concentration (see Section IX and X);

III. Specific interfacial areas

Assumptions

1. It is assumed that all the pores in the CL are identical and with the same cylinder shape (as shown in the Figure C.1);
2. It is assumed that the electrolyte in the CL is evenly distributed throughout the pore and forms an equivalent film (blue portion in the Figure C.1) with the thickness of δ_{ele}; typical value of δ_{ele} in a fuel cell is 10 nm[1,17].
3. The gas phase is only trapped within the pores and occupies the rest of pore volume;
4. It is assumed that catalysts are evenly distributed across the CL pores.

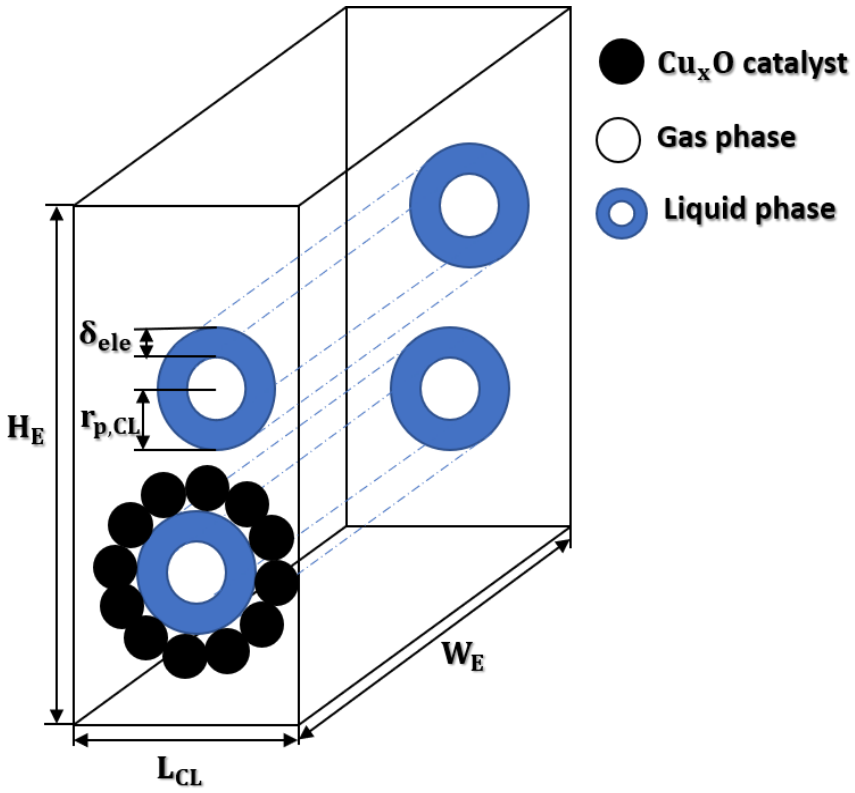

Figure C.1 Conceptual schematic of multiphase distribution in the CL.

Calculation

It is assumed that there are n_p pores in the CL. The total pore volume in the CL, V_p is:

$$V_p = \pi {r_{p,CL}}^2 W_E n_p \tag{C.1}$$

The total gas volume in the CL, V_g is:

$$V_g = \pi (r_{p,CL} - \delta_{ele})^2 W_E n_p \tag{C.2}$$

The definition of saturation coefficient in the CL, S_{CL} is:

$$S_{CL} = V_l / V_P \tag{C.3}$$

Based on the third assumption above:

$$V_p = V_l + V_g \tag{C.4}$$

The relationship between $r_{p,CL}, \delta_{ele}$ and S_{CL} is derived by coming Eqs. (C.1) to (C.4):

$$\delta_{ele} = r_{p,CL}(1 - \sqrt{1 - S_{CL}}) \tag{C.5}$$

Eq. (C.5) is consistent with the equation reported by the reference[1].

The number of pores in the CL is calculated by Eq. (C.1) and the definition for the intrinsic porosity in the CL, ϵ_{CL}^{o}:

$$n_p = \frac{\epsilon_{CL}^{0} V_{CL}}{\pi {r_{p,CL}}^2 W_E} \tag{C.6}$$

Thus, the specific interfacial surface area of solid-liquid interface (i.e. total solid-liquid interfacial area per bulk volume of CL), a_{sl} is:

$$a_{sl} = \frac{2\pi r_{p,CL} W_E n_p}{V_{CL}} = 2\frac{\epsilon_{CL}^{o}}{r_{p,CL}} \tag{C.7}$$

Similarly, the specific interfacial surface area of gas-liquid interface (i.e. total gas-liquid interfacial area per bulk volume of the CL), a_{gl} is:

$$a_{gl} = \frac{2\pi (r_{p,CL} - \delta_{ele}) W_E n_p}{V_{CL}} = 2\frac{\epsilon_{CL}^{0}(r_{p,CL} - \delta_{ele})}{{r_{p,CL}}^2} \tag{C.8}$$

IV. Specific electrical energy consumption (SEEC)

Potential distribution

V_{app} represents the required cell voltage, which is the consequence of the potential drop between the applied cathode potential and theoretical reversible anode potential adding a series of uncompensated overpotentials (losses): (i) overall activation overpotential, η_{act} induced by slower electrode kinetics; (ii) overall concentration overpotential, η_{con} due to lower mass transfer, and (iii) ohmic overpotential, η_{ohm} describing the resistance of such as electrolyte, membrane to the ions flow. The V_{app} can be obtained according to the voltage balance (see Figure C.2) and here we supposed that all calculated V_{app} are below the compliance voltage of the instrument (i.e. potentiostat):

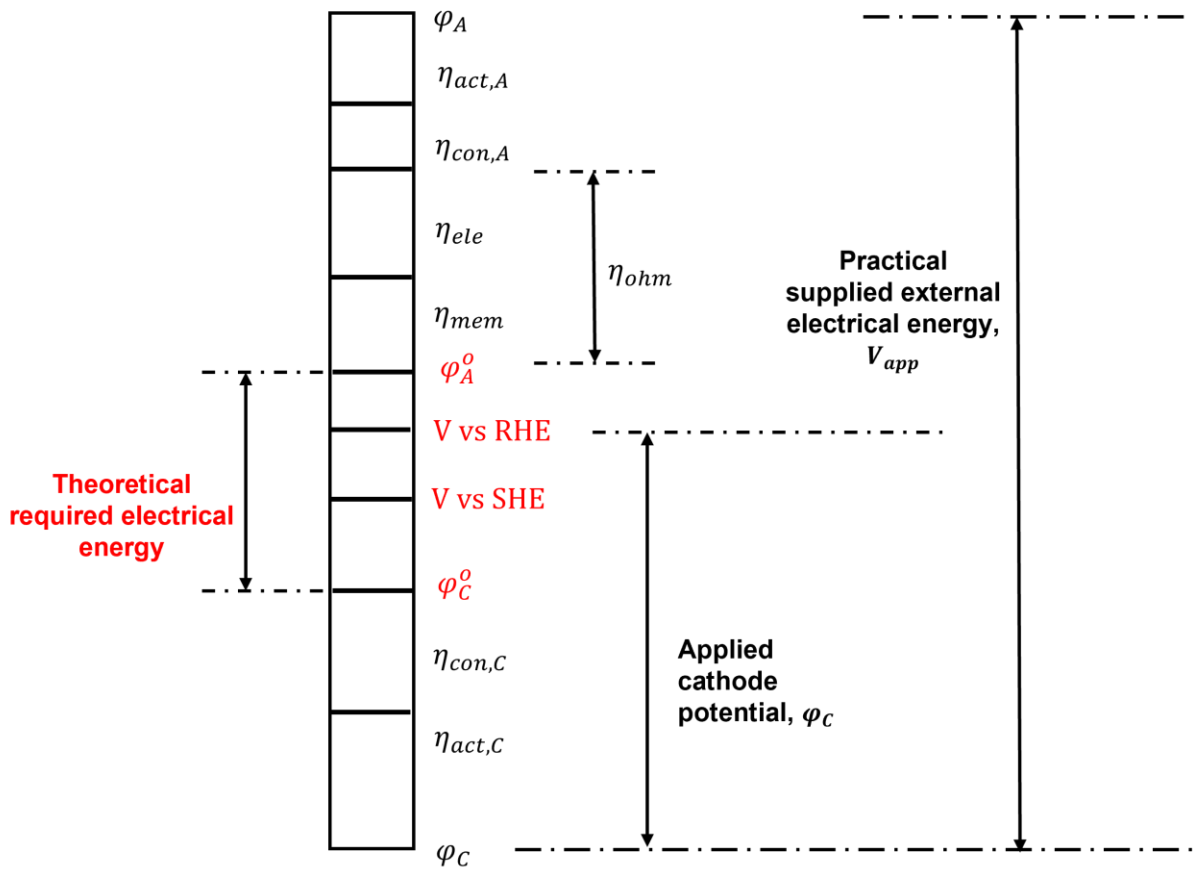

Figure C.2 Schematic representation of potential distributions in the three-electrode potentiostat system.

Anodic reaction

Oxygen evolution reaction (OER) takes place at the anode[7]:

$$4OH^- - 4e^- = O_2 + 2H_2O \qquad \text{(RC.1)}$$

Calculation

$$V_{app} = -(\varphi_C - \varphi_A^o) + \eta_{act,A} + \eta_{con,A} + \eta_{ohm} \qquad \text{(C.9)}$$

where φ_C (negative value) and φ_A^o (positive value) are the applied constant cathodic potential and theoretical reversible potential for anodic reaction, respectively; $\eta_{act,A}, \eta_{con,A}$ are the anodic activation overpotential and the anodic concentration overpotential, respectively; η_{ohm} is the ohmic overpotential across the whole cell. Note that V_{app} and all the overpotential terms assume positive values.

Given the relatively slow kinetics of the anodic reaction (i.e. OER), its activation overpotential cannot be neglected. It has been proposed that the OER on Platinum (Pt) in the alkaline condition is kinetically controlled by the step of Pt binding hydroxide ion to form the species of $\mathrm{Pt}^{\delta} - \mathrm{OH}_{\mathrm{ads}}$ ($\mathrm{Pt} + \mathrm{OH}^{-} = \mathrm{Pt}^{\delta} - \mathrm{OH}_{\mathrm{ads}} + \mathrm{e}^{-}$)[18]. Thus, the activation overpotential and concentration overpotential, which have been reported to follow a logarithmic relationship with current density, are approximated by[9,19,20]:

$$\eta_{act,A} = \frac{R_g T}{\alpha_A F} sinh^{-1}(\frac{i_A}{2i_{o,A}}) \tag{C.10}$$

$$\eta_{con,A} = -\frac{R_g T}{n_A F} ln(1 - \frac{i_A}{i_{L,A}}) \tag{C.11}$$

where i_A is the current density with respect to the anode geometrical surface area; α_A is the symmetry factor for the anodic reaction, which is set as 0.5 for the method of hyperbolic sine approximation[19]; $i_{o,A}$ and n_A are the exchange current density and the number of transferred electrons for the anodic reaction, respectively. i_A can be linked to the superficial overall current density with respect to the cathode geometrical surface area, i_C by the anode and cathode geometrical surface areas, A_A and A_C:

$$I = i_A A_A = |i_C| A_C \tag{C.12}$$

where I represents the overall current passing though the circuit.

$i_{L,A}$ is the anodic limiting current density corresponding to the maximum reactant consumption rate. Its value is obtained by applying the assumption of no reactant at the reaction site[9,19]:

$$i_{L,A} = \frac{n_A F D_{OH} C_{OH,A,b}}{\delta_d} \tag{C.13}$$

where D_{OH} is the diffusivity for the anodic reactant, OH^{-}; $C_{OH,A,b}$ is the bulk (anolyte) concentration of the anodic reactant, OH^{-}; δ_d is the diffusion layer thickness.

For the ohmic overpotential, the resistance caused by the bubble effect on the anode and the circuit are negligible[21–23]. The ohmic overpotential from ions transportation across the electrolyte and membrane is calculated by[20]:

$$\eta_{ohm} = I(\frac{1}{k_{ele}L_{AC}} + A_{mem}R_{mem}) \quad \text{(C.14)}$$

where L_{AC} is the distance between the two electrodes; k_{ele} is the electrolyte conductivity; A_{mem} and R_{mem} are the geometrical surface area and the specific resistance of the cation exchange membrane, respectively.

The parameter values for SEEC calculations can be found in the following table and Section II.

Parameter values for SEEC calculation

Table C.5 Parameter values for SEEC calculation.

Definition and symbol	Value	Reference
SEEC		
Faraday efficiency for $HCOO^-$, FE_{HCOO}	Simulation results	
Theoretical reversible potential for anodic reaction, φ_A^o	+0.40 V vs SHE	23
Activation overpotential		
Anode geometrical surface area, A_A	4 cm^2	7
Bulk concentration of the anodic reactant, $C_{OH,A,b}$	5.0 M***	7
Diffusion layer thickness, δ_d	0.05 cm**	24
Distance between anode and cathode, L_{AC}	2.6 cm*	7
Electrolyte conductivity, k_{ele}	35 S m^{-1}***	7
Exchange current density for the anodic reaction (OER), $i_{o,A}$	1×10^{-7} A m^{-2}**	25
Geometrical surface area of CEM, A_{mem}	3.6 cm × 2.4 cm	7
Number of transferred electrons of anodic reaction (OER), n_A	4	
Specific resistance of CEM, R_{mem}	2 Ω cm^{-2}**	26
Symmetry factor for anodic reaction (OER), α_A	0.5	19

* The value is derived from experimental data. $L_{AC} = L_A + L_C + L_w$. L_A, L_C, L_w denote the thickness of anodic chamber, cathodic chamber and the plate with window. $L_A = 1.4$ cm; $L_C = 0.9$ cm; $L_w = 0.3$ cm.

**The value was measured and reported in others‘ work

- For δ_d: the value used here is the estimated diffusion layer thickness for unstirred solutions, which was reported by the reference[24];
- For $i_{o,A}$: the value used here was measured from the experiment[25], where OER takes place on Platinum (Pt) electrode in alkaline condition. In our experiment[7], the anode was Platinum plated Titanium mesh and 5.0 M KOH was employed as anolyte (i.e. electrolyte in the anode chamber). Given these two experiments[7,25] are similar, the reported value 1×10^{-7} A m^{-2} was directly applied for the calculation;
- For R_{mem}: The value used here was for one of the types of CEM (FKD), measured in 0.5 M NaCl solution at 298K.

*** The values obtained from our experiment together with assumptions:

- For $C_{OH,A,b}$: It is assumed that bulk concentration of anodic reactant, OH^- is constant;
- For k_{ele}: the values for 2.0 M KOH is employed here by assuming identical electrolyte conductivity for 2.0 M KOH and 5.0 M KOH.

Distribution of applied potential

Figure C.3 reveals the distribution of the applied potential, V_{app} in detail. One can see that the sum of the ohmic overpotential and the anodic activation overpotential forms a significant part of the potential loss, with the dominance of the latter shifting to that of the former as the applied cathode potential becomes more negative. These losses could be reduced by measures such as the use of superior anode material with faster kinetics, application of the electrolyte with higher conductivity and reduction of the distance between electrodes by using membrane-less cells.

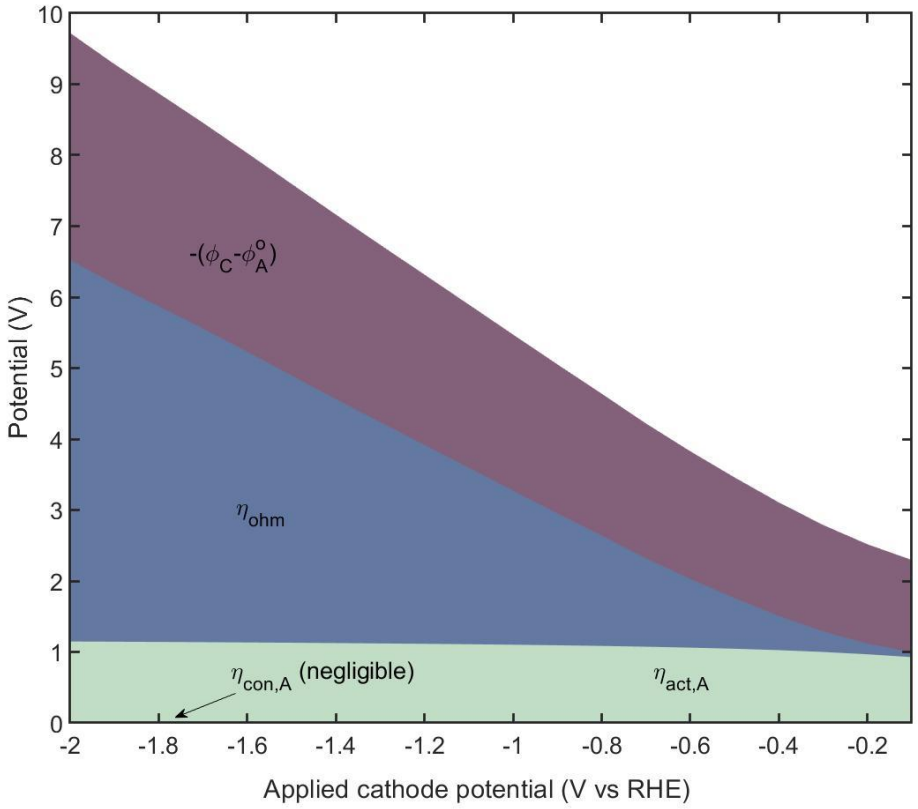

Figure C.3 Applied potential distribution.

V. Additional model validation based on $KHCO_3$ electrolyte

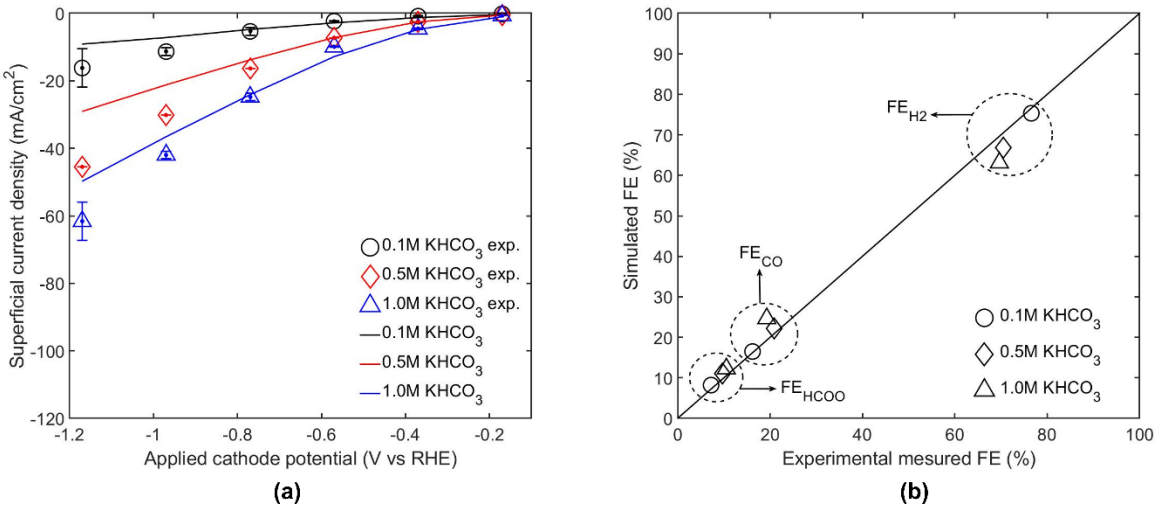

Figure C.4 (a) Overall superficial current density with respect to the cathode geometrical surface area; (b) averaged selectivity from data for different cathode potential levels, with various $KHCO_3$ concentrations, compared with the experimental data.

The experimental data and the detailed experiment setup can be found in reference[7]. From the Figure C.4(b), it is clear that our model is capable of capturing the selectivity (i.e. FE_{HCOO}, FE_{CO} and FE_{H_2}) with very good fidelity for all tested scenarios (i.e. all tested $KHCO_3$ concentrations and values of applied cathodic potential). In terms of the overall superficial current density (Figure C.4(a)), our model could predict its value well for all systems (i.e. with all tested $KHCO_3$ concentrations) when the cathode was imposed with relatively positive values. For the system with more negative cathodic potential, the apparent departure of our simulation from experimental results, similar to that observed in the model validation presented in the main text for the system using KOH as the electrolyte, could be attributed to (i) larger random errors of experimental measurements[7], and (ii) more pronounced impact of dynamic changes with increasing current[7].

VI. $CO_2(aq)$ diffusivity, $D_{CO_2(aq)}$ in various KOH concentration

The diffusivity of dissolved CO_2 in pure water, $D_{CO_2(aq),w}$ is given by[27]:

$$D_{CO_2(aq),w} = 2.35 \times 10^{-6} exp\left(\frac{-2119}{T}\right) \text{ m}^2 \text{ s}^{-1} \quad \text{(C.15)}$$

where T(K) is the operating temperature and equals to 293K in our case.

The CO_2(aq) diffusivity in various KOH concentrations can be calculated by[28]:

$$\frac{D_{CO_2(aq)}}{D_{CO_2(aq),w}} = 1 - 1.29 \times 10^{-4} C_{OH} \quad \text{(C.16)}$$

where C_{OH} (M) is the OH^- concentration. Therefore, the CO_2(aq) diffusivity in various KOH concentrations in our case are obtained and listed in the Table C.6.

Table C.6 CO_2(aq) diffusivity in various KOH concentration.

KOH concentration	**CO_2(l) diffusivity in water, $D_{CO_2(aq),w}$ ($m^2 s^{-1}$)**	$\frac{D_{CO_2(aq)}}{D_{CO_2(aq),w}}$	**CO_2(aq) diffusivity in KOH, $D_{CO_2(aq)}$ ($m^2 s^{-1}$)**
0.1 M	1.70×10^{-9}	1.00	1.70×10^{-9}
0.5 M		1.00	
1.0 M		1.00	

2.0 M	1.00

VII. Calculation of Henry's constant taking into account salting-out effect

The effect of dissolved ionic species on the Henry's constant, known as the salting-out effect[29–31]. For CO_2, H_{CO_2} should be considered when different composition and concentration of electrolyte is employed and compared[29,30,32].

Combining the Sechenov[30,31] (or written as the German transliteration of 'Setschenow'[29]) relationship that mathematically describes the effect of salinity and the Henry's law, which is applicable for our system[29,32,33], the Henry's constant is given by:

$$log\, H_{CO_2} = log\, H_{CO_2,w} + k_s C_{ele} \tag{C.17}$$

where $H_{CO_2,w}$ and H_{CO_2} (Pa M^{-1}) are the Henry's constant for CO_2 in pure water and electrolyte, respectively; k_s (M^{-1}) is the 'Sechenov constant' and C_{ele} (M) denotes the electrolyte salinity.

As stated in the main text, the fresh electrolyte was continuously supplied through the electrolyte channel and the CL is sufficiently thin, therefore we assume the value of C_{ele} remains identical to the feed concentration. $H_{CO_2,w}$ can be calculated from the value of Henry's constant in the pure water at the reference temperature (T^{ref}), $H^{ref}_{CO_2,w}$ using the following correction which is based on the Van't Hoff equation[29,31]:

$$\frac{1}{H_{CO_2,w}} = \frac{1}{H^{ref}_{CO_2,w}} exp\left(-\frac{\Delta_{sol}H}{R_g}\left(\frac{1}{T} - \frac{1}{T^{ref}}\right)\right) \tag{C.18}$$

where $\Delta_{sol}H$ (J mol^{-1}) is the enthalpy of dissolution and R_g (J mol^{-1} K^{-1}) is the ideal gas constant. The value of $\Delta_{sol}H$ at T^{ref} has been used for the calculation (note the narrow difference between T, 293 K and T^{ref}, 298.15 K).

The effect of salinity is actually determined by the dissolved species and ionic strength[31]. For our case, the value of the k_s is given by[30]:

$$k_s = \sum (h_i + h_G)\, n_i \tag{C.19}$$

where h_G (M^{-1}) is the gas-specific constant; h_i (M^{-1}) is the ion-specific parameter of ion i and n_i is the index of ion i in the salt formula. Analogous to the Henry's constant, the 'Sechenov constant' varies with temperature and this assumed linear trend can be captured by the S. Weisenberger & A. Schumpe model[30]:

$$h_G = h_G^{ref} + h_T(T - T^{ref}) \tag{C.20}$$

where h_G^{ref} (M^{-1}) is the gas-specific constant measured at the reference temperature, T^{ref}; the second term of Eq. (C.20) is the correction term for the effect of temperature and h_T ($\mathrm{M}^{-1}\mathrm{K}^{-1}$) is named as the temperature coefficient here.

It is worthy to mention that the value of k_s remains constant for each of modelled system with various electrolyte, due to the applied isothermal assumption[30]. The parameters used for Henry's constant calculation are listed in Table C.7 and the results are tabulated in Table C.8.

Table C.7 Parameter values for H_{CO_2} calculation.

	Value	**Reference**
Reference temperature, T^{ref}	298.15 K	31
The referenced Henry's constant for $\mathrm{CO_2}$ in the pure water, $H_{CO_2,w}^{ref}$	29 atm M^{-1}	31
Term of $\frac{-\Delta_{sol}H}{R_g}$ in the Eq. (C.18)	2400 K	31
Ion-specific parameter of $\mathrm{K^+}$, h_{K^+}	0.0922 M^{-1}	30
Ion-specific parameter of $\mathrm{OH^-}$, h_{OH^-}	0.0839 M^{-1}	30
Ion-specific parameter of $\mathrm{HCO_3^-}$, $h_{HCO_3^-}$	0.0967 M^{-1}	30
The referenced gas-specific constant for $\mathrm{CO_2}$, h_G^{ref}	-0.0172 M^{-1}	30
The temperature coefficient for $\mathrm{CO_2}$, h_T	-0.338×10^{-3} $\mathrm{M}^{-1}\mathrm{K}^{-1}$	30

Table C.8 Values for H_{CO_2} at various KOH and $KHCO_3$ concentrations.

	KOH	**$\mathbf{KHCO_3}$**

Concentration (M)	0.1	0.5	1.0	2.0	0.1	0.5	1.0
H_{CO_2} (atm M^{-1})	26	30	35	49	26	30	36

VIII. Reversible hydrogen electrode (RHE) potential

According to the Nernst equation:

$$V\ (\text{vs RHE}) = 0 - 0.059\text{pH} \tag{C.21}$$

It should be noted here that pH value used for Eq. (C.21) refers to the pH of bulk catholyte, which are measured by the experiment[7] and listed below:

Table C.9 pH of bulk catholyte at various KOH and $KHCO_3$ concentrations.

	KOH				**$KHCO_3$**		
Concentration (M)	0.1	0.5	1.0	2.0	0.1	0.5	1.0
pH	13.02	13.56	13.96	14.30	8.55	9.04	9.67

The constant pH value of bulk catholyte is maintained by supplying fresh electrolyte during the experiment[7].

IX. Density of different concentrations of aqueous solutions of KOH and $KHCO_3$ at 293K

The density of KOH (kg m^{-3}) of various molarity (M) at 293K can be calculated based on the following formula:[16]

$$\rho_l = -0.4824M^2 + 45.649M + 1001 \tag{C.22}$$

The values of density of KOH and $KHCO_3$ at various concentrations (M) at 293K are summarised below:

Table C.10 Values of density of KOH and $KHCO_3$ at various concentrations (M) at 293K.

	KOH	**$KHCO_3$**

Concentration (M)	0.1	0.5	1.0	2.0	0.1	0.5	1.0
Density (kg m^{-3})	1006	1024	1046	1090	1005	1031	1065

X. Values of specific conductivity of KOH and $KHCO_3$ at various concentrations (M)

Table C.11 Values of specific conductivity of KOH and $KHCO_3$ at various concentrations (M).

	KOH				**$KHCO_3$**		
Concentration (M)	0.1	0.5	1.0	2.0	0.1	0.5	1.0
Conductivity (S m^{-1})	2.26	10.74	20.13	35.18	1	5	8

The data of specific conductivity for KOH are from the experimental measurements[7]. The data of specific conductivity for $KHCO_3$ are from the literature[34].

XI. Testing parameter data

Table C.12 Testing parameter data.

Parameter	**Default value**	**Testing range**	**Unit**
V_C	-0.5	$[-0.1:-0.1:-2.0]$	V vs RHE
ξ	1*	$[1:5:20]$	Dimensionless
$u_{g,in}$	1**	$[1:1:10]$	$u_{g,in}^0$(m s^{-1})
$x_{CO_2(g),in}$	99.99	[60,70,80,90,99.99]	%
ϵ_{CL}^o	0.6	$[0.4:0.1:0.8]$	Dimensionless
m_{cat}	5	$[1:1:5]$	mg cm^{-2}

* $\xi = 1$ corresponds to the default cathode geometrical surface area of 2×10^{-4} m^2.

**default value for $u_{g,in}^0$ is 3.85×10^{-3} m s^{-1} .

XII. Effect of inlet gas composition and velocity

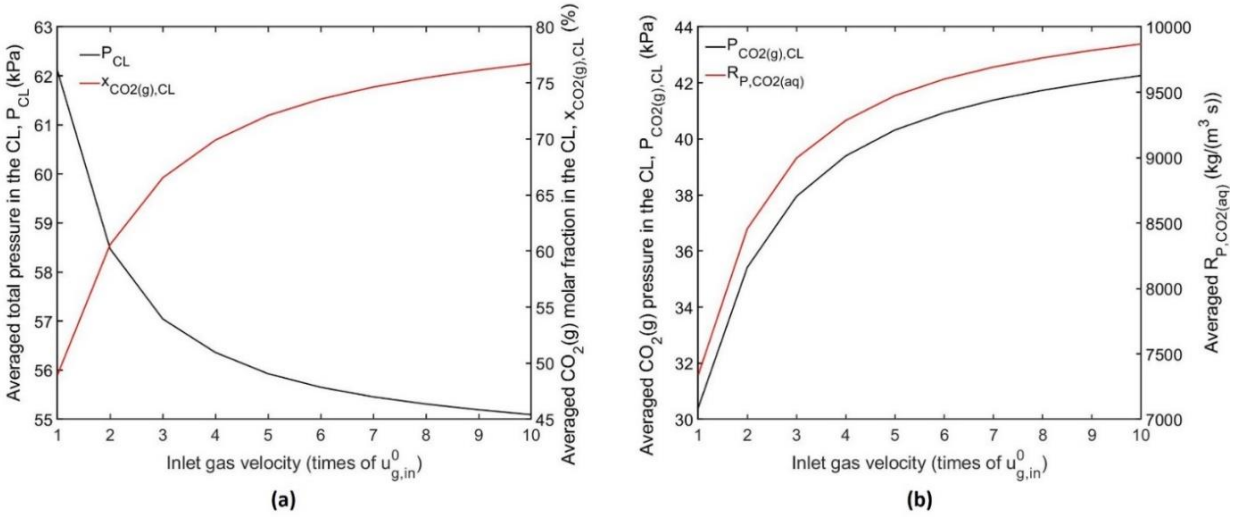

Figure C.5 (a) Average total pressure and CO_2(g) molar fraction in the CL and (b) CO_2(g) partial pressure and gas-liquid mass transfer rate in the CL, as the function of inlet gas velocity.

XIII. Effect of catalyst loading and arrangement

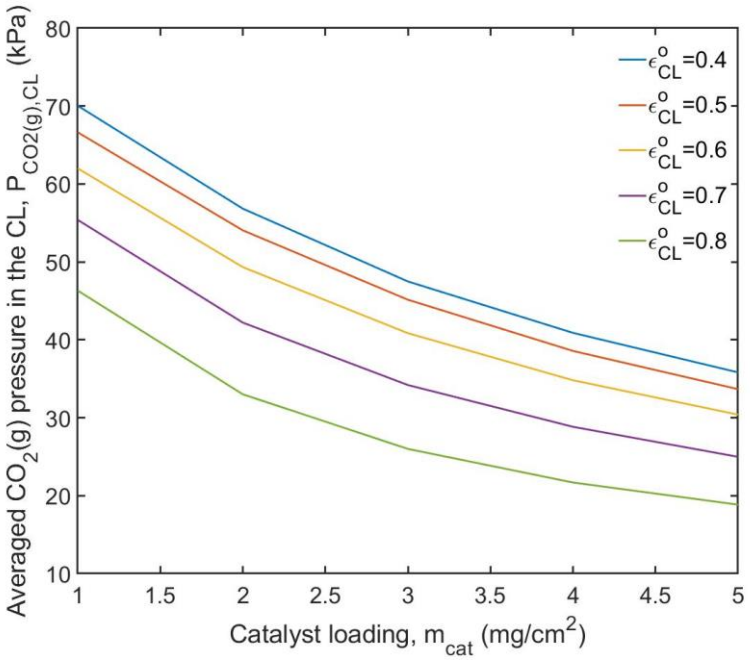

Figure C.6 CO_2(g) partial pressure in the CL, as the function of catalyst loading and CL intrinsic porosity.

References

(1) Weng, L. C.; Bell, A. T.; Weber, A. Z. Modeling Gas-Diffusion Electrodes for CO2 Reduction. *Phys. Chem. Chem. Phys.* **2018**, *20*, 16973–16984.

(2) Wang, H.; Leung, D. Y. C.; Xuan, J. Modeling of a Microfluidic Electrochemical Cell for CO2 Utilization and Fuel Production. *Appl. Energy* **2013**, *102*, 1057–1062.

(3) Suter, S.; Haussener, S. Optimizing Mesostructured Silver Catalysts for Selective Carbon Dioxide Conversion into Fuels. *Energy Environ. Sci.* **2019**, *12*, 1668–1678.

(4) Weng, L. C.; Bell, A. T.; Weber, A. Z. Towards Membrane-Electrode Assembly Systems for CO2 Reduction: A Modeling Study. *Energy Environ. Sci.* **2019**, *12*, 1950–1968.

(5) Sheng, W.; Myint, M.; Chen, J. G.; Yan, Y. Correlating the Hydrogen Evolution Reaction Activity in Alkaline Electrolytes with the Hydrogen Binding Energy on Monometallic Surfaces. *Energy Environ. Sci.* **2013**, *6*, 1509–1512.

(6) Qiao, J.; Fan, M.; Fu, Y.; Bai, Z.; Ma, C.; Liu, Y.; Zhou, X. D. Highly-Active Copper Oxide/Copper Electrocatalysts Induced from Hierarchical Copper Oxide Nanospheres for Carbon Dioxide Reduction Reaction. *Electrochim. Acta* **2015**, *153*, 559–565.

(7) Xiang, H.; Rasul, S.; Scott, K.; Portoles, J.; Cumpson, P.; Yu, E. H. Enhanced Selectivity of Carbonaceous Products from Electrochemical Reduction of CO2 in Aqueous Media. *J. CO2 Util.* **2019**, *30*, 214–221.

(8) Li, H.; Oloman, C. Development of a Continuous Reactor for the Electro-Reduction of Carbon Dioxide to Formate - Part 2: Scale-Up. *J. Appl. Electrochem.* **2007**, *37*, 1107–1117.

(9) Qiao, J.; Liu, Y.; Zhan, J. *Electrochemical Reduction of Carbon Dioxide: Fundamentals and Technologies*; Taylor & Francis, 2016.

(10) Verma, S.; Lu, X.; Ma, S.; Masel, R. I.; Kenis, P. J. A. The Effect of Electrolyte Composition on the Electroreduction of CO2 to CO on Ag Based Gas Diffusion

Electrodes. *Phys. Chem. Chem. Phys.* **2016**, *18*, 7075–7084.

(11) Jeanty, P.; Scherer, C.; Magori, E.; Wiesner-Fleischer, K.; Hinrichsen, O.; Fleischer, M. Upscaling and Continuous Operation of Electrochemical CO2 to CO Conversion in Aqueous Solutions on Silver Gas Diffusion Electrodes. *J. CO2 Util.* **2018**, *24*, 454–462.

(12) Wu, K.; Birgersson, E.; Kim, B.; Kenis, P. J. A.; Karimi, I. A. Modeling and Experimental Validation of Electrochemical Reduction of CO2 to CO in a Microfluidic Cell. *J. Electrochem. Soc.* **2015**, *162* (1), F23–F32.

(13) Sabharwal, M.; Pant, L. M.; Putz, A.; Susac, D.; Jankovic, J.; Secanell, M. Analysis of Catalyst Layer Microstructures: From Imaging to Performance. *Fuel Cells* **2016**, *16* (6), 734–753.

(14) Ostadi, H.; Rama, P.; Liu, Y.; Chen, R.; Zhang, X. X.; Jiang, K. 3D Reconstruction of a Gas Diffusion Layer and a Microporous Layer. *J. Memb. Sci.* **2010**, *351*, 69–74.

(15) Zenyuk, I. V.; Medici, E.; Allen, J.; Weber, A. Z. Coupling Continuum and Pore-Network Models for Polymer-Electrolyte Fuel Cells. *Int. J. Hydrogen Energy* **2015**, *40*, 16831–16845.

(16) Gilliam, R. J.; Graydon, J. W.; Kirk, D. W.; Thorpe, S. J. A Review of Specific Conductivities of Potassium Hydroxide Solutions for Various Concentrations and Temperatures. *Int. J. Hydrogen Energy* **2007**, *32*, 359–364.

(17) Cetinbas, F. C.; Ahluwalia, R. K.; Kariuki, N.; De Andrade, V.; Fongalland, D.; Smith, L.; Sharman, J.; Ferreira, P.; Rasouli, S.; Myers, D. J. Hybrid Approach Combining Multiple Characterization Techniques and Simulations for Microstructural Analysis of Proton Exchange Membrane Fuel Cell Electrodes. *J. Power Sources* **2017**, *344*, 62–73.

(18) Favaro, M.; Valero-Vidal, C.; Eichhorn, J.; Toma, F. M.; Ross, P. N.; Yano, J.; Liu, Z.; Crumlin, E. J. Elucidating the Alkaline Oxygen Evolution Reaction Mechanism on Platinum. *J. Mater. Chem. A* **2017**, *5*, 11634–11643.

(19) Noren, D. A.; Hoffman, M. A. Clarifying the Butler-Volmer Equation and Related Approximations for Calculating Activation Losses in Solid Oxide Fuel Cell Models. *J.*

Power Sources **2005**, *152*, 175–181.

(20) Givirovskiy, G.; Ruuskanen, V.; Ojala, L. S.; Lienemann, M.; Kokkonen, P.; Ahola, J. Electrode Material Studies and Cell Voltage Characteristics of the in Situ Water Electrolysis Performed in a PH-Neutral Electrolyte in Bioelectrochemical Systems. *Heliyon* **2019**, *5*, e01690.

(21) Kim, H.; Hwang, H.; Baek, S.; Kim, D. Design, Fabrication and Performance Evaluation of a Printed-Circuit-Board Microfluidic Electrolytic Pump for Lab-on-a-Chip Devices. *Sensors Actuators, A Phys.* **2018**, *277*, 73–84.

(22) Zeng, K.; Zhang, D. Recent Progress in Alkaline Water Electrolysis for Hydrogen Production and Applications. *Prog. Energy Combust. Sci.* **2010**, *36*, 307–326.

(23) Wang, M.; Wang, Z.; Gong, X.; Guo, Z. The Intensification Technologies to Water Electrolysis for Hydrogen Production - a Review. *Renew. Sustain. Energy Rev.* **2014**, *29*, 573–588.

(24) Bockris, J. O.; Huq, A. K. M. S. The Mechanism of the Electrolytic Evolution of Oxygen on Platinum. *Proc. R. Soc. London. Ser. A. Math. Phys. Sci.* **1956**, *237* (1209), 277–296.

(25) Damjanovic, A.; Dey, A.; Bockris, J. O. M. Kinetics of Oxygen Evolution and Dissolution on Platinum Electrodes. *Electrochim. Acta* **1966**, *11*, 791–814.

(26) Długołecki, P.; Anet, B.; Metz, S. J.; Nijmeijer, K.; Wessling, M. Transport Limitations in Ion Exchange Membranes at Low Salt Concentrations. *J. Memb. Sci.* **2010**, *346*, 163–171.

(27) Versteeg, G. F.; van Swaal, W. P. M. Solubility and Diffusivity of Acid Gases (CO2, N2O) in Aqueous Alkanolamine Solutions. *J. Chem. Eng. Data* **1988**, *33* (1), 29–34.

(28) Darmana, D.; Henket, R. L. B.; Deen, N. G.; Kuipers, J. A. M. Detailed Modelling of Hydrodynamics, Mass Transfer and Chemical Reactions in a Bubble Column Using a Discrete Bubble Model: Chemisorption of CO2 into NaOH Solution, Numerical and Experimental Study. *Chem. Eng. Sci.* **2007**, *62*, 2556–2575.

(29) Valderrama, J. O.; Campusano, R. A.; Forero, L. A. A New Generalized Henry-

Setschenow Equation for Predicting the Solubility of Air Gases (Oxygen, Nitrogen and Argon) in Seawater and Saline Solutions. *J. Mol. Liq.* **2016**, *222*, 1218–1227.

(30) Weisenberger, S.; Schumpe, A. Estimation of Gas Solubilities in Salt Solutions at Temperatures from 273 K to 363 K. *AIChE J.* **1996**, *42* (1), 298–300.

(31) Sander, R. Compilation of Henry's Law Constants (Version 4.0) for Water as Solvent. *Atmos. Chem. Phys.* **2015**, *15*, 4399–4981.

(32) Carroll, J. J.; Mather, A. E. The System Carbon Dioxide-Water and the Krichevsky-Kasarnovsky Equation. *J. Solution Chem.* **1992**, *21* (7), 607–621.

(33) Moore, J. C.; Battino, R.; Rettich, T. R.; Handa, Y. P.; Wilhelm, E. Partial Molar Volumes of "Gases" at Infinite Dilution in Water at 298.15 K. *J. Chem. Eng. Data* **1982**, *27*, 22–24.

(34) Rosemount Analytical. *Conductance Data for Commonly Used Chemicals*; 2010; Vol. 44.